Doctoral theses at NTNU, 2010:23

Jørgen Hals

Modelling an phase control of wave-energy converters

Doctoral Thesis

Jørgen Hals

ISBN 978-82-471-2003-3 (printed version)
ISBN 978-82-471-2004-0 (electronic version)
ISSN 1503-8181

NTNU – Trondheim
Norwegian University of
Science and Technology

NTNU
Norwegian University of Science and Technology
Thesis for the degree of philosophiae doctor
Faculty of Engineering Science and Technology
Department of Marine Technology

Doctoral theses at NTNU, 2010:23

NTNU – Trondheim
Norwegian University of
Science and Technology

Jørgen Hals

Modelling and phase control of wave-energy converters

Thesis for the degree of philosophiae doctor

Trondheim, May 2010

Norwegian University of Science and Technology
Faculty of Engineering Science and Technology
Department of Marine Technology

NTNU – Trondheim
Norwegian University of
Science and Technology

NTNU
Norwegian University of Science and Technology

Thesis for the degree of philosophiae doctor

Faculty of Engineering Science and Technology
Department of Marine Technology

ISBN 82-471-2003-3 (printed ver.)
ISBN 82-471-2004-0 (electronic ver.)
ISSN 1503-8181

ITK Report 2010-58

Doctoral Theses at NTNU, 2010:23

Printed by Skipnes Kommunikasjon as

Abstract

Current prognoses are that, unless counteracted by very strong political measures, the world will meet both energy shortage and climate crisis within a horizon of a few decades, both of which are strongly related to our dependence on fossil fuels. Renewable energy sources may be harvested sustainably, and developing technology for their exploitation therefore forms an obvious part of strategies to reduce emissions and secure energy supply.

Wave energy is a resource with relatively high power density, readily available along the coasts, and thus coinciding with the areas where industry and people tend to be accumulated. In some regions this resource is large enough to form a significant part of the energy mix. The technology for harnessing the power of ocean waves is today still on the research and development stage. The challenge is to make a design where the costs of investment, operation and maintenance (in terms of money, resources and energy) can be justified by the availability and potential earnings.

This thesis focuses on two aspects of systems for wave energy conversion: How to model such systems, which is important for understanding and design, and how to control their motion, which is crucial for the primary power conversion – the inevitable step that forms the basis for revenues and energy output from such a device. The dissertation is based on articles published in scientific conferences and journals, as well as an account for background of the undertaken research and the methods used.

The bond graph modelling language has been chosen as a promising aid for the modelling of the power converter dynamics. It enables a systematic and transparent approach to the path from drawing board to mathematical equations. Examples show how energy conversion systems may be modelled and simulated within this framework. These include heave-motion models for a semi-submerged sphere, a platform/buoy two-body system and a small-scale oscillating water column (OWC), as well as wave-to-wire models of two made-up systems. The OWC model was also studied by laboratory experiments.

A range of control strategies has been studied and compared by numerical simulation, and in one case also by laboratory experiments. These strategies include phase control by latching and by clutching, approximations to complex-conjugate control, and model predictive control (MPC). Constraint handling and real-time parameter tuning are discussed, too. The constrained optimal power absorption is investigated, and for the example of a semi-submerged heaving sphere in irregular waves it is found that MPC in combination with a Kalman filter predictor is able to provide an absorbed power in excess of 90 % as compared to the non-causal (and hence not completely realisable) constrained optimum.

Other causal controller implementations gives an absorbed power ranging from 10 to 90 % of that achieved with MPC. The best performing control strategies, however, involve a large flow of reactive power through the machinery, which in normal irregular-wave operation may give peak-to-average power ratio as high as 25 and above. This represents a challenge to the design of machinery and controller.

An interesting observation from the numerical simulations is the possibility of increased absorbed power in irregular waves as compared to regular waves having about the same wavelength characteristics and the same wave power level. An explanation is suggested for this phenomenon.

Acknowledgements

This study came about as a result of an initiative within the Centre of Renewable energy (NTNU/SINTEF/IFE) led by Professor Johan Hustad, and has been carried out during the period from 2006 to 2009. The Norwegian Research Council is acknowledged for financing the work.

Most of all I wish to thank Professor Emeritus Johannes Falnes, who first presented me to the field of wave energy, and who has patiently supported and supervised me during the work with this PhD thesis: Your insight, dedication, kindness and thoroughness has been a key inspiration both for my education and for the completion of this work.

Next I owe huge thanks to Professor Torgeir Moan, who has been my main supervisor: Thank you for giving me the opportunity to perform this work as a part of the Centre for Ships and Ocean Structures, and for keeping me on (or at least close to) the track when my ideas have been too many and diverging. I have learned a lot from your focus on quality without compromise, and the ability to pinpoint the core issue. Thanks also to Professor Thor Inge Fossen, who has been the third person of my supervisor team: Your helpful comments, ideas and suggestions have been highly valuable.

One of the main delights during my PhD study, was the introduction to the bond graph modelling language. I wish to thank Associate Professor Eilif Pedersen and Professor Emeritus Hallvard Engja for teaching me this fascinating method. Hallvard Engja contributed heavily to the work presented at the European Wave and Tidal Energy Converence in 2007, and so did PhD Reza Taghipour. Thanks to Reza for solid work, lively discussions and a joyful cooperation.

A special thanks goes to Nicolai Løvdal and PhD Marta Molinas (now Professor) for the very inspiring collaboration we had during the first part of my study, and which led to the establishment of the International Network on Offshore Renewable Energy (INORE).

Furthermore I wish to thank friends and colleauges at Instituto Superior Técnico and the Wave Energy Centre in Lisbon for the valuable and memo-

rable time I spent there from September 2007 to January 2008. I owe special thanks to Professor Antònio Falcão for hosting me as a visiting researcher, and to Miguel Lopes, with whom I had the pleasure to work both within INORE and on one of the published articles.

I am also grateful to those colleagues and friends at NTNU and elsewhere who have contributed to an enjoyable and motiving atmosphere at work during these years.

Finally my warmest thanks go to Linn who stood beside me throughout this period, with whom I could share my ups and downs, and who surprisingly well did stand the absent-mindend moments of a researcher about to find the solution to an intriguing problem.

Trondheim, February 2010
Jørgen Hals

Contents

Abstract i

Acknowledgements iii

Nomenclature ix

List of published articles xiii

Declaration of authorship xv

1 Introduction 1

1.1 Background and motivation 1

1.2 Ocean wave energy 3

1.2.1 Historical and technical context 4

1.2.2 The resource 5

1.2.3 Conversion principles for wave energy 10

1.3 Thesis 13

1.3.1 Outline 13

1.3.2 Scope 13

1.3.3 Objective 15

2 Modelling 17

2.1 Conversion system outline 18

2.2 Effects governing the converter motion 19

2.3 Conventional mathematical formulation 21

2.4 Bond graph modelling 22

2.4.1 Absorber model – one degree of freedom 22

2.4.2 The radiation force 24

2.4.3 The excitation force 31

2.4.4 A two-body system 36

2.4.5 Models with several bodies and all modes of motion . 38

2.5 Discussion of contributions 40

3 Control **43**
3.1 Controller aim 43
3.2 Main control variable: The machinery force 44
3.3 Absorbed power and control principles 45
3.3.1 Maximum absorbed power: the optimal linear solution 45
3.3.2 The optimum is non-causal 46
3.3.3 Causal approximation to the optimum 46
3.3.4 The passive converter 47
3.3.5 Latching and clutching control strategies 48
3.3.6 Other controller implementations 49
3.3.7 Constraints 50
3.4 Discussion of contributions 50

4 Simulation **53**
4.1 Numerical integration algorithms 53
4.1.1 Matlab/Simulink 53
4.1.2 20-sim 54
4.2 Accuracy and convergence 54
4.3 Numerical experiments and statistical measures 55

5 Conclusion **57**
5.1 Overall summary 57
5.2 Original contributions 58
5.3 Recommendations for further work 59

References **61**

Appendices **73**

A Publications **73**

B Modelling of integrated WEC systems **191**
B.1 Machinery systems 191
B.1.1 Hydraulic equipment 192
B.1.2 Electric generators 193
B.1.3 Latching control using a direct-coupled generator . . . 199
B.2 Power conditioning and grid connection 200
B.2.1 Power converters 200
B.2.2 Hydraulic and electric analogies 203

B.2.3 The electric distribution grid 204
B.3 Mooring systems 204
B.3.1 Approximation based on equivalence to FEM results . 205
B.3.2 Lumped mooring line model 206
B.3.3 Coordinate transform: Linear 208
B.3.4 Coordinate transform: Nonlinear 209
B.4 Wave-to-wire models 210
B.4.1 WEC with hydraulic PTO 210
B.4.2 WEC with direct-coupled generator 212

C Structure of simulation algorithms **221**
C.1 Functional level 221
C.2 Routines 224
C.3 Stored variables 225

Nomenclature

For variables where the unit is undetermined, or for matrices having element-wise units, "SI" is written in the unit column signifying that SI units have been used also for these. In general scalars are given by normal lowercase (a) or uppercase (A) letters, vectors are given by boldface lowercase letters (**a**) and matrices are given by boldface uppercase letters (**A**).

$\delta(\cdot)$	[1]	Dirac's delta function
ϵ	SI	tolerance
ζ	[m]	wave elevation
η	[m]	body position (6-dimensional vector)
θ	[rad]	rotation angle about intermediate y axis
λ	[1]	damping factor
ρ	[kg/m^3]	water density
σ	[s]	Hankel singular values
τ_c	[s]	time shift
ϕ	[rad]	phase angle
ϕ	[rad]	rotation angle about final x axis
ψ	[Vs]	flux linkage
ψ	[rad]	rotation angle about initial z axis
ω	[rad/s]	angular frequency
$\mathbf{A}$	SI	system matrix
$A_\perp$	[rad]	projected area perpendicular to flow direction
a	[m/s^2]	acceleration
$\mathbf{B}$	SI	input matrix
$\mathbf{C}$	SI	output matrix
C_d	[kg/m^3]	drag coefficient
$\mathbf{D}$	SI	feed forward matrix
E	[N]	collection of force terms
e	SI	effort, power variable
F	[N]	force
f	SI	flow, power variable

$f(\cdot)$	SI	general function
$\mathbf{f}$	SI	vector with forces and moments as elements
$\mathbf{G}$	[1]	matrix
G	$[\Omega^{-1}]$	power converter control variable
g	$[\mathrm{m/s^2}]$	acceleration of gravity
H	[m]	wave height
$H_{F\zeta}$	SI	transfer function
$h_{F\zeta}$	SI	excitation force coefficient
I	SI	inertia
i	[A]	electric current
J	[W/m]	wave power level
k	[N/m]	impulse response function for the radiation force
k_J	$[\mathrm{kg/s^4}]$	wave power level proportionality constant
L	[H]	electric inductance
m, $\mathbf{M}$	SI	mass
m_r, $\mathbf{M}_r$	SI	added mass
N	[1]	total number of components or elements
P	[W]	power
p	[m]	position
p	SI	generalised momentum, energy variable
q	SI	generalised displacement, energy variable
R, $\mathbf{R}$	SI	resistance (mechanical or electric)
$\Re\{\cdot\}$		real part of a complex number
S, $\mathbf{S}$	SI	stiffness
S	SI	energy spectrum
T	[s]	wave period
t	[s]	time
u	[m/s]	velocity
u	[V]	electric voltage
X	SI	mechanical reactance
x	[m]	cartesian coordinate
y	[m]	cartesian coordinate
y	SI	output variable
Z	SI	impedance
z	[m]	cartesian vertical coordinate
$\mathbf{z}$	[1]	additional state vector

Abbreviations, acronyms and bond graph notation

1	junction: common flow
0	junction: common effort
C	capacitor
AC	alternating current
DC	direct current
GY	gyrator
HP	high pressure
I	inertia
LP	low pressure
M	modulated
MPC	model-predictive control
ODE	ordinary differential equation
PTO	power take-off
R	resistor
RAO	response amplitude operator
Se	source of effort
Sf	source of flow
TF	transformer

Subscripts and superscripts

$\hat{}$	complex amplitude
$'$	modified
a	absorbed
a	AC signal phase a
Bs	Bretschneider
b	AC signal phase b
c	AC signal phase c
e	excitation
i	integer
k	integer
l	mooring line
m	machinery
o	other
opt	optimal
p	peak
R	regarding the convolution part of the radiation force

r	radiation
ref	reference point
s	stiffness
s	significant
T	transpose
u	useful

List of published articles

Article A Engja, H. and Hals, J.: Modelling and simulation of sea wave power conversion systems. *Proceedings of the 7th European Wave and Tidal Energy Conference*, Porto, Portugal, 2007.

Article B Hals, J.; Taghipour, R. and Moan, T. Dynamics of a force-compensated two-body wave energy converter in heave with hydraulic power take-off subject to phase control. *Proceedings of the 7th European Wave and Tidal Energy Conference*, Porto, Portugal, 2007.

Article C Lopes, M.; Hals, J.; Gomes, R.; Moan, T.; Gato, L. and Falcão, A. O.: Experimental and numerical investigation of non-predictive phase-control strategies for a point-absorbing wave energy converter. *Ocean Engineering*, 2009, 36, 386 - 402.

Article D Hals, J.; Falnes, J. and Moan, T.: Constrained Optimal Control of a Heaving Buoy Wave Energy Converter. Accepted for publication in *Journal of Offshore Mechanics and Arctic Engineering*.

Article E Hals, J.; Falnes, J. and Moan, T.: A comparison of selected strategies for adaptive control of wave energy converters. Accepted for publication in *Journal of Offshore Mechanics and Arctic Engineering*.

Additional related work not defended as a part of the thesis

1. Molinas, M.; Skjervheim, O.; Andreasen, P.; Undeland, T.; Hals, J.; Moan, T. and Sørby, B: Power electronics as grid interface for actively controlled wave energy converters. *2007 International Conference on Clean Electrical Power (ICCEP)*.

2. Schoen, M. P.; Hals, J. and Moan, T. Wave: Prediction and Fuzzy Logic Control of Wave Energy Converters in Irregular Waves. *Pro-*

ceedings of the 16th Mediterranean Conference on Control and Automation, 2008.

3. Schoen, M. P.; Hals, J. and Moan, T.: Robust Control of Heaving Wave Energy Devices in Irregular Waves. *Proceedings of the 16th Mediterranean Conference on Control and Automation*, 2008.

4. Hals, J.; Lopes, M. F. P.; Moan, T.; Gato, L. M. C. and Falcão, A. F. d. O.: Demonstration of a simple latching-control strategy for a wave-energy converter in irregular waves. *2nd International Conference on Ocean Energy (ICOE)*, 2008

Declaration of authorship

Article A: Engja and Hals, EWTEC 2007

This work was initiated by me, but written mainly by Professor Emeritus Hallvard Engja, who is also the main author. We worked out the mathematical model in collaboration, and I performed the numerical simulations given as examples.

Article B: Hals et al., EWTEC 2007

This article was written by me with active co-authoring by Reza Taghipour. He contributed numerical simulation algorithms, and also models for solving the hydrodynamic problem. Mathematical modelling of the machinery system, programming of control algorithms, simulation campaigns, analysis and discussion is mainly my work.

Article C: Lopes et al., Ocean Engineering 36 (2009)

A paper that was initiated during my stay in Lisbon between September 2007 and January 2008. It was elaborated with equal contributions from Miguel Lopes and myself; him being responsible for the experimental model and experiments, while I had the main responsibility of mathematical modelling and numerical simulation. We both, however, took part in eachother's working domains, which made this a true joint work. Rui Gomes participated in some of the experimental preparations and experimental runs, while the remaining three co-authors served as scientific supervisors.

Article D: Hals et al., accepted for pulication in Journal of OMAE

This work was planned, carried out and reported by me with oral and written inputs from my supervisors.

Article E: Hals et al., accepted for pulication in Journal of OMAE

This work was planned, carried out and reported by me, with some oral and written inputs from my supervisors.

Chapter 1

Introduction

1.1 Background and motivation

Already in the early 19th century it was pointed out by several thinkers (e.g. Thomas Robert Malthus, Charles Fourier, Mary Shelley and John Stuart Mill [27, Chapter 1] that the path of industrialisation and population growth then under development would eventually lead to depletion and scarcity of resources if the occurring trends were projected far enough into the future. Restricting ourselves to consider only energy and materials from earth's own reserves there is an inevitable *resource finitude*. All non-renewable resources will eventually run out, if their use is not relieved by change of technology or lapse of demand due to other reasons. Seen from today's perspective, the accelerating use of petroleum and natural gas has an especially short future [29], and has received a lot of attention lately, while other resources, such as clean water, fertile soil and stable animal stocks, may have become just as scarce [82], although it may be less obvious for people living in urban well-off societies.

The concept of *sustainability* came to wide use after it was introduced in the report *Our common future* by the UN World Commission on Environment and Development (also called The Brundtland Commission) issued in 1987. By then there was a high degree of realisation and international consensus that the ever increasing population of the earth and their societies would have to make forced changes towards a more sustainable path of development in order to avoid collapse of several natural resources that humans depend on.

Many of the most prominent challenges to sustainable life today are related to the use of energy, either as the indirect cause of excessive exploitation of other recourses enabled by powerful and efficient technology,

or directly by the emissions caused by conversion of non-renewable energy resources. At the same time as the global primary energy consumption is currently rising about 1.5 % per year [5], the confidence that emissions caused by the extraction and conversion of fossil fuels is leading to anthropogenic climate changes is larger and larger [22; 9].

The available energy resources hosted by earth are large enough to destroy the basis for human existence. This was brutally illustrated by the development and use of nuclear weapons in the 20th century. The issue of nuclear weapons illustrate a key point in the question of sustainable use of energy; namely the *rate* at which the energy resources are harnessed. Both fossil and nuclear fuels may be harnessed in a sustainable manner if the conversion rate is so low that the biosphere - the *sink* for their emissions - can absorb the formed pollution without suffering damage. However, fossil fuels that have been formed over millions of years are now consumed within a few centuries, and this is an unsustainable rate, leading to overloaded sinks and corresponding environmental problems.

The other unsustainable dimension of today's consumption of fossil fuels is the fact that the resource is tapped at a higher rate than the capacity of alternative energy supply is established. A farmer would know that he has to invest some of his surplus (in terms of labour and money) into next season's crop, if not he will finally starve. In order to have a sustainable supply, a non-renewable resource needs to be substituted by other resources to yield a corresponding supply of power before it runs out, as advocated by Herman Daly [25, Chapter 4].

The energy sources we depend on today may be divided in three categories (today's share of primary energy demand given in parenthesis [5])

Nuclear fuels (5.5 %) Today mainly heavy fissionable elements such as uranium and thorium

Fossil fuels (88.1 %) Coal, petroleum and natural gas

Renewable energy (6.4 %) Energy derived from the sun (normally renewed over the time frame of a year or less), tidal and geothermal energy

The use of nuclear energy is a topic of great concern due to its close link with nuclear weapons and the challenge of safe handling of radioactive waste. If the human society develops into a more stable state, nuclear power may develop into a safe and long-lasting (although non-renewable) source of energy.

The most easily accessible deposits of fossil fuels have already been harnessed, and the oil and gas production is expected to reach its maximum production rate within about 20 years from now [29]. Many of the petroleum exporting countries have already reached their *peak oil* production. Notwithstanding, if the current understanding of atmospheric heat-balance processes is correct, the carbon emissions due to fossil fuel combustion represents a serious threat to human-friendly climate as we know it.

Direct sunlight, wood, wind, precipitation in highlands and geothermal heat are renewable sources of energy that since long have been converted to useful work by man. Technologies for harnessing tides, ocean waves, thermal gradients and various kinds of modern biofuels have come shorter in development, but have prospects of supplying cheap and clean renewable energy for future generations.

In light of the foregoing aspects, the cultivation of a sustainable energy supply needs several branches:

- reduced consumption per capita through reduced consumption and increased efficiency
- increased harnessing of renewable energy resources
- reduced combustion of fossil fuels, or carbon capture in the fossil fuel conversion chain

The use of renewable energy resources is sustainable as long as they are consumed at a lower rate than they are formed at earth and their use does not lead to harmful emissions. From Figure 1.1 we see that the total amount of available renewable energy resources largely outdoes the current energy demand. The question is whether they can be harnessed with reasonable efforts in terms of money and energy, and without causing excessive amounts of harmful emissions or damage to the natural environment in that process.

1.2 Ocean wave energy

Wave energy conversion, like other ocean energy technologies, have prospects of supplying useful energy at high energy pay-back factors and low life cycle emissions [94; 21]. Although some research on ocean wave energy has been ongoing intermittently for several decades, the technology is still in its infancy, or at best in its early youth. Developing a wave energy converter is a highly cross-disciplinary task, met by a wide range of challenges: Structural design for good absorption capabilities and high robustness, efficient use of

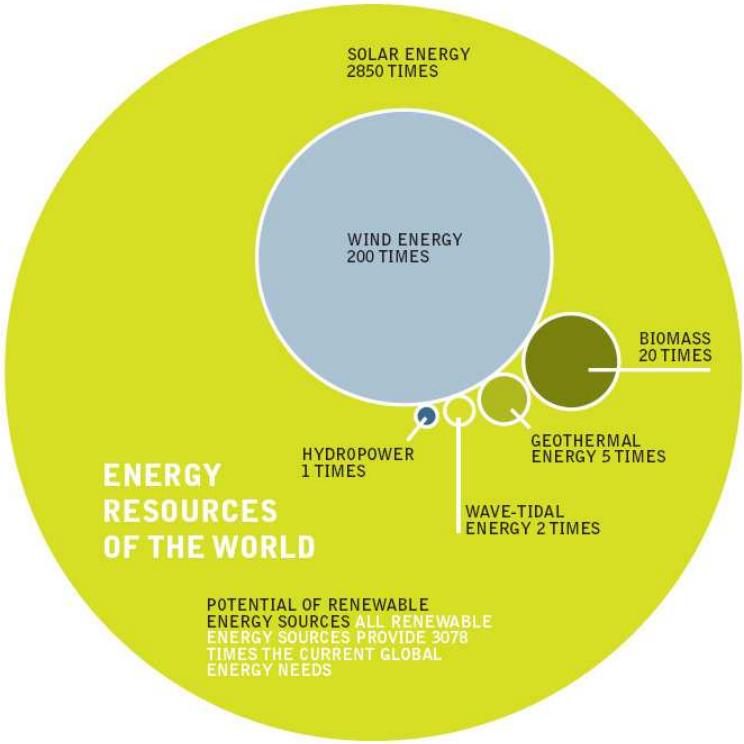

Figure 1.1: Illustration of how renewable energy from the sun is converted into other forms, and their relative energy content compared to today's global energy need [118].

materials, development of machinery principles and components, design for extended component lifetime and safe, efficient transport of energy to shore (see Figure 1.2). Furthermore, it is essential to ensure minimal influence on marine life, minimise conflicts with other uses of the sea, as well as to find good solutions for installation, operation and maintenance in an often rugged environment.

1.2.1 Historical and technical context

The last two centuries have seen a series of ingenious trials on building wave conversion machinery — the book by McCormick [80] provides examples of some early proposals and also more recent patents. The task of inventing a viable wave energy converter has, however, proved to be challenging in terms of achieving a sufficiently low cost–benefit ratio. A commercial break-

through for wave energy technology has yet not been seen.

The era of modern research on ocean wave energy followed after the 1973 oil crisis shed new light on the question of energy security and the need for a sustainable energy supply. It made the British researcher Stephen Salter publish his article *Wave power* in *Nature* in 1974 [108]. After a period of diminishing funding and reduced activity starting already in the 1980's, wave energy development again flourished in the new millennium, partly due to re-newed interest in the topic by the European Union.

As stated before, the development of wave energy technology draws on knowledge and competence from a number of fields. Referring again to Figure 1.2, the work in this thesis is focused around hydrodynamics and control engineering, and mainly concerns the primary conversion of wave energy to mechanical energy in the converter unit. The basic theory for this conversion was developed already during the early days of wave energy research, with works e.g. by McCormick [81], Evans [35; 33], Budal and Falnes [15; 16; 17; 37], Mynett et al. [87], Sarmento and Falcão [112], Mei [83] and Newman [89].

Today, technology research and development concerning the primary conversion is revolving about how to design efficient equipment (structures, machinery and moorings) for viable conversion concepts, how to accurately model and assess the loads and stresses on the converters, how the power absorption is influenced by array and mooring configurations, and how to implement an approximation to the optimal power absorption by realisable controllers (cf. Section 3.3.2) and power take-off systems.

1.2.2 The resource

Waves travelling the oceans are a concentrated form of solar energy (see Figure 1.3). Winds generated by pressure differences caused by the heating from the sun represent an average power flow typically up to about five times more dense (about $0.5\,\mathrm{kW/m^2}$) than in the solar radiation reaching the surface of the earth (about $0.1\text{-}0.3\,\mathrm{kW/m^2}$). In the transition from wind blowing over the ocean surface to waves the energy flow intensity it is again concentrated about five times, to about $2\text{-}3\,\mathrm{kW/m^2}$ in the upper layer of the oceans [43]. Thus although only a tiny part (approximately 10^{-4}) of the solar irradiation ends up as wave power it is a quite concentrated form of renewable energy, something which should give prospects for efficient harvesting.

It has been estimated that the theoretical wave energy potential is in the order of 1 to 10 TW [93], or approximately equal to the primary energy demand/consumption on earth today. The practically exploitable potential

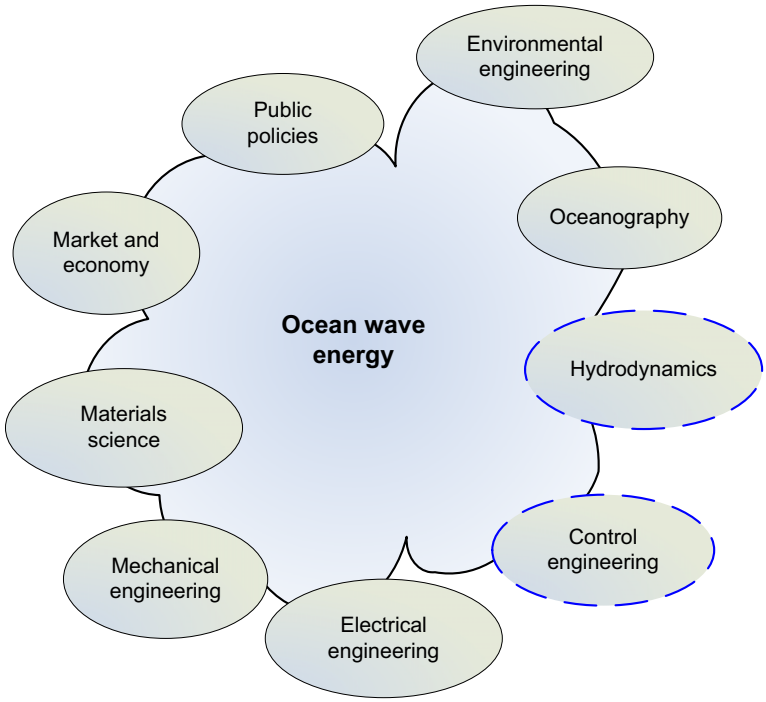

Figure 1.2: Fields of competence relevant for the development of wave energy technology. In this thesis the focus has been on hydrodynamics and control engineering.

will, of course, be considerably smaller and depends on factors such as technology, policies and conflicts with other uses of the oceans.

The wave power level J [W/m], counted as the energy transported per time and per width of the wave crest, has both a spatial and a temporal variability at different scales. The resource is strongest in the regions between latitudes 40° and 60° on both the northern and southern hemispheres, and local variations occur due to differences in climate, sea bed topology and wave interference. A map showing the global distribution of annual average wave energy transport is given in Figure 1.4. The average wave power level differs between years, and outside equatorial waters there is a seasonal variation, especially in the northern hemisphere where the typical mid-winter month experiences up to thrice the average wave power level of the typical mid-summer month (see Figure 1.5). In addition to these variations, which are connected to variations in wind levels, there are wave grouping effects working on the scale of minutes, as well as the change from wave cycle to

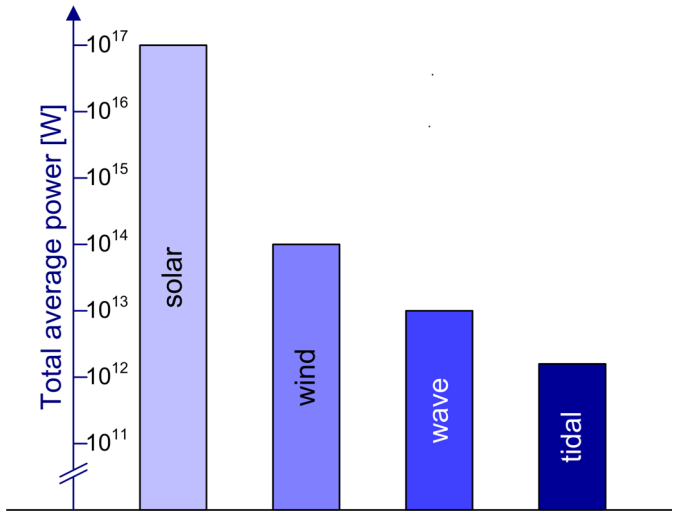

Figure 1.3: Comparison of the global resource for solar energy and selected marine energy recourses. The colour illustrates how the energy is concentrated in the conversion steps from solar (relatively sparse and thus light) through wind to wave energy (denser and hence darker). The global tidal energy resource, which is found in even denser form than wave energy, is included for comparison. Based on approximate data found in [12].

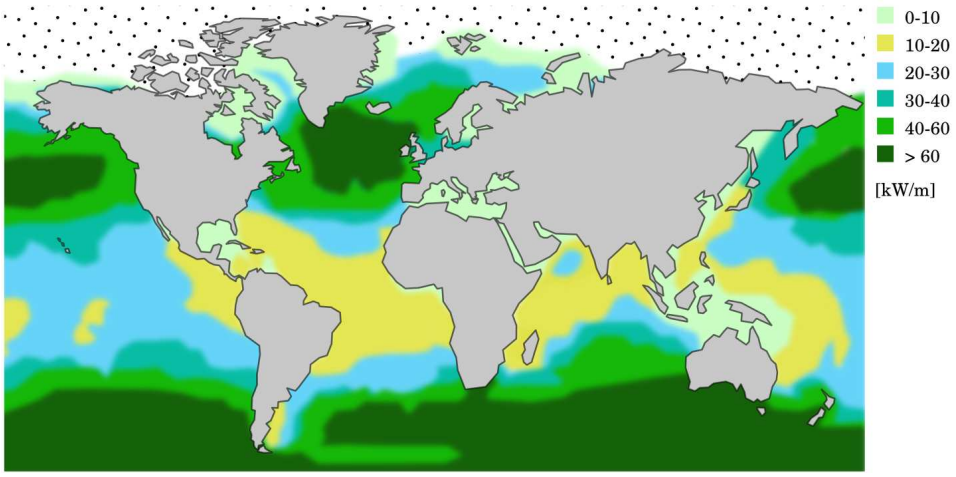

Figure 1.4: Annual average wave energy transport [kW/m]. The map is approximate, redrawn from [8].

wave cycle (on the scale of seconds).

Due to the irregular energy input from the wind, also the waves become highly irregular. Ocean waves typically have periods between 6 and 15 seconds, and heights in the range from 0.5 to 3.0 m counted between zero up- or down-crossings. The wave-power level (the energy transported per unit crest length) for a regular wave may be computed by the formula [26, Chapter 4]

$$J = k_J T H^2 \tag{1.1}$$

As $k_J = \rho g^2/(32\pi)$ is approximately equal to $1\,\mathrm{kW/m^3s}$, a monochromatic wave of period $T = 9\,\mathrm{s}$ and height $H = 1.0\,\mathrm{m}$ carries a power of about $9\,\mathrm{kW/m}$.

In order to represent the irregularity/variability, a real sea wave, or equivalently a sea state, may be characterised by its energy spectrum. An example is shown in Figure 1.6. It shows how the energy in the wave is distributed over the frequency range of ocean waves.

Various mathematical models have been proposed and used for analytical representation of real-sea spectra, of which the most commonly used are the JONSWAP, Bretschneider and Pierson-Moskowitz spectra [84]. Such representations may be used for the synthesis of time series needed in numerical simulation and laboratory testing (see e.g. [26]).

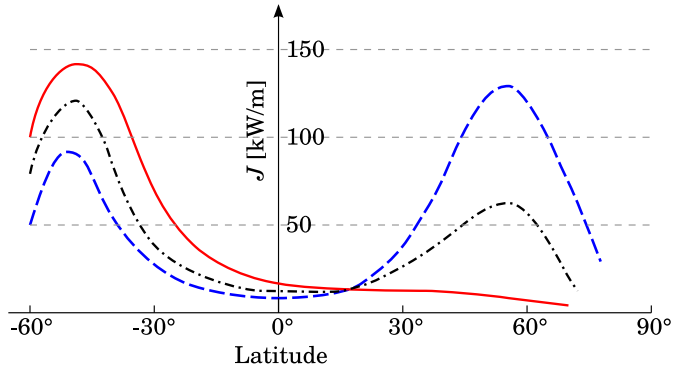

Figure 1.5: Seasonal variation of the wave energy transport J [kW/m] at different latitudes. The curves represent typical trends: Monthly average for July (red fully drawn curve) and January (blue dashed curve). The black dash-dotted curve shows a typical annual average. Data taken from Barstow *et al.* [8].

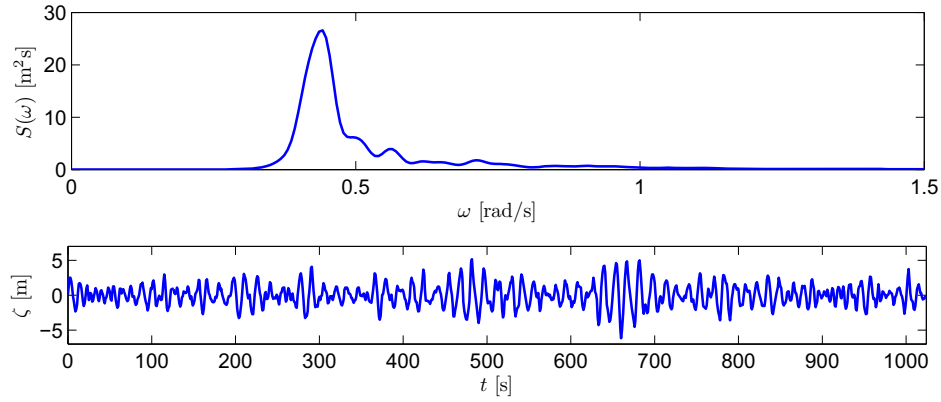

Figure 1.6: An energy spectrum (top) for the measured wave elevation time series shown (bottom). The data are taken from a measurement in the Barents sea (N73°30', E15°30') in October 2008, courtesy of Stephen Barstow/Fugro OCEANOR.

1.2.3 Conversion principles for wave energy

The first known proposal for extracting power from ocean waves stems from 1799 [54]. In more recent times many concepts have been brought to daylight, but the technology has still not reached a level where convergence to one or a few concepts of industrial maturity can be seen. In 1992 George Hagerman categorised the most well-known principles in an illustrative diagram as shown in Figure 1.7 [57]. It is still useful as a reference in assessing the working principles for wave energy converters. The basic classifications shown in the diagram are based on:

Mode of motion for energy absorption Pitch, heave and/or surge

Type of absorber Free surface of the water or fabricated structure (rigid or flexible)

Type of force reaction Fixed structure (concrete foundations or land), sea-floor anchor (deadweight or pile) or inertial structure (suspended plate/body or buoyant spine)

Type of working fluid Air, sea water or hydraulic fluid

The same classifications would be valid today, maybe with the exception that also direct conversion to electricity is now possibly seen as viable solution. We may observe that the distinction between *oscillating water columns* (OWCs), *overtopping devices* and *oscillating bodies*, which are widely used terms today, is also implicitly covered by Hagerman's diagram.

A distinction is often made between *point-absorbing* devices (having a horizontal extension small compared to the wavelength), *attenuators* (large devices aligned with the predominant direction of wave propagation) and *terminators* (large devices aligned with the wave crests). The difference in their absorption properties is related to their wave-radiation pattern; large devices may radiate plane or almost plane waves, whereas point absorbers will have a circular or dipole-shaped radiation pattern.

The basic principle

Because ocean wave energy is a wave phenomenon its transmission and absorption is governed by interference with other waves. Thus the most fundamental task of a wave energy converter is to generate a wave that interferes destructively with the incident wave [44; 15].

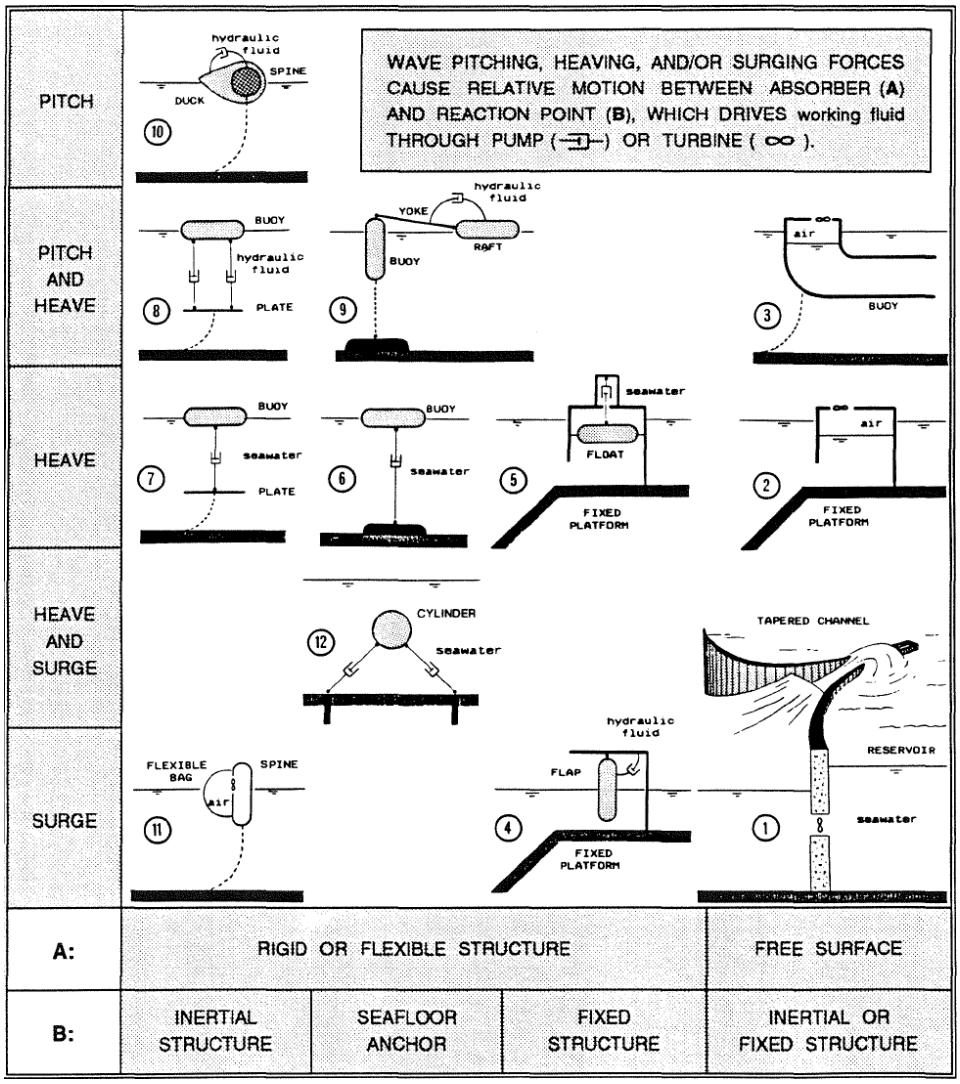

Figure 1.7: Categorisation of wave energy conversion principles [57].

Fundamental requirements

Many lessons have been learned about the conversion of wave energy and the development of viable solutions, and although results are often kept in confidential reports or not even documented, some of the experiences have fortunately been reported in public articles and reports. Experienced researchers within the field have tried to summarise their insight in qualified advices for the further development of the technology [50; 110; 42; 4]. Some of the most important points made are:

- The absorbing body must work at or in the vicinity of the ocean surface. This is where the power flow is concentrated.

- While conventional marine structures that serve various purposes (transport, support for oil&gas platforms, fish farming) should be made so as to minimise forces and motions, a structure for wave energy conversion must be designed to endure a combination of relatively large forces and large motions (i.e. velocities). Because power is the product of force and velocity, this is an unalterable requirement.

- In principle wave energy absorbers have to be good wave generators. This means that the radiation resistance, also called the wave damping coefficient, is the key factor for the income side of wave energy conversion; it governs the amount of power that can be absorbed and subsequently sold.

- The two main requirements for a wave wave energy converter are to resist extreme loads as well as the repetitive action due to storm waves, and moreover be able to convert enough power in average sea conditions to justify the investment made in terms of energy and money.

If these are requirements that designs *must* comply with, another set of requirements may be extracted from various publications and listed under the notion *should* comply with, some of which are still debated:

- A wave energy power station should consist of many small units rather than a few large ones [31; 38]

- The development of wave energy technology should go through steps of experimental testing in reduced scale in order to avoid expensive failure and loss of construction at full scale. This is usually one of the main rules in guidelines developed within the field [4; 23].

- Structures for wave absorption should be designed such that as large a part as possible of the exterior surface participates in the wave absorption (i.e. is useful for wave generation) [15; 38; 50].
- To be successful a wave energy converter should exploit more than one mode of motion [110].
- All wet surfaces should be smooth — avoid sharp corners that increases the viscous losses through vortex shedding [41, Section 5.6.1]
- Station-keeping moorings should not reduce the power capture [63; 48; 52; 119].

1.3 Thesis

1.3.1 Outline

The research performed in this PhD study is documented in articles listed in Appendix A. In this dissertation it is tried to clarify the ideas behind the work, the methods used and the links between the individual articles.

Chapter 2 presents the modelling methods that have been used in deriving published results. A detailed account is given for the primary conversion, which is essential for the power available downstream in the conversion chain. Mathematical modelling of the other subsystems are, however, demonstrated by examples in Appendix B.

Next, Chapter 3 defines the control problem to be solved and gives an account for the background theory. Analyses of alternative control methods have been one of the core activities in this PhD study, and Article E (on page 157) summarises the achieved results.

Furthermore, Chapter 4 presents an overview of the numerical method that has been used in time-domain solution of the mathematical models for the dynamic systems. More detailed information about the developed simulation algorithms are found in Appendix C.

The main conclusions and an explicit formulation of the contributions to the research field achieved through the published results are given in Chapter 5 along with recommendations for further work.

1.3.2 Scope

Although there hasn't yet been any clear convergence in the principal design of wave energy converters, some indications and advice on the direction to follow may be derived from existing research results and experience [38; 50].

The path followed in the present work has been based on the following understanding:

- Energy, in the form of mechanical work, is equal to force times distance, and the hydrodynamic force on a body exposed to ocean waves equals the integrated dynamic pressure on the wetted surface area of the body. The energy that, at most, can be absorbed by a floating device over a wave cycle is therefore proportional to its volume stroke or swept volume.

- The constructional cost of a floating device increases with both volume and surface area due to material costs and labour. At the same time it is known that the ratio between power and swept volume increases with decreasing volume [41, Section 6.2.2]. Thus it must be expected that many small units have the potential to give cheap wave energy (in terms of both money and energy spendings).

- Wave power converters will eventually be installed offshore due to the larger resource, less conflicting interests and less visual impact than for installation in near-shore areas. This favours floating point-absorber devices in place of large constructions of the terminator type (which are more suitable for shoreline construction).

- Small units also enable series production and component optimisation to a larger extent, which will drive costs further down.

- The energy that can be absorbed is directly related to the ability of radiating power and creating destructive interference with the incident waves. The wave radiation is governed by the radiation resistance, which is therefore the key property for the absorption ability [43]. For small units, the radiation resistance is larger in heave than in other modes of motion. The examples in this work has therefore been chosen to be small heaving bodies.

- Small floating bodies tend to have large Q factors, i.e. the frequency response has a sharp, narrow resonance peak [33]. Because the ocean waves are irregular, this means that automatic control is needed in order to ensure efficient use of the installed equipment [31].

- An early result of wave energy research was the principles of phase and amplitude control for achieving maximum power absorption [81; 15; 33; 111; 109]. In irregular waves the optimal control problem becomes non-causal [88; 39]. Different causal approximations have

been proposed by several authors [100; 10], but there is a lack both of understanding regarding the implications of different control strategies and of a framework for comparing them.

- To be successful, the development and refinement of a design for a wave energy converter must build on a good understanding of the basic principles and dominating physical effects experienced by the device. This understanding is usually established through a combination of physical and mathematical modelling. A systematic and transparent method for building mathematical models of such systems may be a good tool in avoiding sub-optimisation and overlooking dependencies. Whenever possible, also controller design usually builds on a firm understanding of the system dynamics.

On this basis, the focus have been given to phase control of point-absorbing systems placed offshore, with extensive use of heaving buoys as converter examples.

1.3.3 Objective

Motivated by considerations given above, the main objective of this work has been to test the following hypotheses:

1. The dynamics of floating wave-energy converters can be modelled in a systematic and transparent way by the use of bond graphs (see Chapter 2). It will give a satisfactory level of accuracy, and the important effects and dependencies will be well represented.

2. There exist causal alternatives to the non-causal optimal controller (see Chapter 3) for wave-energy absorption that can operate in a realistic irregular sea with energy absorption only slightly reduced compared to the theoretical (non-causal) optimum.

3. Different choices of how to control the motion of wave energy absorbers have strong implications for the operation of the machinery and the quality of the power output. The choice of conversion principle, control algorithm and machinery system must consequently be seen in combination in order to ensure a well-performing system.

Chapter 2

Modelling

The working principles of wave-energy converters can often be assessed by considering idealised systems, i.e. we may assume linear and unconstrained dynamics and only take the primary conversion into account. As the activity is moving closer to prototyping and detailed design, more realistic models must be developed to enable adequate synthesis and analysis. These have to include constraints and nonlinear effects, and should cover the whole conversion chain (see Figure 2.1).

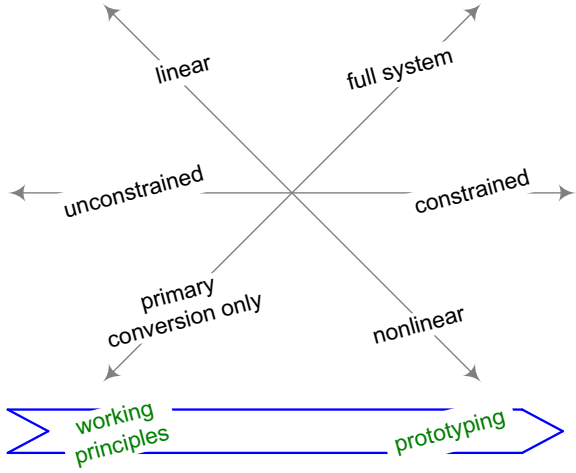

Figure 2.1: Trends in the need for modelling and control as the focus moves from the investigation of working principles to device development and prototyping.

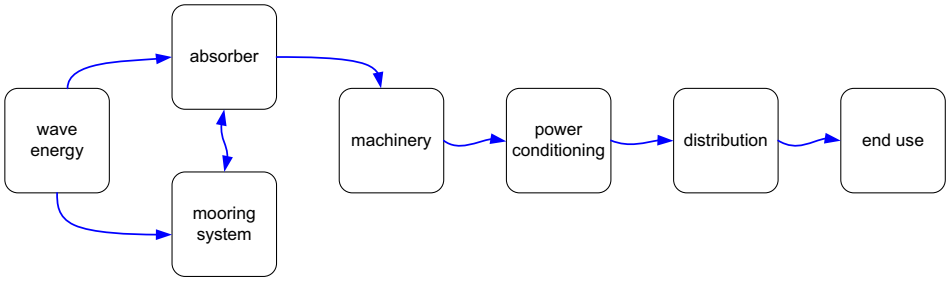

Figure 2.2: View of a wave energy converter on a technical component level, where the conversion chain has been divided in subsystems.

2.1 Conversion system outline

As illustrated by the system outline in Figure 2.2, the energy conversion path of a typical wave energy device based on floating bodies may be divided into the following sub-systems:

Absorber Hydrodynamic theory describes the interaction between free-surface fluids and floating bodies. The conversion of power from gravity waves on the ocean to mechanical energy in a wave absorber is governed by the interaction between the hydrodynamic pressure on the wetted body surface and the motion of the body.

Machinery The role of the machinery is to convert the wave energy to a usable or distributable form. Depending on the design, the machinery will typically involve hydraulic, pneumatic and/or electric machinery components.

Mooring system A mooring system is needed to keep the floating wave energy device in place. If the absorbing unit is reacting against the sea bottom, the mooring system or line may be closely linked to the machinery. Otherwise, slack-moored or tension-line designs may typically be used, which will also influence on the wave-absorber dynamics.

Power conditioning and energy transport Seen from a power-supply perspective, the last part of our system is devoted to the distribution and delivery of the converted power. In the case of electricity generation, which is often the aim, this involves power conditioning and integration with a land-based power grid.

We continue by looking at the governing physical effects for the dynamics of a wave energy converter, and give the correspond mathematical

formulation in the most conventional form.

2.2 Effects governing the converter motion

In general, a rigid body is free to move in six independent modes of motion: surge, sway, heave (translational) and roll, pitch, yaw (rotational). We shall here use bold lowercase symbols (e.g. $\boldsymbol{\eta}$ for the position) to indicate vectors of all six modes, i.e. the last three elements of the vector are angular positions. Bold uppercase symbols (e.g. $\mathbf{M}$) are 6×6 matrices. The conventional way of modelling the motion of a floating structure is to account for the following forces acting on it:

Inertia forces The force needed to accelerate a mass $\mathbf{M}$ with acceleration $\ddot{\boldsymbol{\eta}}$ is $\mathbf{M}\ddot{\boldsymbol{\eta}}$, where dot ($\dot{}$) denotes the derivative with respect to time t.

Net hydrostatic stiffness It is usual to assume that the body is initially floating in its equilibrium position where the buoyancy force due to displaced water balances the gravity force of the body and possible pre-tension forces . A requirement is that the body is *hydrostatically stable*, which depends on the location of the *centre of mass*, the *centre of buoyancy*, and the surface moment of the body taken at the water plane [59]. The net hydrostatic force $\mathbf{f}_s$ then depends on the deviation $\boldsymbol{\eta}$ from the equilibrium position, $\mathbf{f}_s = \mathbf{S}\boldsymbol{\eta}$, where $\mathbf{S}$ is the (possibly nonlinear) hydrostatic matrix.

Hydrodynamic radiation The oscillation of the body causes waves, and the force on the body from the dynamic water pressure due to these waves is called the radiation force $\mathbf{f}_r$. Considering only the linear approximation for a monochromatic oscillation with frequency ω_k, the radiation force may be represented by a superposition of two terms, $\mathbf{f}_r = \mathbf{M}_r(\omega_k)\ddot{\boldsymbol{\eta}} + \mathbf{R}_r(\omega_k)\dot{\boldsymbol{\eta}}$. In this case the matrices of proportionality coefficients $\mathbf{M}_r(\omega_k)$ and $\mathbf{R}_r(\omega_k)$ are the *added mass* and *radiation resistance* matrices, respectively. Because of the frequency dependency, the radiation force must in the time domain be represented by a convolution term when polychromatic waves are considered. See Section 2.4.2 for further details about the radiation force.

Hydrodynamic excitation This is the force $\mathbf{f}_e$ on the body due to the dynamic pressure resulting from the incident wave (including the diffracted wave but excluding the radiated wave). In the linear approximation it may be decomposed into one part due to the undisturbed pressure

field (as if the body were not there) known as the Froude-Krylov force, and one part due to the diffracted wave, which is the correction due to the presence of the body [90].

Machinery forces The machinery force $\mathbf{f}_m$ used to convert the power must work against a fixed reference (e.g. a rigid connection to the sea bed or the shore) [102; 75], against an internal inertia [109; 51; 28] or against other immersed (possibly oscillating) bodies [30; 60; 123]. Friction and other losses in the conversion machinery should be included here along with any additional control forces (e.g. for latching control or other). A more detailed discussion on machinery alternatives is given in Section B.1.

Viscous damping When the fluid is assumed to be inviscid (see below) in the calculation of hydrodynamic forces, corrective terms may be included in order to represent the power lost by viscous drag (form drag and skin friction drag). For steady flow, these viscous forces have a quadratic dependence on the relative velocity u_{rel} between the fluid and the body, $F_v = \frac{1}{2} C_d A_\perp u_{\text{rel}} |u_{\text{rel}}|$. The drag coefficient C_d then depends on the Reynolds number, flow regime, geometry and surface roughness (depending on the type of drag). For oscillatory flow around submerged structures the problem becomes more complex, and viscous forces are usually approximated by the drag part of the Morison equation [85] assuming a similar relationship as for steady flow. The drag coefficient C_d is then found by measurements or chosen by experience. Its value is typically around 0.7, but may be as high as 1.5 [113]. For oscillatory flow the Keulegan-Carpenter number plays an important role for C_d, expressing the relative importance of viscous forces over inertia forces.

Mooring forces Mooring lines hold the device in place and may also influence on the dynamics and the power absorption [63; 48; 119; 52]. A more detailed account for mooring lines and the force $\mathbf{f}_l$ they provide is given in Section B.3.

Other environmental forces Influences from loads like winds, currents and tides may have an important influence on the dynamics of conversion systems for wave energy, but this depends heavily on the location and on the type of converter system considered. Such forces $\mathbf{f}_o$ have not been discussed in this work.

The hydrodynamic forces (excitation and radiation) on the body are caused by the motion of the fluid, and have, in principle, to be found through

modelling of the whole fluid domain. This may be done by applying the Navier-Stokes equations [90] and integrating numerically in a finite element scheme, c.f. for instance [47]. A simplified problem arises if the fluid is assumed to be inviscid and irrotational. Then a velocity potential exists for the fluid, which potential may be found numerically by solving a boundary element problem (see e.g. [90, Chapter 4] or [45, Chapter 4]). An approximate solution is found by assuming the solution to be a linear superposition of the solutions found for each mode of motion and each body. As confirmed by experiments, this linear solution is usually sufficiently accurate for the study of wave energy conversion in normal wave conditions. Higher-order corrections may then be added according to the need for accuracy. Typically, inclusion of second-order wave forces is necessary in order to study mooring system dynamics [45]. Standard commercial software for finding the velocity potential and hence the hydrodynamic parameters by boundary element methods include WAMIT, AquaDyn, ShipX/veres, OCTOPUS Office 6 [23; 120; 46; 65].

2.3 Conventional mathematical formulation

For force balance, the inertia forces from the body are equated against the sum of the other forces,

$$\mathbf{M}\,\ddot{\boldsymbol{\eta}}(t) = \mathbf{f}_e(t) + \mathbf{f}_r(t) + \mathbf{f}_s(t) + \mathbf{f}_m(t) + \mathbf{f}_v(t) + \mathbf{f}_l(t) + \mathbf{f}_o(t). \tag{2.1}$$

This is a vector equation where each element is equated with the corresponding element of the other vectors. Keeping only linear terms and disregarding the viscous forces $\mathbf{f}_v$, mooring forces $\mathbf{f}_l$ and environmental forces $\mathbf{f}_o$, this equation may be represented using complex amplitudes as

$$\left\{ i\omega\left(\mathbf{M} + \mathbf{M}_r(\omega)\right) + \mathbf{R}_r(\omega) + \frac{\mathbf{S}}{i\omega} \right\} \hat{\mathbf{u}}(\omega) = \hat{\mathbf{f}}_e(\omega) + \hat{\mathbf{f}}_m(\omega), \tag{2.2}$$

where the velocity is given by $\mathbf{u}(t) = \Re\{\hat{\mathbf{u}}(\omega)\, e^{-i\omega t}\}$ (It is thus assumed that taking the real part of Equation (2.2) gives the real variables, cf. [41, Chapter 1]). Here the radiation and hydrostatic terms appear on the left-hand side (rewritten according to the discussion above), while the external forces; the excitation and the machinery forces, are retained on the right-hand side. This equation now holds a linear approximation to the dynamic behaviour of a rigid body in water, and can be used to study the energy conversion from ocean waves to useful power delivered by a generic machinery.

Following the terminology of Falnes (cf. [41, Chapter 5] or [58]) the curly braced parenthesis is called the *intrinsic impedance* $\mathbf{Z}_i$ of the floating body,

$$\mathbf{Z}_i(\omega) = i\omega\left(\mathbf{M} + \mathbf{M}_r(\omega)\right) + \mathbf{R}_r(\omega) + \frac{\mathbf{S}}{i\omega} = \mathbf{R}_r(\omega) + i\mathbf{X}(\omega), \tag{2.3}$$

where we have introduced the *intrinsic reactance* $\mathbf{X}(\omega) = \omega(\mathbf{M} + \mathbf{M}_r(\omega)) - \mathbf{S}/\omega$.

Conversion systems for wave energy may become quite complex, spanning several energy domains. The conversion chain may e.g. include both hydrodynamic, mechanical, structural and electrical power flow. Systematic and structured approaches to the modelling may therefore be very useful for the design as well as for the analysis. This is one of the strengths of bond graphs. In the following sections it will only be shown how the bond graph language may be applied in the modelling of the absorber subsystem. For bond graph examples of wave-to-wire models, see Appendix B.

2.4 Bond graph modelling

The bond graph modelling language is a cross disciplinary and systematic approach to the modelling of dynamic systems initiated by MIT professor H. M. Paynter in 1959 [96]. It is based on the fundamental property of energy conservation, and yields a graphical representation of systems, where dependencies and physical effects are visualised by power flow between a set of basic elements. Using these elements, the modeller's knowledge and understanding of a system's dynamics may be represented in a graph, which becomes equivalent to a set of state equations for the system once governing relationships has been specified for each element. A thorough introduction to the bond graph modelling language may be found for instance in the textbook by Karnopp *et al.* [69]. A brief overview of bond graph modelling is also given in Article A (page 75) as a basis for the modelling of wave energy converters.

In the following the bond graph representation will be used in the discussion of the radiation and excitation forces.

2.4.1 Absorber model – one degree of freedom

Let us first assume a very simple system – a heaving buoy reacting against the sea bottom – and disregard motions in other directions. We further assume that the buoy behaves like a rigid body. In the bond graph its velocity can then be represented by a common-flow element: the one junction

(cf. Figure 2.3). The dynamic properties of the body and its connection to the surroundings can be represented by three of the basic one-port elements of the bond graph language: an inertia (I), a compliance (C) and a resistor (R). The two first only stores energy, while the third usually transfers power out of the system, e.g. through dissipation or radiation. The effects included in this bond graph for the buoy dynamics may be summarised (in analogy with Section 2.2) as:

Inertia (I) Represents kinetic energy stored in a moving inertia I and the power needed to change its momentum p: the inertia force e_I may be written $e_I = dp/dt = I\,f = (m + m_r)\,f$, since in our case the inertia equals the sum of buoy mass m and added mass m_r. In accordance with bond graph terminology the force is written as an effort variable e and the velocity as a flow variable f.

Capacitor (C) The hydrostatic restoring force stores potential energy and acts as a compliance. Hydrostatic restoring forces will not be discussed any further here. For a reference, consult e.g. [59].

Resistor (R) When the body moves, outgoing waves carry energy away from the system. Remember that in the case of wave absorption, the energy carried away by the radiated wave cannot be regarded as a loss; it is necessary for the creation of destructive interference with the incoming waves. The resisting force resulting from wave radiation is governed by the hydrodynamic radiation resistance, see Section 2.4.2.

Excitation force (MSe: F_e) The hydrodynamic force on the body due to incident waves, see Section 2.4.3.

Machinery force (MSe: F_m) The machinery force will depend on the control strategy, which is discussed in Chapter 3 and treated thoroughly in Article E.

If we regarded a machinery only capable of exerting resistive force on the system, it should be modelled as an R element. In the general case we want, however, to consider a machinery that is able both to extract power from and feed power to the system, and hence model it as a *source of effort*, labelled Se. The M in front (for *modulated*) is added because the forces are modulated by an external parameter. In our case both the excitation force and the machinery force are time-variant — the former with parameter values read from a data file or calculated from a function, the latter based on a computed control signal.

2.4.2 The radiation force

Using complex amplitudes, the radiation force is normally written as (cf. Section 2.2)

$$\hat{F}_R(\omega) = m_r(\omega)\,\hat{a}(\omega) + R_r(\omega)\,\hat{u}(\omega). \tag{2.4}$$

Correspondingly, in the time-domain, the velocity $u(t) = \dot{\eta}(t)$ and the acceleration $a(t) = \ddot{\eta}(t)$. The parameter $m_r(\omega)$ is known as the added mass, and is due to the near-field standing wave caused by the body motion. The second term contains the radiation resistance $R_r(\omega)$, which is related to the far-field outgoing waves [41, Chapter 5].

Cummins [24] showed that the linearised radiation force could be modelled in the time domain as:

$$F_r(t) = m_r(\infty)\ddot{\eta} + \int_0^t k(t-\tau)\dot{\eta}(\tau)\,d\tau. \tag{2.5}$$

A constant, the added mass at the limit of infinite frequency $m_r(\infty) \equiv \lim_{\omega\to\infty} m_r(\omega)$, is separated out in order to ensure a finite integral when integrated over $\omega \to \infty$ (where $m_r(\omega)$ is still finite)[41, Chapter 5.3.1], and the frequency-dependent part of the added mass and radiation resistance parameters give rise to the convolution integral. The integration kernel $k(t)$ is given as the inverse Fourier transform of $k(\omega) = \mathcal{F}\{k(t)\} = i\omega\,\{m_r(\omega) - m_r(\infty)\delta(\omega)\} + R_r(\omega)$.

In the linear and monochromatic case with only linear system elements the convolution term is unproblematic as Equation (2.4) translates to $F_r(t) = m_r(\omega_k)\,a(t) + R_r(\omega_k)\,u(t)$ with parameter values corresponding to the input frequency ω_k. For solving the equations of motion in the polychromatic case or the non-linear case, however, we can rather do one of the following:

- calculate the convolution term of Equation (2.5) by numerical integration at each simulation time step using the convolution kernel and the history of state values.

- approximate the convolution term of Equation (2.5) with a state space model.

- approximate the radiation parameters with constant (frequency independent) coefficients such that $F_r(t) = m'_r\,\ddot{\eta}(t) + R'_r\,\dot{\eta}(t)$, with added mass and damping chosen e.g. according to the average value within the range of relevant frequencies.

Convolution replacement by constant terms

If there are loss effects (for instance viscous losses or friction) connected to the motion of the body and these are large compared to the radiated wave power, the last option in the list above may give a good approximation because the variation of the radiation resistance then has little significance for the body motion (the radiation becomes negligible compared to the dissipative forces). Also, the relative variation of mass and added mass summed is usually quite small with changing frequencies, and can therefore be well approximated by a constant.

If the machinery force is only resistive (no reactive power) and the oscillation is far from resonance, $R_{m,opt} >> R_r$ — cf. Equation (3.4) — the radiation force will be overshadowed by the machinery damping, and again the constant-parameter approximation may give reasonably accurate results.

The bond graph model resulting for this modelling choice is shown in Figure 2.3. The added mass has been included in the inertia element together with the physical mass of the buoy. Except for the excitation and machinery forces (PTO: power take-off), this model looks like a damped harmonic oscillator. The state equations derived from the graph are:

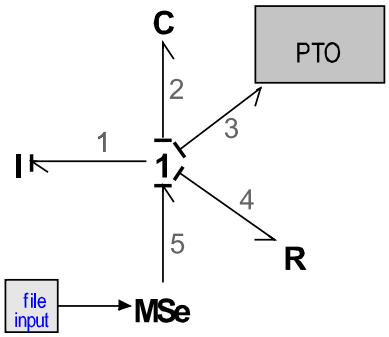

Figure 2.3: Bond graph for a heaving sphere reacting against a fixed reference. The I element gives the inertia force (including the effect of added mass), the C element represents the hydrostatic stiffness and the R element models the hydrodynamic radiation force, where the radiation parameters have been approximated by constant terms. Furthermore the machinery force is represented by a submodel to be further defined (PTO), and the modulated source of effort (MSe) represents the excitation force, which in this case is set according to time series data saved on a file.

$$\dot{p}_1 = \frac{1}{1 + m_r(\infty)/m}\left(-S\, q_2 - e_4 + e_3 + e_5\right) \tag{2.6}$$

$$\dot{q}_2 = p_1/m, \tag{2.7}$$

where the two state variables are the linear momentum $p_1(t) = m\, u(t)$ and the heave displacement $q_2(t) = \eta(t)$. Equation (2.6) may be recognised as Newton's second law for the buoy motion, and the two equations (2.6) and (2.7) together are equivalent to Equation (2.2). The e variables are forces, such that $e_3 = F_m$ is the machinery force, $e_4 = F_R$ the radiation force and $e_5 = F_e$ the excitation force. (The reason for keeping the bond graph notation in the derivation of equations becomes evident when the graph includes elements from different energy domains.)

On the other hand, if the absorber is operated close to optimum (with reactance cancelling, see Section 3.3.1), it is very important to model the radiation forces precisely, as the active power fed through the machinery will be of the same size as the radiated power, cf. Equation (3.2). In Figures 2.4 and 2.5 examples are given on the difference in computed heave response between constant-term approximation and the exact linear results for an incident irregular wave. At 4.5 s peak period, which is close to the buoy resonance period of about 4.4 s, it may be observed that the error of the constant-term approximation is significant (about 10 %), while at 9 s peak period it is considerably smaller (about 3 %).

Convolution replacement by state-space models

Looking now to the two other procedures suggested, the state-space approximation is a more attractive alternative than computing the convolution by numerical integration as it enables more efficient calculations if a low-order state-space model can be found. A good state-space model for the radiation force will give reasonably accurate results, and at the same time enables use of state-space formulation throughout the solution of the problem. The last decades have brought about several works on how to approximate the convolution term by linear state-space models, with matrices $\mathbf{A}_k$, $\mathbf{B}_k$, and $\mathbf{C}_k$ [62; 122; 117]. A citation from Yu and Falnes [122] might be in place:

> The models of impulse response function and of transfer function are equally good descriptions of a linear system. An exact description is possible also with a state-space model of finite order, provided the system genuinely possesses a finite (possibly large) number of states. Approximations are possible to reduce the number of states from a large finite value or from an infi-

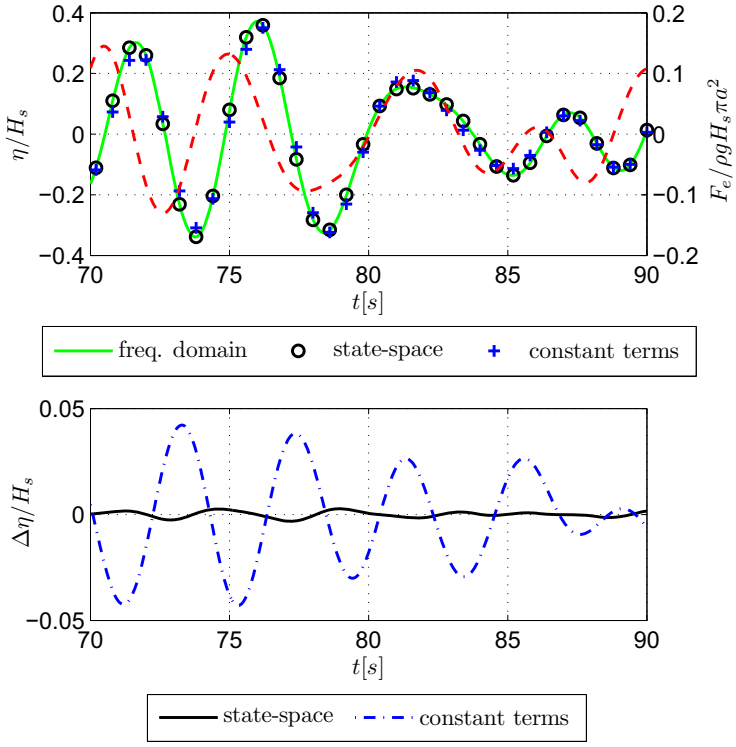

Figure 2.4: Upper: Response of a heaving semi-submerged sphere of diameter 10 m in irregular waves. Comparison of the exact linear solution from the frequency domain (green fully drawn line) and approximations. The frequency domain solution is found as a superposition of the solutions at each frequency component of the incident wave. The machinery was set to act as a linear resistor, c.f. Equation (3.5), with the load resistance optimised for the peak frequency of the wave spectrum. The approximate solution found by using constant radiation coefficients (added mass and wave damping) is given by the blue crosses, and the solution from state-space approximation is given by the black circles. The red dashed curve gives the heave excitation force. Lower: The difference between the exact solution and the approximations (blue, dash-dotted line for constant-term and black line for state-space). The incoming wave is generated from the Bretschneider spectrum with parameters $\{H_s, T_p\} = \{1.41\,\text{m}, 4.5\,\text{s}\}$. Since the solutions in all cases are linear, both response amplitudes and excitation forces have been made non-dimensional.

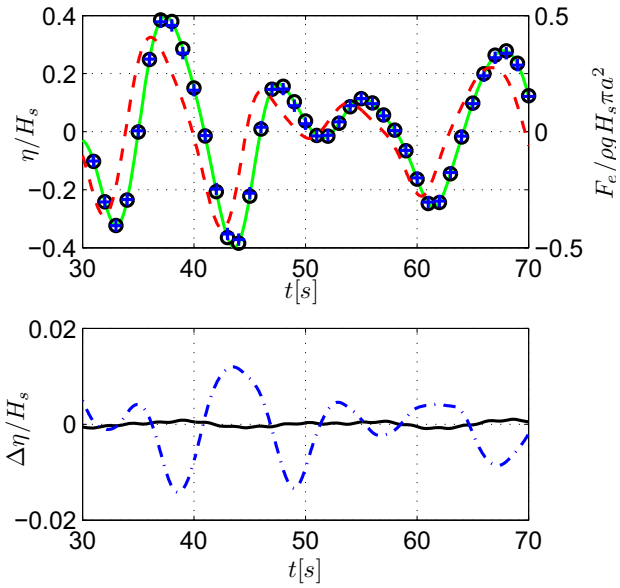

Figure 2.5: The figure corresponds to Figure 2.4, but with a peak period of 9 s.

nite number of states, which are required to describe a spatially distributed dynamic system, which is typical in hydrodynamics.

Taghipour *et al.* [117] give an overview of different methods for deducing state-space approximations, from other representations of system models:

- Impulse response curve fitting
- Regression in the frequency domain
- Realisation theory

The first one is the same method as discussed by Yu and Falnes, while regression in the frequency domain fits a rational transfer function to the radiation parameters. Here we will focus on the last method, realization theory, which is the method used in the Matlab function *imp2ss* [79], and also described by Kristiansen *et al.* [72]. More precisely it is named system realization via Hankel singular value decomposition, a method proposed by Kung [73]. It is equivalent to doing balanced truncation on an exact state space realization of the finite impulse response $\{y(1), ...y(N)\}$, with a

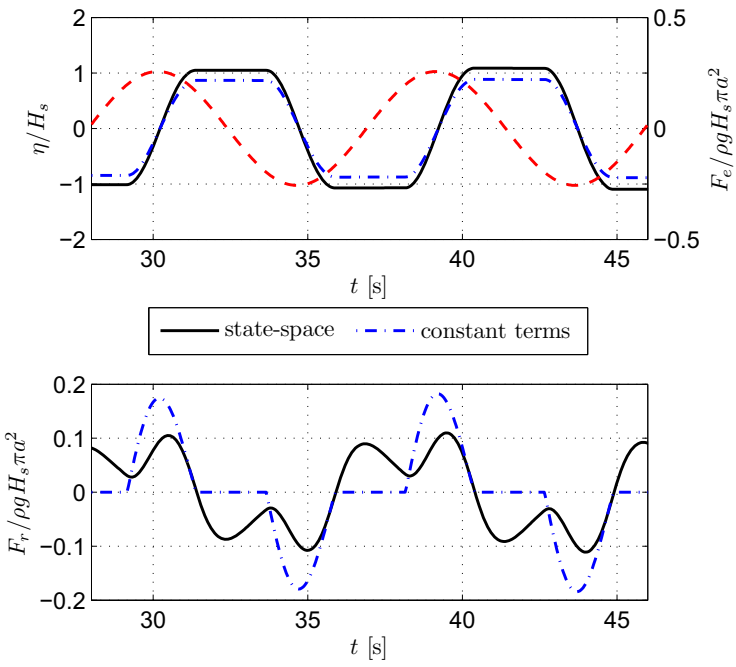

Figure 2.6: Upper: Heave response with latching control in a regular wave of 9 s period and 1 m height. The fully drawn curve gives the solution using state-space approximation for the radiation force, and the blue cross-markers give the solution using a linear term with constant coefficient (corresponding to a period equal to the resonance period). The excitation force is also included as a red dashed curve with scales on the right-hand axis. Lower: The radiation force for the same solutions; fully drawn for the state-space approximation and dash-dotted for the linear-term approximation.

predefined error tolerance, such that

$$||\mathbf{G}_k - \mathbf{G}_N||_\infty \leq 2 \sum_{i=k+1}^{N} \sigma_i \tag{2.8}$$

where σ_i are the Hankel singular values. Further, $\mathbf{G}_k$ is the reduced model with order k and $\mathbf{G}_N$ is the initial model with order N. The bound for the infinity norm tells that the maximum row sum should be less than the sum of the discarded Hankel singular values σ_i, $i \in \{k+1, \ldots N\}$. For a stable system these values indicate the respective states' energy of the system. Hence, an accurate, reduced-order representation can be directly

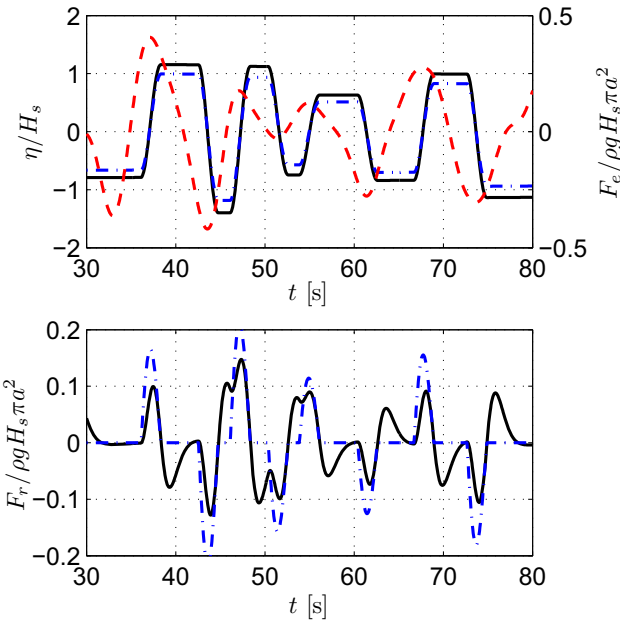

Figure 2.7: The figure corresponds to Figure 2.6, but with an irregular wave input, having peak period 9 s and significant wave height equal to 1.41 m.

determined by examining the system Hankel singular values [79]. This is the method followed in the hydrodynamic modelling herein.

The state-space representation gives

$$\dot{\mathbf{z}}(t) = \mathbf{A}_k \mathbf{z}(t) + B_k\, u(t) \tag{2.9}$$

$$F_r(t) = \mathbf{C}_k \mathbf{z}(t), \tag{2.10}$$

with the new state vector $\mathbf{z}$ for the radiation force model. The more precise bond graph is now as shown in Figure 2.8. The radiation force is calculated by the state-space block, which takes its input signal (the velocity $u(t)$) from the 1-junction. The added mass at infinite frequency (m_∞) has been included in the I element together with the body mass m.

Again, refer to Figures 2.4 and 2.5 for an example which compares the approximate solutions and the exact linear solution. It is observed that the error is substantially reduced with the state-space approximation as compared to the constant-term approximation.

A further example involving latching control (see Section 3.3.5) is shown in Figures 2.6 and 2.7. Because latching control means that the system is time-variant, this example does not include a frequency domain solution.

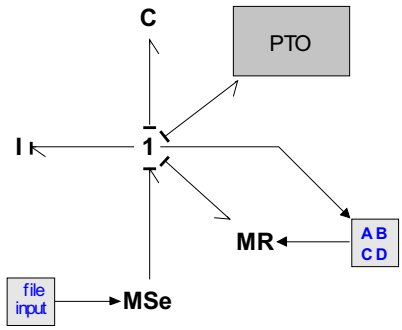

Figure 2.8: Bond graph for a heaving floating body with a more accurate representation of the radiation force than shown in Figure 2.3. The radiation force is now approximated by a state-space model feeding its output into a *modulated resistor element* MR.

The chosen plots show an example where the response error is quite large. We also see that the trace of the radiation force in this case becomes quite different for the two approximations. With latching control the memory effect of the radiation force becomes important, which can clearly be seen from the curves. Although the error in amplitudes for the constant R_r model can be reduced by adjusting the coefficient, the shape of the radiation force curve will still be wrong (also in the intervals of motion), which means that the computed absorbed energy will be inaccurate.

2.4.3 The excitation force

As input to the dynamic system it is common to take the undisturbed incident wave elevation $\zeta(x_{\text{ref}}, y_{\text{ref}}, t)$ measured at some chosen point $(x_{\text{ref}}, y_{\text{ref}})$, often at the centre axis of the body. The relation between elevation ζ of the incident wave and the excitation force F_e on the body is given by the excitation force coefficient $\hat{H}_{F\zeta}$ (often alternatively called the force response amplitude operator, RAO) such that

$$\underbrace{\hat{F}_e(\omega) = \hat{H}_{F\zeta}(\omega)\hat{\zeta}_{\text{ref}}(\omega)}_{\text{frequency domain}} \qquad \underbrace{F_e(t) = h_{F\zeta}(t) \star \zeta_{\text{ref}}(t).}_{\text{time domain}} \tag{2.11}$$

The excitation force coefficient depends on the body geometry and is in general non-causal [39]. An example of the excitation force coefficient for heave is given in Figure 2.9, where we see that the impulse response is non-vanishing for $t < 0$.

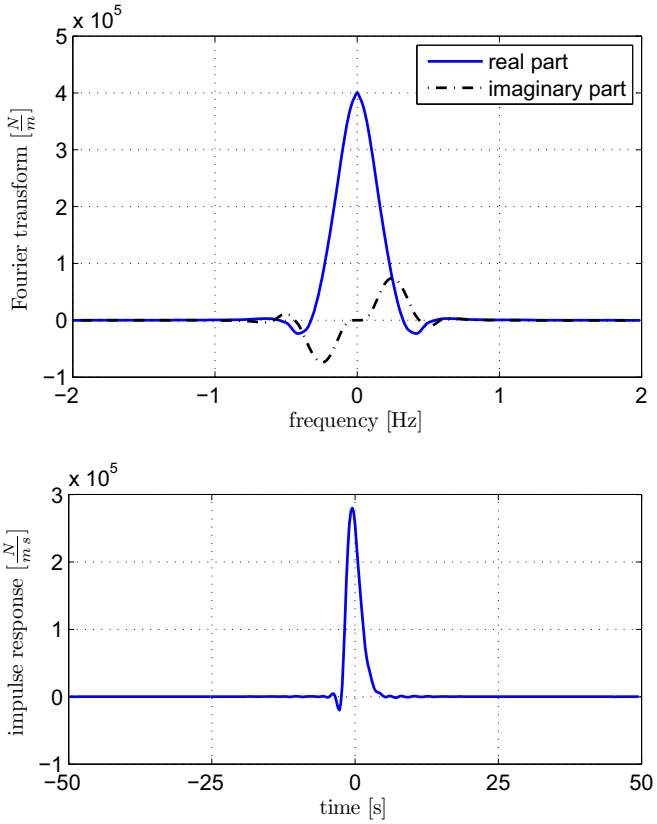

Figure 2.9: Excitation force coefficient for the heave mode of a semi-submerged sphere (referred to the position of the centre of the sphere). The frequency domain function (top) has even real part and odd imaginary part, giving a real impulse response (bottom). The impulse response is, however, non-causal (i.e. non-vanishing for $t < 0$).

Causalised impulse response

For time-domain simulation, the impulse response function may be made approximately causal by introducing a small time shift τ_c [121], which according to the Fourier transform is done by a multiplication factor $e^{j\omega\tau_c}$,

$$\underbrace{\hat{F}_{e,c}(\omega) = \hat{H}_{F\zeta}(\omega)\, e^{-j\omega\tau_c}}_{\text{frequency domain}} \qquad \underbrace{F_{e,c}(t) = h_{F\zeta}(t-\tau_c) = h_{F\zeta}(t) \star \delta(t-\tau_c).}_{\text{time domain}} \tag{2.12}$$

If the remaining function values for negative t are then negligible, the function can be approximated by zero for $t < 0$. See Figure 2.10.

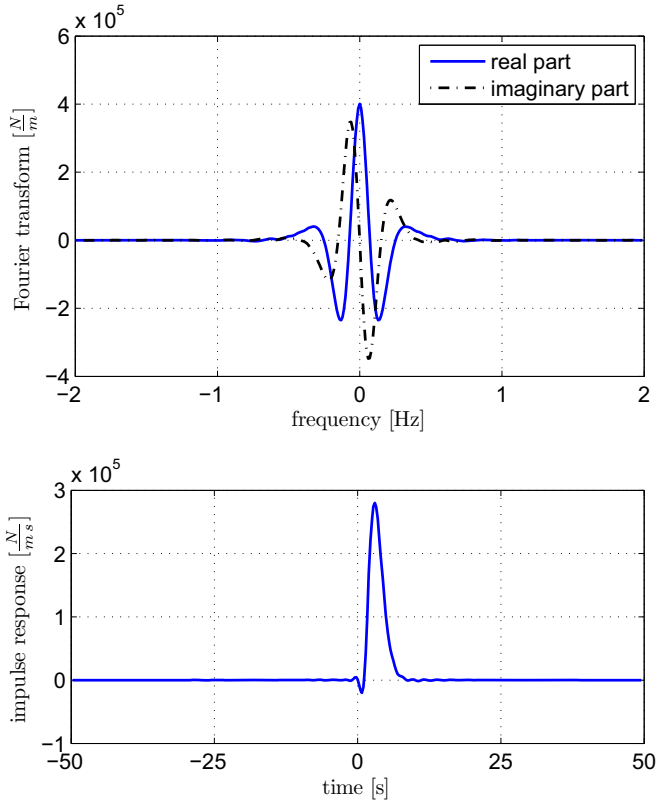

Figure 2.10: Causalised version of the function showed in Figure 2.9, achieved by a time shift as given by Equation (2.12).

In time-domain simulations, the convolution of Equation (2.11) must be evaluated if the wave elevation is taken as input. With the causalised impulse response, a state-space approximation for the convolution may then be found in the same manner as for the radiation-term convolution:

$$\dot{\mathbf{z}} = \mathbf{A}\mathbf{z} + \mathbf{B}\zeta \tag{2.13}$$

$$F_e(t - \tau_c) = \mathbf{C}\mathbf{z}(t) + \mathbf{D}\zeta. \tag{2.14}$$

An example of the corresponding approximation is included in Figure 2.10. Using this approximation in simulations, the calculated response will be shifted with regard to the wave-elevation input, so this must be adjusted for in the analysis.

If one intends to use a local wave-elevation measurement to directly estimate the excitation force by this method in a real-time application, a prediction of the wave elevation must be provided as long into the future as the impulse-response have been shifted. Alternatively, the excitation force may be approximated by the use of an estimator based on measured hydrodynamic pressure or a measurement of the body's motion response to the incident wave.

A third alternative would be to use remote monitoring to estimate the wave propagating towards the body, but this approach will not be treated here.

Pre-calculated time series

In stead of using the wave elevation as input, one can in time-domain simulations use the excitation force directly, which can then be pre-calculated based on the hydrodynamic parameters. If the spectrum $S_\zeta(\omega)$ for the incident wave is known, a good approximation to the excitation force can be constructed by summing components made from the discretised wave spectrum. For frequency component k corresponding to angular frequency $\omega_k = k\Delta\omega$, we find the excitation force spectrum $S_{F,k}$ from the evenly spaced wave elevation spectrum $S_{\zeta,k} = S_\zeta(k\Delta\omega)$ by use of the excitation force coefficients $\hat{H}_{F\zeta,k} = \hat{H}_{F\zeta}(\omega_k) = |\hat{H}_{F\zeta}(\omega_k)|\, e^{j\angle \hat{H}_{F\zeta}(\omega_k)}$:

$$S_{F,k} = |\hat{H}_{F\zeta,k}|^2\, S_{\zeta,k}, \quad \phi_{F,k} = \angle \hat{H}_{F\zeta,k}. \tag{2.15}$$

Furthermore, the complex excitation force amplitude for component k is now given as (for details see e.g. [26, Chapter 7]):

$$\hat{F}_{e,k} = \sqrt{2\, S_{F,k}\, \Delta\omega}\, e^{j\,(\phi_{\zeta,k}+\phi_{F,k})}. \tag{2.16}$$

It is assumed that the wave elevation spectrum $S_\zeta(\omega)$ with phase information $\phi_{\zeta,k}$ is known from measurements or has been synthesised with random phase components.

Alternatively, if the wave spectrum is given in the form of complex wave elevation amplitude $\hat{\zeta}_k = \sqrt{2S_{\zeta,k}\,\Delta\omega}\, e^{j\phi_{\zeta,k}}$, we can go directly to the excitation force amplitude:

$$\hat{F}_{e,k} = \hat{H}_{F\zeta,k}\, \hat{\zeta}_k. \tag{2.17}$$

With N frequency components, the excitation force time series is now calculated as

$$F_e(t) = \sum_{k=1}^{N} \Re\left\{ \hat{F}_{e,k}\, e^{j\omega_k t} \right\}. \tag{2.18}$$

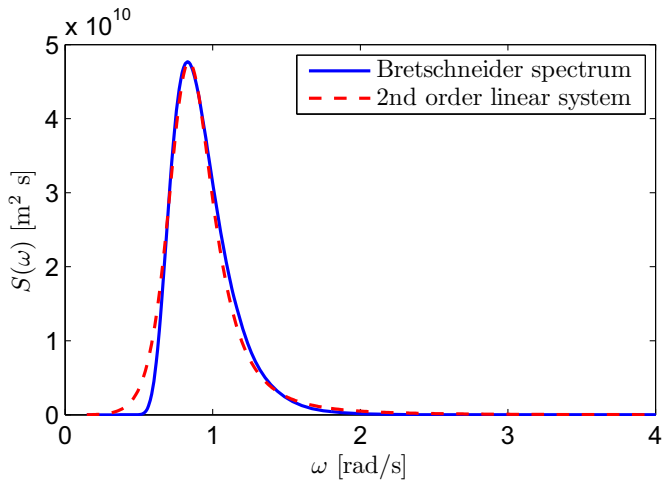

Figure 2.11: Accurate and approximated Bretschneider spectra for $H_s = 1.41\,\mathrm{m}$ and $T_e = 6\,\mathrm{s}$. The dashed line result from the approximation given by Equation (2.19).

For use in time-domain simulations, discretised time series may be pre-calculated (with time step Δt) and saved on file. During simulations the excitation force can then be found by interpolation in the pre-calculated time series. If the resolution is made high enough, simple and fast linear interpolation yields results that are sufficiently accurate.

Other cases

Yet another alternative is to take the excitation force as input to the system, not the wave elevation, and model this directly. An approximation to the Bretscneider spectrum by a second-order linear system can then be generated by feeding a Gaussian white noise to the Laplace-domain transfer function

$$H_{\mathrm{Bs}}(s) = \frac{K}{s^2 + \lambda\,\omega_1\,s + \omega_1^2}, \tag{2.19}$$

with $\lambda = 0.15$ as proposed by Sælid and Jenssen [106]. A comparison of this spectrum and the force spectrum in a Bretschneider sea state for the heaving buoy is shown in Figure 2.11. The gain factor K must be adjusted to give the desired wave loading.

2.4.4 A two-body system

Extending now to a two-body system consisting of two heaving buoys (Figure 2.12) we may use our experience from the previous section to draw a bond graph. Using the state-space convolution replacement we may suggest the graph in Figure 2.13, where oscillations in other modes have been disregarded.

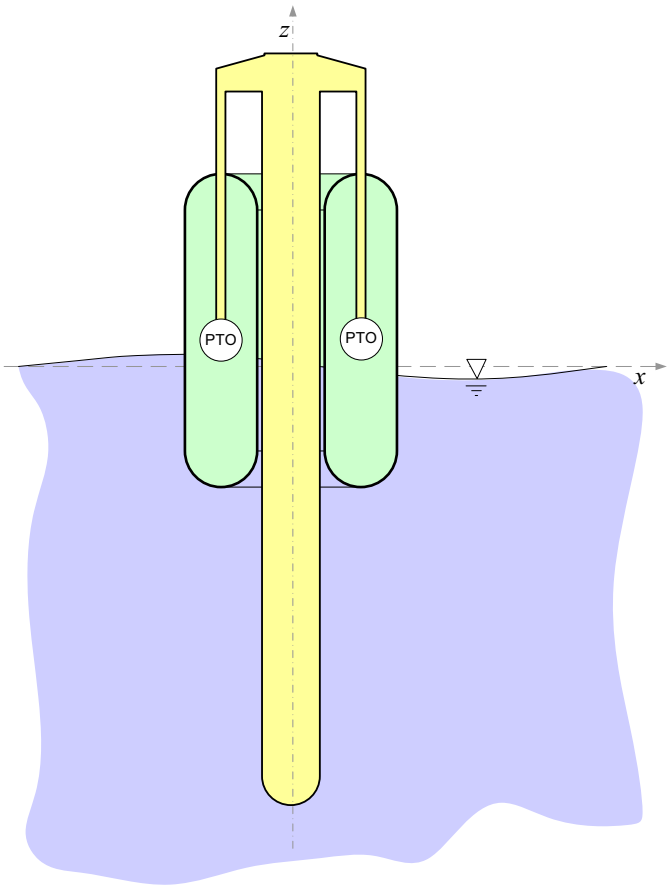

Figure 2.12: Sectional drawing of a circular-symmetric two-body system for wave energy conversion. The power is extracted from the relative motion of the two bodies — a tubular outer floater and an inner cylindrical floater, both with rounded submerged surfaces.

The bond graph now yields four state variables p_3, p_{10}, q_4 and q_9 corresponding to the two I and C elements, respectively. Additionally, the state variables of the radiation force approximation must be included. This

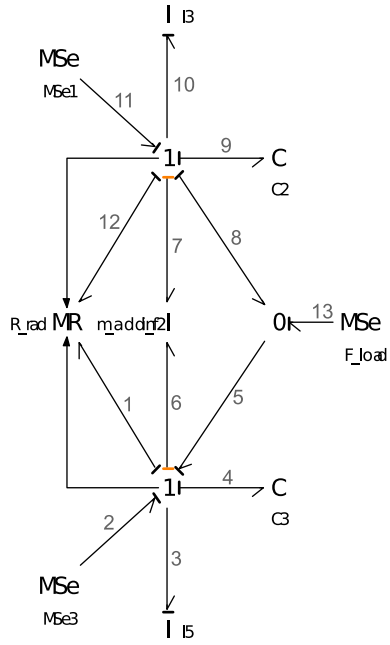

Figure 2.13: A bond graph for the two-body heaving wave energy converter sketched in Figure 2.12. The added mass may be modelled as an I-field, whereas the wave damping may be represented by a modulated R field.

time this approximation is a 2×2 multiple-input multiple-output (MIMO) model. The equations derived from the graph are:

$$\begin{aligned} \dot{p}_3 &= -S_4\, q_4 - e_{r,a} + e_2 + e_{13} \\ \dot{q}_4 &= p_3/m_3 \\ \dot{p}_{10} &= -S_9\, q_9 - e_{r,b} + e_{11} - e_{13} \\ \dot{q}_9 &= p_{10}/m_{10} \\ \dot{\mathbf{z}} &= \mathbf{A}\mathbf{z} + \mathbf{B}\,[p_3/m_3 \quad p_{10}/m_{10}]^{\mathrm{T}}, \end{aligned} \tag{2.20}$$

where

$$\begin{bmatrix} e_{r,a} \\ e_{r,b} \end{bmatrix} = [e_7 \quad e_6]^{\mathrm{T}} + [e_{12} \quad e_1]^{\mathrm{T}} = \mathbf{m}_r(\infty) \begin{bmatrix} \dot{p}_3/m_3 \\ \dot{p}_{10}/m_{10} \end{bmatrix} + \mathbf{C}\mathbf{z}(t). \tag{2.21}$$

In general, both the added mass matrix $\mathbf{m}_r(\omega)$ and the radiation resistance matrix $\mathbf{R}_r(\omega)$ will have non-zero cross terms, meaning that there is hydrodynamic interaction between the bodies. Because of the time-derivatives

occurring on the right side of Equation (2.21), the set of equations (2.20) is implicit. This may also be seen from the differential causality of the corresponding added mass inertia elements in Figure 2.13. Inserting for the radiation force, the equations can be rewritten as

$$\begin{aligned}
\dot{p}_3 &= [1 \quad 0]^{\mathrm{T}}\,\mathbf{G}^{-1}\,[E_a \quad E_b]^{\mathrm{T}} = [\overline{G}_{1,1} \quad \overline{G}_{1,2}][E_a \quad E_b]^{\mathrm{T}} \\
\dot{q}_4 &= p_3/m_3 \\
\dot{p}_{10} &= [0 \quad 1]^{\mathrm{T}}\,\mathbf{G}^{-1}\,[E_a \quad E_b]^{\mathrm{T}} = [\overline{G}_{2,1} \quad \overline{G}_{2,2}][E_a \quad E_b]^{\mathrm{T}} \\
\dot{q}_9 &= p_{10}/m_{10} \\
\dot{\mathbf{z}} &= \mathbf{A}\mathbf{z} + \mathbf{B}\,\mathbf{m}^{-1}[p_3 \quad p_{10}]^{\mathrm{T}},
\end{aligned} \tag{2.22}$$

where we have introduced the matrix $\mathbf{G}$ and vector elements E_a and E_b. They are given by

$$\begin{aligned}
\mathbf{G} &= \mathbf{I} + \mathbf{m}_r(\infty)\mathbf{m}^{-1} \\
E_a &= -S_4\,q_4 - C_{1,1}\,p_3 - C_{1,2}\,p_{10} + e_2 + e_{13} \\
E_b &= -S_9\,q_9 - C_{2,1}\,p_3 - C_{2,2}\,p_{10} + e_{11} + e_{13}.
\end{aligned} \tag{2.23}$$

Furthermore, in Equation (2.22), $\overline{\mathbf{G}} = \mathbf{G}^{-1}$ and $\mathbf{m} = [1 \quad 0]^{\mathrm{T}}[m_3 \quad 0] + [0 \quad 1]^{\mathrm{T}}[0 \quad m_{10}]$.

Since both the wave damping (radiation resistance) and the added mass depend on couplings between body motions, they have to be modelled by two-port field elements in bond graph notation. The added mass is an inertia effect and is thus modelled by an I field, whereas the wave damping is a resistance effect and is modelled by a modulated R field. The modulation occurs because of the frequency dependence of R_r and m_r, which is resolved by the state-space approximation.

2.4.5 Models with several bodies and all modes of motion

In general a rigid body has six possible modes of motion. Instead of drawing the flow (i.e. velocity) of each of these motions as a separate one junction, we use multi-bonds where all six modes are represented by a six-dimensional one junction and connect these to vector elements representing all modes. Now assume that the two bodies of Figure 2.12 are moving in all six degrees of freedom, except that they are constrained to move together in all other modes than heave. A two-body system may then be represented as shown in Figure 2.14, where the machinery is converting energy through the relative motion. The bodies are connected through very stiff springs in the rotational modes, which ensure that the upper body moves along the guide of the

second body. A damper is included to remove oscillations in these modes. This gives a a small flexibility, which may correspond to a real compliance in the construction.

In this case the bodies have been represented by 3D rigid-body models as proposed by Karnopp et al.[69, Chapter 9], and given by the star-like symbyls in Figure 2.14. There will be 12 equations for the momentum variables and 12 equations for the displacement variables, all coupled. Furthermore, the radiation force model will have 12 inputs corresponding to the six velocities of both bodies and 12 outputs corresponding to the radiation force components on both bodies.

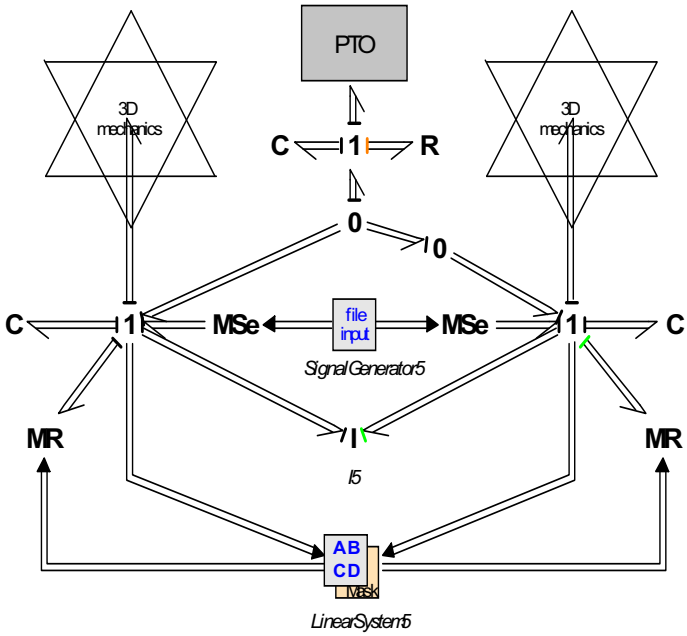

Figure 2.14: bond graph for a two-body wave energy converter free to move in all six rigid body modes. The state-space model for the radiation force and the calculation procedure for the excitation force includes interaction effects between the two bodies.

2.5 Discussion of contributions to modelling theory for wave energy converters

The publications enclosed in Appendix A all treat systems with constraints or non-linearities. This means that the analysis is mainly carried out by time-domain methods. The intention has been to go one step closer to realistic operation than the well-established frequency-domain description of wave-energy converting systems. Also, the modelling framework has been chosen with full system representation in mind, as further exemplified by Appendix B. A focus has therefore also been kept on producing irregular-wave results for the control methods, and on finding meaningful ways to present and compare these results.

The conventional approach in wave energy modelling, as in many other research and engineering branches has been to base the derivation on *first principles*, see e.g. Prado [102], Beirão [10], Ó'Cathàin et al. [123] and Josset et al. [64]. For the modelling of integral systems, involving several fields of engineering, this may become a very confusing task, and Article A was written in order to demonstrate the application of bond graph modelling language to the field of wave energy conversion. The reason for choosing bond graphs as the modelling framework within this thesis is their systematic and powerful ability to represent dynamic systems where physical effects in different energy domains occur in an interdependent manner. To the author's knowledge the application of bond graphs to wave energy modelling has earlier only been reported in the master thesis by Marré [78], of which the modelling in this thesis may be seen as an extension. Article C gives another example of a non-linear model derived by the use of bond graphs. It is expected that this method may be fruitful also for the study of other converters for ocean renewable energy, such as floating wind turbines.

Article B is a companion to Article A where the developed model is used to analyse the dynamic behaviour of the two-body system. The results are relevant for a number of devices currently under development, like the Wavebob [1] and Aquabuoy [2] devices. The work includes a discussion of the principle of force compensation (ensuring opposing excitation forces on the two bodies) and its influence on the wave absorption abilities. The application of this principle to wave energy absorption was treated by Budal [14] and has recently been investigated to some degree by Alves [6]. The treatment of this question in Article B was relatively limited, and is suggested as a task for future investigations. It is also related to the wider question of how self-referencing, floating systems best can be designed, a topic that has been discussed by several authors, e.g. [55; 7; 50; 91]. Newman [91]

showed that a self-referencing elongated and articulated body should have the length of about one wave length, and that two hinges is enough for efficient absorption. French [50] built an argument on how to make economic wave energy converters, and argued that the viable options can be divided in four categories of conversion systems, of which three are self-referencing systems. One of these three is the heaving two-body configuration, and the fourth category is heaving buoys reacting against the sea bed. In light of that study, the examples studied herein is thus regarded as representatives of promising concepts for economic wave energy conversion.

In the prototyping stages of wave energy converters, the need for *wave-to-wire* models becomes prominent. Recent examples may be found in [10] and [64]. Appendix B includes examples of how the bond graph language can be a useful aid in building such models.

Chapter 3

Control

This chapter gives some background and general considerations about wave energy controllers, and tries to motivate the choices made for the control strategy investigations carried out as a part of this thesis. Article E (on page 157) presents descriptions and comparisons of all controllers that have been studied as a part of this thesis work and will thus not be repeated here.

3.1 Controller aim

The primary aim of a controller applied to wave energy conversion is to maximise the average power output under the constraints set by the equipment and the capacity of the downstream energy carrier. Both of these two goals, optimisation and constraint handling, point to techniques of optimal control theory and model-based control.

Depending on the design, a third but equally important goal for the controller may, if possible, be to help in protecting the device and its machinery under severe storm conditions. In this thesis, however, this part of the control problem, which belongs to robust control, has not been considered. Another relevant topic is fault-tolerant control; the ability of the controller to give safe operation (or safe shut-down if necessary) under failure situations. This has also been defined out of the scope of the current thesis work.

In general, an effect of improved control of a wave energy converter is to increase the average oscillation amplitude, resulting in better exploitation of the deployed structural volume. One might say that the converter should be designed to work at full stroke for a substantial part of the operational time, and the controller is the key element in achieving this in an irregular

wave climate.

3.2 Main control variable: The machinery force

In the analysis of optimisation and constraint handling for a wave energy converter, the key control variable is the machinery force. Often a linear behaviour of the machinery force is assumed, and the resulting requirements for optimal control under that assumption will be given in Section 3.3. Although idealised in many ways, the approach within this thesis has taken a step away from the assumption of linearity, and focuses more on a time-domain description where control forces, and partly system state equations, are allowed to be non-linear. This allows for real-time implementation with constraint handling (see, in particular, Article E).

The machinery force typically falls into one of the following categories

Resistive loading: $F_m(t) = R_m\,\dot{\eta}(t)$, with the requirement that $R_m \geq 0$. This definition for the machinery force means that the machinery is only able to *extract* power from the system, i.e. it cannot work as a motor. This is a reasonable assumption for some types of machinery. In its simplest form the machinery load resistance R_m is constant, such that the machinery force becomes linearly dependent on the buoy velocity, which makes it suitable for frequency domain analysis. Otherwise, the load resistance may be taken to be time-variant, $R_m(t)$, which opens for the possibility of latching and clutching control (treating the latching mechanism as a machinery force with infinite resistance), see Section 3.3.5. Time-variance also opens for adaptive control, where the load resistance is tuned according to the current sea state.

Reactive loading: $\hat{F}_m(\omega) = Z_m(\omega_k)\,\hat{u}(\omega)$ (frequency domain) or $F_m(t) = m_m\ddot{\eta}(t) + R_m\dot{\eta}(t) + S_m\eta(t)$ (time domain). In this case the impedance Z_m is a complex number giving the possibility of machinery forces proportional to e.g. position and acceleration. This results in reactive and inverted power flow (i.e. the machinery works partly as a motor). Again, time-variant impedances $Z_m(t)$ opens for adaptive tuning, but it disqualifies the use of frequency domain descriptions.

Non-linear loading: $F_m(t) = f(t, F_e(t), \boldsymbol{\eta}(t))$. In this case no initial restrictions are put on the representation of the machinery force, which typically depends on system states and an estimate of the excitation force. Strategies that involve nonlinear feed-back terms, switching

controllers or online numerical optimisations, typically belong here. A non-linear load force gives the possibility of constraint handling; exemplified e.g. by resistive and reactive controllers extended with state-dependent coefficients $R_m(t, \mathbf{x}(t))$ and $Z_m(t, \mathbf{x}(t))$.

Adaptive control by online tuning of the control parameters, as well as constraint handling in the control function, is treated in Article E. Most of the controllers studied there would belong to the last category defined above.

3.3 Absorbed power and control principles

The amount of power absorbed by a body oscillating in ocean waves is simply equal to the sum of pressure forces on the body due to the incident, diffracted and radiated waves, multiplied by the body velocity. In order to analyse this more in detail we use the mathematical representation (2.2) of the motion. This section builds heavily on Chapter 6 of [41].

3.3.1 Maximum absorbed power: the optimal linear solution

Assume that we now convert power through one mode of motion only, say mode 1: surge (choosing pitch or heave would yield analogous equations). Writing the machinery force as $\hat{F}_m = Z_m \hat{u}_1$ the average useful converted power is given by

$$P_u = \frac{1}{2} \Re\{Z_m\} |\hat{u}_1|^2. \tag{3.1}$$

With the machinery force defined as $\hat{F}_m = Z_m \, \hat{u}_1$, it may be found that the optimum machinery impedance Z_m, giving maximum useful power, then is

$$Z_{m,\text{opt}} = -Z^*_{i,11}; \tag{3.2}$$

the negative complex-conjugate of the first diagonal-term of the intrinsic impedance matrix. A controller aim of fulfilling Equation (3.2) has therefore been named *complex-conjugate* control.

This condition for maximum unconstrained power conversion may equivalently be expressed by two requirements:

Optimum phase The body must oscillate with its velocity $\hat{u}$ in phase with the excitation force $\hat{F}_e$, i.e. $\phi = \angle \hat{F}_e - \angle \hat{u} = 0$

Optimum amplitude The oscillation amplitude must be adjusted such that the radiated power $P_{r,1} = \frac{1}{2} R_{r,11} |\hat{u}|^2$ equals half the excitation power $P_{e,1} = \frac{1}{2} |\hat{F}_{e,1}| |\hat{u}_1| \cos(\phi)$.

Control with the aim of satisfying these two conditions are sometimes referred to as *phase and amplitude control*. As mentioned, it is equivalent to complex-conjugate control. Optimum phase occurs naturally at resonance, which is characterised by the cancellation of inertia and stiffness terms (i.e. the reactance $X_{i,1}(\omega)$ is zero).

These requirements are valid for extraction of power from one mode of motion. For more complicated configurations the optimum conditions take the form of a matrix equation.

3.3.2 The optimum is non-causal

The control problem resulting from the optimality conditions given above is, in general, non-causal: due to the complex conjugated intrinsic impedance, which is anti-causal, the optimal control force becomes dependent on future values for the excitation force [88; 39; 42]. This may be remedied by predicting the future excitation based on local measurements, or by computing it from remote measurements [88; 104].

In contrast to the notion complex-conjugate control, *reactive control* may be used as a more general term, referring to the aim of cancelling the intrinsic reactance (giving optimal phase). It may be combined with various strategies for controlling the amplitude, where restricting the amplitudes to within the machinery capabilities may be part of the goal (adding non-linear effects to the controller). However, the problem is in principle still non-causal.

3.3.3 Causal approximation to the optimum

If we, in addition to the velocity-proportional term of Equation (3.5), allow for forces proportional to the acceleration $\hat{a}$ and the position $\hat{p}$, we get

$$\hat{F}_m = m_m(\omega)\,\hat{a} + R_m(\omega)\,\hat{u} + S_m(\omega)\,\hat{p}. \tag{3.3}$$

The first and third force terms on the right-hand side give reactive power; when multiplied by velocity and integrated over one period, $\overline{P} = \frac{1}{T}\int_T F_m u\,dt$, they give an average power of zero. The optimal choice for the coefficients m_m, R_m and S_m would be the one corresponding to Equation (3.2), which we have learned is non-causal.

If the incident wave is regular with an angular frequency ω_k, the problem becomes causal and optimal operation is achieved by choosing coefficient values that cancel the intrinsic reactance at that frequency, $m_m = m_{i,11}(\omega_k) = m + m_{r,11}(\omega_k)$ and $S_m = S_{i,11}$, and a machinery damping $R_m = -R_{i,11}(\omega_k) = -R_{r,11}(\omega_k)$ (remember that $\hat{F}_m = Z_m\hat{u}$ is defined with

a placement on the right hand side of Equation (2.2)). In real seas, however, another path must be found. An example of motion response and performance extending this idea to irregular waves is shown in Figure 3.1. This is covered in Article E.

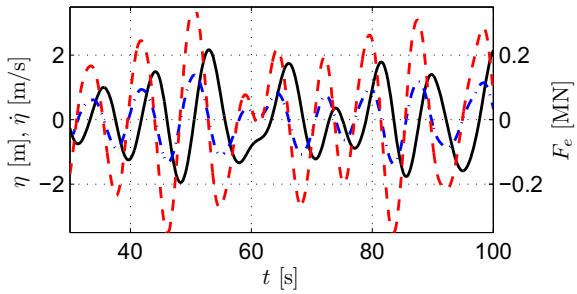

Figure 3.1: Feedback control using constant parameters in irregular seas.

One alternative to having PID feedback from velocity would be to only use the velocity-proportional force and one other term. As shown by Price [103] this gives an inferior performance in irregular seas.

As pointed out by Hals *et al.* [58], a common challenge to these strategies is the inherent large reactive power flow. Using the machinery to achieve optimal motion requires the handling of a large power flow, typically many times larger than the average absorbed power. Another challenge is motion and machinery constraints. The controller should take into account amplitude restrictions and limits on e.g. machinery capacity.

3.3.4 The passive converter

In many cases a purely resistive and time-invariant loading has been used (i.e. resistive loading), both in implementations for prototypes and as a reference in performance studies of wave energy converters. For maximum power absorption with such a machinery force, the load impedance must be chosen to be real and with the value:

$$Z_m(\omega) = R_m = -|Z_{i,11}(\omega)| = -\sqrt{R_{r,11}(\omega)^2 + X_{i,11}(\omega)^2}, \tag{3.4}$$

such that

$$\hat{F}_m = -\sqrt{R_{r,11}(\omega)^2 + X_{i,11}(\omega)^2}\,\hat{u}_1. \tag{3.5}$$

In this case the machinery is restricted not to provide any reactive power to the system (the imaginary part of the machinery impedance is zero). The

increased value of the machinery resistance as compared to (3.2) reduces the velocity amplitude but ensures a better phase relation between the excitation and the velocity.

3.3.5 Latching and clutching control strategies

Subsequent to the formulation of the conditions for optimal wave power absorption, several authors independently suggested a control strategy to achieve optimum phase without having to supply reactive power [44; 49; 56]. It became later known as *latching control*, because the motion is latched during parts of the oscillation cycle. More recent studies [66; 92] have also shown that a similar performance may be achieved by clutching the connection between the machinery and the oscillating device. We may thus define:

Latching control: The motion is stopped during parts of the cycle ($u = 0$) by means of a latching mechanism, and power is taken out by $F_m = f(u)$ during motion.

Clutching control: The machinery is engaged (with $F_m = f(u)$) only during parts of the cycle, and the device is oscillating freely ($F_m = 0$) otherwise.

Typical time traces for position and velocity with these two control strategies are shown in Figure 3.2.

With latching control the typical procedure is to latch the motion when the velocity becomes zero (i.e. when the oscillator is in the extreme position) and unlatch at the right moment for the velocity to fall into phase with the excitation force. For the clutching strategy the normal way would be to engage the machinery at zero velocity and, again, disengage it in time for the velocity to have the same phase as the excitation force. In both cases the main challenge for the controller is to determine the instant of unlatching or disengagement, as well as to set the right level of damping during power take-off.

The determination of optimal instants for unlatching/disengagement in an irregular wave is subject to the same non-causality problem as optimal control. However, successful latching control implementation have been achieved by short-time wave predictions [18]. A recent study by Price and Wallace [105] investigated alternative predictive methods for the determination of unlatching instants. Also, methods working without predictions have recently been proposed [36], and have also been pursued during this doctoral work (article Article C and Article E).

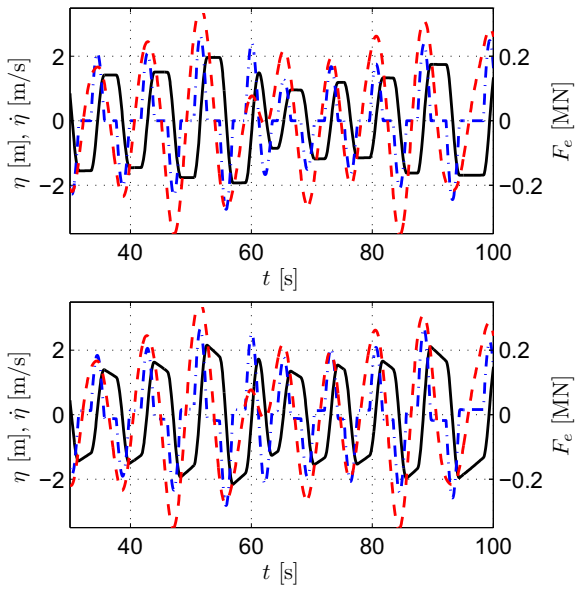

Figure 3.2: Characteristic time traces of position (black, fully drawn curves) and velocity (blue, dash-dotted curves) for latching control (upper) and clutching control (lower). The excitation force is shown by the red dash-dotted curve.

3.3.6 Other controller implementations

In addition to the more established methods for controlling wave energy devices mentioned above a range of other possibilities have been suggested. Beirão [10] applied both feedback linearisation (useful for non-linear systems [70]) and internal model control [76] to a dynamic model of the Archimedes Wave Swing [102]. He achieved best the results using feedback linearisation control, and also concluded that causalised feedback control based on the non-causal relation (3.2) was not able to compete with strategies such as latching, feedback linearisation and internal model control.

Biologically inspired controllers have been proposed by Mundon *et al.* [86], and also by Patel *et al.* [95], where the Pelamis device [60] and its resemblance with a lamprey was used as an example. By relaxing the biological constraints faced by the lamprey, it was shown that the swimming function controller could be evolved to provide substantially better performance in terms of swimming efficiency, which was taken as an indication of promising potential for application to wave energy.

Furthermore, fuzzy logic controller design for wave energy conversion

was studied by Schoen *et al.* [115], who also combined this strategy with a robust control design in order to compensate for inaccuracies in the plant model [114].

Finally, the method of model-predictive control (MPC) was recently applied to a wave energy converter by Gieske [53]. In Article D the theory for application of MPC to wave energy converters is developed further. This control principle, and the discrete-time optimisation algorithm contained as a part of it, gives the possibility of exploring the true optimal performance of a wave energy converter under machinery and motion constraints.

3.3.7 Constraints

The question of amplitude constraints for wave energy converters have been addressed in [34], [101] and [40] based on frequency domain analysis. It is shown how the absorbed power is restricted by global constraints under the assumption that the motion response is linear.

Operation with the optimality conditions fulfilled give one upper limit to the power that can be absorbed from the wave for a given wave energy converter. Budal showed that, for a heaving device, another upper bound exists for the absorbed power [43]. This bound may be seen as a physical amplitude constraint due to the finite volume that can be swept by the device during the oscillation cycle. More restrictive constraints may be necessary in order to protect the machinery and other equipment, e.g. from excessive wear, acceleration or power flow.

If we allow for the machinery forces to be non-linear, the analysis of constrained operation must be done in the time-domain. This issue is treated in Article D of this PhD work.

3.4 Discussion of contributions to control theory for wave energy conversion

The main driver behind the works of Article B to Article E has been the goal of finding practical methods for the implementation of high-yield control strategies. Starting with investigations of the latching control principle (Article B and Article C), the question of time-domain constrained optimal control is illuminated in Article D before the most well-identified control strategies for wave energy conversion are compared in Article E.

Although its successful implementation for a realistic case was reported already in the early 1980's [19; 20; 18], the latching control principle has not come to extensive use. However, some new results have been reported

in recent years [36; 86; 7; 71; 11]. It may be speculated that the limited use of latching control is partly due to the complications of determining the unlatching instants; and also partly due to the abrupt operation of mechanical components needed in applying the strategy.

Addressing the first of these challenges, the main motivation behind Article C was thus to experimentally verify the applicability of a simplified method proposed by Falcão [36] for determining suboptimal but acceptable unlatching instants in irregular waves. The verification was successful, and comparisons to other control methods undertaken in Article E showed that the method has indeed attractive properties in terms of both performance and simplicity. In Article C an approximate analytic expression for setting the threshold level was proposed and assessed.

Article B includes an investigation of latching control for a two-body system equipped with an ingenious hydraulic power take-off, and shows how the absorbed power may be increased in regular waves. It is suggested that the control of such a system in irregular waves is pursued in further work, looking both at latching control and other options.

In the frequency-domain treatment of constrained optimum for the power absorption [34; 101; 40], a linear response to the excitation force is implicitly assumed. The true constrained optimum only reveals itself once a general nonlinear response is allowed for. Earlier application of optimal control theory has been restricted to latching control (e.g. [61; 7; 71]). In Article D the constrained optimal solution is found by use of a discretised time-domain model of the converter system. Furthermore, the discrete-time optimisation is integrated as a part of a model-predictive controller similar to the approach proposed by Gieske [53]. There, however the formulation of the optimum was only approximative. With the formulation derived in Article D, real-time control in irregular waves with performance close to the theoretical optimum may be achieved. A novel observation made in that work was that the absorbed power for a certain device can be larger in irregular waves than in corresponding regular waves (i.e. having similar characteristic wave lengths and equal wave power level).

In Article E the control strategies of Article B to Article D are compared to other candidate strategies, and differences are highlighted. A similar comparison, although less general, was carried out by Beirão [10], where the conclusions were somewhat different. One of the reasons for the differing conclusion must surely have been that the controllers were implemented with a very detailed model of a specific converter system, obscuring some of the basic properties of each controller alternative. The constrained optimum revealed in Article D is the true reference point that should be used when

assessing converter performance. Similar investigations should be undertaken on other modes of motion and other types of wave energy converters. Using the MPC results (Article D) as a benchmark gives the possibility to purposefully quantify the performance of various other strategies as shown in Article E.

A final remark is that the controllers investigated in this thesis have mainly been applied to a simplified model of a wave-energy converting, heaving buoy. Nevertheless, the derived results will be partly or fully extendable to other absorber designs, as the underlying physics of wave interference are the same. This claim is well supported by the work of Falnes [41, Chapters 5, 6 and 7].

Chapter 4

Simulation

The numerical simulation results presented in this thesis are derived from time-domain simulations of dynamic systems modelled by state-space equations, i.e. sets of first order ordinary differential equations. A brief account is here given for the numerical integration tools, simulation set-up and accuracy.

4.1 Numerical integration algorithms

Today a large number of software packages offer preprogrammed numerical integration algorithms. In the present study, the solution of the mathematical models have been obtained by implementation in Matlab/Simulink and 20-sim.

4.1.1 Matlab/Simulink

Numerical integration of ordinary differential equations is provided by the *ODE solver* package of Matlab [79]. It contains both fixed-step and variable-step solvers, suitable for different degrees of stiffness and needs for accuracy. For the models reported herein, which occasionally have been relatively stiff, the solvers named *ode4* (4th order Runge-Kutta), *ode15s* (numerical differentiation formulas) and *ode23tb* (implicit Runge-Kutta formula with first stage trapezoidal rule and second stage backward differentiation formula) have been used. In order to use these solver functions the state equations must be provided in a separate function file.

A range of Matlab scripts and functions have been developed to prepare and run simulations, and for storing and analysing simulation results. An overview of these programs is given in Appendix C.

Simulink is a block-diagram front-end integrated with Matlab, primarily made for the modelling and simulation of dynamical systems, and with easy inclusion of control algorithms. It uses the *ODE solvers* for the numerical integration.

4.1.2 20-sim

Among the existing software tools for bond graph modelling (e.g. CampG and MS1) 20-sim [3] developed by Controllab Products B.V. in the Netherlands is one of the most advanced. It offers a graphical interface where the user can draw the model graphs and enter the governing equations for each element. The state equations derived from the graph may be exported for use with other software, or solved by the included integration algorithms. The simulation results may easily be plotted or visualised by simple 3D animations. This makes the software well suited for system design, as models are easily modified and tested. The numerical integration algorithms that proved most useful for the systems studied as a part of this thesis, were the Runge-Kutta 4, Vode-Adams and Backward Differentiation Formula solvers of 20-sim.

4.2 Accuracy and convergence

In modelling and simulation work, reality always gives the final answer as to whether a model has been successful in representing the effects under investigation. In one of the published articles (Article C), the simulation results have been validated by comparison to experimental results. For the other works, the validation has been limited to comparisons with theoretical limits and similar cases found in literature. The mathematical models are, however, based on well-established theory, so that the results and the conclusions drawn from them are believed to be correct within the given assumptions.

With the assumption of linear hydrodynamics and linear hydrostatic stiffness along with other idealisations used in the modelling, the overall accuracy of the simulation results is expected to be in the order of 10-20 %, but depending strongly on which variable is measured. These errors are due to the mathematical model itself, and not the way it has been solved. Although this might seem rough, the nature of dominating effects have been correctly represented in the models such that observed trends will be valid. This was also the conclusion reached based on the comparisons made in Article C.

While the mathematical model with its assumptions governs the accuracy of the overall results, the numerical simulation procedure governs the precision. If the error at each time step becomes too large, the solver will not converge to the correct solution. For the fixed-step solvers, the precision of the solution is governed by the step length. It must be chosen small enough to give a converged solution, which may be ensured by reducing the time step until further reduction does not have significant influence on the computed solution. In the case of stiff models, this might require very small time steps and a correspondingly large computational efforts. Then a variable-step solver might perform better.

For variable-step solvers the precision is controlled by setting tolerances for the error at each time step, typically in terms of two parameters – the relative error ϵ_{rel} and the absolute error ϵ_{abs}. In Matlab/Simulink ϵ_{rel} is a scalar factor (common to all variables), while ϵ_{abs} can optionally be supplied as a vector giving the tolerance for each state variable. In 20-sim only scalar values are allowed (giving the same absolute tolerance for all state variables). According to Shampine *et al.* [116] numerical ODE solvers of Matlab aim at satisfying

$$|y_i(t_n) - y_{n,i}| \leq \epsilon_{\text{rel}}|y_i(t_n)| + \epsilon_{\text{abs},i} \tag{4.1}$$

where $y_i(t_n)$ is state variable number i at time step number n. The default settings in Matlab are 10^{-3} for the relative error and 10^{-6} for the absolute error, whereas typical settings for scientific computing is 10^{-5} and 10^{-6}, respectively. This, of course, depends on the problem at hand.

As a rule of thumb, the tolerances may be chosen in the following way [13, p. 131]: Let m be the number of significant digits required for the solution of component y_i. Then set $\epsilon_{\text{rel}} = 10^{-(m+1)}$. Furthermore, set $\epsilon_{\text{abs},i}$ equal to the value at which $|y_i|$ is essentially insignificant.

Some of the simulation models appeared to be very stiff (e.g. due to control algorithms and/or valve components), which made stability and convergence of the solutions a delicate issue. The choice of solver algorithm and tolerance settings has been critical in arriving at converged solutions.

4.3 Numerical experiments and statistical measures

In the comparative studies of converter performance in irregular waves, the length of the time series has been chosen to be about 100 average wave periods. This was found to give a sufficiently constant value for the derived average power measures. For each chosen set of sea state parameters in

each comparative study, the same excitation time series was used for all converter configurations and controller alternatives.

The wave elevation and excitation force time series have been pre-calculated based on synthesised wave spectra $S_\zeta(\omega_k)$. The spectra have been generated using 800 frequency components ω_k with randomised phase ϕ_k and randomised frequency for each frequency interval $(\omega_k - \omega_{\min})/\Delta\omega \in [k,\ (k{+}1)\rangle$. The wave elevation time series are then constructed by (see for instance [26, Chapter 7], as well as [45, page 26] for some advice)

$$\zeta(t) = \sum_k \Re\left\{\sqrt{2\,\Delta\omega\,S_\zeta(\omega_k)}e^{i\omega_k t+\phi_k}\right\}, \tag{4.2}$$

and the excitation force is found by Equations (2.15) to (2.18). The time series have in general been generated with a time step Δt of between 0.05 and 0.1 s at prototype scale. Linear interpolation have been used for simulation input in between stored values.

In analysis, the first few wave periods are excluded to avoid influence from startup transients. The more damped the system is, the shorter the length of this transition period needs to be. An exclusion interval of about five wave periods is usually enough for the transients to die out with the models studied herein.

For the recorded results, the variables have been saved with the same time resolution as the input time series of force and wave elevation. For integrated measures, the trapezoid rule have been used.

Chapter 5

Conclusion

5.1 Overall summary

Bond graphs are graphical representations of lumped dynamical systems. One aim of this work has been to explore the use of bond graphs for developing mathematical models of wave energy conversion systems. A challenge for the modelling of such systems is that they span several energy domains, with each domain belonging to different engineering disciplines. It is shown how the most common elements across the energy conversion chain may be modelled in a systematic and transparent way by means of bond graph models.

Furthermore, carefully selected strategies for controlling the motion of wave energy converters have been investigated by numerical simulations using mathematical models derived from the bond-graphs, and, in one investigated case, by laboratory experiments. In theory, maximising the average absorbed power from wave energy devices requires the evaluation of a non-causal control function. The main result of the thesis work is to show how the non-causal control function may be approximated by sub-optimal but high-performing causal control algorithms.

One of the control algorithms is based on model-predictive control – MPC – where constraint handling (e.g. on motion amplitudes and machinery forces) is an integral part of the controller implementation. Also for other control strategies, ways to handle constraints are proposed. These strategies, however, do not offer any inherent optimisation, which is one of the strengths of MPC. This was partially remedied by the use of gain scheduling and extremum-seeking control.

Detailed conclusions are given in each published article.

5.2 Original contributions

The author considers his main original contributions through the performed work to be

1. demonstrating the systematic modelling of wave energy conversion systems by the use of bond graphs;

2. implementing and comparing, by numerical simulations and on an unbiased basis, the working principles and performance of several causal control algorithms for wave energy conversion in irregular waves;

3. discussing and demonstrating how amplitude constraints can be included as a part of control algorithms for real-time operation in irregular waves;

4. suggesting and testing techniques for adaptive setting of control parameters as a part of algorithms for real-time operation in irregular waves;

5. applying a numerical method for determining the constrained optimal response (without assumptions of linear control, and where *optimal* means a response giving the maximum absorbed power);

6. showing, by numerical computations, how the maximum absorbed power P_a is bounded by a surface in the H-T-P_a space (where H is the wave height and T is the wave period);

7. highlighting and quantifying challenges regarding large reactive power flow through the machinery, expressed by the peak-to-average power ratio. For the studied examples the ratio reached up to 25 and above in normal irregular wave operation for conventional control strategies. This represents a challenge to the design of machinery and controller.

8. observing and suggesting an explanation for the possibility of increased absorbed power in irregular waves as compared to corresponding regular waves (i.e. having about the same wavelength characteristics and the same wave power level);

9. experimentally verifying the threshold unlatching principle for phase control proposed by Falcão [36], and suggesting an expression for setting the threshold value;

10. characterising analytically, with comparison to numerical and experimental results, the transient oscillations that may occur during latched parts of the cycle for pneumatic and hydraulic power take-off systems;

11. proposing a way to implement model-predictive control (MPC) for wave energy converters that makes it possible to approach (even for typical irregular waves) the theoretical non-causal upper bound for absorbed power;

12. investigating how increased viscous damping, as a means of establishing firmer reference in a two-body system, influences the amount of absorbed energy — with the conclusion that increased viscous damping also monotonically decreases the absorbed power, at least for the investigated two-body system.

5.3 Recommendations for further work

Regarding future research tasks, the author would like to propose the following issues that are related to the work carried out:

Submodel library Developing a modular bond graph library for the modelling of wave-energy conversion systems. As these systems are usually multifaceted and the various concepts are composed very differently, it is challenging to model the complete systems with conventional software tools. A bond graph library containing such elements as floating bodies, mooring lines, hydraulic pumps and motors, valves and tubes, electric machinery and power converters, and different types of controllers would ease the modelling of new or existing proposals.

Model validation Validation by laboratory experiments should be carried out for the unvalidated models and simulation results presented in this thesis. The different control algorithms could then be emulated by the use of a servo-motor to validate also the estimated differences in absorbed power.

Applying control strategies to other systems The comparison of control strategies has here only been carried out for heaving point-absorbers. The investigation should be extended to other converter types and other modes of motion, including multibody systems.

Power bounds for surge and pitch modes The existence and shape of Budal curves (cf. Article D and Article E) should be investigated for

other source-type modes of motion (e.g. heave and oscillating water columns). This will give a more complete picture of the restriction on absorbed power due to finite volume strokes.

Validation of $\mathbf{P}_{\mathrm{IR}} > \mathbf{P}_{\mathrm{R}}$ The observed effect of possible increases in absorbed power for irregular waves compared to corresponding regular waves should be validated experimentally.

Wave force prediction Other improved methods for wave force prediction, possibly with remote monitoring, should be identified and implemented with the MPC algorithm. It is expected that the gap between MPC results and the constrained optimum can then be further decreased.

Robust and fault-tolerant control An investigation of the robustness and stability of the different controller implementations should be carried out, such that safe operation of wave-energy conversion systems can be assured in varying conditions. This should include strategies for protecting the device and the machinery in periods of excessive wave power levels, and also in the case of failures in sensors, actuators or other system components.

Non-linear MPC The application of model-predictive control to systems with strong non-linearities should be investigated. This gives a non-linear prediction equation, which may not be solved with the standard quadratic programming (QP) formulation.

Cost estimation The estimated amount of power converted with different controller alternatives should be included in tools to estimate the cost of delivered power. As they influence heavily on both average absorbed power and on peak-to-average ratios, they will also directly influence the earnings potential.

Two-body self-referencing systems The dynamics and control for two-body self-referencing systems should be further investigated. With good design such systems may enable installation and operation in deep water where fixed reference is not an option.

References

[1] http://www.wavebob.com/, visited on 22 May 2009.

[2] http://finavera.com/en/wavetech, visited on 22 May 2009.

[3] 20-sim, version 3.6. Controllab products B.V., The Netherlands, http://www.20sim.com/.

[4] Ocean energy: Development & evaluation protocol. Technical report, Hydraulics and Maritime Research Centre, University College Cork, September 2003.

[5] BP Statistical review of world energy June 2009. Technical report, BP, 2009.

[6] M. A. A. Alves. Wave energy absorption through the relative motion between two heave oscillating bodies. Private communication, not published, 2009.

[7] A. Babarit. *Optimisation hydrodynamique et contrôle optimal d'un récupérateur de l'énergie des vagues*. PhD thesis, Ecole Centrale de Nantes, Nantes, 2005.

[8] S. Barstow, G. Mørk, D. Mollison, and J. Cruz. *Ocean wave energy*, chapter 4. The wave energy resource, pages 93–132. Springer, 2008.

[9] B. Bates, Z. W. Kundzewicz, S. Wu, and J. Palutikof. Climate change and water. Technical report, Intergovernmental Panel on Climate Change, IPCC, 2008.

[10] P. J. B. F. N. Beirão. *Modelling and Control of a Wave Energy Converter: Archimedes Wave Swing*. PhD thesis, Universidade Tecnica de Lisboa, Instituto Superior Tecnico, Delft, May 2007.

[11] T. Bjarte-Larsson and J. Falnes. Laboratory experiment on heaving body with hydraulic power take-off and latching control. *Ocean Engineering*, 33(7):847 – 877, 2006.

[12] G. Boyle. *Renewable Energy - Power for a sustainable future*. Number ISBN 0-19-926178-4. Oxford University Press, Oxford OX2 6DP, 2004.

[13] K. E. Brenan, S. L. Campbell, and L. R. Petzold. *Numerical Solution of Initial-Value Problems in Differential-Algebraic Equations*. Number ISBN 0-89871-353-6. Society for Industrial and Applied Mathematics (SIAM), 2, illustrated, revised edition, 1996.

[14] K. Budal. Floating structure with heave motion reduced by force compensation. In *Proceedings Fourth International Offshore Mechanics and Arctic Engineering Symposium*, pages 92–101, Dallas, Texas, February 1985. ASME, N.Y.

[15] K. Budal and J. Falnes. A resonant point absorber of ocean waves. *Nature*, 256:478–479, 1975. With Corrigendum in Vol. 257, p. 626.

[16] K. Budal and J. Falnes. Optimum operation of wave power converter. Technical report, Institutt for eksperimentalfysikk, NTH, Trondheim, Norge, 1976.

[17] K. Budal and J. Falnes. Interacting point absorbers with controlled motion. In B. Count, editor, *Power from Sea Waves*, pages 381–399. Academic Press, London, 1980. (ISBN 0-12-193550-7).

[18] K. Budal and J. Falnes. Wave power conversion by point absorbers: A Norwegian project. *International Journal of Ambient Energy*, 3(2):59 – 67, 1982.

[19] K. Budal, J. Falnes, T. Hals, L. C. Iversen, and T. Onshus. Model experiment with a phase controlled point absorber. In H. S. Stephens and C. A. Stapleton, editors, *Proceedings of Second International Symposium on Wave and Tidal Energy*, number ISBN 0-906085-43-9, pages 191–206, Cambridge, UK, 23–25 September 1981. BHRA Fluid Engineering (Cranford, Bedford).

[20] K. Budal, J. Falnes, L. C. Iversen, P. M. Lillebekken, G. Oltedal, T. Hals, T. Onshus, and A. S. Høy. The Norwegian wave-power buoy project. In H. Berge, editor, *Proc. Second International Symposium on Wave Energy Utilization*, number ISBN 82-519-0478-1, pages 323–344. Tapir, Trondheim, Norway, 1982.

[21] J. Callaghan and R. Boud. Future Marine Energy – results of the Marine Energy Challenge: Cost competitiveness and growth of wave and tidal stream energy. Technical report, The Carbon Thrust, 2006.

[22] R. Core Writing Team, Pachauri and A. e. Reisinger. Climate change 2007: Synthesis report. contribution of working groups i, ii and iii to the fourth assessment report of the intergovernmental panel on climate change. Technical report, IPCC, Geneva, Switzerland, 2007.

[23] J. Cruz, editor. *Ocean wave energy*. Number ISBN 978-3-540-7489-6. Springer, 2008.

[24] W. E. Cummins. The impulse response function and ship motions. *Schiffstechnik*, 9:101–109, 1962.

[25] H. E. Daly. *Beyond growth: the economics of sustainable development*. Beacon Press, Boston, 1996.

[26] R. G. Dean and R. A. Dalrymple. *Water wave mechanics for engineers and scientists*. Number ISBN 0-13-946038-1. Prentice Hall, Inc., Englewood Cliffs, New Jersey 07632, 1984.

[27] S. Dresner. *The principles of sustainability*. Number ISBN 1-85383-841-1. Earthscan Publications Ltd., London, 2002.

[28] M. Durand, A. Babarit, B. Pettinotti, O. Quillard, J. Toularastel, and A. Clément. Experimental validation of the performances of the SEAREV wave energy converter with real time latching control. In *Proceedings of the 7th European Wave and Tidal Energy Conference*, Porto, Portugal, September 2007.

[29] L. Eagles, editor. *Medium-Term Oil Market Report July 2008*. International Energy Agency, 2008.

[30] H. Eidsmoen. Hydrodynamic parameters for a two-body axisymmetric system. *Applied Ocean Research*, 17(2):103–115, 1995.

[31] H. Eidsmoen. *On the theory and simulation of heaving-buoy wave-energy converters with control*. PhD thesis, NTH (now NTNU), Trondheim, December 1995.

[32] M. Eriksson. *Modelling and experimental verification of direct drive wave energy conversion – Buoy-generator dynamics*. PhD thesis, Uppsala Universitet, 2007.

[33] D. V. Evans. A theory for wave-power absorption by oscillating bodies. *Journal of Fluid Mechanics*, 77:1–25, 1976.

[34] D. V. Evans. Maximum wave-power absorption under motion constraints. *Applied Ocean Research*, 3(4):200–203, 1981.

[35] D. V. Evans. Power from water waves. *Ann. Rev. Fluid Mech.*, 13:157–187, 1981.

[36] A. F. d. O. Falcão. Phase control through load control of oscillating-body wave energy converters with hydraulic PTO system. In *Proceedings of the 7th European Wave and Tidal Energy Conference*, Porto, Portugal, September 2007.

[37] J. Falnes. Radiation impedance matrix and optimum power absorption for interacting oscillators in surface waves. *Applied Ocean Research*, 2(2):75–80, 1980.

[38] J. Falnes. Small is beautiful: How to make wave energy economic. In *1993 European Wave Energy Symposium*, pages 367–372, Edinburgh, Scotland, 1994. (ISBN 0-903640-84-8).

[39] J. Falnes. On non-causal impulse response functions related to propagating water waves. *Applied Ocean Research*, 17(6):379–389, 1995.

[40] J. Falnes. Maximum wave-energy absorption by oscillating systems consisting of bodiew and water culumns with restricted or unrestricted amplitudes. *Proceedings of the International Offshore and Polar Engineering Conference*, 1:420–426, 2000.

[41] J. Falnes. *Ocean waves and oscillating systems: linear interactions including wave-energy extraction.* Cambridge University Press, Cambridge, 2002.

[42] J. Falnes. Optimum control of oscillation of wave-energy converters. *International Journal of Offshore and Polar Engineering*, 12(2):147–155, June 2002.

[43] J. Falnes. A review of wave-energy extraction. *Marine Structures*, 20(4):185–201, Oct. 2007.

[44] J. Falnes and K. Budal. Wave-power conversion by point absorbers. *Norwegian Maritime Research*, 6(4):2–11, 1978.

[45] O. M. Faltinsen. *Sea Loads on Ships and Offshore Structures*. Cambridge University Press, 1990.

[46] D. Fathi and J. R. Hoff. *ShipX Vessel Responses (VERES)*. MARINTEK A/S, 13 February 2004.

[47] J. H. Ferziger. *Computational methods for fluid dynamics*. Number 3rd, rev. ed. Springer, Berlin, 2002.

[48] J. Fitzgerald and L. Bergdahl. Including moorings in the assessment of a generic offshore wave energy converter: A frequency domain approach. *Marine Structures*, 21(1):23 – 46, 2008.

[49] M. French. A generalized view of resonant energy transfer. *Journal Mechanical Engineering Science*, Vol.21:pp.299–300, 1979.

[50] M. French. On the difficulty of inventing an economical sea wave energy converter: a personal view. *Proceedings of the Institution of Mechanical Engineers, Part M: Journal of Engineering for the Maritime Environment*, 220(3):149–155, Jan. 2006.

[51] M. J. French and R. Bracewell. Heaving point absorbers reacting against an internal mass. pages 247 – 255, 1985.

[52] Z. Gao and T. Moan. Mooring system analysis of multiple wave energy converters in a farm configuration. In *Proceedings of the 8th European Wave and Tidal Energy Conference*, Uppsala, Sweden, 7–10 September 2009.

[53] P. Gieske. Model predictive control of a wave energy converter: Archimedes Wave Swing. Master's thesis, Delft University of Technology, Delft, 2007.

[54] Girard, Père et fils. Pour divers moyens d'employer les vagues de la mer, comme moteurs. Patent filed in Paris, 12 July 1799.

[55] C. Grove-Palmer. Wave energy in the UK – a review of the programme june 1975–march 1982. In H. Berge, editor, *Wave energy utilization: proceedings of the 2nd International Symposium on Wave Energy Utilization, The Norwegian Institute of Technology, Trondheim, Norway, June 22-24, 1982*, number ISBN 82-519-0478-1, pages 23–28, Trondheim, 1982. Tapir, Trondheim, Norway.

[56] J. D. Guenther, D.A. and D. Brown. An investigative study of a wave-energy device. *Energy*, Vol.4:pp.299–306, 1979.

[57] G. Hagerman. Wave energy resource and economic assessment for the state of hawaii. Technical report, SEASUN Power Systems, 1992.

[58] J. Hals, T. Bjarte-Larsson, and J. Falnes. Optimum reactive control and control by latching of a wave-absorbing semisubmerged heaving sphere. *Proceedings of the International Conference on Offshore Mechanics and Arctic Engineering - OMAE*, 4:415 – 423, 2002.

[59] L. Hamill. *Understanding Hydraulics*. Palgrave Macmillan, 2nd edition edition, 2001.

[60] R. Henderson. *Ocean wave energy*, chapter 5.4 Case Study: Pelamis, pages 169–188. Springer, 2008.

[61] R. E. Hoskin and N. K. Nichols. Optimal strategies for phase control of wave energy devices. In M. E. McCormick and Y. C. Kim, editors, *Utilization of Ocean Waves - Wave to energy conversion*, pages 184 – 199. American Society of Civil Engineering, New York, 1987.

[62] E. R. Jefferys. Simulation of wave power devices. *Applied Ocean Research, 1984, Vol. 6, No. 1*, 6:31–39, 1984.

[63] L. Johanning, G. Smith, and J. Wolfram. Mooring design approach for wave energy converters. *Proceedings of the Institution of Mechanical Engineers, Part M (Journal of Engineering for the Maritime Environment)*, 220(M4):159 – 74, 2006/11/. mooring design;wave energy converters;high wave energy density;offshore floating devices;wave energy industry;generic station-keeping arrangements;mooring systems;preliminary design procedure;.

[64] C. Josset, A. Babarit, and A. Clément. A wave-to-wire model of the SEAREV wave energy converter. *Proceedings of the Institution of Mechanical Engineers, Part M: Journal of Engineering for the Maritime Environment*, 221(2):81–93, Jan. 2007.

[65] J. M. J. Journée and L. J. M. Adegeest. *Theoretical Manual of Strip Theory Program "SEAWAY for Windows"*. TU DELFT Ship Hydromechanics Laboratory and AMARCON Advanced Maritime Consulting, www.amarcon.com, September 2003. TUD Report 1370.

[66] M. Kamenský and M. Guglielmi. Optimal control of power take-off from mass-spring-damper system. In *16th International on Process Control 2007*, 2007.

[67] D. Karnopp. Bond graph models for electromagnetic actuators. *Journal of the Franklin Institute*, 319(1/2):173–181, 1985.

[68] D. Karnopp. Understanding induction motor state equations using bond graphs. Downloaded from the internet. Unpublished? Year estimated from references., 2002.

[69] D. C. Karnopp, D. L. Margolis, and R. C. Rosenberg. *System Dynamics: Modeling and Simulation of Mechatronic Systems*. Wiley, 4 edition edition, January 2006.

[70] H. K. Khalil. *Nonlinear systems*. Number ISBN 0-13-228024-8. Prentice Hall, Upper Saddle, N.J., 2 edition, 1996.

[71] U. A. Korde. Latching control of deep water wave energy devices using an active reference. *Ocean Engineering*, 29(11):1343 – 1355, 2002.

[72] E. Kristiansen, A. Hjulstad, and O. Egeland. State-space representation of radiation forces in time-domain vessel models. *Ocean Engineering*, 32(17-18):2195–2216, Dec. 2005.

[73] S. Kung. A new identification and model reduction algorithm via singular value decompositions. In *Proc.Twelth Asilomar Conf. on Circuits, Systems and Computers*, pages 705–714, November 6-8 1978.

[74] K. Larsen and P. C. Sandvik. Efficient methods for the calculation of dynamic mooring line tension. In *The First European Offshore Mechanics Symposium*, pages 482 – 489, Golden, CO, USA, 1990.

[75] M. Leijon, C. Bostrom, O. Danielsson, S. Gustafsson, K. Haikonen, O. Langhamer, E. Stromstedt, M. Stalberg, J. Sundberg, O. Svensson, S. Tyrberg, and R. Waters. Wave energy from the north sea: Experiences from the Lysekil research site. *Surveys in Geophysics*, 29(3):221 – 240, 2008.

[76] W. S. Levine, editor. *The Control handbook*. Number ISBN 0-8493-8570-9. CRC Press, Boca Raton, Fla., 1996.

[77] H. Lie and N. Sødahl. Simplified dynamic model for estimation of extreme anchorline tension. In *Offshore Australia - the 2nd Australian International Oil, Gas and Petrochemical Exhibition and Conference*, volume 2, 23-26 November 1993.

[78] I. R. Marré. Modelling and simulation of a wave energy converter using a bond graph approach. Master's thesis, Department of Marine Technology, Norwegian University of Science and Technology, June 2006.

[79] Matlab, 2006. Version 7.2, The Mathworks Inc.

[80] M. McCormick. *Ocean Wave Energy Conversion*. J. Wiley, 1981.

[81] M. E. McCormick. Analysis of a wave energy conversion buoy. *Journal of Hydronautics*, 8(3):77 – 82, 1974.

[82] D. Meadows, J. Randers, and D. Meadows. *Limits to growth — the 30-year update*. Earthscan publications Ltd., 2004.

[83] C. C. Mei. Power extraction from water waves. *Journal of Ship Research*, 20:63–66, 1976.

[84] W. H. Michel. Sea spectra revisited. *Marine Technology*, 36(4):211 – 227, 1999.

[85] J. R. Morison, M. P. O'Brien, J. W. Johnson, and S. A. Schaaf. The forces exerted by surface waves on piles. In *Petroleum Transactions of AIME*, volume 189, pages 149–157, 1950.

[86] T. Mundon, A. Murray, J. Hallam, and L. Patel. Causal neural control of a latching ocean wave point absorber. *Artificial Neural Networks: Formal Models and their Applications - ICANN 2005 15th International Conference. Proceedings, Part II (Lecture Notes in Computer Science Vol. 3697)*, pages 423 – 9, 2005.

[87] A. E. Mynett, D. D. Serman, and C. C. Mei. Characteristics of Salter's cam for extracting energy from ocean waves. *Applied Ocean Research*, 1(1):13 – 20, 1979.

[88] S. Naito and S. Nakamura. Wave energy absorption in irregular waves by feed forward control system. In D. V. Evans and A. F. d. O. Falcao, editors, *Hydrodynamics of Ocean Wave-energy Utilization*, number ISBN 0-387-16115-5, pages 269–280. Springer, Berlin, 1986.

[89] J. N. Newman. The interaction of stationary vessels with regular waves. In *Proc. 11th Symposium on Naval Hydrodynamics*, pages 491–501, London, 1976.

[90] J. N. Newman. *Marine Hydrodynamics*. Number ISBN 0-262-14026-8. MIT Press, Cambridge, Massachusetts, 1977.

[91] J. N. Newman. Absorption of wave energy by elongated bodies. *Applied Ocean Research, vol. 1, Oct. 1979, p. 189-196. Navy-NSF-supported research.*, 1:189–196, Oct. 1979.

[92] G. Nolan, J. Ringwood, W. Leithead, and S. Butler. Optimal damping profiles for a heaving buoy wave energy converter. In *Proceedings of the fifteenth intenatinal offshore and polar engineering conference*, number ISBN 1-880653-64-8, Seoul, Korea, 19-24 June 2005. ISOPE.

[93] N. Panicker. Power resource potential of ocean surface waves. In *Proceeding of Wave and Salinity Gradient Workshop*, pages pp. J1–J48., Newark, Delaware, USA, 1976.

[94] R. Parker, G. Harrison, and J. Chick. Energy and carbon audit of an offshore wave energy converter. *Proceedings of the Institution of Mechanical Engineers, Part A (Journal of Power and Energy)*, 221(A8):1119 – 30, 2007.

[95] L. N. Patel, A. Murray, and J. Hallam. Super-lampreys and wave energy: Optimised control of artificially-evolved, simulated swimming lamprey. *Neurocomputing*, 70(7-9):1139–1154, Mar. 2007.

[96] H. A. Paynter. *Analysis and Design of Engineering Systems*. Number ISBN-13: 978-0-262-16004-9. The MIT Press, Cambridge, Massachusetts, June 1960.

[97] E. Pedersen and H. Engja. Mathematical modelling and simulation of physical systems. Lecture Notes, Department of Marine Technology, NTNU, 2003. UK-01-89, Rev July 2003.

[98] T. A. Pedersen. Modelling of marine seismic streamer cable configurations. Master's thesis, NTNU, 2002.

[99] T. A. Pedersen. *Bond graph modeling of marine power systems*. Phd thesis, NTNU, Trondheim, Norway, March 2009. Doctoral theses at NTNU, 2009:56, ISBN 978-82-471-1486-5.

[100] J. N. B. A. Perdigão and A. J. N. A. Sarmento. A phase control strategy for OWC devices in irregular seas. In J. Grue, editor, *The fourth International Workshop on Water Waves and Floating Bodies*, pages 205–209, Dept. Mathematics, University of Oslo, 1989.

[101] D. Pizer. Maximum wave-power absorption of point-absorbers under motion constraints. *Applied Ocean Research*, 15(4):227 – 234, 1993.

[102] M. S. Prado, F. Gardner, M. Damen, and H. Polinder. Modelling and test results of the Archimedes wave swing. *Proceedings of the Institution of Mechanical Engineers, Part A: Journal of Power and Energy*, 220(8):855 – 868, 2006.

[103] A. A. E. Price, D. I. M. Forehand, and A. R. Wallace. Frequency domain techniques for numerical and experimental modelling of wave energy converters. In *Proceedings of the 8th European Wave and Tidal Energy Conference*, Uppsala, Sweden, 7–10 September 2009.

[104] A. A. E. Price, D. I. M. Forehand, and A. R. Wallace. Time-span of future information necessary for theoretical acausal optimal control of wave energy converters. In *Proceedings of the European Control Conference 2009*, number ISBN 978-963-311-369-1, pages 3761–3766, Budapest, Hungary, 23–26 August 2009.

[105] A. A. E. Price and A. R. Wallace. Non-linear methods for next wave estimation. In *Proceedings of the 7th European Wave and Tidal Energy Conference*, Porto, Portugal, 9 2007.

[106] S. Saelid and N. Jenssen. Adaptive ship autopilot with wave filter. *Modeling, Identification and Control*, 4(1):33 – 45, 1983.

[107] D. Sahm. A two-axis bond graph model of the dynamics of synchronous electrical machines. *Journal of The Franklin Institute*, September 1979. Pergamon Press.

[108] S. H. Salter. Wave power. *Nature*, 249:720–724, 1974.

[109] S. H. Salter. Power conversion systems for ducks. In *Proceedings of International Conference on Future Energy Concepts*, pages 100–108, London, January 1979. Institution of Electrical Engineers. Publication 171.

[110] S. H. Salter. *Ocean wave energy*, chapter 2 Looking Back, pages 7–39. Springer, 2008.

[111] S. H. Salter, D. C. Jeffery, and J. R. M. Taylor. The architecture of nodding duck wave power generators. *The Naval Architect*, pages 21–24, 1 1976.

[112] A. J. N. A. Sarmento and A. F. D. . Falcao. Wave generation by an oscillating surface-pressure and its application in wave-energy extraction. *Journal of Fluid Mechanics*, 150:pp. 467–485, 1985.

[113] T. Sarpkaya. Past progress and outstanding problems in time-dependent flows about ocean structures. In *Proceedings - Separated Flow Around Marine Structures*, pages 1 – 36, Trondheim, Norw, 1985.

[114] M. P. Schoen, J. Hals, and T. Moan. Robust control of heaving wave energy devices in irregular waves. In *Proceedings of the 16th Mediterranean Conference on Control and Automation*, Ajaccio, France, June 2008.

[115] M. P. Schoen, J. Hals, and T. Moan. Wave prediction and fuzzy logic control of wave energy converters in irregular waves. In *Proceedings of the 16th Mediterranean Conference on Control and Automation*, Ajaccio, France, June 2008.

[116] L. F. Shampine, I. Gladwell, and S. Thompson. *Solving ODEs with MATLAB*. Cambridge University Press, 2003.

[117] R. Taghipour, T. Perez, and T. Moan. Hybrid frequency–time domain models for dynamic response analysis of marine structrues. *Ocean Engineering*, 35(7):685–705, May 2008.

[118] S. Teske, A. Zervos, and O. Schäfer. Energy [r]evolution – a sustainable world energy outlook. Technical report, Greenpeace International, European Renewable Energy Council (EREC), 2007. Editor: Crispin Aubrey.

[119] P. C. Vicente, A. F. de O. Falcão, L. M. Gato, and P. A. Justino. Dynamics of arrays of floating point-absorber wave energy converters with inter-body and bottom slack-mooring connections. *Applied Ocean Research*, In Press, Corrected Proof:–, 2009.

[120] WAMIT. *WAMIT User Manual*. http://www.wamit.com, 2006. Version 6.3.

[121] Z. Yu and J. Falnes. State-space modelling of a vertical cylinder in heave. *Applied Ocean Research*, 17(5):265 – 275, 1995.

[122] Z. Yu and J. Falnes. State-space modelling of dynamic systems in ocean engineering. *Journal of Hydrodynamics*, (1):1 – 17, 1998. Ser. B, China Ocean Press, Beijing.

[123] M. Ó'Cathàin, B. J. Leira, J. V. Ringwood, and J.-C. Gilloteaux. A modelling methodology for multi-body systems with application to wave-energy devices. *Ocean Engineering*, 35(13):1381–1387, Sept. 2008.

Appendix A

Publications

Article A: Engja and Hals, EWTEC 2007

Modelling and Simulation of Sea Wave Power Conversion Systems

Hallvard Engja[1] and Jorgen Hals[2]

Centre for Ships and Ocean Structures at Norwegian University of Science and Technology (NTNU),
Otto Nielsens V. 10, N-7491 Trondheim, Norway
[1]E-mail: hallvard.engja@ntnu.no
[2]E-mail: jorgen.hals@ntnu.no

Abstract

Ocean energy conversion has been of interest for many years. Recent developments such as concern over global warming have renewed interest in the topic. Wave energy converters are complex and expensive to develop, and for this reason is this paper introducing the use of mathematical models and computer simulation as an important tool in system development.

The computational capabilities are not a problem any longer, but model construction still seems to be a hurdle.

A method well established as a valuable aid in constructing models of physical systems is the method of bond graphs. It is a multi-domain concise pictorial representation of the energy exchange in a system. In this paper we discuss issues related to physical system modelling and an outline of the bond graph language. A complete mathematical model of a floating buoy and semi-submersible platform with downstream hydraulic system is presented in addition to simulation results.

Keywords: Bond Graphs, system modelling, simulation

Introduction

The conversion of the slow reversing energy flows in sea waves into electricity with power quality acceptable to a utility network is a challenge for engineering designers. This conversion process into electricity and fed into a grid consists of four major steps:

- absorption
- conversion
- transmission
- grid connection

These steps form a very complex system where all parts are intimately linked to each other. It is the performance of the whole system that is the interesting parameter and not the isolated performance of one single component. That means that it is very important to have an overall view and understanding of the interactions between the different components in the system. This is what we call a "system viewpoint" because we are concerned with the design and operation of a complete system.

In system design, the object is to develop a system concept which is believed to satisfy a set of specified or implied requirements. System analysis on the other hand aims at understanding how a proposed or existing system operates. That means predicting the behaviour at the design stage in order to test a concept for its capacity to satisfy demands placed on it.

The role of analysis or experimentation in device and system engineering provides a contrast. The device engineer can usually experiment readily with a device, but experimentation with systems is often costly and might be almost impossible. Thus for a system engineer to be certain of the overall performance of his system at the design stage, computer studies and computer simulations are often his only method of experimentation. Simulation is therefore, an experimental and applied methodology which seeks to predict future behaviour, that is, the effect that will be produced by changes of system parameters or in its method of operation. Simulation can therefore, be perceived as a bridge between design and operation.

Computer simulation means "experiments performed on a mathematical model". This means that the idea of a model of the system is the first and central point in a simulation study. Despite the existence of powerful numerical methods and computer capabilities, the preparation of a mathematical model in the proper form is not a trivial task, particularly when the system is non-linear, involves more than one energy domain and with embedded control systems. To proceed from a schematic diagram to a reasonable model, a great deal of judgement is required. For simple systems, equation formulation according to well-established rules may pose no great difficulties. However, in many practical cases the modeller is required to use considerable ingenuity to organise the component models into a system model in the absence of standard procedures. This often proves to be a major impediment to those using simulation for system design.

It is therefore, highly desirable to have a logical procedure for transposing a physical reality into a mathematical model which is amendable to direct computer solution. One method which satisfies this requirement is the unified graphical modelling methodology called Bond Graphs. The main applications of bond graphs are to physical systems in which power and energy interactions are important. These multi-energy domain interactions are characteristic of wave energy conversion systems and therefore, well suited for bond graph modelling.

The main objective of this paper is therefore, to discuss issues related to constructing models of physical systems, introducing the basic features of bond graphs and through an example of a wave energy conversion system show how the modelling process can be organised in a systematic manner. A complete mathematical model of the example and simulation results will be presented.

1 Modelling

Since the early 1960's general purpose simulation programs have been developed for continuous systems.

These programs are significant aids in the design and optimisation of nonlinear dynamic systems since a variety of mathematical operations are pre-programmed for simulation, analysis and presentation of results. Despite the fact that almost no real programming skill is needed to use such a continuous system simulation program, they require as input a mathematical model in the proper form which is not a trivial task, particularly when the system is nonlinear and involves more than one energy domain. Thus, central to the concept of system simulation and indeed, central to much of human activity is the creation and use of models. It can be argued in fact, that all intellectual activities involve models of sorts since we always make conceptual simplifications in order to comprehend a real world object.

There is no single accepted meaning of the word model, but we will here take it to mean "a representation of an object". Models are therefore, not reality. Thus, a model, no matter how complex, is only a representation of reality and should never be confused with it. This means that the characteristic feature of a model is that "some, but not all" of the features of the real system are reflected in the model and that no system can be modelled exactly.

Creating a model or modelling can be defined as the process of translating the most important aspects of a real or proposed system from its real environment to an expression by which it is more conveniently studied. It is the first and most important step, but also one of the most difficult tasks in applying quantitative analysis to the study of systems. In many cases it seems that modelling proceeds either intuitively or in an ad hoc way, using special intermediate steps. This is likely to give rise to errors, and in fact, hardly any engineer of even modest experience, can claim to have avoided the embarrassing experience of writing an equation set that subsequently was found to admit of no solution at all. In spite of these difficulties, modelling is often thought of as "simply" a process involving the application of physical laws and principles to establish a set of equations which describe a given system. Looking through the literature on the subject, it appears that it is not "simply", but reveals enormous diversity of approaches used and, hence the difficulties associated with developing relevant computable models and in a form which engineers can comprehend and understand.

The construction of models with an acceptable validity requires a profound understanding of the system being modelled and the area or discipline to which it belongs. The modelling process is by no means to be divorced from the physical processes to which it is applied. Physical system modelling differs from "applied mathematics" in that it puts the emphasis on the physical system to be modelled and not on the mathematical solution techniques. This indicates a need for a transparent language to be able to think, to reason and communicate in a multi-disciplinary manner. A very powerful realisation of such an approach is found in the Bond Graph language. It is a transparent graphical language in which the basic features of engineering systems can be described and which is amendable to direct computer solution.

The main applications of bond graphs are to physical systems in which power interactions are important. These multi-energy domain interactions are characteristics of ocean wave conversion systems and, therefore, well suited for bond graph modelling.

Before we discuss the challenge of using this modelling methodology to wave conversion systems, an introduction of the basic features of bond graphs are presented. We will try to make this paper self-contained and understandable even for those who are unfamiliar with bond graphs. Because of space limitations, we cannot explain all features of the bond graph methodology or describe the associated techniques in detail. Those interested in learning more should consult references [1, 2].

2 Bond Graph Basics

Physical systems that interact all store, transport, or dissipate energy among subsystems. Bond graphs provide a concise pictorial representation of these interacting dynamic systems. They account for all energy and, in so doing, provide the common link among various engineering systems.

Bond graphs consist of letters standing for components which are connected by lines or bonds standing for power interactions between components. Each bond carries power and is used to couple the energy ports of system components as shown in Figure 1. A "bond" is therefore, the fundamental component

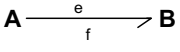

Figure 1: Power bond.

of a bond graph. The direction in which the positive power is flowing is indicated by a half arrow as from A to B in Figure 1.

The successful use of bond graphs depends to a great extent on choosing a set of variables which describes the instantaneous power balance within a system. In a wide class of energetic systems, the propagation of energy or power, is given by the product of two quantities, an effort variable e, and a flow variable f. Since their product represents power flowing between subsystems, the effort and flow variables are called power variables.

$$\text{Power flow} = e(t)\, f(t) \tag{1}$$

Two other variables of importance is the generalised momentum p, defined as

$$p = \int e(t)\, dt \tag{2}$$

and generalised displacement q, defined as

$$q = \int f(t)\, dt \tag{3}$$

The p and q variables are called "energy variables" since p and q is a measure of stored energy in a system. The analogy employed seems natural from the point of view of basic physical laws as shown below.

Domain	Effort	Flow	Momentum	Displacem.
Mechanics	Force	Velocity	Impulse	Position
(Translation)	[N]	[m/s]	[N s]	[m]
Mechanics	Moment	Ang. Vel.	Ang. Imp.	Angle
(Rotation)	[N m]	[rad/s]	[N m s]	[rad]
Hydraulics	Pressure	Vol. Flow	Press. Imp.	Volume
	[Pa]	[m^3/s]	[Pa s]	[m^3]
Electrical	Voltage	Current	Flux link.	Charge
	[V]	[A]	[V s]	[C]

Using the classification of power and energy variables presented, it turns out that only nine basic types of multi-port elements are required in order to represent models in a variety of energy domains. These multi-ports function as components of subsystem and system models. They are, in many cases, idealised mathematical version of real components or models of physical effects.

The constitutive relations for the nine basic 1-port, 2-port and the two multiport elements are summarised in Table 1. As

Table 1: Basic bond graph elements.

Bond graph element	Elemental relations
e / f — R — Resistor	General: $e = \Phi_R(f)$ Linear: $e = R \cdot f$
e / f — C — Capacitor	General: $q = \Phi_c(e)$ Linear: $q = C \cdot e$
e / f — I — Inertia	General: $p = \Phi_I(f)$ Linear: $p = I \cdot f$
Se — e / f — e-source	$e = e(t)$
Sf — e / f — f-source	$f = f(t)$
e_1 / f_1 — TF — e_2 / f_2 — Transformer	$e_1 = e_2 \cdot m$ $f \cdot m_1 = f_2$
e_1 / f_1 — GY — e_2 / f_2 — Gyrator	$e_1 = f_2 \cdot r$ $f_1 \cdot r = e_2$
e_3 / f_3; e_1 / f_1 — 0 — e_2 / f_2 — 0-junction	$e_1 = e_2 = e_3$ $f_1 - f_2 + f_3 = 0$
e_3 / f_3; e_1 / f_1 — 1 — e_2 / f_2 — 1-junction	$f_1 = f_2 = f_3$ $e_1 - e_2 + e_3 = 0$

an example, in translational mechanics C, I, and R stand for spring, mass, and damper components, Se and Sf stand for effort (force), and flow (velocity) sources, and 0 and 1 are junction elements that indicate how the components are connected.

Using these nine basic elements, a graphical model can be constructed of a system. It is a remarkable fact that models based on apparently diverse branches of engineering science can all be expressed using the notation of bond graphs. The nature of the parts of the model and the manner in which the parts interact can be made evident in a graphical format for linear and nonlinear systems.

For computer algorithms to solve equations representing the physics of real systems, it is essential that proper input and output causality or cause and effect be maintained. Some perfectly reasonable physical models simply will not compute because of causal problems. Thus, before the equations can be written from the graph, causal information must be added to the graph. That means obtaining an explicit indication of which power variable for an element is to be considered independent and which are to be considered dependent. Said another way, which is the input and which is the output variable. With bond graphs, causality is indicated by a perpendicular stroke at the end of a bond as shown in Figure 2. The effort signal is directed toward the causal stroke, and consequently, the flow signal is directed in the opposite direction. Thus bond graphs express the natural actions and reactions occurring in coupled systems that exchange

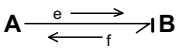

Figure 2: Meaning of causal strokes.

energy at significant levels. Causality as a concept and as a tool is uniquely associated with bond graphs. It should be noted that the causal direction has nothing in common with the power direction.

Before we can start to derive the mathematical equations from a bond graph we must prepare the graph with information that will make the writing of equations follow an orderly systematic pattern. These steps are:

- number all bonds in the graph
- assign a power direction to each bond
- assign causality to each bond

The numbering of the bonds assures unambiguous referral to system variables.

When assigning causality to I and C elements, we want to maximise the number of elements with integral causality and hence the number of state variables. Integral causality means the following causal assignments.

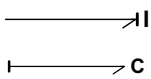

$$f = \frac{\int e(t)\,dt}{I}$$

$$e = \frac{\int f(t)\,dt}{C}$$

The opposite causality is called derivative causality as indicated below

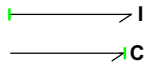

$$e = I\frac{df(t)}{dt}$$

$$f = C\frac{de(t)}{dt}$$

When derivative causality is forced on an I or C element, the corresponding p or q is not independent and therefore, not a state variable. Integral causality is also called preferred causality since nature only integrates; only mathematicians differentiate. Differential causality signifies that an implicit equation will occur.

From an augmented bond graph, differential equations can be written in a systematic manner which indicates that the graph is perfectly equivalent to the differential equations of the form

$$\frac{d\mathbf{X}}{dt} = g(\mathbf{X}, \mathbf{U}(t), t) \tag{4}$$

with state vector $\mathbf{X}$, and input vector $\mathbf{U}(t)$. This type of model is described as a "state-determined" system model which has become known as the standard form.

It follows that converting a bond graph into differential equations is a straightforward process and can easily be computerised [3].

Bond graph modelling and some useful features of causality and its implications for writing differential equations will now be illustrated by an example of a wave conversion system.

3 Wave Conversion Example System

In Figure 3 is shown a schematic diagram of a wave-energy conversion system for which we first will construct a bond graph model, and from it write the differential equations which describe the dynamic performance. The system consists of a floating buoy moving relative to a semi-submersible platform.

The buoy is connected to the platform by a piston and cylinder, which again is connected to a hydraulic system as in [4].

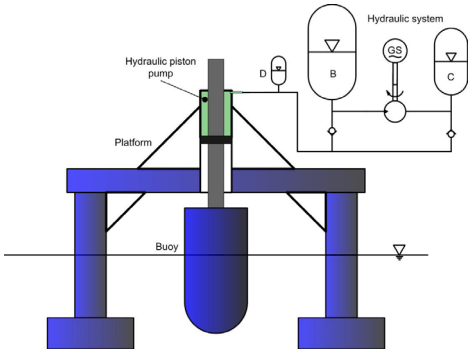

Figure 3: Wave conversion system example.

Conversion of the hydraulic energy from the buoy piston pump into mechanical power is performed by a positive displacement hydraulic motor. Upstream and downstream of the hydraulic motor is mounted gas-loaded accumulators which are there for the purpose of storing energy and to absorb parts of the pulsating flow of hydraulic fluid. The third gas accumulator is meant to reduce pressure peaks. The two valves shown are check valves which is meant to prevent reverse flow of fluid in the high and low pressure lines.

In Figure 4 is shown a bond graph model of the system shown in Figure 3. It should be noted that we use the expression "a bond graph model" and not "the bond graph model" because the model presented is actually a reflection of the modeller's decision of what effects he want to include in the model. There is no unique model and no unique solution to a real world problem. The bond graph in Figure 4 is shown with causality, power directions and numbers on all the bonds.

The left part of the graph is the model of the platform and buoy and the right part is the model of the hydraulic system. To proceed from a physical system representation such as a sketch to a bond graph model there exist a systematic procedure [1]. We will here only explain briefly how the graph in Figure 4 was constructed.

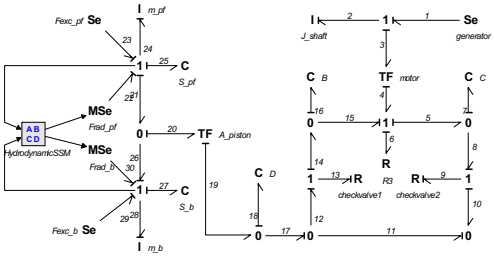

Figure 4: Example system bond graph.

Starting with the platform and buoy, we first establish the two 1-junctions representing the vertical velocities of the two objects. To these 1-junctions are coupled inertia I representing the mass, stiffness C representing the hydrostatic stiffness and excitation forces Se and MSe. The excitation forces denoted MSe are called modulated forces since they are modulated by signals shown by a full arrow in contrast to a half arrows for power direction. The square box represents the radiation forces explained in the following.

The wave forces on structures interacting with ocean waves can be expressed as

$$F_w(t) = F_e(t) + F_r(t) \tag{5}$$

where these forces can be represented by convolution integrals.

The excitation force can be expressed as

$$F_e(t) = \int N(\tau) g(t-\tau)\, d\tau \tag{6}$$

where $N(t)$ is the elevation due to the incident wave at the origin and $g(t)$ is the excitation force kernel. The radiation force on the bodies can be expressed as

$$F_r(t) = M_r(\infty)\frac{dq}{dt} - \int k(t-\tau) f(\tau)\, d\tau \tag{7}$$

where M_r is the added mass of the bodies at infinite frequency, $f(t)$ the vertical velocity of the bodies and $k(t)$ is the radiation force kernel.

As a convenient approximation, the integrals in Equation 6 and 7 can be replaced by a set of first-order differential equations [5] which give the total model the same mathematical form as the rest. If we in a simulation assume the wave elevation time series to be known, the convolution in Equation 6 can be computed in advance to yield time series for the excitation force.

In Equation 7 is shown that the radiation forces are a function of the vertical velocities of the bodies. These dependencies are indicated on the bond graph in Figure 4 by the signal bonds from the two 1-junctions representing the two vertical velocities to the block representing the radiation force model. The output signal bonds from the radiation force model block are shown as inputs to the two modulated effort sources, MSe.

The 0-junction inserted between the two 1-junctions is used to determine the relative velocity between the platform and the buoy on bond 20. Between bond 19 and 20 is used a transformer representation (TF) of the piston, which is the interface between the mechanical and hydraulic domains. The transformer modulus is the area A_p of the hydraulic piston pump. On bond 19 on the other side of the transformer is the hydraulic energy domain. To start the modelling in this domain, we first establish 0-junctions for each distinctive pressure point, five in number. The three 0-junctions at the lower part of the hydraulic submodel all represent the output pressure from the piston pump, but are drawn separate for clarity. When we define all pressures relative to atmospheric pressure, we can connect the three C elements representing the gas accumulators to their appropriate 0-junctions. The two R elements representing the two check valves are then inserted via a 1-junction between appropriate 0-junctions. The hydraulic motor is represented as a transformer which is connected to a 1-junction representing the flow between the two accumulators. At this 1-junction is also connected a resistance element representing the hydraulic loss in the motor. To the downstream side of the transformer is a 1-junction representing the motor rotational velocity to which is connected an I element representing the motor inertia, and an effort source Se representing the load torque on the motor.

If we compare Figures 3 and 4 the graphical structure of the complete bond graph model is similar to the structure of the schematic drawing. This property of the bond graph is convenient in order to keep the physical understanding of the mathematical model through the process of modelling and analysis of the system. The simultaneous representation of physical and computational structure is a unique and very powerful property of the bond graph method, which other representations do not have.

For the example system bond graph model shown in Figure 4, the loading on the hydraulic motor is a torque input. In a real conversion system the intention is to couple an electrical generator to the hydraulic motor in place of the torque on bond 1. In Figure 5 is shown an augmented bond graph model of a two-axis synchronous generator based on the so-called d-q transformation of Park [6]. This bond graph model contains two

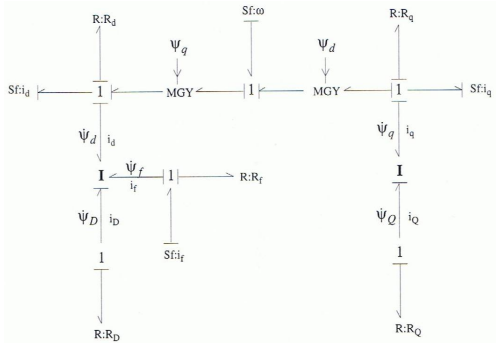

Figure 5: Bond graph of electric generator.

gyrators modulated by flux-linkages and multiport I elements called fields. The three-port I field to the left has integral causality only on one bond and differential causality on the two other bonds. As explained earlier, only one state equation needs to be written but implicit equations results. The same is true for the field on the right side.

The important result of the bond graphs in Figures 4 and 5 is that the sub-models in the mechanical, hydraulic and electrical energy domains are presented in a graphical unified manner.

4 Derivation of System Equations

The bond graph augmented as shown in Figure 5 contains exactly the same mathematical information as the differential equations. It therefore follows that converting a bond graph into a set of differential equations should be a systematic straightforward process. The algorithmic procedure for deriving the system equations will now be illustrated. From the causality assignment shown in Figure 4 we find eight storage elements with integral causality which means that we need to write eight state equations in addition to the forcing state equations. From this the following state vector $\mathbf{X}$ can be written as

$$\mathbf{X} = \{p_2, q_7, q_{16}, q_{18}, p_{24}, q_{25}, q_{27}, p_{29}\}$$

In short, the idea of writing the state equations is to express the derivatives of the state variables as efforts or flows and to proceed through the graph following the causal stroke information until all expressions are evaluated in terms of state variables, system constants and input source variables. To derive the governing equations, starting with p_2, the procedure is as follows:

$$\frac{dp_2}{dt} = e_2 \tag{8}$$

by definition of momentum. From the definition of the 1-junction we write

$$e_3 - e_1 - e_2 = 0 \tag{9}$$

For the hydraulic motor represented as a transformer with a modulus equal to the motor displacement D_m, we can write

$$f_4 = D_m\, f_3, \quad \text{and} \quad D_m\, e_4 = e_3 \tag{10}$$

From the next 1-junction we sum efforts to yield

$$e_{15} - e_4 - e_5 - e_6 = 0 \tag{11}$$

Following the causal marks, we find that e_{15} is equal to and "caused by" e_{16}, and that e_5 is equal to and "caused by" e_7. Substituting these causal facts into Equation 11 in addition to replacing e_6 with the constitutive relation for the R element we obtain

$$e_4 = e_{16} - e_7 - R_6\, f_4 \tag{12}$$

since f_6 is "caused by" f_4 according to the causal marks at the 1-junction.

The next step is then to obtain the constitutive relation-ship for the gas-charged accumulators which consist of a gas filled bladder within a steel chamber. Oil entering the accumulator displaces an equal volume of gas. If we assume an isentropic or polytropic process the following relations exist

$$P\, V^k = constant \tag{13}$$

With a reference volume V0 the relationship for the instantaneous volume V_1 is given as

$$V_1 = V_0 - q \tag{14}$$

and the constitutive relation for the instantaneous pressure P_1 in the accumulators takes the form

$$P_1 = P_0 \left[\frac{V_0}{V_0 - q}\right]^k \tag{15}$$

Referring back to the bond graph notation we can write the following relation for the accumulator pressures as

$$e_i = P_{0,i} \left[\frac{V_{0,i}}{V_{0,i} - q_i}\right]^k, \quad i = 7,\ 16,\ 18 \tag{16}$$

To eliminate f_4, we recognise that it is given in Equation 10 as a function of f_3, which again is "caused by" f_2 and according to the constitutive relationship for the I element given in Table 1 we obtain

$$f_4 = D_m\, f_3 = D_m\, f_2 = D_m\, \frac{p_2}{I_2} \tag{17}$$

Substituting f_4 from Equation 17 for f_4 in Equation 12, and inserting the resulting expression for e_4 in Equation 10 yields e_3, which can be used with Equations 8 and 9 to obtain the following equation

$$\frac{dp_2}{dt} = D_m(e_{16} - e_7) - R_6\, D_m^2\, \frac{p_2}{I_2} - Se_1 \tag{18}$$

Equation 18 contains only state variables, system constants and input variables, and thus is a state equation.

Continuing on to the next equation we write

$$\frac{dq_7}{dt} = f_7 = f_5 - f_8 \tag{19}$$

The flow f_5 is equal to and "caused by" f_4, which is given by Equation 17, and the flow f_8 is equal to and "caused by" f_9.

Assuming the flow f_9 through the check valve with flow area A_v, discharge coefficient C_d, and oil density ρ_o, is given by the orifice equation of the form

$$f_8 = f_9 = C_d\, A_v \sqrt{\frac{2}{\rho_o}\,(e_7 - e_{18})} \tag{20}$$

when $(e_7 - e_{18})$ is positive, and zero when $(e_7 - e_{18})$ is negative.

The state equation for q_{16} then becomes

$$\frac{dq_{16}}{dt} = f_{16} = f_{14} - f_{15} \tag{21}$$

Following the causal marks we find that f_{14} is caused by f_{13}, and f_{15} is caused by f_4. From Equation 20 the flow f_{13} is given as

$$f_{13} = C_d\, A_v \sqrt{\frac{2}{\rho_o}\,(e_{18} - e_{16})} \tag{22}$$

when $(e_{18} - e_{16})$ is positive, and zero otherwise. The state equation then becomes

$$\frac{dq_{16}}{dt} = f_{13} - f_4 \tag{23}$$

The last state equation on the hydraulic system can now be written as follows

$$\frac{dq_{18}}{dt} = f_{19} - f_{17} \tag{24}$$

The constitutive equations for the transformer between the mechanical and hydraulic subsystems take the form

$$f_{19} = A_p\, f_{20}, \qquad A_p\, e_{19} = e_{20} \tag{25}$$

where the piston area A_p is the transformer modulus.

The flow f_{19} is the flow of hydraulic fluid in and out of the cylinder, and the flow f_{20} is the relative velocity between the two floating bodies. This means that

$$f_{19} = A_p\,(f_{21} - f_{26}) \tag{26}$$

Flow f_{26} is equal to and caused by f_{28}, and flow f_{21} is equal to and caused by f_{24}. From the constitutive relationship for the I element shown in Table 1, we can write the state equation as

$$\frac{dq_{18}}{dt} = A_p\,(\frac{p_{24}}{I_{24}} - \frac{p_{28}}{I_{28}}) - f_{17} \tag{27}$$

where

$$f_{17} = f_{13} \quad \text{when} \quad [e_{18} - e_{16}] > 0$$

or

$$f_{17} = f_9 \quad \text{when} \quad [e_7 - e_{18}] > 0$$

For the last four state equations for the floating bodies we will only present the equations directly as they are obtained from causality and constitutive relations for the I and C storage elements. Hence

$$\frac{dp_{24}}{dt} = e_{24} = MSe_{22} + Se_{23} - \frac{q_{25}}{C_{25}} - e_{20} \tag{28}$$

where the compliance C_{25} is the inverse of the hydrostatic stiffness given as

$$C_{25} = \frac{1}{\rho_o\, g\, A_w}$$

with ρ as the water density, g the acceleration of gravity and A_w the water plane area. From Equation 25 we obtain

$$e_{20} = A_p\, e_{19} = A_p\, e_{18}$$

and the state equation can be written as

$$\frac{dp_{24}}{dt} = MSe_{22} + Se_{23} - \frac{q_{25}}{C_{25}} - A_p\, e_{18} \tag{29}$$

The state equation for p_{28} is of the same form as Equation 29 and can be written directly to yield

$$\frac{dp_{28}}{dt} = MSe_{30} + Se_{29} - \frac{q_{27}}{C_{27}} + A_p\, e_{18} \tag{30}$$

For the two remaining state equations we obtain

$$\frac{dq_{25}}{dt} = f_{25} = \frac{p_{24}}{I_{24}} \tag{31}$$

and

$$\frac{dq_{27}}{dt} = f_{27} = \frac{p_{28}}{I_{28}} \tag{32}$$

The systematic manipulations of equations to develop the resulting state equations have shown that the physical understanding necessary for the modelling process is in constructing the bond graph and not in writing the differential equations.

5 Simulation Results

Model verification is always a nagging question especially by the sceptics. The ideal case in which simulation results can be verified against at least some partial experimental results is, in our experience, more the exception than the rule. Our experience with hydraulic and mechanical models is that when applying basic physical relations and proper geometrical and fluid properties, very accurate qualitative simulation results are obtained. An illustration from the simulation of the nonlinear mathematical model of the example system is presented in Figure 6. The results are from simulations of the example system in

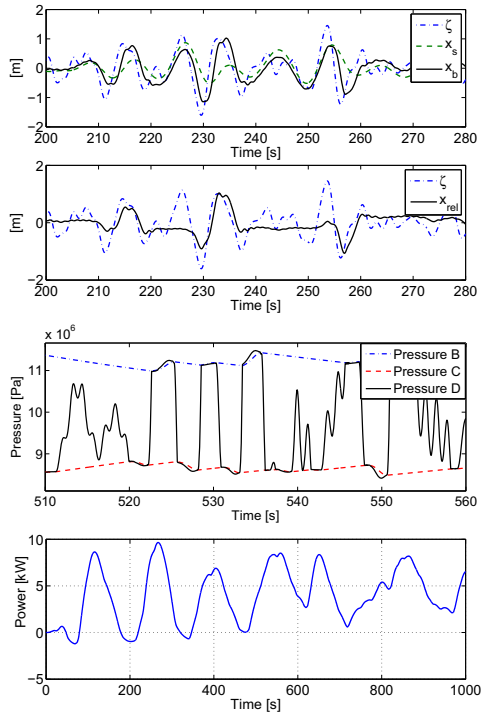

Figure 6: Simulation results for an irregular wave generated from a Pierson-Moskowitz spectrum with significant wave height 2 m and peak period 8 s. Observe that the time scales are different. ζ is the wave elevation and x the vertical position. Subscript s refers to the semi-submersible platform, b to the buoy and rel stands for relative.

irregular waves generated from a Pierson Moskowitz spectrum

with significant wave height of two meters and a peak period of eight seconds. Results from simulations with changing parameters are not presented since the aim of the paper is to present a modelling methodology for wave conversion systems.

6 Conclusions

The formulation of a system model is the crucial step in a simulation study. Accurate simulation of a faulty model is of little use. Yet many system modellers do not have easy ways to assess the effects of adding or removing elements in their systems. This paper has presented the bond graph methodology as a unified systematic approach to modelling sea wave conversion systems. The basic elements used in constructing bond graphs of physical sys- systems are discussed, and the construction of a bond graph model and derivation of the system state equations is demonstrated for an example of a wave energy conversion system. Each equation is itself as simple as possible and the constitutive laws of each component of the system appear separately.

Subsystems can be modelled independently and then assembled into an overall system model in much the same way as assembling the actual hardware. This means that modifications are easy to make by adding new elements to the bond graph. Following the rules of causality, one can readily see the effects on the number and kind of state variables required even before equations are written. Thus, parameter studies, as well as studies of the effect of changing component models entirely, are easily accomplished. To our mind, simulation has most to contribute in the preliminary design of conceptually new systems

The nonlinear state equations for the total system with torque loading are solved and typical results from a simulation are presented.

However, what cannot be relegated to the computer is the development of realistic parameters and final judgement of the simulation results. Intelligent and experienced human beings are still necessary to sort sense from nonsense in simulation results.

Acknowledgements

The authors would like to thank the Norwegian research council for funding.

References

[1] D.C. Karnopp and R. C. Rosenberg. *System Dynamics: A Unified Approach*. Wiley and Sons, New York, 1975.

[2] The bond graph compendium. http://www.ece.arizona.edu/∼cellier/bg.html.

[3] Controllab Products Inc., P. O. BOX 217, 7500 AE Enshede, The Netherlands.

[4] H. Eidsmoen. Tight-moored amplitude-limited heaving-buoy wave-energy converter with phase control. *Applied Ocean Research*, 20(3):157 – 161, 1998.

[5] Z. Yu and J. Falnes. State-space modelling of a vertical cylinder in heave. *Applied Ocean Research*, 17(5):265 – 275, 1995.

[6] D. Sahm. A two-axis bond graph model of the dynamics of synchronous electrical machines. *Journal of The Franklin Institute*, September 1979. Pergamon Press.

Article B: Hals et al., EWTEC 2007

Dynamics of a force-compensated two-body wave energy converter in heave with hydraulic power take-off subject to phase control

Jørgen Hals[1], Reza Taghipour and Torgeir Moan

Centre for Ships and Ocean Structures (CeSOS),
Norwegian University of Science and Technology (NTNU),
Otto Nielsens V. 10, N-7491, Trondheim, Norway
[1]Corresponding author: jorgen.hals@ntnu.no

Abstract

In this study we use a hybrid frequency-time domain model to study the dynamics of a two-body wave-energy converter with hydraulic power take-off subject to phase control. Both bodies - a buoy and a semi-submersible platform - are restricted to move in the heave mode only, and the power is extracted from their relative motion.

The geometry of the buoy and the platform is chosen so as to obtain so-called force compensation, i.e. the vertical wave excitation forces on the two bodies are opposite and approximately equally large. The effect of force compensation is studied by varying the geometry of the platform in order to reveal its effect on the system dynamics and power absorption. Furthermore, one-body oscillation is compared to two-body oscillation for power absorption, and the effect of viscous damping of the platform motion is studied.

Simulation results are given both for regular and irregular waves, and they show that the platform geometry and degree of force compensation strongly influences the performance of the system. It is further shown that flow losses in a hydraulic power take-off system can be substantial, and should thus be thoroughly assessed. Also, the large potential increase in power output using phase control is demonstrated.

Keywords: Bond graph, numerical simulation, ocean waves, renewable energy

Nomenclature

β [Pa]	=	bulk modulus of hydraulic oil
ζ [m]	=	wave surface elevation
λ [m]	=	wave length
ρ [$\frac{\mathrm{kg}}{\mathrm{m}^3}$]	=	density
τ [Nm]	=	torque
τ [s]	=	time integration variable
ϕ [$\frac{\mathrm{m}^2}{\mathrm{s}}$]	=	velocity potential
ω [$\frac{\mathrm{rad}}{\mathrm{s}}$]	=	angular frequency
a	=	$D_p/D_{p,0}$, pontoon diameter factor
$\tilde{\mathbf{A}}$, $\tilde{\mathbf{B}}$, $\tilde{\mathbf{C}}$, $\tilde{\mathbf{D}}$	=	linear system matrices
$\mathbf{A}$ [kg]	=	added mass matrix
A [m^2]	=	area
b	=	$H_p/H_{p,0}$, pontoon height factor
$\mathbf{B}$ [$\frac{\mathrm{Ns}}{\mathrm{m}}$]	=	damping coefficient matrix
B [$\frac{\mathrm{Ns}}{\mathrm{m}}$]	=	damping coefficient
$\mathbf{C}$ [$\frac{\mathrm{N}}{\mathrm{m}}$]	=	hydrostatic stiffness matrix
C_d	=	drag coefficient (pontoons)
C_d	=	discharge coefficient (valves)
d_a [m]	=	absorption width
D [m]	=	diameter
D_m [$\frac{\mathrm{m}^3}{\mathrm{rad}}$]	=	hydraulic motor displacement
e	=	effort, here: pressure [Pa]
$\mathbf{F}$ [N]	=	force vector
F [N]	=	force
g [$\frac{\mathrm{m}}{\mathrm{s}^2}$]	=	acceleration of gravity
I1-I5	=	irregular-wave sea states
J [kg m^2]	=	moment of inertia
J [$\frac{\mathrm{W}}{\mathrm{m}}$]	=	wave energy transport
$\mathbf{K}$ [$\frac{\mathrm{N}}{\mathrm{m}}$]	=	retardation function
m [kg]	=	mass
$\mathbf{M}$ [kg]	=	mass matrix
p [Pa]	=	pressure (for fluids)
p [$\frac{\mathrm{kgm}}{\mathrm{s}}$]	=	momentum (for bodies)
P [W]	=	power
PH	=	passive hydraulic power take-off
PHL	=	latching hydraulic power take-off
PL	=	passive linear power take-off
PTO	=	power take-off
q	=	generalised displacement: volume for hydraulics
R_m [$\frac{\mathrm{Pas}}{\mathrm{m}^3}$]	=	linear loss factor for hydraulic motor
R1-R5	=	regular-wave sea states
t [s]	=	time
T [s]	=	period
v [m]	=	velocity
V [m]	=	velocity in frequency plane
V [m^3]	=	volume
x [m]	=	vertical excursion from equilibrium position

X [m s] = vertical excursion in the frequency plane
$\mathbf{z}$ = radiation force state vector

Subscripts

0	=	initial or default value,
abs	=	absorbed
A, B, C, D	=	accumulator A, B, C or D
b	=	buoy
control	=	used for phase control
D	=	diffraction
exc	=	excitation
g	=	generator
H	=	hydraulic
HP	=	high pressure
j	=	component index
l	=	load
LP	=	low pressure
nl	=	non-linear
p	=	pontoon
rad	=	radiation
rel	=	relative between buoy and platform
s	=	semi-submersible platform
v	=	valve
visc	=	viscous
wp	=	water plane
z	=	z direction

Superscripts

∞	=	infinite frequency
D	=	diffraction
v	=	velocity
R	=	radiation (modified)

Introduction

There are two crucial criteria for a wave energy device to be viable. The first one is that it must give payback of investments in order to be realised, and this will of course depend both on how well the technology performs and on the market with possible adaptation actions from governments. The second one is that it must at least during its lifetime be able to return more energy than was spent in manufacturing, installing, operating and eventually decommissioning it. The task for technology providers is thus to increase the power output-to-cost ratio, whether we speak about energy or financial cost.

This article concerns the power part of this fraction, by considering an example system of a heaving buoy and platform connected through a power take-off (PTO) mechanism. The application of closed-loop control is usually regarded as a necessary means of improving performance of oscillating-type wave energy converters. Here we pursue the ideas of phase control by latching [1, 2] and investigate how this feature influences the power output for an example system by comparing it with more passive approaches, still having optimised parameters.

Budal [3] and Falnes [4] investigated the principle of force compensation for heaving two-body devices, and numerical results are here presented to support their qualitative discussions. Submerged plates or pontoons experience downward vertical excitation forces under the influence of a passing wave crest.

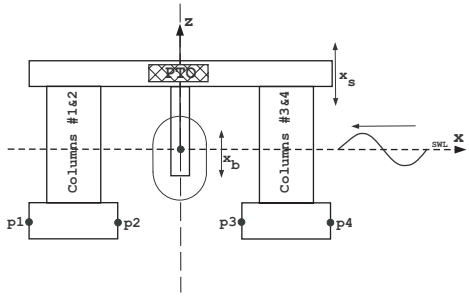

Figure 1: Schematic view of the wave energy converter. Only heave motion of the two bodies is considered, and the power is taken out from their relative motion. The velocities at points p1 to p4 are used for calculating the viscous damping. Only head seas waves are considered.

This leads to the possibility of having, within a limited frequency range, close to equally large but opposite excitation forces on a floating column and an attached submerged structure. The total force is thus approximately zero over that range. This force compensation is exploited in the design of offshore platforms in order to reduce wave induced motions. In our example system this effect gives opposite forces on the buoy and the platform, and we study this effect on the system dynamics and power output.

A dynamic model is the basis for understanding the behaviour of wave energy converters, such as energy absorption, mean and extreme loads and their effect on the mechanical and structural system. In this study the bond graph method has been used in the modelling work, and this is a very suitable tool for the modelling of wave energy devices, as discussed in [5].

1 System configuration

The example system consists of a four-legged semi-submersible platform and a cylindrical buoy with hemispherical bottom, both subject to head seas waves and moving in heave as shown in Figure 1. Their geometries have been chosen such that we are close to the above-mentioned force compensation for the relevant range of wave periods, which we have defined to be from 5 to 12 s. As indicated in Figure 2, the platform has cylindrical pontoons attached to its legs, and the cylindrical buoy has a straight submerged part of height 3 m, indicating a maximum excursion relative to the mean free surface of ± 3 m. Figure 3 shows a projection sketch of the system for the default dimension settings. See also Table 3. The eigen periods of the system are $T_s = 13.65$ s (the platform mode), $T_0 = 9.08$ s (the common mode of bodies locked together) and $T_b = 2.77$ s (the buoy mode). We studied two hydraulic systems for power take-off (Figure 5 and 6). In both cases the system is pretensioned by the initial hydraulic pressure. Compared to the Archimedean mass of the submerged volume, the mass is therefore reduced for the buoy and increased for the platform in order to have the same equilibrium position for the two bodies as before. This is given in Table 1.

A variation of the force-compensation level is made by varying the pontoon diameter D_p while keeping both the total displacement and the column diameter constant. This means a changing pontoon height H_p, which has been achieved by ad-

Table 1: Characteristic values and parameter settings for the system, with and without latching. The minus sign (-) indicates that the parameter is not relevant, and equal sign (=) indicates that the parameter value is the same for the two systems.

Quantity	Passive hydraulic PH Value	Latching hydraulic PHL Value
β	$1.3 \cdot 10^9$ Pa	=
ρ_H	850 kg/m^3	=
ρ_w	1025 kg/m^3	=
ω_s	0.46 rad/s	=
ω_b	2.26 rad/s	=
ω_0	0.69 rad/s	=
C_d	0.9	=
D_m	$1.2 \cdot 10^{-5}$ m^3/rad	=
J_g	2.5 kg m^2	=
m_s	239.2 Mg	259.6 Mg
m_b	35.42 Mg	15.04 Mg
$p_{A,0}$	-	20 MPa
$p_{B,0}$	10 MPa	30 MPa
$p_{C,0}$	10 MPa	10 MPa
$p_{D,0}$	10 MPa	20 MPa
Piston area	0.02 m^2	0.02 m^2
Pretension	200 kN	400 kN
R_{m}	$2 \cdot 10^8$ Pa s/m^3	=
τ_g	50 Nm	220 Nm
$V_{A,0}$	-	0.2 m^3
$V_{B,0}$	0.8 m^3	0.5 m^3
$V_{C,0}$	0.55 m^3	0.2 m^3
$V_{D,0}$	0.005 m^3	0.0875 m^3
V_s	213.5 m^3	=
V_b	54.45 m^3	=
Valve areas	0.002 m^2	=

justing the draft of the pontoon, while keeping the column height H_c constant. We first take $D_{p,0}$ as the diameter and $D_{p,0}$ as the height of the pontoon for the default case (3). If we define a diameter factor $a = D_p/D_{p,0}$ for change in diameter and a height factor $b = H_p/H_{p,0}$ for change in height, we get that the submerged platform volume $V \propto D_p^2 H_p = a^2\, b\, D_{p,0}\, H_{p,0}$. The requirement of keeping the volume constant then yields $a^2 b = 1$. We first try a 20 % increase/decrease in the diameter as shown in Table 3. The resulting excitation force coefficients for the platform and the buoy are shown in Figure 4. The frequancy domain parameters are calculated by the boundary-element method code WAMIT [6].

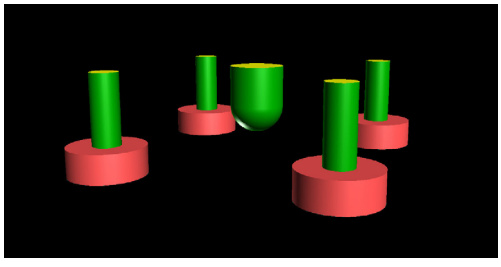

Figure 2: 3D view of submerged parts of the buoy and platform.

Table 2: Dimensions for the buoy and platform in the default case, i.e. with $a = 1$.

Symbol	Value [m]	Dimension
D_b	4.0	Buoy diameter
$R_b = D_b/2$	2.0	Buoy radius
H_b	3.0	Height of buoy's straight part
$d_b = H_b + R_b$	5.0	Buoy draught
D_c	1.7	Column diameter
$R_c = D_c/2$	0.85	Column radius
H_c	7.9	Column height
D_p	4.75	Pontoon diameter
R_p	2.375	Pontoon radius
H_p	2.0	Pontoon height
$d_p = H_c + H_p$	9.9	Platform total draught
L_{dist}	12.0	Distance between column centres

Table 3: Parameter variations keeping the pontoon volume constant. The corresponding results for the excitation force coefficients are shown in Figure 4. We have chosen the default values $D_{p,0} = 5.50$ m and $H_{p,0} = 2.50$ m for the pontoon diameter and height, respectively. The pontoon diameter factor a gives the ratio of the actual diameter to the default diameter, such that $D_p = a\, D_{p,0}$. The pontoon height factor b gives the ratio of the actual height to the default height, such that $H_p = b\, H_{p,0}$.

a	$b = 1/a^2$	D_p	H_p
1.0	1.0	4.75	2.000
1.20	0.694	5.70	1.389
0.80	1.563	3.80	3.125

1.1 PTO mode of operation

The power take-off (PTO) consists of a passive hydraulic system as studied also by Eidsmoen [7], and is shown in Figure 5. The PTO is located between the buoy and platform taking out power from their relative motion through a hydraulic ram (see also [5]). We will refer to this type of PTO using the label PH. In the case of latching control, an extra accumulator (A) is included in the system along with a control valve, as proposed by Budal [8] and shown in Figure 6. We label this system PHL.

For the passive hydraulic system (PH, see Figure 5) the relative distance starts changing once the relative force is strong enough to either pump to the high pressure reservoir (accumulator B) or suck from the low pressure reservoir (accumulator C). Then, during the following relative translation, hydraulic liquid flows between the storage accumulators and the piston. Accumulator D is included in order to account for the compressibility of oil in the hydraulic piston.

For the latching hydraulic system (PHL, see Figure 6) the piston pumps liquid to accumulator A during relative motion between the bodies and upward motion of the piston. Finally the control valve will close at zero relative velocity. While keeping the bodies at almost fixed distance by the closed valve, the force from the piston will decrease the pressure in the piston chamber and eventually get large enough to open the check valve from accumulator C, such that liquid can flow. This results in an increased pressure difference between B and C due to falling pressure p_C, as well as a downward motion of the piston. When the control valve opens again, the pressure difference between the piston cylinder and accumulator A will accelerate the downward motion. Eventually the relative distance between the platform and buoy will reach a maximum as the liquid is drawn from accumulator A and the piston chamber pressure falls. Here the

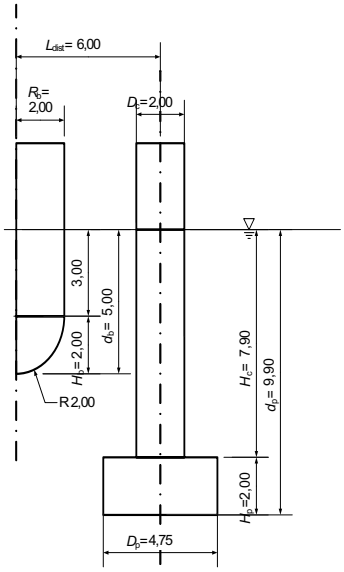

Figure 3: Projected 2D view of the buoy and platform with default dimensions. A complete list of dimensions is given in Table 2.

control valve will again be closed at zero velocity. Now the same sequence will follow, but this time with the piston force building a high pressure and pumping liquid into accumulator A.

The benefits of these hydraulic system used in the power take-off is that they store energy such that the power delivery to the electric generator can be evened out. Also they have an inherent protective mechanism limiting the relative motion. As the wave energy transport increases and waves get larger, the pressure level in B (C) will increase (decrease). Then a larger force is needed to move the piston toward the chamber ends.

A third option implemented for the power take-off is through an ideal linear load force, which is proportional to the relative velocity of the buoy and platform. This PTO is denoted by PL.

As a reference case, the platform was considered to be fixed. For this case, only the moving buoy is able to absorb power.

2 Mathematical model

We assume a two degree of freedom system by considering the semi-submersible platform and the buoy to move independently in heave. Additionally, we assume the hydrodynamic excitation and radiation forces, as well as the hydrostatic stiffness forces, to be linear. Thus we assume that the platform and buoy do not undergo large amplitude motions. The forces due to the viscous damping of the pontoon motion and the hydraulic system are, however, nonlinear.

Below we first give the state-space description of the model following after derivation of equations from the bond graph model of the system, as shown in [5]. The equations are commented and motivated in a qualitative fashion, with a more detailed description of some of the terms, before conformity with the more classical form of the equation of motion is shown. For a more complete treatment please consult the given reference.

The complete model is determined by a set of state space

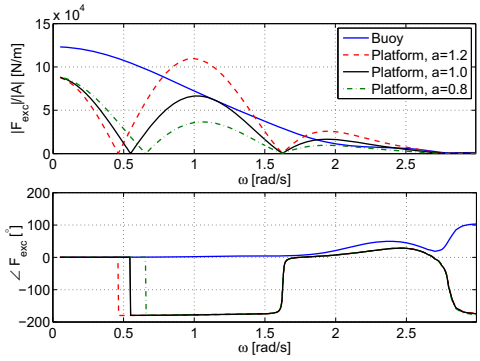

Figure 4: Excitation force coefficients (top) and the corresponding phase angles (bottom) for the three different configurations given by the parameter variation in Table 3.

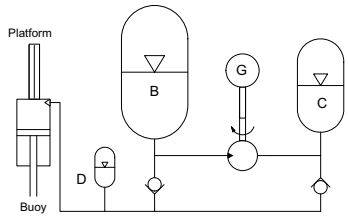

Figure 5: Schematic diagram of the passive hydraulic system, which is labelled PH [8, 9, Manuscript C]. The system consists of a hydraulic piston (left), gas accumulators (B, C and D), check valves, a motor and an electric generator (G).

equations, i.e. coupled first-order differential equations. First, letting q, e, p, x and F be time-dependent variables, the body dynamics are given by

$$\dot{p}_\mathrm{s} = m_\mathrm{s}\,\ddot{x}_\mathrm{s} = A_p\,e_D + F_{\mathrm{rad,s}} + F_{\mathrm{exc,s}} + F_{\mathrm{viscous,s}} - \rho\,g\,A_{\mathrm{wp,s}}\,x_\mathrm{s} \quad (1)$$

$$\dot{x}_\mathrm{s} = \frac{p_\mathrm{s}}{m_\mathrm{s}} \quad (2)$$

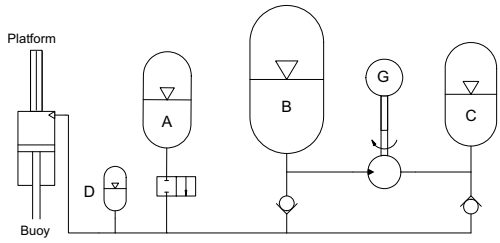

Figure 6: Schematic diagram of the hydraulic system with latching control, as proposed by Budal [8] (PHL). Compared to the PH system, this system contains an additional gas accumulator (A) and a control valve.

for the semisubmersible platform, and

$$\begin{aligned}\dot{p}_{\rm b} &= m_{\rm b}\,\ddot{x}_{\rm b} = -A_p\,e_D + F_{\rm rad,b} \\ &\quad + F_{\rm exc,b} - \rho\,g\,A_{\rm wp,b}\,x_{\rm b} \qquad (3)\\ \dot{x}_{\rm b} &= \frac{p_{\rm b}}{m_{\rm b}} \qquad (4)\end{aligned}$$

for the buoy. These four equations comprise all body forces and motions included in the model. The momentum of the vertical body motions is denoted p, and x is the vertical position. The masses m_s and m_b are the physical masses of the semisubmersible platform and the buoy, respectively. The meaning of the constants are found by conferring with the nomenclature list. The $A_p\,e_D$ terms in Equations 1 and 3 gives the coupling to the hydraulic PTO, and the radiation force $F_{\rm rad}$ contains both the added mass and wave damping forces. Moreover, the excitation force $F_{\rm exc}$ includes the Froude-Krylov and diffraction forces, and $F_{\rm viscous}$ represents viscous damping on the platform pontoons. Finally, the $\rho\,g\,A_{\rm wp}\,x$ terms give the hydrostatic stiffness forces. Both and $F_{\rm rad}$ and $F_{\rm viscous}$ are further discussed below.

The state equations for the hydraulic system are:

$$\dot{V}_A = C_d A_{\rm v,control}\sqrt{\frac{2}{\rho}|e_D - e_A|}\,\mathrm{sign}(e_D - e_A) \qquad (5)$$

$$\dot{V}_B = C_d A_{\rm v,HP}\sqrt{\frac{2}{\rho}\max[(e_D - e_B), 0]} - D_m\frac{p_g}{J_g} \qquad (6)$$

$$\dot{V}_C = D_m\frac{p_g}{J_g} - C_d A_{\rm v,LP}\sqrt{\frac{2}{\rho}\max[(e_C - e_D), 0]} \qquad (7)$$

$$\begin{aligned}\dot{V}_D &= A_p\left(\frac{p_{\rm b}}{m_{\rm b}} - \frac{p_{\rm s}}{m_{\rm s}}\right) \\ &\quad - C_d A_{\rm v,LP}\sqrt{\frac{2}{\rho}\max[(e_C - e_D), 0]} \\ &\quad - C_d A_{\rm v,HP}\sqrt{\frac{2}{\rho}\max[(e_D - e_B), 0]} \\ &\quad - C_d A_{\rm v,control}\sqrt{\frac{2}{\rho}|e_D - e_A|}\,\mathrm{sign}(e_D - e_A) \qquad (8)\end{aligned}$$

with

$$e_i = e_{0,i}\left(\frac{V_{0,i}}{V_{0,i} - V_i}\right)^k, \quad \mathrm{i} \in \{\mathrm{A, B, C, D}\}$$

In accordance with bond graph notation, e here represents effort, which for the hydraulic system is the pressure, V is the fluid volume in the different accumulators, and p_g is the angular momentum for the generator.

Equations 5 to 8 relates the change in accumulator liquid levels to the pressure differences over the valves and the motor in the system, where the accumulators are modelled assuming isentropic expansion and compression. The check valves and the control valves are all modelled according to the orifice equation (pressure loss proportional to the square of the flow rate) giving rise to the square roots in the equations.

The last state equation concerns the coupling between the motor and the generator:

$$\dot{p}_g = \tau_g + D_m(e_B - e_C) - \frac{D_m^2 R_m}{J_g}p_g, \qquad (9)$$

where the electric generator is simply modelled as a constant torque on the motor shaft, given by the first term on the right hand side. The second term is the torque due to the pressure difference across the hydraulic motor. The loss in the motor is taken to be proportional to the flow as given by the last term of Equation 9.

The coupling between the hydraulic power take-off and the oscillating bodies is given by the first term on the right-hand side of Equation 8, and the $A_p\,e_D$ terms in Equations 1 and 3.

Equations 1 to 9 give the total mathematical description of our model. We see that the model has nine state variables which can be determined by the nine state equations. For the system without latching control the terms containing the state variable q_A simply vanishes, leaving eight state variables and eight equations.

The radiation force terms $F_{\rm rad}$ in Equations 1 and 3 are given by Cummins [10]:

$$\mathbf{F}_{rad}(t) = \begin{bmatrix} F_{\rm rad,s}(t) \\ F_{\rm rad,b}(t) \end{bmatrix} = \mathbf{A}^\infty\,\ddot{\mathbf{x}}(t) + \mathbf{F}^{\mathbf{R}}(t)$$

where $\mathbf{A}^\infty$ is the matrix of added mass at infinite frequency and x is the position vector;

$$\mathbf{x}(t) = \begin{bmatrix} x_s(t) \\ x_b(t) \end{bmatrix},$$

$$\mathbf{A}^\infty = \begin{bmatrix} A^\infty_{ss} & A^\infty_{sb} \\ A^\infty_{bs} & A^\infty_{bb} \end{bmatrix}$$

and

$$\mathbf{F}^{\mathbf{R}}(t) = -\int_0^t \mathbf{K}(t-\tau)\,\dot{\mathbf{x}}(\tau)\,d\tau,$$

The retardation function $\mathbf{K}$ appearing in this convolution integral can be related to the frequency-domain potential damping as

$$\mathbf{K}(t) = \frac{2}{\pi}\int_0^\infty \mathbf{B}(\omega)\cos(\omega t)d\omega,$$

with

$$\mathbf{B} = \begin{bmatrix} B_{ss} & B_{sb} \\ B_{bs} & B_{bb} \end{bmatrix}.$$

The off-diagonal coupling terms represent the hydrodynamic interactions between the semi and the buoy.

These radiation forces can be approximated by a linear state-space model, in which case we can write the convolution term as [11]:

$$\begin{aligned}\dot{\mathbf{z}}(t) &= \tilde{\mathbf{A}}\,\mathbf{z}(t) + \tilde{\mathbf{B}}\dot{\mathbf{x}}(t) \\ \mathbf{F}^{\mathbf{R}} &\approx \tilde{\mathbf{C}}\,\mathbf{z}(t) + \tilde{\mathbf{D}}\dot{\mathbf{x}}(t) \qquad (10)\end{aligned}$$

We then need to solve for the additional state vector $\mathbf{z}$, whose length depends on the complexity of the retardation function and the required accuracy.

Now, viscous damping due to the pontoon motions is modelled in the usual way as

$$F_{\rm viscous,s} = B_{nl}(\dot{x_s} - v_z)\,|\dot{x_s} - v_z| \qquad (11)$$

where

$$\mathbf{B}_{nl} = \frac{\pi}{8}\rho C_d {D_p}^2, \qquad (12)$$

and v_z is the water particle velocity in the z direction. Values for the drag coefficient C_d is chosen based on an experimental work by Sauder and Moan [12], where the viscous forces were measured for different forcing amplitudes and frequencies. In the present work a default value of $C_d = 2$ has been used, with a variation from 1 to 8 to study its effect.

The water particle velocity v_z is here evaluated as the average of the water particle velocities at points p_1, p_2 for force evaluations for columns 1 and 2 and at points p_3 and p_4 for columns 3 and 4, respectively (see Figure 1). The description

of the velocities is carried out by a potential flow formulation, writing the total velocity potential in the frequency domain as

$$\phi = \phi_D + \sum_j \phi_j \dot{X}_j, \qquad j = s, b. \tag{13}$$

The water particle velocity in the z direction at a point in the fluid domain is then obtained by

$$V_z = \frac{\partial \phi}{\partial z} = \frac{\partial \phi_D}{\partial z} + \sum_j \frac{\partial \phi_j}{\partial z} \dot{X}_j \tag{14}$$

The second term on the right hand side of Equation 14 is the water particle velocity in z direction due to radiation, and in the time domain it becomes

$$v_z^R(t) = \sum_j \int_0^t K_j^{v_z}(t-\tau)\dot{x}_j(\tau)d\tau, \tag{15}$$

where

$$K_j^{v_z}(t) = \frac{1}{\pi}\int_0^\infty [\Re(\frac{\partial \phi_j}{\partial z})\cos(\omega t) - \Im(\frac{\partial \phi_j}{\partial z})\sin(\omega t)]d\omega. \tag{16}$$

Again, the convolution terms can be represented by a state space model in the same manner as for the radiation force, giving

$$\begin{aligned} \dot{\mathbf{z}}(t) &= \tilde{\mathbf{A}}_{\mathbf{v_z,j}}\,\mathbf{z}(t) + \tilde{\mathbf{B}}_{\mathbf{v_z,j}}\dot{\mathbf{x}}(t) \\ v_{z,j}^R(t) &\approx \tilde{\mathbf{C}}_{\mathbf{v_z,j}}\,\mathbf{z}(t) + \tilde{\mathbf{D}}_{\mathbf{v_z,j}}\dot{\mathbf{x}}(t) \end{aligned} \tag{17}$$

Regarding the diffraction component $\partial\phi/\partial z$ of the water particle velocity in z direction we use the following formulation:

$$v_z^D(t) = \sum_{j=1}^n v_j^D \sin(\omega_j t + \epsilon_j), \tag{18}$$

where v_j^D and ϵ_j are the magnitude and phase of the water particle velocity at a specific point due to the jth wave component. It is obtained from the spectral density function of the sea waves and the transfer function of the water particle velocity corresponding to the incident wave component j.

The mathematical model described above comprises a coupled system of first order differential equations. The equations of motion for mechanical systems are more often presented as second order differential equations. By combining and rearranging Equations 1 to 4 we arrive at the following matrix equation, probably more familiar to some of the readers[1]:

$$[\mathbf{M}+\mathbf{A}^\infty]\ddot{\mathbf{x}}(t)+\int_0^t \mathbf{K}(t-\tau)\,\dot{\mathbf{x}}(\tau)\,d\tau+\mathbf{C}\mathbf{x}(t) = \mathbf{F}(t), \tag{19}$$

where, in this case

$$\mathbf{A}^\infty = \begin{bmatrix} A_{ss}^\infty & A_{sb}^\infty \\ A_{bs}^\infty & A_{bb}^\infty \end{bmatrix},$$

$$\mathbf{C} = \begin{bmatrix} \rho\, g\, A_{\mathrm{wp,s}} & 0 \\ 0 & \rho\, g\, A_{\mathrm{wp,b}} \end{bmatrix},$$

$$\mathbf{F}(t) = \begin{bmatrix} F_{\mathrm{exc,s}} + F_{\mathrm{H}} + F_{\mathrm{visc}} \\ F_{\mathrm{exc,b}} - F_{\mathrm{H}} \end{bmatrix},$$

$$\mathbf{M} = \begin{bmatrix} m_s & 0 \\ 0 & m_b \end{bmatrix},$$

and $F_{\mathrm{H}} = A_p\, e_D$. This is the form in which equations 1 to 9 has been implemented and solved in our numerical Simulink [13] model.

[1] We refer to this model as a hybrid frequency-time domain model. See [11] for details.

2.1 Power take-off and control alternatives

Two of the PTO alternatives has already been mentioned. Altogether, three alternative mechanisms have been tested:

PH Passive hydraulic system with optimised parameters

PHL Hydraulic system with latching control by a shut-off valve

PL Simple resistor power take-off, with PTO load force proportional to velocity: $F_l = R_l\,\dot{x}_{\mathrm{rel}}$. The force F_l enters in the equations instead of the $A_p\,p_D$ term. The load resistance is set to $R_l = 1.24$ Ns/m, chosen as described in Section 3.

For latching control, the operation of the control valve is based on knowledge about the values of the excitation forces up to about two seconds into the future. In the simulations, these are taken to be known in advance as we pre-calculate the excitation force time series, whereas in reality they must be predicted by a combination of measurement and signal processing.

The control algorithm closes the control valve at zero relative velocity. With a given natural period T_b for the buoy, it then checks for a maximum of the excitation force in the interval $[t + T_b/4, t + T_b/2]$, and opens the control valve when this maximum is $T_b/4$ ahead and the force is in the right direction. The result is that the relative velocity will be in phase with the excitation force.

3 Simulation results

Simulations have been run for five different regular waves and five different irregular wave sea states chosen such that the wave energy transport is equal for equal index, as shown in Table 4. For each irregular wave sea state, the same wave elevation time series has been used in the simulations, so that no stochastic variation is introduced between simulation runs for different system configurations. The length of the time series have been taken to be 1000 s, and the dominating wave period is typically around 8 s. We thus expect reasonably good estimates of the average quantities. However, we cannot expect to achieve good representation of extreme values, as this requires a much larger number of oscillation cycles.

Table 4: Chosen sea states for numerical simulation. The combinations of regular wave period T and height H has been chosen such that the wave energy transport J matches the one for an irregular Pierson-Moskowitz sea state of peak period T_p and significant wave height H_s.

Regular wave	T [s]	H [m]	J [kW/m]
R1	6.00	1.31	10.1
R2	8.00	0.65	3.4
R3	8.00	1.31	13.5
R4	8.00	1.96	30.3
R5	10.00	1.31	16.8

Irregular wave	T_p [s]	H_s [m]	J [kW/m]
I1	6.00	2.00	10.1
I2	8.00	1.00	3.4
I3	8.00	2.00	13.5
I4	8.00	3.00	30.3
I5	10.00	2.00	16.8

A very simple scheme has been followed for choosing the initial and operational parameters of the system. Once the di-

mensions of the system have been determined by limiting pressures and forces, the energy absorption is mainly governed by the applied generator torque τ_g, or the load resistance R_l in the case of the PL machinery. These are assumed here to be non-varying parameters. In the case of latching control, also the time constant for unlatching plays an important role. All these parameters where optimised by variation through a number of runs with wave R3 (cf. Table 4), leading to the identification of their best setting. These values where then used for all runs, also with other wave inputs.

Both for the passive and latching hydraulic system we see the occurrence of a resonance oscillation due to the compressibility of the piston cylinder (oil and other), represented by accumulator D. This occurs when the fluid pressure is within the range where both check valves to accumulator B and C are closed.

In the following tables, the simulation results are analysed in terms of the following quantities:

P_{useful} is the power delivered at the generator output.

P_{abs} is the power absorbed from the waves.

$P_{\mathrm{loss}} = P_{\mathrm{abs}} - P_{\mathrm{useful}}$.

$x_{\max}$ and $x_{\min}$ are the maximum and minimum relative excursions between the platform and the buoy.

P_{visc} is the power dissipated at the pontoons of the platform.

d_a is the absorption width, defined as $d_a = P_{\mathrm{abs}}/J$, where J is the wave energy transport.

Results for the hydraulic system in regular and irregular waves are shown in Table 5, and some examples of the motion response are shown in Figures 7 to 10. Results for latching control are only presented for regular waves, as latching algorithms for irregular waves are currently under investigation.

Table 5: Power output obtained by the hydraulic system, with and without latching control in regular waves R1 to R5. For the passive system (without latching) results are also given for irregular waves I3 to I5. The generator output P_{useful} is given together with the absorption width d_a and the power P_{loss} lost in the hydraulic system.

Wave	PTO	P_{useful} [kW]	d_a [m]	$P_{\mathrm{loss}}/P_{\mathrm{abs}}$
R1	PH	1.01	0.10	0.012
R2	PH	1.52	0.45	0.018
R3	PH	6.83	0.55	0.076
R4	PH	10.84	0.41	0.117
R5	PH	3.43	0.21	0.039
R1	PHL	12.44	1.72	0.027
R2	PHL	3.75	1.28	0.010
R3	PHL	10.02	0.78	0.028
R4	PHL	16.26	0.57	0.045
I1	PH	4.08	0.42	0.071
I2	PH	1.35	0.42	0.035
I3	PH	5.31	0.42	0.081
I4	PH	10.01	0.36	0.130
I5	PH	4.71	0.30	0.081

The effect of viscous damping on the platform pontoons have been investigated by varying the drag coefficient at four levels. Increased drag will force the platform pontoons to closer follow the motion of the water. Table 6 presents results for the I3 wave time series.

The level of force compensation was varied as shown in Figure 4 for irregular wave and hydraulic power take off PH. The result in terms of power output and maximum excursion is given in Table 7.

Table 6: The effect of varying the viscous damping on the platform pontoons. The drag coefficient C_d has been chosen in steps between 1 and 8, and the resulting effect on useful power output P_{useful}, extreme platform excursions $x_{\mathrm{s,max}}$ and $x_{\mathrm{s,min}}$, and relative viscous loss $\frac{P_{\mathrm{visc}}}{P_{\mathrm{abs}}}$ for irregular wave I3 input and passive hydraulic power take-off PH is shown.

C_d	P_{useful} [kW]	$x_{\mathrm{s,max}}$ [m]	$x_{\mathrm{s,min}}$ [m]	$P_{\mathrm{visc}}/P_{\mathrm{abs}}$
1.0	5.47	0.74	-0.78	0.040
2.0	5.31	0.71	-0.77	0.073
4.0	5.05	0.67	-0.75	0.125
8.0	4.77	0.65	-0.69	0.188

Table 7: The effect of force compensation between the buoy and the platform. The pontoon diameter factor a (see Table 6) has been varied from 0.8 to 1.2 resulting in changes in power yield and maximum of relative excursion $x_{\mathrm{rel,max}}$. Input wave is I3 and the PTO is passive hydraulic (PH).

a	P_{useful} [kW]	P_{abs} [kW]	$x_{\mathrm{s,max}}$ [m]	$x_{\mathrm{rel,max}}$ [m]
0.8	6.30	7.00	0.90	1.59
1.0	5.31	5.69	0.71	1.13
1.2	3.49	4.02	0.62	1.04

In order to assess the performance of the hydraulic power take-off, a comparison to power output using a simple linear power take-off (PL) as described above was done. Results are presented in Table 8.

Table 8: Comparison of useful power output for a simple linear power take-off (PL) and the hydraulic system (PH) for different wave inputs.

Wave	PTO	P_{useful} [kW]	P_{abs} [kW]
R3	PL	7.81	7.81
R3	PH	6.83	7.38
I2	PL	1.67	1.67
I2	PH	1.35	1.41
I3	PL	6.32	6.32
I3	PH	5.31	5.69
I4	PL	13.49	13.49
I4	PH	10.01	10.86

Also comparison with the case of a fixed platform has been made for the passive hydraulic power take-off PH. This is simply done by setting its velocity equal to zero. This is reported in Table 9.

4 Discussion

From Table 5 we see that the absorption width (calculated on the basis of absorbed power) of the system varies from about 0.1 to 0.55 m for the passive hydraulic system, which should be compared to the actual horizontal extension of 4 m for the buoy and 1.7 m for each of the columns. The theoretical maximum absorption width for a point absorber is known to be $d_a \leq \lambda/2\pi$, which in this case is about 16 m for the R3 wave. We would expect a well-designed converter system based on the

Table 9: Comparison of output for the system with both bodies moving and only the buoy moving. The power take-off was PH, and the last column gives the power P_{loss} lost in the hydraulic system.

Wave	Platform	P_{useful} [kW]	P_{abs} [kW]	$P_{\text{loss}}/P_{\text{abs}}$
R3	fixed	7.72	9.12	0.15
R3	moving	6.83	7.38	0.08
I2	fixed	1.25	1.31	0.07
I2	moving	1.35	1.41	0.03
I3	fixed	6.61	7.81	0.15
I3	moving	5.31	5.69	0.08
I4	fixed	11.44	14.27	0.24
I4	moving	10.01	10.86	0.13

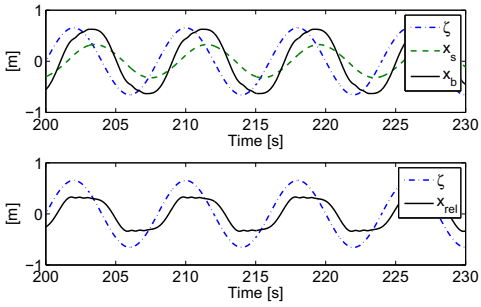

Figure 7: Motion response for the buoy and platform (upper) and relative motion (lower) for an ingoing regular wave of height 1.31 m and period 8 s (R3) using the passive hydraulic power take-off (PH).

point absorber to have an absorption width comparable or even larger than its own extension. This is not achieved with the PH system. It should be remembered that for the reported results, the PTO parameters have been optimised for the R3 wave. This means better performance is expected for other sea states.

In regular waves, the absorption width increases significantly for the latched system, reaching up to 1.72 m for the R1 wave (where the upper limit is about 9 m). Figure 9 shows how the phase relation is improved compared to the passive case in Figure 8.

For the PH configuration in irregular waves, the performance is somewhat decreased for wave inputs I3 and I4 compared to R3 and R4, but slightly improved for input I1 and I5 compared to R1 and R5. Here, the equally indexed sea states (for instance I3 and R3) have the same wave energy transport. The increased performance is understandable, since the irregular sea state gives the system some waves closer to the frequency for which its parameters have been optimised than the pure sinusoidal wave.

Looking at power losses in the hydraulic system (Table 5), we observe that they become very large for the most energy-rich sea states (R4 and I4). The lion's share of the loss is due to the motor resistance, which has been modelled as a linear resistive load. This is a simplification that, with our current model, gives unrealistically large losses when the rotational speed of the motor is high. On the other hand, the valve losses are more accurately modelled, and with the chosen valve diameters these are about 1.3 % of the absorbed power for the I4 sea state. This

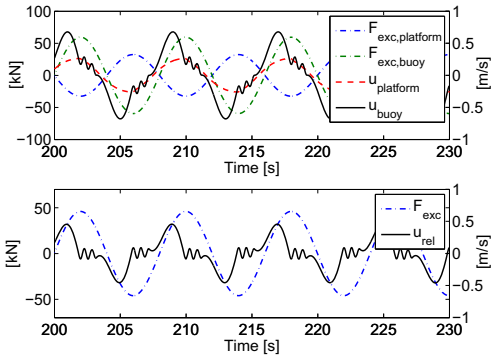

Figure 8: Excitation forces and velocities for the buoy and platform (upper) and for the relative motion (lower). The incoming wave is regular with a height of 1.31 m and a period of 8 s (R3), and the power take-off is PH. The wave elevation at the central axis of the buoy is given by ζ.

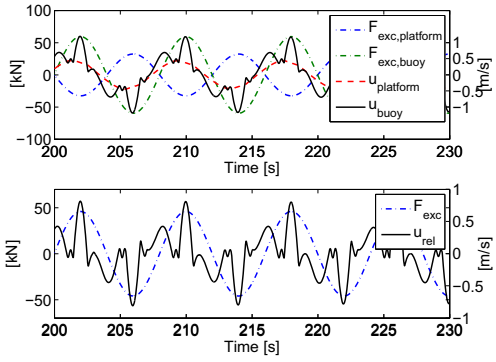

Figure 9: Forces and velocities for the hydraulic latching power take-off (PHL). Absolute (upper) and relative (lower) quantities for an incoming regular wave with height 1.31 m and period 8 s.

is still a quite high value, showing that such losses may become important if they are not seriously taken into account in the dimensioning of the equipment.

Table 6 shows the effect of increasing the viscous damping on the platform pontoons. The power output decreases slowly but steadily as the viscous damping is increased. This is in accordance with claims that shapes should be rounded and viscous losses avoided. Although the platform tend to oscillate in phase with the buoy (cf. Figure 10), reducing the viscous loss gives both increased power output and increased oscillation amplitudes.

One of the goals has been to assess the effect of varying the force compensation between the platform and the buoy. From Table 7 it is clear that this variable has a strong effect on the power output. According to the presented results, the power output increases when the opposing wave force on the platform is decreased, i.e. when the diameter of the pontoon is decreased (referred to as undercompensation of the wave force on the platform relative to the force on the buoy). Then both the excitation force on and the added mass of the platform decreases. Again,

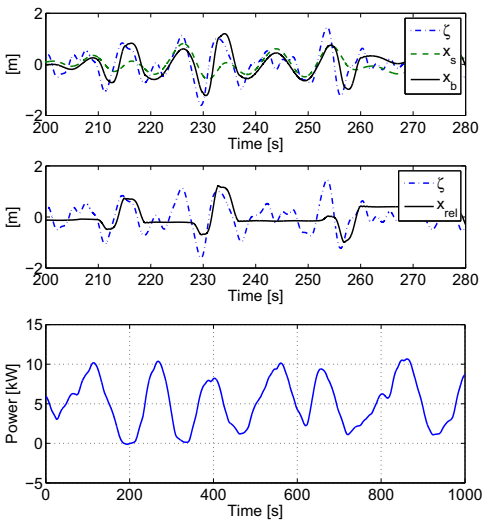

Figure 10: Motion response for the passive hydraulic power take-off (PH) in regular wave I3. The lowermost figure gives the power output (with a differing time scale). The wave elevation at the central axis of the buoy is given by ζ.

the platform motions are larger for the best performing geometries.

The simulation results in Table 8 indicate that the hydraulic power take-off (PH) performs inferior to an idealised linear power take-off (PL), both in terms of useful and absorbed power. In addition to losses in the PTO system, which are not present in the case of the PL configuration, this is due to less beneficial amplitude and phase of the of the buoy and platform motion, giving rise to the difference in absorbed power. On the contrary, when the pontoon diameter factor a is chosen to be 0.8 (see Table 7) the picture changes. Then the amplitude and phase relations are improved such that the PH system performs better than the PL system for the I3 sea state.

Finally, (cf. Table 9) shows that the output is larger when the platform is not allowed to move, except for the I2 sea state. This exception examplifies that having the two bodies moving may give better absorption than achieved with just the buoy moving. As we have seen, the platform geometry (here: the a factor) largely influences the power absorption and, by choosing it right, the performance with the platform moving could probably be improved compared to the case with fixed platform.

5 Conclusion

A two-body, heaving wave-energy converter with a hydraulic power take-off system has been studied with and without latching control. The first body is semisubmersible platform giving force reference to the the second body, which is a cylindrical buoy with hemispherical bottom. For the default platform geometry, the system performance shows to be somewhat inferior to what obtained by a simple linear load force for power take-off. The power output was shown to increase considerably using a latching control strategy for the hydraulic power take-off in regular waves. Flow losses in the hydraulic system may become large, and must be thoroughly assessed during the design process for such a system.

Taking out power from the relative motion between two heaving bodies instead of from one body with fixed reference (if possible) can be beneficial in terms of power output if the geometry and parameters are chosen right. If not, having two oscillating bodies instead of only one might only represent an extra cost. The system presented here performs better if the opposing excitation force on the platform is made smaller than the excitation force on the buoy (undercompensation).

Further work will assess the effect of latching control in irregular waves.

Acknowledgements

Thanks to professor emeritus Johannes Falnes for valuable input and guidance. Also thanks to the Norwegian research council for funding.

References

[1] Kjell Budal and Johannes Falnes. Wave power conversion by point absorbers: A norwegian project. *International Journal of Ambient Energy*, 3(2):59 – 67, 1982.

[2] R. E. Hoskin, N. K. Nichols, D. A. C. Nicol, and B. M. Count. Latching control of a point absorber. In *Water for Energy*, pages 317 – 330. BHRA Fluid Engineering Centre, Brighton, England, 1986.

[3] K. Budal. Floating structure with heave motion reduced by force compensation. In *Proceedings Fourth International Offshore Mechanics and Arctic Engineering Symposium*, pages 92–101, Dallas, Texas, February 1985. ASME, N.Y.

[4] J. Falnes. Wave-energy conversion through relative motion between two single-mode oscillating bodies. *Journal of Offshore Mechanics and Arctic Engineering (ASME Transactions)*, 121:32–38, 1999.

[5] Hallvard Engja and Jørgen Hals. Modelling and simulation of sea wave power conversion systems. In *Proceedings of the 7th European Wave and Tidal Energy Conference, Porto, Portugal, 2007*, 2007.

[6] *WAMIT User Manual*. (http://www.wamit.com).

[7] H. Eidsmoen. Tight-moored amplitude-limited heaving-buoy wave-energy converter with phase control. *Applied Ocean Research*, 20(3):157 – 161, 1998.

[8] J. Falnes and P.M. Lillebekken. Budal's latching-controlled-buoy type wave-power plant. In Anthony Lewis and Gareth Thomas, editors, *Fifth European Wave Energy Conference: Proceedings of an International Conference held at University College Cork, Ireland, 17-20 September 2003*, pages pp. 233–244, Cork, Ireland, 2005. Hydraulics & Maritime Research Centre, Hydraulics & Maritime Research Centre. ISBN 0-9502440-5-8.

[9] Håvard Eidsmoen. *On the theory and simulation of heaving-buoy wave-energy converters with control*. PhD thesis, NTH, December 1995.

[10] W.E. Cummins. The impulse response function and ship motions. *Schiffstechnik*, 9(1661):101–109, 1962.

[11] R. Taghipour, T. Perez, and T. Moan. Hybrid frequency–time domain models for dynamic response analysis of marine structrues. *To appear*, 2007.

[12] T. Sauder and T. Moan. Experimental investigation of the hydrodynamic characteristics of a novel column design for semi-submersible platforms. In *The Seventeenth (2007) International Offshore and Polar Engineering Conference -ISOPE 2007*, 2007.

[13] Simulink. The MathWorks, Inc. 3 Apple Hill Drive Natick, MA 01760-2098 USA.

Article C: Lopes et al., Ocean Engineering 36 (2009)

Ocean Engineering 36 (2009) 386–402

Contents lists available at ScienceDirect

Ocean Engineering

journal homepage: www.elsevier.com/locate/oceaneng

Experimental and numerical investigation of non-predictive phase-control strategies for a point-absorbing wave energy converter

M.F.P. Lopes [a,*], J. Hals [b], R.P.F. Gomes [a], T. Moan [b], L.M.C. Gato [a], A.F.de O. Falcão [a]

[a] IDMEC, Instituto Superior Técnico, Technical University of Lisbon, 1049-001 Lisbon, Portugal
[b] CeSOS, Norwegian University of Science and Technology NTNU, NO-7491 Trondheim, Norway

ARTICLE INFO

Article history:
Received 31 July 2008
Accepted 18 January 2009
Available online 1 February 2009

Keywords:
Ocean waves
Wave energy
Latching control
Point-absorber
Threshold unlatching
Oscillating water column

ABSTRACT

Phase control may substantially increase the power absorption in point-absorber wave energy converters. This study deals with validation of dynamic models and latching control algorithms for an oscillating water column (OWC) inside a fixed vertical tube of small circular cross-section by small-scale testing. The paper describes experimental and numerical results for the system's dynamics, using simple and practical latching control techniques that do not require the prediction of waves or wave forces, and which will be relevant to any type of point-absorbing devices.

In the experimental set-up, the upper end of the tube was equipped with an outlet duct and a shut-off valve, which could be controlled to give a latching of the inner free surface movement. The pressure drop through the open valve is used as a simplified measure of the energy extraction. The control was realized by using the real-time measurement signals for the inner and outer surface displacement.

A mathematical model of the system was established and applied in numerical simulation. In the case the OWC's diameter is much smaller than the wavelength and the wave amplitude much smaller than the draft, the free surface movement inside the tube can be described as an oscillating weightless piston. For this hydrodynamic problem an analytical solution is known. In addition, the mathematical model includes the effects of viscous flow losses, the air compressibility inside the chamber and the pressure drop across the valve. Experimental results were used to calibrate some of the model parameters, and the total model was formulated as a coupled system of six non-linear, first-order differential equations. Time-domain integration was used to simulate the system in order to test the control strategies and compare with experimental results.

1. Introduction

Point-absorbing wave energy converters have been studied since the late 1970s, including testing at laboratory scale and under real-sea conditions. Presently there are several concepts under development within this category.

An oscillating water column (OWC) device in the form of a vertical tube of small circular cross-section is a geometrically simple point absorber that was studied analytically in the frequency domain by Evans (1978). He obtained a solution for the hydrodynamic coefficients based on linear water wave theory by assuming a small radius compared with the cylinder draft and with the wavelength. Since sloshing is not significant at frequencies relevant for wave energy conversion for these conditions, the movement of the inner free surface is practically identical to that of a weightless piston, or even to the motion of a heaving body in waves. His formulation also includes the possibility of adding a force on the conceptual piston, which could for instance be modelled as a linear inertia–spring–dashpot system representing a power take-off (PTO) mechanism.

This simplified theoretical model was later improved by considering a uniform pressure distribution on the inner free surface (Sarmento and Falcão, 1985; Evans, 1982), which yields a more realistic representation of the (in general non-flat) free surface shape. Numerical codes based on the boundary element method were developed and applied to model the OWC hydrodynamics assuming a uniform distribution of the pressure on the inner free surface (Delauré and Lewis, 2003; Lopes et al., 2007). The effect of air compressibility was found to be relevant in full-sized OWCs (Sarmento and Falcão, 1985). A time-domain representation can be developed from the frequency-domain model by applying Fourier transform techniques. This formulation

* Corresponding author. Tel.: +351 21 8417273.
E-mail addresses: mlopes@hidro1.ist.utl.pt (M.F.P. Lopes), jorgen.hals@ntnu.no (J. Hals).

0029-8018/$ - see front matter © 2009 Elsevier Ltd. All rights reserved.
doi:10.1016/j.oceaneng.2009.01.015

Nomenclature

A, **B**, **C**	state-space matrices for approximation of F_R
A_{OWC}	waterplane area of OWC
A_v	nominal valve area
a_r	added mass
$a_{r\infty}$	added mass at infinite frequency
b_r	radiation resistance
C_{dc}	valve discharge coefficient
c_1	linear term constant for Φ
c_2	quadratic term constant for Φ
f	frequency
f_e	energy frequency, $f_e = 1/T_e$
F_e	excitation force
F_R	convolution part of radiation force
g	acceleration of gravity
H	wave height
H_s	significant wave height
h_c	chamber height
h_0	tube draft
$L(t)$	radiation memory function
k_v	valve state, 'open' = 1, 'closed' = 0
k_c	stiffness of air chamber
m	mass
m_c	mass of air in the chamber
P_u	useful power
p	air pressure
p_0	pressure at reference conditions
p_c	air pressure in the chamber
p_3	vertical linear momentum of the water column
r	tube inner radius
r_o	tube outer radius
S	hydrostatic stiffness
T	period
T_e	energy period
t	time variable
V	volume
x	horizontal coordinate
z	sate vector for approximation of F_R, here: size 3×1
γ	specific heat ratio for air
γ'	JONSWAP spectrum shape factor
ω	angular frequency
η	vertical displacement of OWC
ϱ_w	water density
ϱ	air density
ϱ_0	air density reference conditions
τ	time integration variable
τ_d	delay for operation of valve
Φ	viscous force
ω_n	natural frequency of chamber oscillation

is required in order to deal with a non-linear PTO mechanism, and is an appropriate tool to model the energy absorption from irregular waves.

The amount of power absorbed from ocean waves by an oscillating body is governed by the amplitude and phase of the oscillation relative to the wave. Thus, the absorption can be optimized by controlling the amplitude, and, when not in resonance, also the phase of motion. Several strategies have been proposed for approaching the theoretically optimal controller, which is non-causal, and a review of the theoretical basis is given by Falnes (2002b). Causal implementations have been described and tested by various authors, of which some of the most recent are Perdigão (1998), Gieske (2007), Valério et al. (2007), and Schoen et al. (2008a, b). An early proposal (Falnes and Budal, 1978), which is further investigated here, was the *latching control* technique where the relative motion between the body and the reference is stopped during specified parts of a wave cycle. Originally, it was counting on a prediction of the wave force for the determination of the unlatching instants. Latching control has continued to receive attention (see e.g. Korde, 2002; Mundon et al., 2005; Babarit and Clement, 2006; Falcão, 2007), and has still the potential to become a viable solution for application to wave energy devices due to its possible easy implementation and high performance.

There are several ways of defining a latching strategy. A common feature for all of them is that they aim at implementing, accurately or approximately, what in optimal control terminology is identified as 'bang-bang' control. Earlier research (Hoskin and Nichols, 1986) showed that if we restrict ourselves to control only the damping coefficient of the PTO system, bang-bang control is the optimal strategy. This means that the control output jumps between two values—one low and one high. The high damping should be set when the velocity of the oscillator becomes zero, leading to a latching of the motion, and the change to the low value (unlatching) should be such that the velocity of the oscillator falls into phase with the excitation force.

A model for the application of latching control to the airflow of OWC type wave energy converters has been presented by Jefferys and Whittaker (1986). In their paper, the effect of air compressibility is accounted for. They showed that it has significant influence on the system's behavior, as the stiffness of the air chamber is not very different from the hydrodynamic stiffness of the water column. An approximate method was used for the optimization of the latching instants.

The problem of simultaneous scaling of hydrodynamics and compressibility effects in small-scale experiments on OWCs was addressed by Weber (2007), who highlighted the fact that the air compressibility cannot be accurately represented by geometrical scaling of the device.

The modelling of the thermodynamic processes related to the air compression and the airflow in and out of the chamber in an OWC was described in detail in Falcão and Justino (1999). This work shows that a complete modelling of these processes is complex and depends on the flow direction (in- or outflow).

Experimental results for latching strategies have previously been reported. Budal et al. (1979) made an early demonstration of the importance of phase control and the benefit of latching the oscillator motion, with subsequent developments reported in Budal and Falnes (1982). Further, Bjarte-Larsson et al. (2002) applied this principle to a hybrid OWC/buoy device with a hydraulic PTO. Bjarte-Larsson and Falnes (2006) performed experiments with a point absorber. Experimental results for latching control of a pitching device are reported by Durand et al. (2007).

2. Mathematical model

A schematic representation of the OWC geometry under consideration is shown in Fig. 1. The following effects are included in the mathematical model of the laboratory set-up: hydrodynamic forces (excitation and radiation); hydrostatic buoyancy; viscous loss in water; air chamber compressibility with mass and

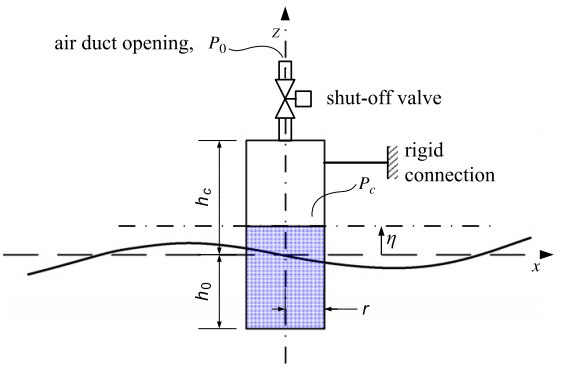

Fig. 1. Schematic representation of the tested OWC.

volume change; valve with pressure drop; opening and closing of the valve.

The water column oscillates inside a surface-piercing thin-walled tube of radius r and draft h_0, due to the action of an oscillating excitation force F_e caused by an incident (regular or irregular) wave propagating in the x direction. Since the radius of the tube is much smaller than both the tube draft and the wavelength, the warping of the inner free surface may be neglected and the free surface regarded as if acted upon by a weightless piston, whose position relative to the still water level is represented by η.

The frequency-dependent hydrodynamic coefficients may be computed from linear water wave theory. The radiation force on the OWC is related to the added mass $a_r(\omega)$ and the radiation resistance $b_r(\omega)$. The hydrostatic restoring force is $S\eta(t) = \varrho_w g A_{\mathrm{OWC}} \eta(t)$, where ϱ_w is the water density, g is the acceleration of gravity and A_{OWC} is the inner cross-sectional area of the tube.

The upper end of the tube is connected to a narrower duct where a shut-off valve can be operated to stop the airflow. Due to the inner free surface motion and the constrained airflow, the absolute air pressure p inside the chamber is time-varying and in general different from the atmospheric pressure p_0. The variation of pressure produces a change in specific volume, which may be modelled approximately as an isentropic process:

$$\frac{p(t)}{\varrho^{\gamma}(t)} = \frac{p_0}{\varrho_0^{\gamma}}, \tag{1}$$

where ϱ_0 is the density of air at reference conditions and $\gamma = c_p/c_v$ is the specific heat ratio ($\gamma = 1.4$ for air).

The balance of forces applied on the weightless piston may be written as

$$a_r(\infty)\ddot{\eta}(t) + \int_{-\infty}^{t} L(t-\tau)\dot{\eta}(\tau)\,d\tau + \Phi(t) + S\eta(t) + (p(t)-p_0)A_{\mathrm{OWC}} = F_e(t). \tag{2}$$

Here, Φ is a force that accounts for the real fluid viscous effects in the water. Based on experimental results (as discussed in Section 6), this force is expressed as a second-degree polynomial in terms of the velocity $\dot{\eta}$:

$$\Phi(t) = c_1\dot{\eta}(t) + c_2\dot{\eta}(t)|\dot{\eta}(t)|. \tag{3}$$

The memory function $L(t)$ is related to the frequency-dependent radiation damping coefficient $b_r(\omega)$ by (see e.g. Falnes, 2002a, Eq. 5.115)

$$L(t) = \frac{2}{\pi}\int_0^{\infty} b_r(\omega)\cos(\omega t)\,d\omega. \tag{4}$$

For purely sinusoidal motion with angular frequency ω, the radiation force, corresponding to the first two terms of Eq. (2), may be written as $a_r(\omega)\ddot{\eta}(t) + b_r(\omega)\dot{\eta}(t)$. However, when this is not the case, the convolution integral

$$F_R(t) = \int_{-\infty}^{t} L(t-\tau)\dot{\eta}(\tau)\,d\tau \tag{5}$$

must be computed. One of the most efficient ways of doing this is to approximate the convolution integral by a state-space model. In the studied case a third-order state-space model was found to give satisfactory results, as shown in Fig. 2. We now introduce the vertical linear momentum of the water column p_3 as a variable. The model for the radiation force $F_R(t)$, with input $\dot{\eta}(t) = p_3(t)/a_r(\infty)$ and state vector $\dot{\mathbf{z}}(t)$, can be written as (Jefferys, 1984; Taghipour et al., 2007)

$$\dot{\mathbf{z}}(t) = \mathbf{A}\mathbf{z}(t) + \mathbf{B}\frac{p_3(t)}{a_r(\infty)},$$
$$F_R(t) = \mathbf{C}\mathbf{z}(t). \tag{6}$$

In order to obtain a set of equations suitable for numerical integration, we write $m_c(t) = V(t)\varrho(t)$, where m_c is the mass of air in the chamber and $V(t) = V_0 - A_{\mathrm{OWC}}\eta(t)$ its volume. Eq. (1) can then be written as

$$p(t) = \frac{p_0}{\varrho_0^{\gamma}}\left(\frac{m_c(t)}{V(t)}\right)^{\gamma}. \tag{7}$$

Furthermore, the differential equation for the chamber volume V is simply

$$\dot{V}(t) = -A_{\mathrm{OWC}}\frac{p_3(t)}{a_r(\infty)}. \tag{8}$$

Assuming the flow–pressure characteristic of the orifice to be of square-root type (which was verified in experimental tests as discussed later), and neglecting the terms of order ε^n for $n \geqslant 2$ in

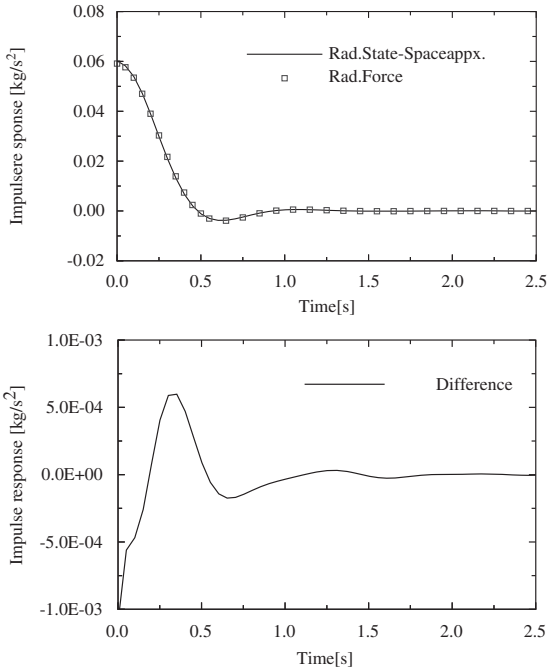

Fig. 2. Top: the impulse response function $L(t)$ for the radiation force (line) and its state-space approximation (symbols). Bottom: difference between both.

$\varepsilon = \Delta p/p_0$, the air mass flow through the valve was characterized by

$$\dot{m}_c(t) = k_v(t) C_{dc} A_v \,\mathrm{sgn}(p(t) - p_0)\sqrt{\frac{2m_c(t)|p(t) - p_0|}{V(t)}}, \tag{9}$$

where $k_v = 1$ if the air valve is open and $k_v = 0$ if it is closed. Further, C_{dc} is the non-dimensional characteristic discharge coefficient and A_v is the nominal cross-sectional area of the valve. These two parameters account for the whole mounting of the valve (in open position) and its connections to the chamber and outside environment.

By choosing the vertical linear momentum $p_3(t)$, the chamber volume $V(t)$ and the mass of air inside the chamber $m_c(t)$ as state variables together with the variables of the radiation force approximation (6), we have six variables to represent the state of system model. Eq. (2) may now be rewritten as

$$\begin{aligned}\dot{p}_3(t) = &-\mathbf{Cz}(t) - \frac{c_1}{a_r(\infty)} p_3(t) - \frac{c_2}{a_r(\infty)^2} p_3(t)|p_3(t)| - S\frac{V_0 - V(t)}{A_{OWC}} \\ &- \left(\left[\frac{m_c(t)}{\varrho_0 V(t)}\right]^{\gamma} - 1\right) p_0 A_{OWC} + F_e(t),\end{aligned} \tag{10}$$

where it has been inserted for pressure $p(t)$ according to Eq. (7). Eqs. (6), (8)–(10) now constitute a set of six first-order ordinary differential equations solvable in the time domain.

The hydrodynamic modelling of other types of point-absorbing devices closely follows that of this simple OWC. The latching control method investigated here and the results to be presented are thus believed to be highly relevant also to those devices.

3. Latching strategies

To implement the latching control, several strategies can be applied. Typically, they all latch the oscillator when its velocity is zero, but differ in their strategy to determine the instant of unlatching.

In order to find the optimum instant for unlatching, prediction of future excitation force is needed. In regular waves, the optimum would be that the peaks of the excitation force and the velocity of the water column are in phase with each other. This can be named *peak-match unlatching*. Although the unlatching instant is then optimal under the assumption of latching control, the control strategy itself is sub-optimal, as there will possibly be other motion paths giving higher energy absorption.

Another strategy is not to focus on phase-matching the peaks, but rather to ensure that the oscillator will always move in the direction of the excitation force when released. Then the power always flows from the sea to the absorber (as long as the wave period is longer than the eigenperiod). This is done by releasing the oscillator at the instant when the excitation force changes direction (i.e. changes sign).

A third method is inspired by the work of Falcão (2008). It is similar to the previous one, but the unlatching is done at the instant when the excitation force (or some other reference variable) passes a chosen threshold. We therefore refer to this as *threshold unlatching*. The input parameter used by Falcão was the pressure in a hydraulic piston pump rather than the excitation force. This may give a particularly simple way for implementation in a real system, as pressure measurements are simple and robust.

This is the kind of strategy investigated in the present work. An important property is that it needs no prediction of future inputs to the system. We see that if the threshold is set to zero, the last method becomes the same as the second, so rectified power flow (method 2) is a special case of threshold unlatching (method 3).

As shown by Lopes et al. (2007), for the case studied in this paper, the phase difference between the outside wave elevation and the excitation force is less than 3° in regular waves for the relevant frequency range. This means that the phase of the free surface elevation outside the tube is a good approximation of the phase of the excitation force, at least in the case of regular waves. The zero-crossing of the excitation force can thus be assumed to be fairly well detected from a sign change of the outside wave elevation. The assumption of approximate signal coincidence between outer wave elevation and excitation force may, however, be doubtful for wave cycles in an irregular sea state where rapid oscillations are prominent. Also for the threshold unlatching case, the trigger signal for unlatching can be obtained by comparing the present and recent values of the reference signal to the threshold value.

In principle, the excitation force is not a causal function of the wave elevation as discussed in Falnes (1995), and also the frequency content does not carry directly over from wave elevation to excitation force. Nevertheless, these effects are so small that the current approach is still useful. Another point is that the radiated wave will interfere with the measured incident wave. In our case, the radiated waves were small enough not to invalidate the chosen method. But if not so, a correction for the radiated wave may be made (Falnes, 2002a, p. 208) in order to improve the estimate for the excitation force. A reasonable approximation may be found by direct proportionality between surface elevation and excitation force if the body draft is not too large and the wave is not too broad-banded.

4. Chamber resonance and pressure variations associated with latching

At the instant of latching, the pressure difference across the valve is close to zero, and the velocity of the internal free surface is ideally zero. However, the acceleration will be different from zero. Then, due to the valve closure, the air pressure will go through a transient process, oscillating (as an effect of air elasticity) about a value different from the pressure previous to closure, producing transient oscillations in the inner free surface.

During the latched part of the cycle, the inner free surface will then tend to behave as a free oscillator about an initial position η_L (neglecting the variation in the excitation force and in the radiation force F_R). The instantaneous air column stiffness k_c is given by the position derivative $\partial/\partial\eta$ of the force

$$F(\eta) = A_{OWC} p(\eta) = A_{OWC} p_i \left(\frac{\varrho(\eta)}{\varrho_i}\right)^{\gamma} \tag{11}$$

on the virtual piston due to the pressure, where the initial air pressure p_i and density ϱ_i are taken at the equilibrium position η_i for the initial amount of gas in the chamber. This yields

$$k_c = \frac{\gamma A_{OWC}^2 p_0}{\varrho_0^{\gamma}} \left(\frac{m}{V}\right)^{\gamma} \frac{1}{V}. \tag{12}$$

For all the described latching strategies the valve closes when the velocity of the inner surface becomes zero, which corresponds approximately to zero pressure difference across the valve. The volume at the latching instant only depends on the instantaneous free surface position η_L and hence the stiffness at this instant will be (assuming that the air density variation is small)

$$k_c \approx \frac{\gamma A_{OWC}^2 p_0}{V_0 - A_{OWC}\eta_L}. \tag{13}$$

The added mass in the column position η is given by

$$I = a_{r\infty} + \eta A_{OWC} \varrho_w, \tag{14}$$

where $a_{r\infty} \approx a_r(\infty)$. The term $\eta A_{OWC}\varrho_w$ represents the change in added mass due to the non-equilibrium position of the inner free surface. The approximation $a_{r\infty} \approx a_r(\infty)$ (0.417 kg) was found to be acceptable for a narrow column in the range of frequencies of interest (Lopes et al., 2007). At a latched position the natural frequency of the oscillator is consequently, from the harmonic oscillator equation $\omega_n = \sqrt{k_c/I}$ and Eqs. (13) and (14):

$$\omega_n \approx \sqrt{\frac{\gamma A_{OWC}^2 p_0}{(V_0 - \eta_L A_{OWC})(a_{r\infty} + \eta A \varrho_w)}}. \quad (15)$$

The free surface tends to oscillate at the frequency given by Eq. (15), in combination with variations associated with the change of the excitation and radiation forces. In a stiff system this is a good approximation during the latched part of the cycle since the variation in air density is small (which was used to obtain Eq. (13)).

The amplitude of the pressure variation is more significant when a high frequency ω_n is associated with low stiffness k_c. For a constant cross-sectional area, this will typically occur for the lower latched positions where the mass is low, cf. Eq. (14). The fast velocity variations can in some cases introduce rapid pressure fluctuations in the chamber.

The sudden opening of the valve introduces an effect that should be considered. The air burst that follows the opening of the valve creates a propagating pressure disturbance whose passage is detected at the measurement point (located half way between the inner free surface and the top of the tube), as well as its reflection on the free surface. These pressure fluctuations, which will be more significant for quicker maneuvres of the valve, together with the resonance oscillation of the chamber pressure, make it difficult to use the pressure measured in the chamber as a basis for calculating a control signal. The same behavior is expected in hydraulic systems used for PTO. This means that we might have to look for another input to the controller. For the present system a good alternative may be to measure the wave elevation close to the device, as actually applied herein, or to use a submerged pressure transducer, and estimate the instantaneous excitation force from these signals, as done for example by Budal et al. (1981).

5. Experimental model

A set of experiments was carried out in the wave flume of the Laboratory of Hydraulics and Water Resources (LHRH) of Instituto Superior Técnico. This flume is 20 m long, 0.70 m wide and the water depth was set to 0.50 m.

A fixed, vertical tube of circular cross-section was placed at a distance of 9 m from the piston wavemaker. The draft h_0 was set to 0.18 m and the height of the chamber h_c was 0.33 m. The inner radius of the tube was 26 mm and the wall thickness 4 mm. The upper end of the tube was covered with a removable airtight covering plate with a centered 12.7 mm (half inch) diameter orifice connecting to a shut-off valve. The laboratory model was not intended to represent a practical full-scale device, so there is no fixed scale factor for geometry or forces.

The shut-off valve is externally piloted by 7 bar compressed air and controlled electrically. The standard valve opening and closing time is specified by the manufacturer to be 29 ms.

The static pressure inside the chamber was measured by a differential low-pressure manometer that allows measurements up to 50 Hz and ±200 Pa to be performed (thus the transient effects due to valve operation were not accurately captured). The surface elevations were measured at a rate of 250 Hz with resistive water-level gauges, one attached to the wall inside the tube and the other placed outside, aligned with the center of the tube (i.e. in the same cross-sectional plane of the flume), at distance of about 0.105 m from the tube wall.

Recordings were made of the outside wave elevation, the inside column elevation, the chamber pressure relative to the ambient pressure, and the control signal sent to the shut-off valve. Calibrations were done prior to each day of experiments. Based on calibration methods and instrument resolutions, the uncertainty of the wave elevation gauges is estimated to about 0.25 mm and the pressure measurement to about 1 Pa.

The signals of the free surface displacement in and outside the tube were acquired by a data acquisition card connected to the wave gauges. A control program was developed in LabVIEW and run on a separate computer to the one used to acquire the data. The result of the control computation ('valve open' or 'valve closed') was transmitted through the data card's analog output, driving a solid state relay that switches the valve state.

The implementation of the control system for the laboratory set-up faced many of the difficulties associated with a latching control system for a full-scale device. As a small change in timing has a large influence on the overall efficiency, overcoming the effect of operational delays is crucial.

The response delay of the control emerges from two factors: the first—the acquisition delay—comes from the acquisition of data from sensors, and the finite update rate in the control software; the second—the operational delay τ_d—is due to the execution of valve commands, which are subject to relay and valve reaction times. Based on separate tests, the operational delay (due to the relay and valve operation), was estimated to be $\tau_d = 160$ ms. The delay in the pressure measurement was estimated to be 64 ms.

The control routine programmed in LabVIEW was based on the decision tree represented in Fig. 3. The basic conditions are the following: the valve closes when the inner velocity becomes zero; and it opens when the excitation force crosses a chosen threshold (with zero as the default value). As explained above, an estimation of the excitation force was found directly from the measurement of the wave outside the cylinder.

At the instant when the 'open' command is issued, the inner velocity is zero or floating around zero depending on the air chamber stiffness and the time since it has been latched, and it will take some time before the column has gained speed. This implies the possibility that the 'open' command will be immediately followed by a 'close' command. Instead, the opening command should prevail until the inner surface has gained some speed. To take care of this, an 'impose open time'—τ_{imp}—is included in the control routine. As the opening command is only effective after the operational delay, this implies that $\tau_{imp} > \tau_d$. In this case τ_{imp} was set to 250 ms, which has proven to be an effective value, even in irregular waves. However, the fact that this time is an important fraction of the cycle limits the performance in irregular waves or waves of frequencies above the natural resonance frequency of the tested OWC, which is about 1.14 Hz.

In this work a short-term anticipation strategy was used by identifying an interval forward in time corresponding to the operational delay. In the case of the outer free surface position, given the instantaneous position and velocity at certain time, the time until next threshold crossing can be estimated by direct extrapolation. This strategy is effective provided that the acquisition rate is much larger than the wave frequency, or if analogue circuits are used. In predicting the next velocity zero-crossing, the same type of strategy was applied, using the instantaneous velocity and acceleration. Here, both these signals were derived from the position measurement, and filtering had to be applied to improve the instantaneous acceleration signal. The whole control

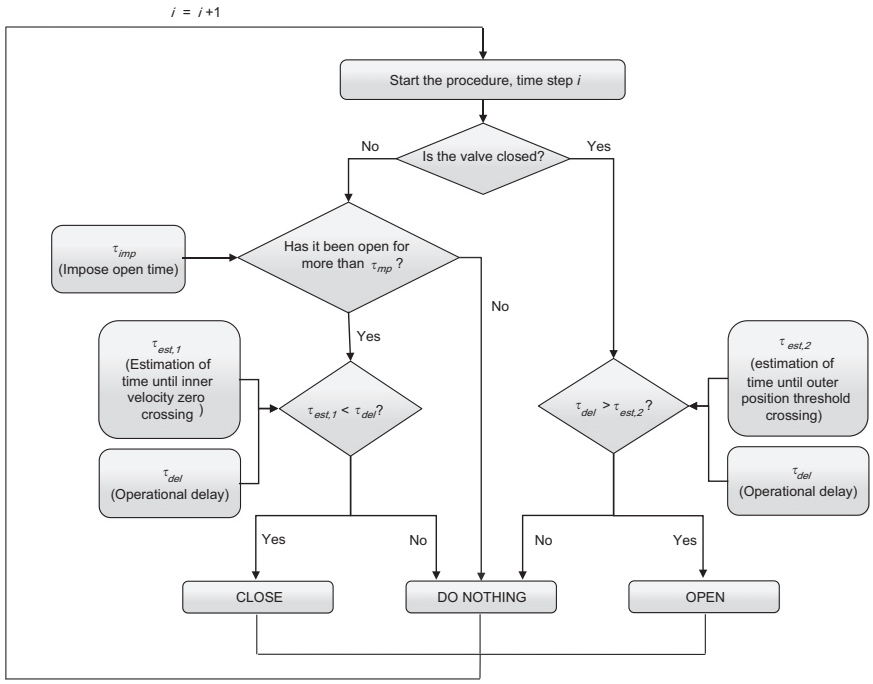

Fig. 3. Decision tree used by the control program. During operation, the loop was run at a frequency of 150 Hz.

routine was run at 150 Hz maximum, due to the real time computation limitations of the equipment used.

6. Parameter fitting and numerical scheme

As already mentioned, a second-degree formulation was adopted to model the viscous forces in terms of Eq. (3), with the coefficients $c_1 = 0.114\,\mathrm{N\,s/m}$ and $c_2 = 0.739\,\mathrm{N\,s^2/m^2}$. The coefficient values were determined using experimental results from tests done without operating the air valve. For the valve pressure drop, a purely quadratic relation with discharge coefficient $C_{dc} = 0.69$ was used. This value was also found from fitting to experimental data, now running with the outlet duct and valve in place. Details of the parameter fitting are given in Appendix A.

The mathematical model was implemented both in Matlab (The Mathworks Inc, 2008) and in 20-sim (Controllab Products B.V., 2008) (a tool for bond graph modelling). Pre-programmed *ode23tb* and *Vode-Adams* algorithms were used to compute numerical solutions. For the Matlab implementation, which was used in most of the simulation work, the absolute tolerances were set to $10^{-5}\,\mathrm{kg\,m/s}$, $10^{-9}\,\mathrm{m^3}$ and $10^{-9}\,\mathrm{kg}$, for the linear momentum, volume and mass, respectively. For the states of the state-space approximation to F_R the setting was 10^{-7}. The relative tolerance was set to 10^{-6}.

For comparison with experimental results, the measurement of the wave elevation close to the tube was used to derive time series for the excitation force (by convolution with the impulse response for the excitation force coefficient). As before, this requires that the radiated wave is small, which also means that a relatively small part of the total available energy is absorbed.

7. Results and discussion

The experimental model was exposed to regular waves with frequencies in the range 0.5–1.2 Hz, and wave heights between 7 and 50 mm. A JONSWAP spectrum with standard parameters (thus a typical North Sea wave, see e.g. Michel, 1999 for explanation) was chosen for the generation of irregular waves, for which four combinations were run, with parameters $T_e = m_{-1}/m_0 = 1/f_e = \{1.30, 1.89\}$ s (energy period, defined as the ratio between spectral moments m of order -1 and 0) and $H_s = \{25.6, 39.0\}$ mm (significant wave height). The wave data refer to the average values measured in the wave flume for each setting of the wavemaker. Waves within this range travel down the flume without breaking and are accurately measured by the installed wave gauges. For experiments with latching control, focus has been on waves with period larger than the eigenperiod of the water column. The same wave inputs have been run with the unlatching threshold set to zero, and a selection of wave inputs have been run with varying values for the threshold. In addition, the same cases were run with the numerical solver for analysis and comparison. Results are given in Sections 7.1–7.3.

In addition, numerical simulations were made with optimized values for the discharge coefficient C_{dc} (giving the load damping) and the threshold value. This is reported in Sections 7.4 and 7.5. Furthermore, Section 7.6 gives an account of the oscillations occurring during the latched intervals.

7.1. Basic response

The measured motion response with the fully open tube (no valve or orifice plate) is shown in Fig. 4 for several frequencies f

and wave heights H. The analytical results from Evans (1978), based on zero wall thickness and using the value of the model's inner diameter, are also shown. The resonance peak may be identified around $f = 1.1$ Hz, and the analytical model gives a value of 1.14 Hz.

An amplification factor $AF = |\hat{\eta}|/|\hat{\zeta}|$ is defined here as the ratio between the response amplitude $|\hat{\eta}|$ and the incident wave amplitude $|\hat{\zeta}|$. The results in Fig. 4 show that there is a clear non-linear effect influencing the response around resonance of the system, as the increase in the incident wave causes lower amplification. This effect is attributed to the vortex shedding near the tube's bottom end. A first consequence of this feature is the necessity of including non-linear terms in Φ, as described by Eq. (3).

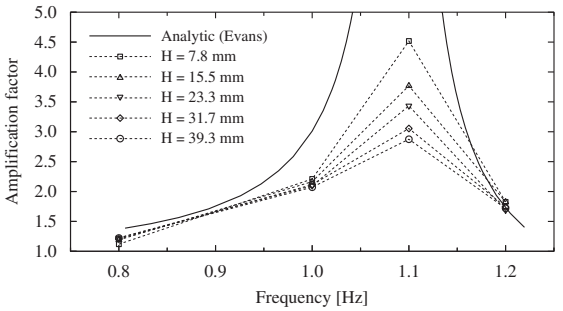

Fig. 4. Measured amplification factor when no plate nor valve are installed. The analytical results are obtained for an inviscid fluid (Evans, 1978). The indicated values of H are the average values of the amplitude of the measured incident wave height.

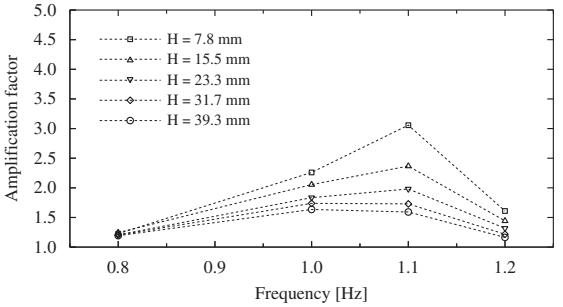

Fig. 5. Amplification factor $|\hat{\eta}|/|\hat{\zeta}|$ when the orifice plate and the valve are installed.

As shown in Fig. 5, the same experiments were repeated with the orifice plate and valve in place. The system continued to behave non-linearly, and the frequency of the highest response is shifted downwards as the input wave height is increased.

Fig. 6 shows characteristic pressure–velocity (p_c vs. $\dot{\eta}$) trajectories computed with the numerical model for several hypothetical configurations. In Fig. 6, the viscous dissipation in water and the energy extraction by the PTO are represented by a second-degree polynomial.

Based on this model, as well as small compressibility effects in the chamber and a small amplitude of motion (case 1), the trajectory becomes quadratic in Fig. 6.

In case 2, the chamber was enlarged, resulting in larger compliance giving a phase difference between the free surface velocity and the chamber pressure. This means in particular that there is energy stored in the chamber—with a small non-zero relative pressure in the chamber even when the free surface velocity is zero.

In case 3, the simulations were run for large incident wave amplitude—implying movements of the free surface over a significant part of the air column height. As a consequence, the system becomes clearly non-symmetric because the stiffness of the air spring changes with the free surface position. The result is that motions in the positive direction are reduced while motions in the negative direction are enlarged.

A delay in the pressure measurement gives a phase difference between the velocity and the pressure, as demonstrated by case 4. The effect is similar to increased compliance (case 2). As a consequence, the delay should be thoroughly investigated and accounted for in order to avoid misinterpretations of measurement data.

Case 5 represents typical trajectories with latching control and compressibility of the air column taken into account. During the latched parts of the cycle there are large variations in the chamber pressure associated with not so large variations in the free surface position. These variations are not associated with substantial energy dissipation, but can stress the system's components. During the non-latched parts, case 5 is similar to case 1.

7.2. Motion response to latching control

In the first set of experimental tests with latching control, the opening threshold was set to zero. To overcome the operational

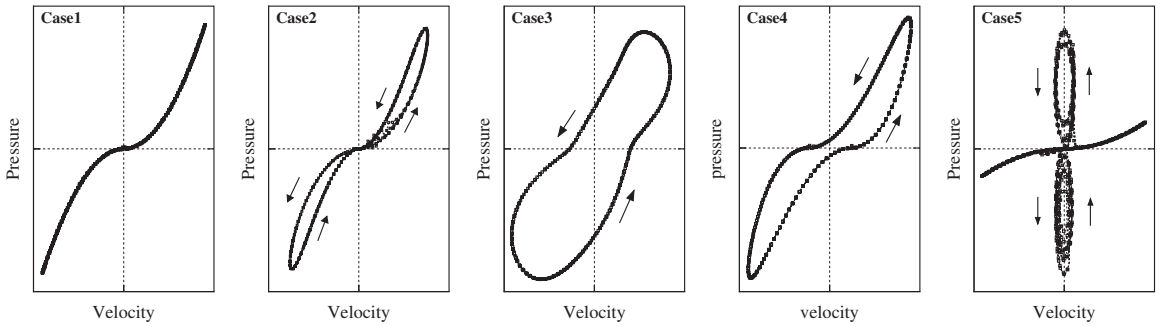

Fig. 6. Numerical computation of pressure–velocity (of the free surface) trajectories with a linear PTO and viscosity losses in several situations: Case 1—basic behavior; Case 2—large compressibility; Case 3—very large compressibility and significant inner amplitude as compared to the chamber height; Case 4—pressure measurement delayed with relation to free surface measurement; Case 5—latching control with significant compressibility.

delays, the control algorithm was run according to the procedure described in Fig. 3. The algorithm aims to close the valve when the velocity of the inner free surface crosses zero, and to open it when the outside elevation is zero (which is close to a zero excitation force situation). This makes the phase difference between excitation force and velocity closer to optimum, and as a consequence larger amplification and maximum velocities are achieved.

Fig. 7 shows time series for the interior free surface elevation, with and without control, for an identical phase-adjusted incident regular wave with a frequency of 0.6 Hz (about half the resonant frequency of the oscillator). It is clearly shown how the latching dramatically influences the system's behavior. The high-frequency oscillations during the latched periods, caused by the chamber compressibility, are visible in the time series presented both in Figs. 7 and 9, and will be analyzed in more detail later (Section 7.6).

The amplification factor, which actually compares the inner surface excursion with the incident wave height with and without control, is shown in Fig. 8. The increase in the amplification factor, together with the phase improvement visible in Fig. 7, indicates that the designed control routine works correctly for regular waves when the wave frequency is lower than the eigenfrequency. With the current implementation, however, the time delays discussed in Section 5 made the controller fail at wave frequencies close to or higher than the resonance frequency. This is the reason why the data points for such frequencies have been omitted in Figs. 8 and 10.

We note that this control program does not require the tuning of frequency-dependent parameters for each regular wave case. For this reason, the same control routine could be applied unchanged to irregular incident waves. A sample result is represented in Fig. 9. The experience has shown that a precise knowledge of the still water level is essential for a good control performance. Under such circumstances, the phase-control algorithm has proven to perform very close to the design specification. In irregular waves, the fact that occasionally the signs of the excitation force and the wave elevation are different means that the procedure may happen to fail during short periods. The most common reason for this is small, rapid oscillations of the outer surface elevation leading to a premature opening of the valve.

7.3. Energy absorption

In the laboratory model, the power loss in the valve plays the role of a PTO, and will be taken to represent the useful power P_u. With the chosen instrumentation, no direct measurement of power is available, but knowing that the air inside the chamber is only slightly compressible, we may approximate the volume flow rate through the valve as directly proportional to the column velocity. We may then estimate the instantaneous useful power dissipated in the valve as $P_u = \Delta p_c Q$, the pressure drop across the valve times the volume flow.

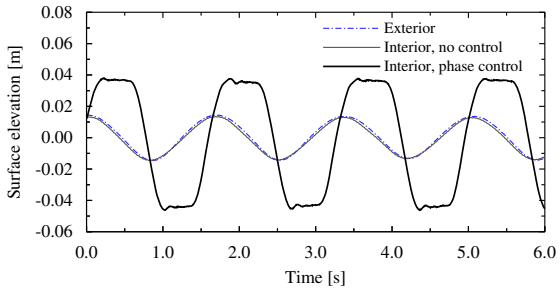

Fig. 7. Measured effect on the surface elevation of the application of phase control at a frequency $f = 0.6$ Hz, equal to about half the resonance frequency, and incident wave height $H = 0.032$ m.

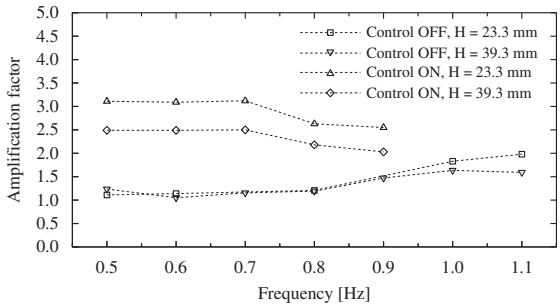

Fig. 8. Amplification factor, for frequencies lower than resonance, for the cases with and without latching control and different incident wave heights.

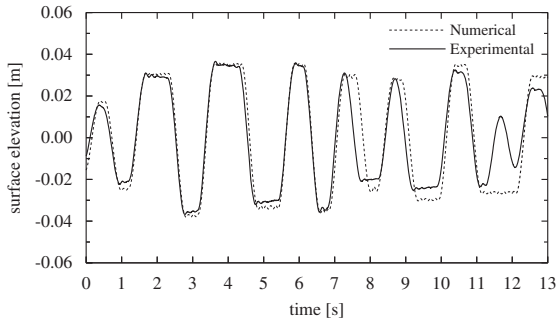

Fig. 9. Effect on the surface elevation of the application of zero-threshold latching control in irregular waves. Incident waves were synthesized from a JONSWAP spectrum with parameters $\gamma' = 3.3$, $T_e = 2$ s, $H_s = 0.05$ m.

This process worked accurately for the runs with constantly open valve, but with latching control the pressure signal became somewhat corrupted due to rapid oscillations of the chamber pressure and probe connections (See Sections 4 and 7.6). As a consequence, it was not possible to process the signal for further use in power calculations. Instead, we decided to use the mathematical model with experimentally fitted parameters (see Section 6) in estimating the pressure drop over the valve as a function of the measured inner-surface velocity. Together with the column velocity (derived from the measured column position) we could then calculate an estimate for P_u as done before.

There are, of course, possible errors introduced by these approximations. In the first place there is, due to air compressibility, a sudden burst of flow through the valve when the valve is opened and before the column has had time to gain velocity. This burst represents a power dissipation, which is ideally only dependent on the initial and final pressures. By simulation we estimated this power dissipation represents at most 6% of the total dissipated power, with an average of about 3%.

Secondly, the actual volume flow rate through the valve might be somewhat different from the one derived from the column velocity. By comparing the estimates of the power dissipation in the laboratory test for the passive valve cases, the difference between the two estimates is found to be up to 30%, but the average deviation is about 6%. With this evaluation carried out, we may have a more detailed, quantitative look at the experimental results.

By comparing the absorbed useful energy with the energy transported by the wave in the flume, the relative capture width (capture width divided by the outer tube diameter) has been calculated for regular wave input as shown in Fig. 10. Close to the resonance frequency, the curves for latching control approach the curves for passive valve runs. As expected, the phase-control effect is to broaden the power response such that the device is able to absorb more efficiently from a wider range of frequencies.

The gain in power absorption achieved by zero-threshold unlatching control strategy is apparent in Fig. 11. We have defined the gain factor as the ratio between the average power absorbed with and without control. It ranges from about 3.7 to numbers as high as 50 for the cases shown. However, these figures must be considered with some caution. Indeed, the pressure drop across the valve of the laboratory model is close to optimal for operation with latching control, whereas a much higher damping (smaller discharge coefficient) would have given higher absorption for the passive valve cases (cf. Section 7.4).

Also worth noticing is the increase in the gain factor with the wave period, i.e. as we get further apart from the eigenperiod of the water column. The point is that the further we go from resonance, the more there is to gain by phase control.

Considering now results for irregular waves, the same algorithms were used as for the regular wave runs, and initially the threshold was set to zero. In Fig. 12 the relative capture widths from these measurements are shown for the cases with and without latching control. The corresponding gains factors are given in Fig. 11. The relative capture width is between 0.004 and 0.02 without control and between 0.038 and 0.067 with control. This gives power gains from 3.5 to 8.8, comparable to the lower range of gains found for the regular wave cases studied.

The same caution applies here as for regular waves regarding the valve's discharge coefficient, which has not been optimized in the experimental set-up. As for the regular wave cases, the relative capture width with control is larger for wave frequencies closer to resonance. Theoretically, in a wave flume and with phase control, the same capture width should be achievable for the whole range of frequencies (below the cross-wave limit), namely equal to half the flume width (Falnes, 2002a, Section 6.4). This is due to the symmetric wave radiation in our set-up, with a maximum absorption equal to 50% of the power transported down the flume. Why does the capture width level off for low frequencies, and why is the capture width not larger?

The answer is viscous damping. If we could avoid the viscous damping completely and adjust the valve damping to optimum, we could achieve a much higher amplification factor, and thus absorb more power, in which case the capture width could approach the theoretical limit. Above a certain level of wave heights, amplitude restrictions would ultimately come into action as the column approached the cylinder ends.

Another factor that could augment the power absorption with the same model would be to make the cylinder submergence smaller. This would increase the radiation ability and hence the excitation force (Newman, 1962), while the viscous losses would remain about the same.

The laboratory model was not optimized with regard to reduction of viscous losses. The sharp edged geometry of our tube evidently must give rise to vortex shedding, which—as shown in Appendix C—dissipates a substantial part of the available power. With more rounded shapes at the tube mouth we would expect lower viscous losses, with increased amplification factors and hence increased valve loss (here, useful power) as a result. This is equivalent to reducing the Keulegan–Carpenter

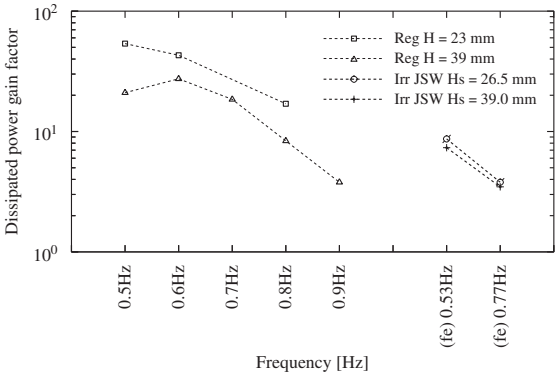

Fig. 11. Gain factor for the average power dissipated in the valve using the zero-threshold unlatching control relative to the corresponding experimental tests without control. The first five points on the horizontal axis refer to regular wave input, whereas the two last points refer to irregular waves synthesized from a JONSWAP spectrum with peakness factor 3.3. Logarithmic scale is used on the vertical axis. The given values for the (significant) wave heights H are average values for all the point on each curve.

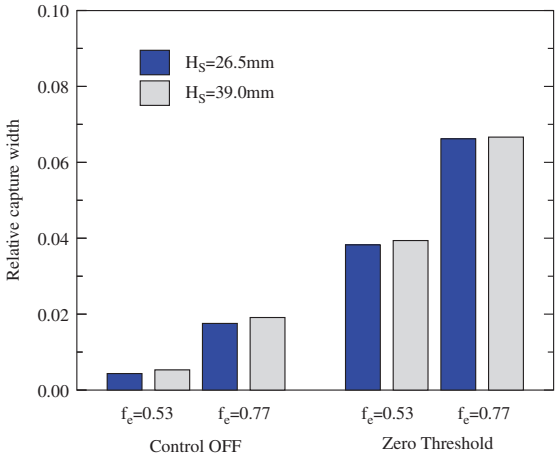

Fig. 12. Experimental results for the capture width, relative to the tube's diameter in irregular waves, with and without zero-threshold latching control. The waves were synthesized from a JONSWAP spectrum of peakness factor $\gamma' = 3.3$.

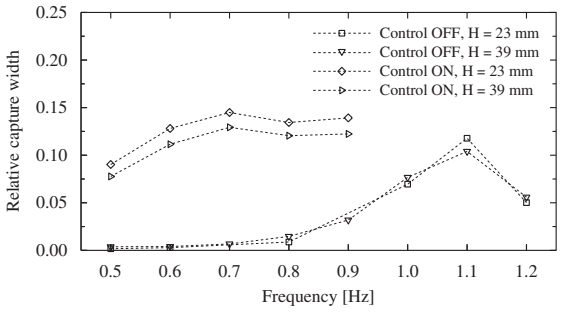

Fig. 10. Capture width relative to the tube's diameter for a range of regular wave inputs, with two different heights of incoming regular waves, for the cases with and without zero-threshold unlatching control. For each curve the wavemaker setpoint for the wave height H has been kept constant across frequencies. The given value for H is an average for the points along each line.

number (see Falnes, 2002a, p. 237), and is important to bear in mind also for full-scale converters of any kind.

7.4. Damping optimization

The word *optimal* is here used to refer to a setting or value that gives the maximum average power-dissipation in the valve under the given conditions. The laboratory model was equipped with a valve and couplings without any means for adjusting the flow restriction. The discharge coefficient was close to optimal for the latching control runs (and at resonance), but excessively large (low damping) for the no-control runs at low frequencies. In order to make a fair comparison between results, numerical simulations were used to find optimal values for the valve discharge coefficient C_{dc} for different input waves and control strategies. This was done by varying the coefficient over a series of runs, and subsequently identifying the optimal value in terms of useful power (i.e. the power dissipated in the valve).

The relative capture width with optimized damping values is given in Fig. 13 for the cases of passive valve and zero-threshold unlatching (see Fig. 15 for irregular wave results). The increase in useful power introduced by the control is here estimated to be up to about 250% in regular waves, and from 150 to 190% in the irregular waves tested, relative to the non-control cases.

Fig. 14 shows how the optimal value for the valve discharge coefficient varies with wave input (see Fig. 15 for irregular wave results). It is clear that the optimal value for the latching control case is relatively constant, and close to the value found around resonance, whereas the passive valve case requires a discharge coefficient that decreases with frequency (corresponding to increased load damping). It is also seen that the optimum depends on the wave amplitude, an effect that stems from the non-linearities in our system.

For the latching control runs, the value of the useful power is quite insensitive to variations in the discharge coefficient. A variation within ±25% for C_{dc} gives a reduction in useful power less than 4% for the latching control case, and less than 7% with no control for the $f = 0.6$ Hz and $H = 30$ mm wave. For the four irregular wave simulations, the variation of the optimum C_{dc} value was 19% for the latching control case and 67% present for the no-control case.

Altogether, these results indicate that, with latching control, a constant discharge coefficient (or load damping) can give a useful power close to maximum, whereas reaching the maximum in the passive case is more dependent on varying the discharge coefficient to harmonize with the instantaneous wave. The reason for this is that with latching control, the phase is being taken care of and the variation in load damping only serves to control the oscillation amplitude. Without control, however, also the phase is

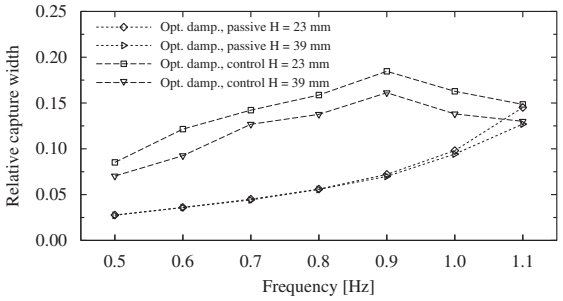

Fig. 13. Calculated relative capture width with optimized damping values in regular waves, with and without zero-threshold latching control.

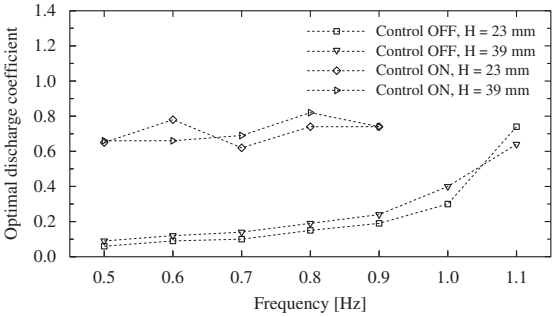

Fig. 14. Optimal discharge coefficient vs. frequency with and without zero-threshold unlatching control in regular waves. The optimal value is chosen as the one giving the largest energy dissipation in the valve for each frequency.

influenced by the level of load damping applied. For off-resonance frequencies, the phase may drastically improve if the damping is sufficiently adjusted. However, in a system designed to operate close to full stroke length, the damping might have to be adjusted also with latching control in order to restrict the oscillation amplitudes.

7.5. Optimizing the threshold

An investigation on how variations of the unlatching threshold influences the performance was carried out in order to identify the best setting for each input wave. For regular waves, the expected optimal setting was used as reference. This reference threshold $\zeta_{th,0}$ is calculated as the value that gives perfect phase match between excitation force and column velocity peaks at each regular wave frequency and height. With the assumption that the column reaches maximum velocity after one quarter eigenperiod (which is quite correct within the relevant range of frequencies), the expression for the reference threshold becomes

$$\zeta_{th,0} = \frac{H}{2}\sin\left[\frac{\pi}{2}\left(1 - \frac{T_0}{T}\right)\right]. \tag{16}$$

For irregular waves, the threshold was calculated as for a regular wave with the same energy period and equivalent power level, i.e. T was replaced by T_e, and H by $H_s/\sqrt{2}$.

Now, at least in regular waves, the maximum energy absorption would be expected to occur at the reference threshold, except that the reference value was not very accurate because it was calculated based on the wave-maker set-point, and not on the actual wave height measured in the flume.

The threshold unlatching strategy starts with the assumption that the wave frequency is lower than the eigenfrequency of the system. As the threshold is increased from zero, the phase difference between the excitation force and the column velocity will get smaller, until we pass perfect phase concurrence and the velocity starts to lead the force. This is illustrated in Fig. 16.

Fig. 17 presents the experimental results for both regular and irregular waves. It may be observed that maximum capture width occurs not far from the reference threshold. Also, a non-zero threshold has increased the energy absorption by about 50% as compared with the zero-threshold run for the chosen regular wave. In irregular waves the improvement was in the range of 27–87%. The larger number corresponds to the lower frequency, which is reasonable, since the misalignment of phases is larger for long period waves.

Furthermore, Figs. 18 and 19 show numerical results for the relative capture width and power gain achieved by optimized threshold and optimized damping (or discharge coefficient)

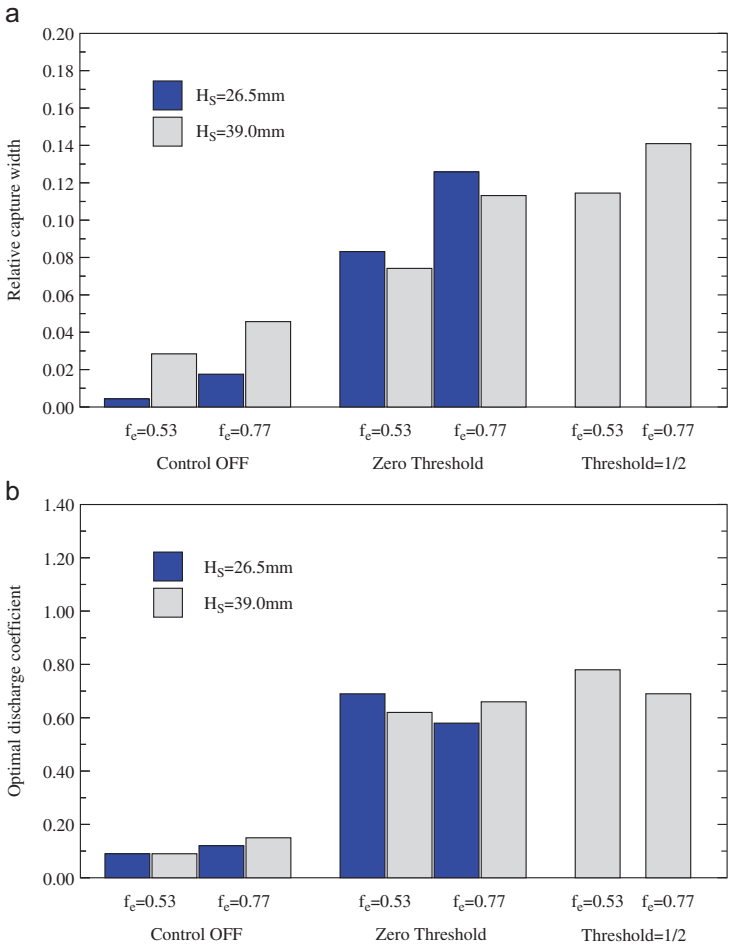

Fig. 15. Relative capture width with optimal damping and irregular waves (upper diagram). The three frequency pairs on the horizontal axis show cases without control (left), threshold equal to zero (middle) and threshold equal to $\frac{1}{2}$ of the reference threshold (right). The lower diagram shows the optimum values for the discharge coefficient C_{dc}.

compared to the simulations with zero-threshold latching control (using the experimentally fitted discharge coefficient, cf. Section 6). They may be compared to Figs. 10 and 11 for the zero threshold and no-control cases. Numerical simulations with an optimized threshold show an increase in the relative capture width in irregular waves between 22% and 55%. This increase becomes 200–350% if compared to optimized results for the passive valve case. As can be seen from Fig. 17, the capture width is not very sensitive to variations in the threshold value around the optimum.

We can conclude that the investigated phase-control strategies are able to increase the power absorption by a substantial amount, in regular as well as irregular waves. Both the experimental and numerical results support this. The introduction of a threshold as trigger for the unlatching event may be an important contribution to the development of a simple and efficient strategy for latching control operation of real-sea devices.

7.6. Rapid pressure oscillations

One of the practical difficulties of implementing a latching control system is dealing with the flow transients originated by an almost instantaneous open/close operation of a shut-off valve. The magnitude of the forces on the floating bodies related to the operation of the latching mechanism may by far exceed the forces originated by the energy extraction, as seen in the experiments described by Falnes and Lillebekken (2003).

In the particular case studied in this paper, the pressure variations in the air chamber associated with the valve operation are much larger than the typical pressure drop across the valve. This fact is illustrated in Fig. 20. During the latched parts of the cycle, the average value of the pressure will be approximately equal to the one needed to balance the head difference between the inner and outer surface level. This is coupled with oscillations at high frequency related to the air-spring stiffness and water column mass, as described in Section 4.

In order to gain an insight in the transient pressure fluctuations upon opening and closing of the valve, the chamber would have to be modelled in more detail. Such fluctuations were captured in the measurements and caused the pressure signals to be unusable for analyzing the column dynamics and for power calculations, as well as an input to the controller.

In the tested system, the resonant frequency calculated from Eq. (15) is between 7 and 9 Hz, depending on the

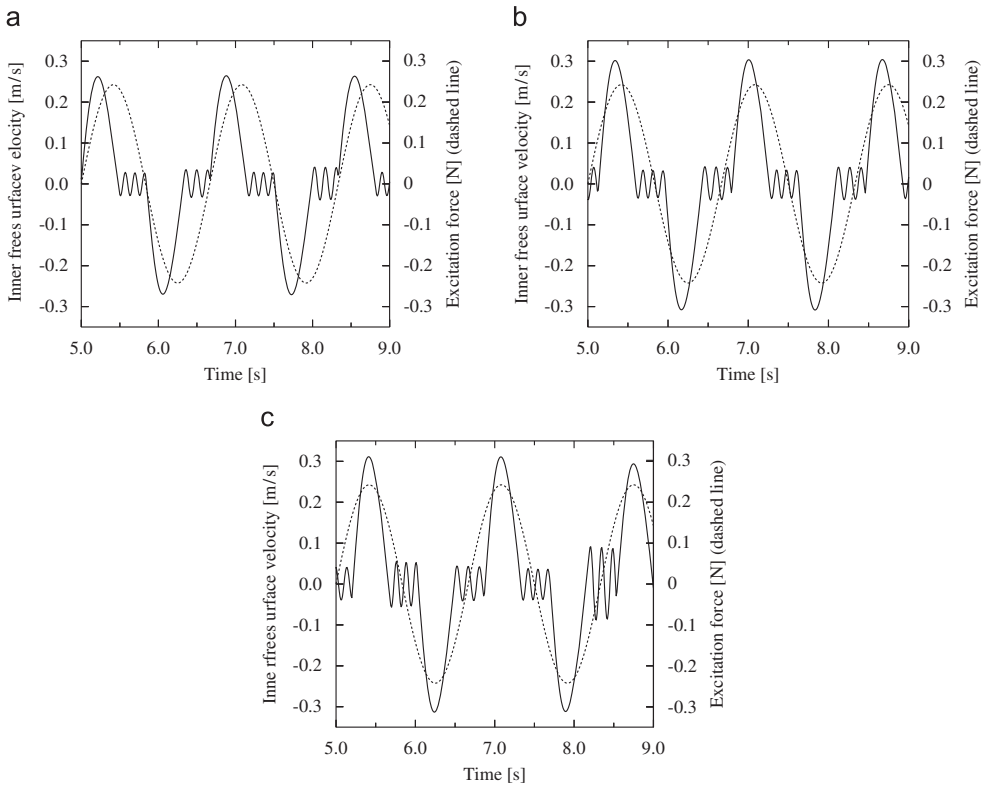

Fig. 16. Excitation force (dashed line) and the corresponding response velocity of the interior free surface, computed by the numerical model. (a) Threshold equal to zero. (b) Threshold equal to $\frac{1}{3}$ of the reference threshold. (c) Threshold equal to the reference threshold. Common incident regular waves with $f = 0.6$ Hz, $H = 23.3$ mm.

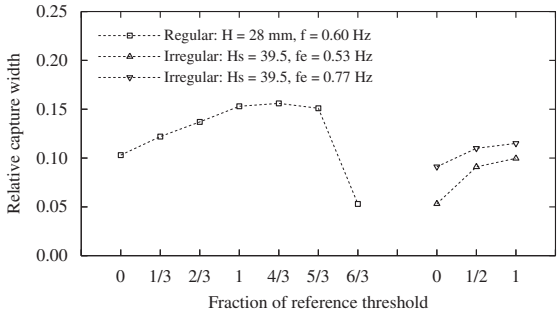

Fig. 17. Experimental results for the capture width relative to the tube's diameter, for cases with threshold latching control. The threshold has been varied from zero to twice the reference threshold in regular waves (left curve), and from zero to the reference threshold for irregular waves (right curves).

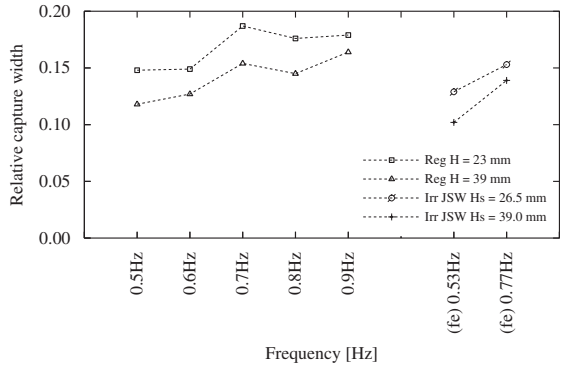

Fig. 18. Numerical results for the capture width, relative to the tube's diameter, using optimized values for the discharge coefficient at each frequency, and an overall best value for the threshold (equal in all cases) chosen by experience.

position of the latched interior water surface. As shown in Fig. 21, the measured frequency of the pressure oscillations, between 6 and 8 Hz, is lower than the calculated one. This difference may have several causes. One of them is the fact that during this oscillation, the inner free surface visibly oscillates in a drum mode, where the amplitude at the center is larger than near the walls, rather than as a uniform axial mode. This is an indication that surface tension is not negligible in the small experimental model. Another factor is the fact that the hydrodynamic characteristics of the system are not so well modelled at such a high frequency. More specifically, the assumptions of a piston type motion and a non-varying added-mass coefficient are not very accurate in the tested model. It was also verified that the fast oscillations in the experimental model were damped more than in the numerical computation, i.e. its oscillation fades faster.

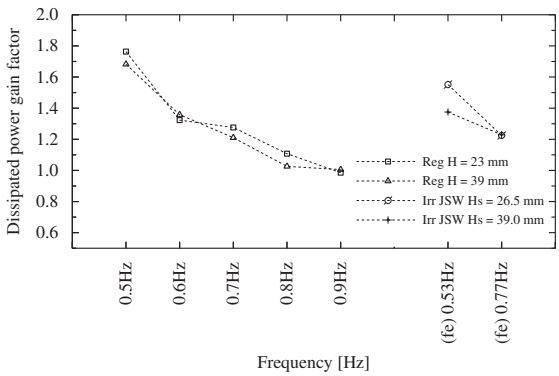

Fig. 19. Numerical results for the gain in energy capture, obtained by applying optimized damping for each frequency and common optimized opening threshold. The reference are the values obtained using the real discharge coefficient estimated for the experimental model together with the zero-threshold unlatching strategy.

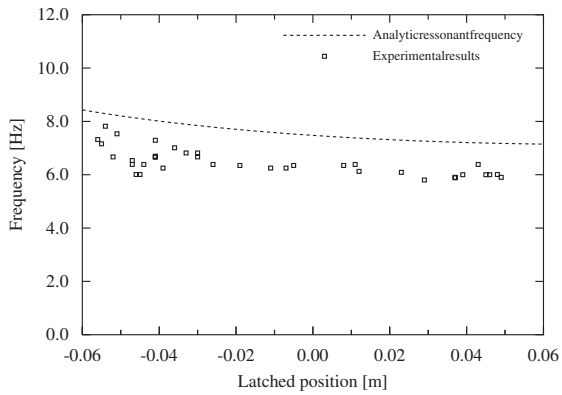

Fig. 21. Frequency of the air pressure oscillations in the chamber during closed-valve periods, when the valve has been closed (or 'latched') at different positions. Each point is measured from an individual period in irregular waves. The curve shows the theoretical value given by Eq. (15).

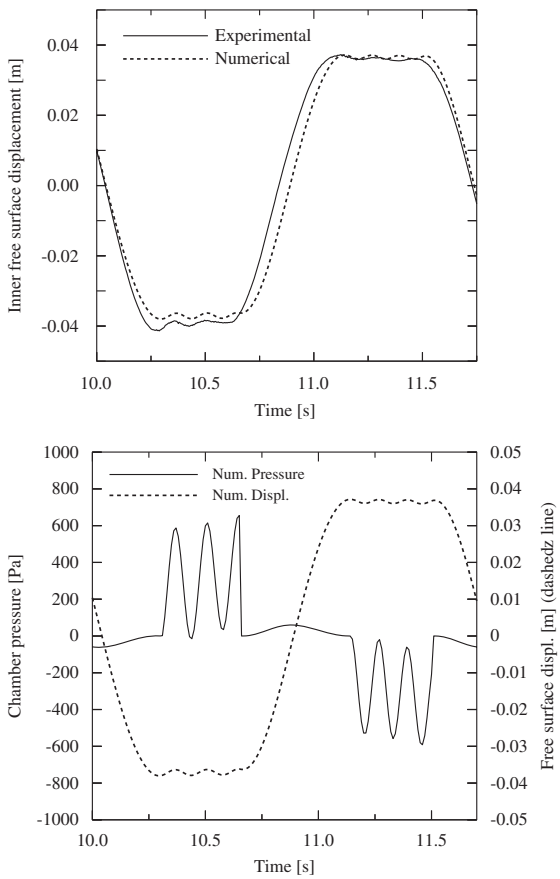

Fig. 20. Upper: comparison of numerical and experimental data for free surface displacement, showing fast oscillations of the free surface during the latched periods. Lower: net chamber pressure $p - p_0$ (estimated from the column motion), showing large pressure variations in the latched parts of the cycle as compared to the pressure amplitude during the parts of the cycle with open valve (for instance between $t = 10.7$ and 11.15 s).

Computing the values for a full-scale system, on the basis of a $\frac{1}{80}$ scale (including for the air chamber geometry), the value of the chamber resonance frequency during the latched periods would be about 20% smaller than the hydrodynamic resonance frequency of the unlatched OWC. This would give the possibility of large dynamic interference if the latching was applied to an OWC. At the same time it would be difficult to achieve firm latching of the water column motion as the chamber's air-spring effect would be very soft at full scale. This is an indication that the application of latching for controlling OWCs may be problematic. The results found in the present work, however, are relevant to point-absorbing devices equipped with other machinery, as the high air-spring stiffness at model scale compares reasonably well to the stiffness found in hydraulic or even mechanical latching mechanisms.

8. Conclusion

The purpose of this work has been to experimentally verify, in irregular waves, a simple phase-control strategy (as the one proposed by Falcão, 2008) for wave energy converters that does not require incident wave prediction. It uses the latching principle, where the motion of the oscillator is halted during parts of the cycle, but has no need for the wave prediction usually tied to control on a wave-to-wave basis. This is achieved by using the measurement of wave elevation as input to the controller, and introducing a threshold value that determines the unlatching instant. Other input signals may also be used for different systems, as long as they are somehow connected to the excitation of the system. Falcão (2008) originally suggested using a pressure measurement as input to the controller, but this did not work in the investigated system due to non-negligible high-frequency pressure oscillations inside the chamber during the latched intervals. The threshold unlatching strategy should be relevant for all converter concepts based on oscillating bodies or water columns, but especially for point absorbers, which tend to have a narrow-banded motion response. The experimental model used was an OWC device, consisting of a fixed tube, terminated at the top by a shut-off valve.

The experimental testing has been accompanied by mathematical modelling and simulation, used for analysis and extended parameter sensitivity variations. The model parameters for

viscous damping and valve pressure drop were estimated by the use of experimental data, and the hydrodynamic parameters were computed from analytical results. Experiments and simulation results were in general found to be in good agreement.

Four different irregular sea states were run, and results show that the investigated control strategies enable the capture width to increase by a factor of 2.5 or more, as compared to running with a passive, open valve. The viscous losses were estimated at 35–60% of the dissipated energy from the wave, depending on the incoming wave and used control, and this limited the relative capture width to about 0.2.

The power output was found to depend only moderately on the threshold value and on the load damping (here, valve discharge coefficient) when using latching control. This makes the threshold unlatching strategy a promising candidate for the development of a simple and high-yield controller for latching control operation in real-sea conditions. Further work will include comparison to other control strategies and application to other systems. The effect of rapid oscillations that occur due to the abrupt operation of the latching mechanism will have to be assessed separately for each system.

Acknowledgments

This work has been partially supported by IDMEC and the Portuguese Foundation for Science and Technology (Ph.D. Grants SFRH/BD/29275/2006, SFRH/BD/35295/2007 and Contract no. PTDC/EME-MFE/66999/2006). The authors thank the LHRH in IST for the use of the wave flume. The authors acknowledge the help from Victor Sena of the LHRH and Prof. Gil Marques of DEEC – IST in the design of the experimental model. The authors acknowledge the valuable input from Prof. Em. Johannes Falnes at NTNU.

Appendix A. Fitting of model parameters

The parameter fitting was done in two sets of experiments. In the first set, the objective was to determine the coefficients c_1 and c_2 that describe the water viscosity effects in the experimental model. To achieve this, a set of experiments were performed for the case when the plate with the valve was not present. The inverse amplification factor (*IAF*), defined as the ratio between the incoming wave height and the water column excursion inside the tube, was measured for regular waves and analyzed. By manipulating the equations of the mathematical model, keeping only terms relevant for the open tube case, and assuming the hydrodynamics of the column to be approximately linear, we arrive at the following expression for *IAF*:

$$\mathrm{IAF}^2 = \frac{\omega^2}{F_e}[(b_r(\omega)+c_1)^2 + (\omega a_r(\omega) - S/\omega)^2 + 2(b_r(\omega)c_2\omega|\dot{\eta}|) + c_2^2\omega^2|\dot{\eta}|^2]. \quad (17)$$

Estimates for the viscous force coefficients were found at each frequency by fitting a second-degree polynomial to the experimental data and using hydrodynamic coefficients from numerical calculation (similar to the one presented in Lopes et al., 2007). This method is rough and only valid when the non-linear effect is weak, but nevertheless it was found to be useful for the fitting of the model parameters.

A total of 20 regular wave experiments, covering five wave height settings and four wave frequencies, were run. In the analysis, the measured wave height (averaged over individual waves) was used to compute the amplification factor for each time series. An average of the coefficient values found for frequencies close to resonance was chosen for use in the remaining work, as this was believed to be most accurate due to the larger amplitudes. In Fig. 22 the laboratory results are compared with numerical simulation using the final parameter settings.

If the system behaved linearly the curves in the diagram would be horizontal. We observe that the non-linearity appears most clearly when the amplification factor is high, i.e. close to resonance, as expected.

The second set of experiments was run with the top plate and air valve in place. The fitting of the C_{dc} coefficient is more complicated as the Reynolds number of the oscillating flow through the valve typically reaches only up to about 8000 at peak velocity. This means that the flow through the orifice always works in or close to the transition regime, with switching between laminar and turbulent flow. The use of a constant parameter may then become insufficient. In spite of this it was decided to simply assume a pressure loss quadratic in the flow velocity in order to avoid a more complex model.

The same 20 regular wave inputs were run again for fitting of the valve discharge coefficient C_{dc}. The pressure/flow

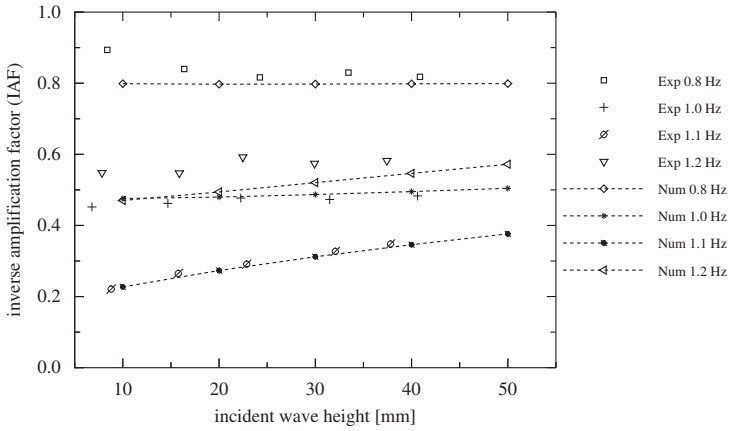

Fig. 22. Inverse amplification factor (IAF) for laboratory measurements and numerical simulation results.

characteristic of the valve, or more correctly the valve with connections and entrance geometries, was then investigated by assuming small air compressibility effect and estimating the volume flow rate directly from the column motion. It was found that the relation was slightly non-symmetric, and also had a slight break in the curve. We interpreted the non-symmetry as being due to the non-symmetric geometry of the valve set-up, and the 'notch' to be caused by the transition between laminar and turbulent flow, as mentioned above.

It was found that assuming a purely quadratic relation and minimizing the deviation between laboratory measurements and numerical simulations yielded good results. In order to find a best value to use for C_{dc}, the sum of squared differences between the numerical and experimental values for the column elevation was calculated with different settings for the discharge coefficient. The results for each run were added to obtain a gross measure of the deviation. This gave a convex curve of deviation vs. discharge coefficient. From the curve a minimizing value of $C_{dc} = 0.69$ was found, and this was used as default value in the simulation runs reported herein.

Appendix B. Accuracy of the numerical model

The deviation between the measured and simulated responses have been characterized by a relative standard deviation $r = d_{num-lab}/\sigma_{lab}$. Here, $d_{num-lab} = [\sum_{i=1}^{N}(\eta_{num} - \eta_{lab})^2/(N-1)]^{1/2}$ is the deviation between the simulated and measured response defined in a standard deviation fashion, and σ_{lab} is the standard deviation of the laboratory measurement itself.

This measure will equal 0 if the data coincide, and 1 if we have perfect phase match but double amplitude. A perfect amplitude match but with a phase difference of $\pi/2$ would give $r = \sqrt{2}$. For the vertical displacements the numerical model reproduces the measured data within about $r = 25\%$ with better fit for the lower frequencies and higher wave amplitudes, as shown by Fig. 23.

For comparison, the relative deviation in amplitude has been calculated, and it has an average value of about 5%.

The deviations in pressure are somewhat larger, as can be seen in Fig. 24. Here the values for the relative standard deviation span from about 20 to 50%.

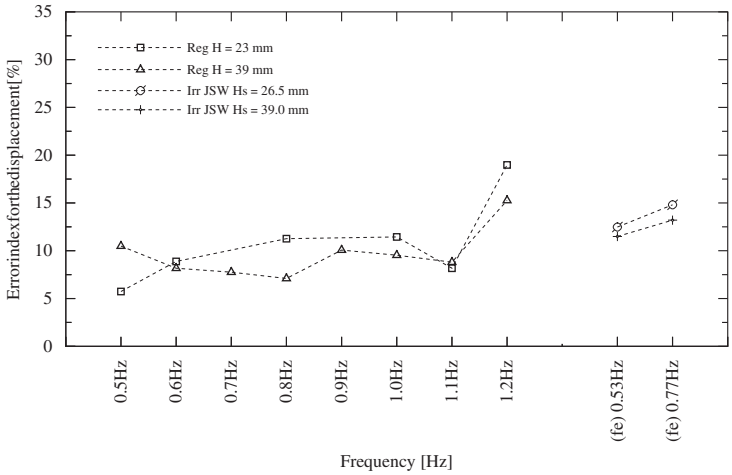

Fig. 23. Error index of the numerical predictions for the free surface displacement (%). Passive cases.

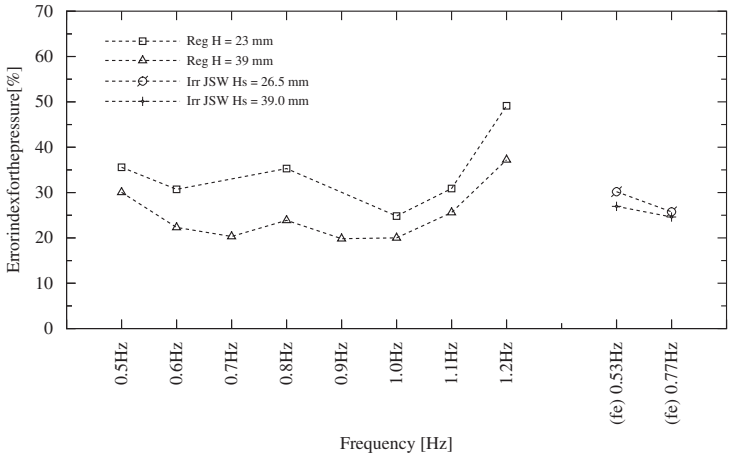

Fig. 24. Error index of the numerical predictions of pressure in the chamber (%). Passive cases.

The obstacles to further reduction in these deviations are the assumptions made in the modelling of the system. Significant reductions would require taking account for (i) the frequency dependency of viscous losses, (ii) the flow regime in the valve, (iii) the change in column mass with the oscillation amplitude, and (iv) the transition between open and closed position of the valve for cases with latching control.

Although there are deviations, the overall observed effects are well captured by the mathematical model. The dependence on wave amplitude and frequency is reproduced, with resonances both due to hydrostatic stiffness and air compressibility. The effect of applying latching control with varying thresholds is the same both in measurements and simulations.

Appendix C. Distribution of dissipated power

Figs. 25 and 26 show how the power is distributed between valve loss, viscous loss and radiation for the cases with and

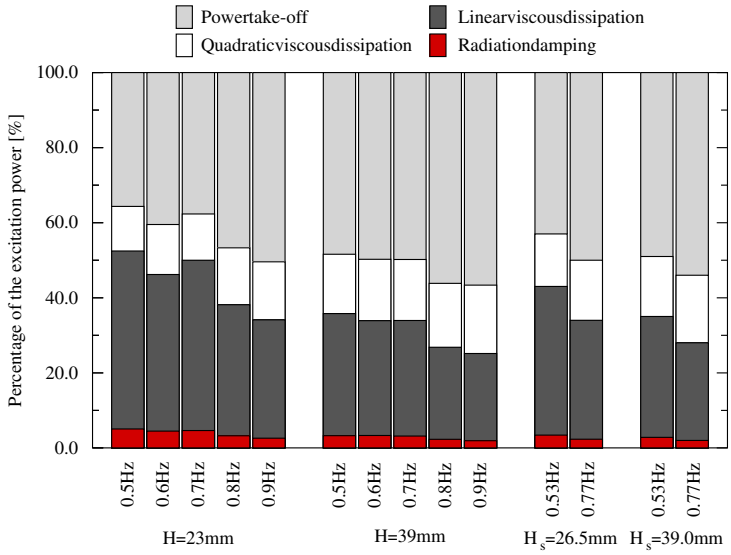

Fig. 25. Distribution of average dissipated power without control. The two bar groups to the left refer to regular incident waves for two different wave height setpoints, and the two groups to the left refer to irregular waves synthesized from a JONSWAP spectrum of peakness factor 3.3. The parameters are then the significant wave height H_s and the energy frequency f_e. The bars show distribution of average power in valve loss (quadratic), viscous damping (quadratic and linear terms) and radiated power, as a fraction of the total excitation power $\overline{F_e(t)\dot{\eta}(t)}$.

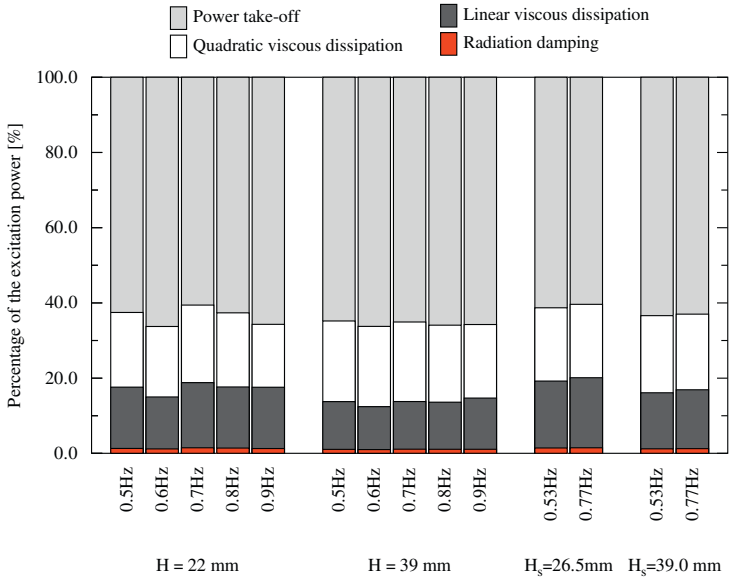

Fig. 26. Same as Fig. 25 with zero-threshold unlatching control.

without latching control, respectively. The viscous losses have a larger share for the non-controlled cases, and amount to between 35% and 60%. The rest is mainly valve loss, as the radiation term is always below 10% of the total power.

The relative importance of the square viscous loss becomes larger in the case of latching control, as would be expected since then velocity amplitudes are larger. The same argument goes also for the relative importance of the valve loss.

The radiation term F_R in Eq. (6) times the velocity represents the power in the radiated waves due to the water column motion. For a linear system, the maximum energy absorption is obtained when the load power plus losses equals the radiated power, and the maximum useful power is obtained for a somewhat smaller oscillation amplitude (i.e. larger damping) (Falnes, 2002a). In our case with a large viscous loss, we expect the maximum useful power to result from rather strong damping and thus small radiation. This agrees with the distribution shown in Figs. 25 and 26.

References

Babarit, A., Clement, A., 2006. Optimal latching control of a wave energy device in regular and irregular waves. Applied Ocean Research 28 (2), 77–91.

Bjarte-Larsson, T., Falnes, J., 2006. Laboratory experiment on heaving body with hydraulic power take-off and latching control. Ocean Engineering 33, 847–877.

Bjarte-Larsson, T., Lillebekken, P.M., Hals, J., Falnes, J., 2002. Model experiment on an OWC-type wave-energy converter with hydraulic power take-off. In: Proceedings of the 21st International Conference on Offshore Mechanics and Arctic Engineering, Oslo, Norway, pp. 23–28.

Budal, K., Falnes, J., 1982. Wave power conversion by point absorbers: a Norwegian project. International Journal of Ambient Energy 3 (2), 59–67.

Budal, K., Falnes, J., Hals, T., Iversen, L., Onshus, T., 1981. Model experiment with a phase controlled point absorber. In: Proceedings of the 2nd International Symposium on Wave and Tidal Energy, Cambridge, England.

Budal, K., Falnes, J., Kyllingstad, Å., Oltedal, G., 1979. Experiments with point absorbers in regular waves. In: Proceedings of the First Symposium on Wave Energy Utilization, Gothenburg, Sweden, pp. 1275–1295.

Controllab Products B.V., 2008. 20-sim version 3.6 ⟨http://www.20sim.com/⟩.

Delauré, Y.M.C., Lewis, A., 2003. 3D Hydrodynamic modeling of fixed oscillating water column wave power plant by a boundary element method. Ocean Engineering 30, 309–330.

Durand, M., Babarit, A., Pettinotti, B., Quillard, O., Toularastel, J.L., Clément, A.H., 2007. Experimental validation of the performances of the SEAREV wave energy converter with real time latching control. In: Proceedings of the 7th European Wave and Tidal Energy Conference, Porto, Portugal.

Evans, D., 1978. The oscillating water column wave energy device. Journal of the Institute of Mathematics and its Applications 22, 423–433.

Evans, D.V., 1982. Wave-power absorption by systems of oscillating surface pressure distributions. Journal of Fluid Mechanics 114, 481–499.

Falcão, A.F. de O., 2007. Modelling and control of oscillating-body wave energy converters with hydraulic power take-off and gas accumulator. Ocean Engineering 34, 2021–2032.

Falcão, A.F. de O., 2008. Phase control through load control of oscillating-body wave energy converters with hydraulic PTO system. Ocean Engineering 35, 358–366.

Falcão, A.F.de O., Justino, P.A.P., 1999. OWC wave energy devices with air flow control. Ocean Engineering 26, 1275–1295.

Falnes, J., 1995. On non-causal impulse response functions related to propagating water waves. Applied Ocean Research 17, 379–389.

Falnes, J., 2002a. Ocean Waves and Oscillating Systems: Linear Interactions Including Wave-energy Extraction. Cambridge University Press, Cambridge.

Falnes, J., 2002b. Optimum control of oscillation of wave-energy converters. International Journal of Offshore and Polar Engineering 12 (2), 147–155.

Falnes, J., Budal, K., 1978. Wave-power absorption by point absorbers. Norwegian Maritime Research 6 (4), 2–11.

Falnes, J., Lillebekken, P., 2003. Budal's latching-controlled-buoy type wave-power plant. In: Proceedings of the 5th European Wave Energy Conference, Cork, Ireland.

Gieske, P., 2007. Model predictive control of a wave energy converter: Archimedes wave swing. Master's Thesis, Delft University of Technology.

Hoskin, R.E., Nichols, N.K., 1986. Latching control for a point absorber wave-power device. Technical Report NA1/86, Department of Mathematics, University of Reading.

Jefferys, E.R., 1984. Simulation of wave power devices. Applied Ocean Research 6 (1), 31–39.

Jefferys, R., Whittaker, T., 1986. Latching control of an oscillating water column device with air compressibility. In: Evans, D.V., Falcão, A.F.de O. (Eds.), Hydrodynamics of Ocean Wave Energy Utilization. Springer, Berlin, pp. 281–291.

Korde, U.A., 2002. Latching control of deep water wave energy devices using an active reference. Ocean Engineering 29 (11), 1343–1355.

Lopes, M.F.P., Ricci, P., Gato, L.M.C., Falcão, A.F.de O., 2007. Experimental and numerical analysis of the oscillating water column inside a surface piercing cylinder in regular waves. In: Proceedings of the 7th European Wave and Tidal Energy Conference, Porto, Portugal.

Michel, W.H., 1999. Sea spectra revisited. Marine Technology 36 (4), 211–227 sea spectrum function; Rayleigh distributions.

Mundon, T., Murray, A., Hallam, J., Patel, L., 2005. Causal neural control of a latching ocean wave point absorber. In: Artificial Neural Networks: Formal Models and their Applications—ICANN 2005 15th International Conference. Proceedings, Part II. Lecture Notes in Computer Science, vol. 3697. Springer, Berlin, pp. 423–429.

Newman, J.N., 1962. The exciting forces on fixed bodies in waves. Journal of Ship Research 6, 10–17.

Perdigão, J.N.B.A., 1998. Reactive-control strategies for an oscillating-water-column device. Ph.D. Thesis, Universidade Técnica de Lisboa, Instituto Superior Técnico.

Sarmento, A.J.N.A., Falcão, A.F.de O., 1985. Wave generation by an oscillating surface-pressure and its application in wave energy extraction. Journal of Fluid Mechanics 150, 481–499.

Schoen, M.P., Hals, J., Moan, T., 2008a. Robust control of heaving wave energy devices in irregular waves. In: Proceedings of the 16th Mediterranean Conference on Control and Automation, Ajaccio, France.

Schoen, M.P., Hals, J., Moan, T., 2008b. Wave prediction and fuzzy logic control of wave energy converters in irregular waves. In: Proceedings of the 16th Mediterranean Conference on Control and Automation, Ajaccio, France.

Taghipour, R., Perez, T., Moan, T., 2007. Hybrid frequency–time domain models for dynamic response of marine structures. Ocean Engineering 35, 285–705.

The Mathworks Inc, 2008. Matlab version 7.4 ⟨http://www.mathworks.com/⟩.

Valério, D., Beirão, P., da Costa, J.S., 2007. Optimisation of wave energy extraction with the Archimedes wave swing. Ocean Engineering 34, 2330–2344.

Weber, J., 2007. Representation of non-linear aero-thermodynamic effects during small scale physical modeling of OWC wave energy converters. In: Proceedings of the 7th European Wave and Tidal Energy Conference, Porto, Portugal.

Article D: Hals et al., accepted for pulication in Journal of OMAE

Constrained Optimal Control of a Heaving Buoy Wave Energy Converter

Jørgen Hals*, Johannes Falnes, and Torgeir Moan
Centre for Ships and Ocean Structures (CeSOS)
Norwegian University of Science and Technology (NTNU)
Otto Nielsens v. 10
7491 Trondheim, Norway

February 23, 2009

Abstract

The question of optimal operation of wave energy converters has been a key issue since modern research on the topic emerged in the early 1970's, and criteria for maximum wave energy absorption soon emerged from frequency domain analysis. However, constraints on motions and forces give the need for time-domain modelling, where numerical optimisation must be used to exploit the full absorption potential of an installed converter.

A heaving, semi-submerged sphere is used to study optimal constrained motion of wave-energy converters. Based on a linear model of the wave-body interactions, a procedure for the optimisation of the machinery force is developed and demonstrated. Moreover, a model-predictive controller is defined and tested for irregular sea. It repeatedly solves the optimisation problem online in order to compute the optimal constrained machinery force on a receding horizon. The wave excitation force is predicted by use of an augmented Kalman filter based on a damped harmonic oscillator model of the wave process.

It is shown how constraints influence the optimal motion of the heaving wave-energy converter, and also how close it is possible to approach previously published theoretical upper bounds. The model-predictive controller is found to perform close to optimum in irregular waves, depending on the quality of the wave force predictions. An absorbed power equal to or larger than 90 % of the ideal constrained optimum is achieved for a chosen range of realistic sea states.

Under certain circumstances the optimal wave energy absorption may be better in irregular waves than for a corresponding regular wave having the same energy period and wave-power level. An argument is presented to explain this observation.

Key words: Reactive control, amplitude constraints, wave prediction, model-predictive control

*Corresponding author, e-mail:jorgen.hals@ntnu.no, phone: +47 97 66 00 28

Nomenclature

$\mathbf{\Phi}$	oscillator system matrix [1]
$\mathbf{\Gamma}$	matrix of the objective function's quadratic term [elementwise SI units]
ρ	water density [kg/m^3]
η	heave position [m]
λ	wave length [m]
λ	damping coefficient [1]
ω	angular frequency [rad/s]
$\mathbf{A}$	system matrix, dynamic model [elementwise SI units]
$\bar{\mathbf{A}}$	system matrix, kinematic model [elementwise SI units]
$\mathbf{A}_r$	system matrix, F_r model [1]
A_w	water plane area [m^2]
$\mathbf{B}$	input matrix, dynamic model [elementwise SI units]
$\bar{\mathbf{B}}$	input matrix, kinematic model [elementwise SI units]
$\mathbf{B}_r$	input matrix, F_r model [s/m]
B_r	radiation resistance [Ns/m]
$\mathbf{C}$	output matrix, dynamic model [elementwise SI units]
$\bar{\mathbf{C}}$	output matrix, kinematic model [elementwise SI units]
C_b	hydrostatic stiffness [N/m]
$\mathbf{C}_r$	output matrix, F_r model [N]
E_a	absorbed energy [J]
F	force [N]
F_e	wave excitation force [N]
F_m	machinery force [N]
F_r	radiation force [N]
$\check{\mathbf{F}}$, $\mathbf{F}$	prediction system matrix [elementwise SI units]
$\check{\mathbf{G}}$, $\mathbf{G}$	prediction input matrix [elementwise SI units]
H	wave height [m]
H_s	significant wave height [m]
J, J'	Objective function [m^2/s^2]
J_E	wave power level [W/m]
N	Number of time steps in prediction horizon [1]
P_a	absorbed power [W]
P_e	excitation power [W]
P_l	power loss [W]
P_r	radiated power [W]
$\mathbf{R}$	constraint matrix [elementwise SI units]
T	wave period [s]
T_0	resonance period [s]
T_e	energy period [s]
T_h	Optimisation horizon [s], $T_h = N\,T_s$. For the MPC controller this is the length of the receding horizon.
T_s	time step for discretisation [s]
V	buoy volume [m^3]

$\mathbf{c}$	constraint vector [elementwise SI units]
c_F	force coefficient [N]
d	buoy diameter [m]
d_a	absorption width [m]
$\hat{\mathbf{f}}$	vector of force predictions [N]
f_c	controller update rate [Hz]
g	acceleration of gravity [m/s^2]
$k(t)$	radiation force retardation function function [N/m]
k	discrete-time step number [1]
k	wave number [1/m]
m_b	mass of buoy [kg]
m_∞	added mass at infinite frequency [kg]
t	time [s]
v	heave velocity [m/s]
v_n	oscillator measurement noise [N]
$\hat{\mathbf{v}}$	vector of velocity predictions [m/s]
u	non-dimensional oscillator velocity [1]
$\mathbf{w}$	kinematic model state vector [elementwise SI units]
$\mathbf{w}_n$	oscillator input noise [1]
x	non-dimensional oscillator position [1]
$\mathbf{x}$	dynamic model state vector [elementwise SI units]
$\mathbf{y}$	output vector
$\mathbf{z}$	state vector for the F_r state-space model [1]

Subscripts and superscripts

$\hat{}$	vector of discrete predictions
$\check{}$	relating to the kinematic model
ct	continuous time
dt	discrete time
ideal	using exact information about the future excitation
IR	irregular wave
kalman	using a Kalman filter predictor for the excitation
lb	lower bound
max,min	maximum and minimum
n	noise
opt	optimal
r	radiation
R	regular wave
ref	reference signal
$^{\mathrm{T}}$	matrix transpose
ub	upper bound

1 Introduction

One of the early results of wave energy research was the condition for maximum absorption of the energy carried by ocean waves incident to an absorbing, oscillating body. It was shown [cf. review articles by Evans [1] and Falnes [2]] that the maximum occurs when the machinery impedance cancels the intrinsic impedance of the mechanical wave-body system, i.e. when the body and its machinery resonates with the incident wave and also has the correct level of resistance to motion. Their results were based on a linear description of the wave-body interactions, and were derived by a frequency domain approach. The terms complex-conjugate control and reactive control were adopted to describe this situation of optimal operation [3, 4, 5]. The latter of these terms is the more general, since it can also be used to describe situations with constraints.

In regular waves such control is straight forward, but in irregular waves it becomes non-causal [6]. Causal frequency domain approximations for feedback control have been proposed by several authors, e.g. [7, 8, 9, 10, 11]. One effect of these approximations is that the controller fails to be optimal on a wave-to-wave time scale. It only optimises the average absorption on the same time scale as the controller parameters are updated, which is typically on a wave group or sea state time scale.

A slightly suboptimal control strategy has been short-time latching of the body motion, which focuses on the phase alignment of the oscillation velocity with the excitation force for each single wave [12]. In implementation it is, however, also challenged by non-causality when computing optimal unlatching instants and the machinery's optimal resistance level. An extensive study of the latching control strategy was carried out by Babarit [13], looking both at analytical and numerical approaches. Practical, sub-optimal methods for overcoming the non-causality problem with latching control have recently been suggested by Falcão [14] and Lopes *et al.* [15].

When implementing a control strategy for a real device, constraints on motion amplitudes, machinery forces and possibly other features must be taken into account. Some theoretical considerations on this topic using frequency domain analysis were given by Evans [16], and later expanded by Pizer [17] and Falnes [18]. In these works global amplitude constraints were imposed on the energy conversion achieved with a system of several oscillating bodies and oscillation modes per body. Backer *et al.* [19] presented numerical results for a heaving buoy under various restrictions imposed in their frequency-domain model, including excursion amplitude, machinery force and a measure used to reduce the probability of water slamming on the buoy, and showed how these influenced the maximum average that could be absorbed by the buoy using a state feedback controller.

If the future excitation force is assumed to be known, a time-domain optimisation of the motion may be formulated. Constraints may then be included as a part of the optimisation problem as shown by Eidsmoen [20], who gave a continuous-time formulation where constraints were included as penalty terms in the cost function. When both the model and constraints are linear and the objective function is quadratic, the problem may be discretised and cast into what is known as a quadratic program (QP), for which many numerical methods and tools are available [21].

A family of control methods that is particularly well suited for handling constraints as a part of the control problem is the various concepts known as model-predictive control

(MPC), see e.g. [22]. While the basic formulation of the MPC methods were developed in the 1960s, they came to extensive use within the process industry during the 1980s. There these methods enabled optimisation of the production within a set of constraints, which could, for instance, be capacity, throughput or environmental limitations. In the following decades, they have been brought to use in an increasing number of fields [23].

The MPC method essentially involves an optimisation problem like the one we have outlined for time-domain constrained optimisation, where the operator or designer has specified the constraints and the function to be optimised. This function may include energy use, time spent, a reference for the output to follow, the expected profit based on market price, or other. A discrete-time model of the process serves as a basis for the optimisation problem, which is solved at each update of the control signal. The states of the system model are updated by measurements, and this makes the controller quite robust with regards to model errors.

By applying the MPC technique to ocean wave energy devices as proposed by Gieske [24], it is possible to develop a controller that maximises the energy conversion within constraints set by the machinery and its auxiliaries. The prerequisite is that the controller is supplied with a sufficiently accurate on-line prediction of the wave excitation force. Price *et al.* [25] discuss the need for knowledge of the future wave excitation in computation of the optimal control command. They introduce the concept of *premonition time* as the difference between the period of required knowledge of the future signal and the duration of available knowledge. It depends on two factors: the geometry of the device, and the sea state. Up to a certain time span into the future, knowledge can be made available by prediction based on local data, i.e. at or in the immediate vicinity of the buoy position. In cases where this is not enough to reduce the premonition time to zero, the future knowledge required for optimal control can only come from information gathered at a remote location.

The present paper applies a time-domain approach to the constrained optimal control of wave-energy converters. Section 2 deals with the hydrodynamic model of a heaving semi-submerged sphere, used as an example in this work. A QP problem is formulated for the optimal motion in Section 3. Its solution is studied by regular wave examples, although applicable also to irregular waves. In Section 4 the results from Section 3 are used in a discussion of the Budal diagram, which is used to express the theoretical limits of absorbed power for a fixed body volume. The diagram is extended to a bounding surface incorporating both wave period and amplitude as variables.

Finally, a model-predictive controller for the heaving sphere is defined in Section 5, and simulation results for its performance in irregular waves are presented and discussed. An excitation force predictor is defined using an augmented Kalman filter with a harmonic oscillator model for the wave process. The influence of optimisation horizon and accuracy on the converter performance is investigated. The predictor uses only local measurements for the filter updates. It is similar to the one implemented already by Budal *et al.* [26].

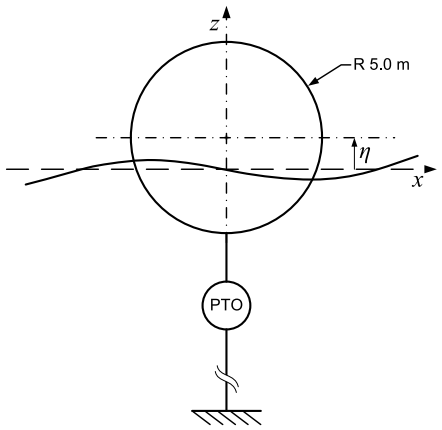

Figure 1: A heaving sphere of radius 5.0 m is used as an example of a point absorber. It is semi-submerged at equilibrium, and connected to the bottom through a power take-off machinery (PTO), which in its most general form can act instantaneously with any vertical force on the sphere. The heave excursion from the equilibrium position is given by $\eta(t)$ and the heave velocity by $v(t) = \dot{\eta}(t)$.

2 Hydrodynamic characteristics of the example converter

A heaving semi-submerged sphere reacting against a fixed reference is used as wave-absorbing body, as sketched in Figure 1. Only the heave mode is considered and linear approximation of hydrodynamic forces in deep water is used. Moreover, the sphere is restricted to move only 3 m in each direction.

In the mathematical model the gravity, buoyancy, inertia, radiation and wave excitation forces are taken into account. No losses are included, and the wave elevation and motions are assumed to be small. By assuming a constant water-plane area A_w for the sphere, the hydrostatic stiffness coefficient may be written as $C_b = \rho g A_w$, with ρ being the water density and g the acceleration of gravity. As long as the incoming waves are small and the oscillation amplitude η is restricted to $|\eta| \leq 3\,\mathrm{m}$, this approximation keeps force errors within $\pm 6\,\%$ [27].

The reaction force due to radiation may be written as

$$F_\mathrm{R} = m_\infty \ddot{\eta}(t) + \int_{-\infty}^{t} k(t-\tau) v(\tau)\, d\tau \equiv m_\infty \ddot{\eta}(t) + F_r(t), \tag{1}$$

where m_∞ denotes the asymptotic value of added mass at infinite frequency and $v(t) = \dot{\eta}(t)$ is the vertical velocity. The convolution part also contains the retardation function $k(t)$, which can be computed by boundary element methods [28, 29] or approximated using analytical solutions existing for the geometry [30, 31]. It is shown in Figure 2. In this paper *radiation force* refers to the convolution term, denoted by F_r. A reasonable state-space approximation for F_r can be achieved with a state-space model of order four by methods as described e.g. by

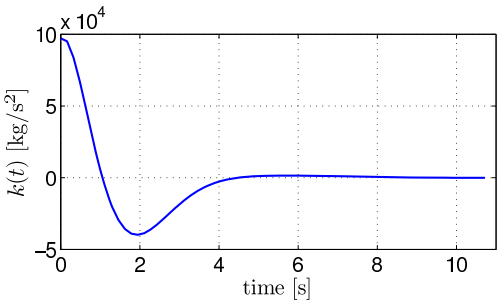

Figure 2: Retardation function $k(t)$ for the heaving sphere, sometimes also referred to as the *memory kernel*. Convoluted with the velocity it gives the radiation force $F_r(t)$ (see e.g.[34], Section 5.3).

Jefferys [32] and Taghipour *et al.* [33]. The convolution integral is then represented by a four-dimensional vector equation:

$$\dot{\mathbf{z}}(t) = \mathbf{A}_r\mathbf{z}(t) + \mathbf{B}_r v(t) \tag{2}$$

$$F_r = \mathbf{C}_r\mathbf{z}(t) \tag{3}$$

Throughout the article, boldface lowercase letters will be used to denote vectors, and boldface uppercase letter to denote matrices. The radiation model's state vector $\mathbf{z} \in R^{4\times1}$ (matrix of real numbers having four rows and one column) is dimensionless and has no physical meaning on its own, and $\mathbf{A}_r \in R^{4\times4}$, $\mathbf{B}_r \in R^{4\times1}$ and $\mathbf{C}_r \in R^{1\times4}$ are the system, input and output matrices, respectively. This subsystem for the radiation force, which has velocity as its input and radiation force as output, can now be included as a part of models describing the motion of the heaving buoy.

In the optimisation problem to be formulated in Section 3 we shall need two kinds of models; one that only describes the kinematic relations for the body motion, and one that incorporates the dynamic equations describing forces and acceleration. The kinematic model has the state vector $\mathbf{w} = [\eta \quad \mathbf{z}^{\mathrm{T}}]^{\mathrm{T}} \in R^{5\times1}$ (superscript T here denotes the transpose of a matrix). Further, it has velocity $v = \dot{\eta}$ as input, and simply relates the heaving body's position η and radiation force F_r to its velocity v:

$$\dot{\mathbf{w}}(t) = \begin{bmatrix} 0 & \mathbf{0}_{1\times4} \\ \mathbf{0}_{4\times1} & \mathbf{A}_r \end{bmatrix} \mathbf{w}(t) + \begin{bmatrix} 1 \\ \mathbf{B}_r \end{bmatrix} v(t) \equiv \bar{\mathbf{A}}\mathbf{w}(t) + \bar{\mathbf{B}}v(t) \tag{4}$$

$$\mathbf{y}(t) = \bar{\mathbf{C}}\,\mathbf{w}(t) \tag{5}$$

The output matrix $\bar{\mathbf{C}} \in R^{1\times5}$ must be tailored to give the desired output $\mathbf{y}(t)$, which here typically is the position ($\bar{\mathbf{C}} = [\,1 \quad \mathbf{0}_{1\times4}\,]$) or the radiation force ($\bar{\mathbf{C}} = [\,0 \quad \mathbf{C}_r\,]$).

The second model is the dynamic equations for the heaving sphere. It includes, in addition, the linear momentum $p = m_b v$ as state variable, and it has the machinery force F_m and the excitation force F_e as inputs. The full set of motion equations for our model of

the heaving sphere, under the assumptions made, are now [11]:

$$\begin{aligned}
\dot{\mathbf{x}}(t) &= \begin{bmatrix} 0 & \frac{-C_b}{1+m_\infty/m_b} & \frac{-\mathbf{C}_r}{1+m_\infty/m_b} \\ 1/m_b & 0 & \mathbf{0}_{1\times 4} \\ \mathbf{B}_r/m_b & \mathbf{0}_{4\times 1} & \mathbf{A}_r \end{bmatrix} \mathbf{x}(t) \\
&\quad + \begin{bmatrix} \frac{1}{1+m_\infty/m_b} \\ 0 \\ \mathbf{0}_{4\times 1} \end{bmatrix} F_m(t) + \begin{bmatrix} \frac{1}{1+m_\infty/m_b} \\ 0 \\ \mathbf{0}_{4\times 1} \end{bmatrix} F_e(t) \qquad (6) \\
&\equiv \mathbf{A}\,\mathbf{x}(t) + \mathbf{B}\,F_m(t) + \mathbf{B}\,F_e(t) \\
\mathbf{y}(t) &= \mathbf{C}\,\mathbf{x}(t) \qquad (7)
\end{aligned}$$

The state vector is here defined as $\mathbf{x} = [p \quad \eta \quad \mathbf{z}^{\mathrm{T}}]^{\mathrm{T}} = [p \quad \mathbf{w}^{\mathrm{T}}]^{\mathrm{T}}$. The first row of the the vector equation (6) may be seen to hold the force balance of Newton's second law of motion, $m_b\dot{v} = \sum F$. In principle the $\mathbf{B}$ matrices appearing in the last two terms of Equation (6) could be different, for instance if the machinery force was working through some mechanism, or if the model included several modes of motion but power was only extracted from one of them. Again the output matrix $\mathbf{C}$ must be tailored to give the output of interest. The buoyancy and inertia effects that are included with the state variables η and p each add one order to the mathematical model. This gives a total of 6 state variables for the full system, taking the wave excitation force and the machinery load force as inputs to the system. Since only linear effects have been included in the model, the total model is linear and yields a matrix equation.

Substitution for numerical values in the matrix equation, including the state-space approximation for the convolution term, gives us (SI units implied)

$$\mathbf{A} = \left[\begin{array}{cc|cccc} \text{0.0e+0} & \text{-5.283e+5} & \text{2.313e+2} & \text{-6.843e+0} & \text{1.018e+2} & \text{-2.075e+1} \\ \text{3.727e-6} & \text{0.0e+0} & \text{0.0e+0} & \text{0.0e+0} & \text{0.0e+0} & \text{0.0e+0} \\ \hline \text{-1.289e-3} & \text{0.0e+0} & \text{-1.110e+0} & \text{1.204e+0} & \text{-1.087e+0} & \text{1.938e-1} \\ \text{-3.812e-5} & \text{0.0e+0} & \text{-1.204e+0} & \text{-1.028e-3} & \text{2.767e-2} & \text{-6.427e-3} \\ \text{5.673e-4} & \text{0.0e+0} & \text{1.087e+0} & \text{2.767e-2} & \text{-2.149e+0} & \text{1.217e+0} \\ \text{1.156e-4} & \text{0.0e+0} & \text{1.938e-1} & \text{6.427e-3} & \text{-1.217e+0} & \text{-3.189e-1} \end{array}\right]$$

$$\mathbf{B} = \begin{bmatrix} 0.6689 & 0 & 0 & 0 & 0 & 0 \end{bmatrix}^{\mathrm{T}} \qquad (8)$$

(The horizontal and vertical lines inside the matrix $\mathbf{A}$ are included to indicate the structure of Equation (6) with $\mathbf{A}_r$ in the lower right corner.)

This mathematical model can now be solved numerically using standard integration procedures for systems of first-order differential equations.

3 The constrained optimal power absorption

The absorption of wave energy by the present system is solely given by the relative motion between the waves and the sphere. If the system is well described by a linear model and there are no constraints for the motion or the inputs, the maximum absorbed power can easily be found by frequency domain analysis (see, e.g. Chapter 6 of [34]). However, constraints on motions and inputs, as well as the random nature of ocean waves complicate the matter.

Under these circumstances the best we can do is to optimise the absorbed power in the time domain.

We will first derive a discrete-time expression for the optimal velocity assuming we have a perfect machinery and no amplitude constraints. Second, amplitude constraints will be assumed. It gives us the maximum power that can be absorbed with the chosen body operating in a certain wave climate. Subsequently restrictions on the machinery force in the form of upper and lower bounds are also taken into account.

3.1 Optimal velocity

The task of finding the maximum absorbed power may be pursued by use of the kinematic model given by Equations (4) and (5). It enables us to treat the velocity as an independent variable in the same way as is often done in frequency domain analysis of this optimisation (see e.g. [34], Section 6.2.1). Here, however, we want to find the optimal time-domain velocity function $v^{\text{opt}}(t)$ directly, and we start by discretising the state-space model. There are several possible ways of doing this, but the most common is to write [35, page 90]

$$\begin{aligned} \mathbf{w}[k+1] &= \bar{\mathbf{A}}_{dt}\mathbf{w}[k] + \bar{\mathbf{B}}_{dt}\, v[k] \\ \mathbf{y}[k] &= \bar{\mathbf{C}}_{dt}\, \mathbf{w}[k] \end{aligned} \tag{9}$$

where the matrices are found by

$$\bar{\mathbf{A}}_{dt} = e^{\bar{\mathbf{A}}_{ct}T_s}, \qquad \bar{\mathbf{B}}_{dt} = \left(\int_0^{T_s} e^{\bar{\mathbf{A}}_{ct}\tau} d\tau\right) \bar{\mathbf{B}}_{ct}, \tag{10}$$

$$\bar{\mathbf{C}}_{dt} = \bar{\mathbf{C}}_{ct} \tag{11}$$

Here $\mathbf{x}[k] \equiv \mathbf{x}(kT_s)$, with T_s being the sampling time. In these equations the subscripts *ct* and *dt* denote *continuous time* and *discrete time*, respectively. Where these are left out in the following, the distinction is made by use of (t) (in parenthesis) for continuous-time equations, and $[k]$ (in brackets) for discrete time.

The discretisation is exact (giving results equal to the continuous-time model) under the assumption of a piecewise constant input. In our case this will be true for the machinery-force input we are about to calculate, but for the effect of the excitation force the discretisation introduces an error, albeit small.

Our goal is to maximise the useful absorbed energy E_a, and this can be expressed by $\int_0^{T_h} P_a\, dt = \int_0^{T_h} (P_e - P_r - P_l)\, dt$; the integral of absorbed power, which equals excitation power $P_e(t) = F_e(t)v(t)$ less radiated power $P_r(t) = F_r(t)v(t)$ and lost power P_l with respect to time [34, pp. 199–204]. The limits of integration are commented below. With the assumption of zero loss, the corresponding discrete-time optimisation problem is (replacing power P by force F times velocity v)

$$\begin{aligned} \max_{\hat{v}} E_a &= \max_{\hat{v}} \left\{ T_s \sum_{i=1}^{N} \left\{ \hat{v}[i]\, \hat{F}_e[i] - \hat{v}[i]\, \hat{F}_r[i] \right\} \right\} \\ &= T_s \max_{\hat{\mathbf{v}}} \left\{ \hat{\mathbf{v}}^{\mathrm{T}} \hat{\mathbf{f}}_e - \hat{\mathbf{v}}^{\mathrm{T}} \hat{\mathbf{f}}_r \right\} \end{aligned} \tag{12}$$

where we have considered N samples and time step T_s. Using terminology of optimisation theory, the absorbed energy may thus here be referred to as the *objective function*, or alternatively $-E_a$ as the *cost function*. If we start at instant k, the involved vectors are defined as

$$\hat{\mathbf{v}} = \begin{bmatrix} \hat{v}[(k+1)|k] \\ \hat{v}[(k+2)|k] \\ \vdots \\ \hat{v}[(k+N)|k] \end{bmatrix} \quad \hat{\mathbf{f}}_r = \begin{bmatrix} \hat{F}_r[(k+1)|k] \\ \hat{F}_r[(k+2)|k] \\ \vdots \\ \hat{F}_r[(k+N)|k] \end{bmatrix} \tag{13}$$

Here $\hat{v}[i|k]$ and $\hat{F}_r[i|k]$ are predicted velocity and radiation force at step $i \leq k$ with knowledge (i.e. measurements) up to step k. The integer N is the discrete-time equivalent of the interval over which the integral is taken, such that the optimisation horizon is $T_h = N\,T_S$. It should ideally be infinite, but the velocity function will converge towards the optimal solution $\hat{\mathbf{v}}^{\text{opt}}$ as long as strong end point effects are avoided by requiring that the final position, as well as the start position, is within a small distance from the equilibrium position $\eta = 0$. A time step T_s of about 0.1 s to 0.2 s has been found to give sufficiently accurate results in the optimisation, and the value $T_s = 0.15$ has been used for most of the results presented herein.

An expression for $\hat{\mathbf{f}}_r$ is found by repeated use of Equation (9) where the output matrix $\bar{\mathbf{C}}$ is set equal to $[\,0 \quad \mathbf{C}_r\,]$. The resulting prediction vector is:

$$\hat{\mathbf{f}}_r = \check{\mathbf{F}}_r \mathbf{w}[k] + \check{\mathbf{G}}_r \hat{\mathbf{v}} \tag{14}$$

with the matrices given by

$$\check{\mathbf{F}}_r = \begin{bmatrix} \bar{\mathbf{C}}\bar{\mathbf{A}} \\ \bar{\mathbf{C}}\bar{\mathbf{A}}^2 \\ \vdots \\ \bar{\mathbf{C}}\bar{\mathbf{A}}^N \end{bmatrix} \tag{15}$$

$$\check{\mathbf{G}}_r = \begin{bmatrix} \bar{\mathbf{C}}\bar{\mathbf{B}} & \mathbf{0} & \cdots & \cdots & \mathbf{0} \\ \bar{\mathbf{C}}\bar{\mathbf{A}}\bar{\mathbf{B}} & \bar{\mathbf{C}}\bar{\mathbf{B}} & & & \mathbf{0} \\ \bar{\mathbf{C}}\bar{\mathbf{A}}^2\bar{\mathbf{B}} & \bar{\mathbf{C}}\bar{\mathbf{A}}\bar{\mathbf{B}} & \bar{\mathbf{C}}\bar{\mathbf{B}} & \cdots & \mathbf{0} \\ \vdots & \ddots & & & \vdots \\ \bar{\mathbf{C}}\bar{\mathbf{A}}^{N-1}\bar{\mathbf{B}} & \bar{\mathbf{C}}\bar{\mathbf{A}}^{N-2}\bar{\mathbf{B}} & \cdots & \bar{\mathbf{C}}\bar{\mathbf{A}}\bar{\mathbf{B}} & \bar{\mathbf{C}}\bar{\mathbf{B}} \end{bmatrix} \tag{16}$$

The check mark $\check{}$ is used to indicate that the prediction matrices $\check{\mathbf{F}}_r$ and $\check{\mathbf{G}}_r$ are based on the kinematic model (9). All the matrices refer to the discrete-time case but the subscripts dt have been omitted for compactness. The subscript r is used to express radiation-force prediction. Corresponding matrices $\check{\mathbf{F}}_\eta$ and $\check{\mathbf{G}}_\eta$ may be defined for position prediction by setting $\bar{\mathbf{C}} = \bar{\mathbf{C}}_\eta = [1 \quad \mathbf{0}_{1\times 4}]$ in equations (15) and (16). For other models, predictors may be constructed in the same way by inserting the corresponding state, input and output matrices $\bar{\mathbf{A}}$, $\bar{\mathbf{B}}$ and $\bar{\mathbf{C}}$, respectively.

The radiated power over the horizon N may now be written:

$$P_r = \hat{\mathbf{v}}^{\mathrm{T}}\hat{\mathbf{f}}_r = \hat{\mathbf{v}}^{\mathrm{T}}(\check{\mathbf{F}}_r \mathbf{w}[k] + \check{\mathbf{G}}_r \hat{\mathbf{v}}) = \hat{\mathbf{v}}^{\mathrm{T}}\check{\mathbf{F}}_r \mathbf{w}[k] + \hat{\mathbf{v}}^{\mathrm{T}}\check{\mathbf{G}}_r \hat{\mathbf{v}} \tag{17}$$

The last term is a quadratic form. It is a scalar, which equal its own transpose and may be written as

$$\hat{\mathbf{v}}^{\mathrm{T}}\check{\mathbf{G}}_r\hat{\mathbf{v}} = \frac{1}{2}\left(\hat{\mathbf{v}}^{\mathrm{T}}\check{\mathbf{G}}_r\hat{\mathbf{v}}\right)^{\mathrm{T}} + \frac{1}{2}\hat{\mathbf{v}}^{\mathrm{T}}\check{\mathbf{G}}_r\hat{\mathbf{v}} = \frac{1}{2}\hat{\mathbf{v}}^{\mathrm{T}}\left(\check{\mathbf{G}}_r^{\mathrm{T}} + \check{\mathbf{G}}_r\right)\hat{\mathbf{v}} = \hat{\mathbf{v}}^{\mathrm{T}}\boldsymbol{\Gamma}\hat{\mathbf{v}}, \tag{18}$$

where $\boldsymbol{\Gamma} = \boldsymbol{\Gamma}^{\mathrm{T}} = \frac{1}{2}(\check{\mathbf{G}}_r^{\mathrm{T}} + \check{\mathbf{G}}_r)$ is a symmetric matrix.

By physical reasoning we know that the radiation power must be positive or zero [34, Section 6.4]. As the initial state may be chosen to be zero, $\mathbf{w}[k] = \mathbf{0}$, we can conclude that $\hat{\mathbf{v}}^{\mathrm{T}}\check{\mathbf{G}}_r\hat{\mathbf{v}} \geq 0$, i.e. the matrix $\boldsymbol{\Gamma}$ is positive semi-definite, a property that will be useful in the following.

Inserting the expression (17) for the radiated power in the objective function (12) yields

$$\begin{aligned} \max_{\hat{\mathbf{v}}} E_a &= \min_{\hat{\mathbf{v}}}(-E_a) = T_s \min_{\hat{\mathbf{v}}}\left\{\hat{\mathbf{v}}^{\mathrm{T}}\hat{\mathbf{f}}_r - \hat{\mathbf{v}}^{\mathrm{T}}\hat{\mathbf{f}}_e\right\} \\ &= T_s \min_{\hat{\mathbf{v}}}\left\{\hat{\mathbf{v}}^{\mathrm{T}}\boldsymbol{\Gamma}\hat{\mathbf{v}} + \hat{\mathbf{v}}^{\mathrm{T}}(\check{\mathbf{F}}_r\,\mathbf{w}[k] - \hat{\mathbf{f}}_e)\right\} \end{aligned} \tag{19}$$

where the optimisation problem has been converted to a minimisation problem.

3.1.1 Unbounded excursion

In cases without constraints on the motion, the optimal velocity can be readily found by analytically minimising the objective function of Equation (19). We write the velocity vector as $\hat{\mathbf{v}} = \tilde{\mathbf{v}} + \boldsymbol{\delta}$, where $\tilde{\mathbf{v}}$ is a solution of the linear algebraic equation

$$\boldsymbol{\Gamma}\tilde{\mathbf{v}} = \frac{1}{2}(\hat{\mathbf{f}}_e - \check{\mathbf{F}}_r\mathbf{w}[k]) \tag{20}$$

and $\boldsymbol{\delta}$ is variable. Inserting for $\hat{\mathbf{v}}$ into the minimisation problem (19) it is found that the minimum is found for $\boldsymbol{\delta} = \mathbf{0}$, i.e. $\hat{\mathbf{v}}^{\mathrm{opt}} = \tilde{\mathbf{v}}$.

If, in addition, the matrix $\boldsymbol{\Gamma}$ is non-singular the optimal velocity may be written explicitly as

$$\hat{\mathbf{v}}^{\mathrm{opt}} = \frac{1}{2}\boldsymbol{\Gamma}^{-1}(\hat{\mathbf{f}}_e - \check{\mathbf{F}}_r\mathbf{w}[k]) = \frac{1}{2}\boldsymbol{\Gamma}^{-1}\hat{\mathbf{f}}_e - \frac{1}{2}\boldsymbol{\Gamma}^{-1}\check{\mathbf{F}}_r\mathbf{w}[k] \tag{21}$$

So far it hasn't been experienced any case where the matrix $\boldsymbol{\Gamma}$ becomes singular (which in this case would mean semi-definite). This may indicate that there is no such case, but this has not however been investigated any further.

It is interesting to recognise the similarity of expression (21)to the corresponding frequency domain result $v^{\mathrm{opt}}(\omega) = 1/2\, B_r^{-1}(\omega)\, F_e(\omega)$ [34, Equation (6.44)], where $B_r(\omega)$ is the "radiation resistance" or "radiation damping coefficient", which is the real part of the Fourier transformation of the retardation function $k(t)$. The last term of Equation (21) represents the influence from the initial conditions $\mathbf{w}[k]$, while the first term is the optimal velocity that would result if all initial states were zero.

The expression (21) is not so useful in practice, though. Due to the finite horizon of the prediction vectors, the solution will contain low-frequency motion. Speaking in terms of a frequency domain description, the heave mode has a very small radiation resistance in the low-frequency range ($B_r(\omega) \to 0$ as $\omega \to 0$), and this means that the amplitude of the corresponding optimal velocity components are very large. The result is that prediction vectors

for the velocity calculated by Equation (21) yield excessive motions far beyond reasonable amplitudes even for small incident waves. This problem may be resolved by introducing an extra term in the objective function that gives penalty to deviations from the equilibrium position $\eta = 0$, at the cost of driving the solution slightly off optimum. As we shall see in the next section, when amplitude constraints are introduced, the problem resolves itself.

3.1.2 Bounded excursion

We proceed by adding symmetric constraints for the heave excursion η. Requiring $|\eta| \leq \eta_{max}$ is equivalent to requiring both $\eta \leq \eta_{max}$ and $\eta \geq \eta_{min} = -\eta_{max}$. In analogy with Equation (14) we now write the position vector as $\hat{\boldsymbol{\eta}} = \check{\mathbf{F}}_\eta \mathbf{w}[k] + \check{\mathbf{G}}_\eta \hat{\mathbf{v}}$ and require that every element of the vector $\hat{\boldsymbol{\eta}}$ has to satisfy both inequalities, which gives:

$$\begin{bmatrix} \hat{\boldsymbol{\eta}} \\ -\hat{\boldsymbol{\eta}} \end{bmatrix} \leq \begin{bmatrix} \boldsymbol{\eta}_{\max} \\ \boldsymbol{\eta}_{\max} \end{bmatrix} \tag{22}$$

where the inequality operator works element-wise in the vector inequality, and the N elements of $\boldsymbol{\eta}_{\max}$ all equal $\eta_{\max}$[1].

By algebraic manipulation, we may write the amplitude constraints as:

$$\mathbf{R}_\eta \hat{\mathbf{v}} \leq \mathbf{c}_\eta \tag{23}$$

where

$$\mathbf{R}_\eta = \begin{bmatrix} \check{\mathbf{G}}_\eta \\ -\check{\mathbf{G}}_\eta \end{bmatrix} \tag{24}$$

$$\mathbf{c}_\eta = \begin{bmatrix} \boldsymbol{\eta}_{max} - \check{\mathbf{F}}_\eta \mathbf{w}[k] \\ \boldsymbol{\eta}_{max} + \check{\mathbf{F}}_\eta \mathbf{w}[k] \end{bmatrix}, \tag{25}$$

If, unlike here, the levels of the upper and lower bounds are different, the two $\boldsymbol{\eta}_{\max}$ vectors of Equation (22) must be replaced by $\boldsymbol{\eta}_{\text{ub}}$ and $-\boldsymbol{\eta}_{\text{lb}}$ for the upper and lower bounds, respectively, giving corresponding changes in Equation (25).

Together, Equations (19) and (23) now constitute a standard quadratic programming (QP) problem since the objective function (19) is quadratic in $\hat{\mathbf{v}}$ with a symmetric weighting matrix $\boldsymbol{\Gamma}$, and the constraint inequalities (23) are linear. It can be solved by conventional numerical tools. Because $\boldsymbol{\Gamma}$ has also been shown to be positive semidefinite the problem is convex, which means that any local minimum is guaranteed to be also a global minimum [21].

Figures 3 illustrates how the solution changes with varying wave amplitude. We may observe that in all cases the velocity peaks are practically in perfect alignment with the excitation force peaks, which agrees with the well-known frequency domain results for unconstrained motion. In the uppermost plot the oscillation is not aligned about the equilibrium position. This is due to the effect discussed in Section 3.1.1 of low-frequency components occurring in the solution.

In the present work we have put constraints on the heave amplitude of the buoy. Instead, constraints could have been put on the relative position of the local surface elevation ζ and

[1]Mathematically, what we define for this context is $\mathbf{a} < \mathbf{b} \Leftrightarrow a_i < b_i \, \forall \, i \in N$.

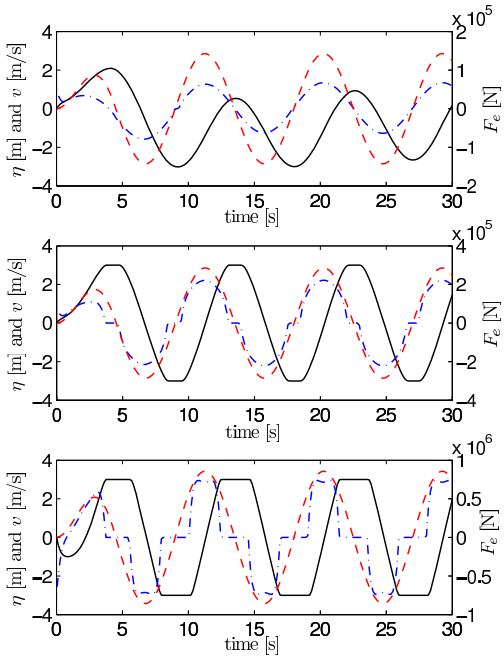

Figure 3: Optimal velocity (blue, dash-dotted) and position (black, fully drawn) for the heaving sphere excited by a regular wave of period 9 s and varying wave height: 0.5 m (top), 1.0 m (middle) and 3.0 m (bottom). The excitation force is a sine function where the amplitude has been attenuated by a factor increasing linearly from zero to one during the first half period (0 to 4.5 s). It is given by the dashed, red curve with scale on the right-hand axis. The heave amplitude was constrained to ± 3 m. The corresponding average absorbed power is 45.9, 183, and 851 kW for the three wave heights, respectively.

the buoy, i.e. the instantaneous submergence. It means replacing the limit for the heave excursion $\boldsymbol{\eta}_{\max}$ in Equations (22) and (25) by a time vector $\hat{\boldsymbol{\lambda}}_{\max} = \boldsymbol{\eta}_{\max} + \hat{\boldsymbol{\zeta}}$, where the last term is the vector of predicted wave elevation. The need for this prediction introduces another source of uncertainty in the controller, possibly leading to performance deterioration. Also, the local surface elevation is strongly influenced by the near-field evanescent wave, which would probably complicate the prediction considerably.

3.2 Optimal machinery force

Now that we have found the optimal velocity under amplitude constraints, we may proceed to find the machinery force needed to achieve it.

3.2.1 Unbounded force

Assuming first that there is no limit to the force the machinery can provide, the optimal force can be derived directly from the optimal velocity by use of the velocity predictor for the full system equations (6) and (7), or more precisely their discretised analogues. The velocity prediction matrices are then constructed in the same manner as for the radiation force predictor. In other words; $\mathbf{F}_v$ and $\mathbf{G}_v$ are found by inserting $\mathbf{A}_{dt}$,$\mathbf{B}_{dt}$ and $\mathbf{C}_{dt} = [1/m_b \quad 0 \quad \mathbf{C}_r]$ instead of $\bar{\mathbf{A}}$, $\bar{\mathbf{B}}$ and $\bar{\mathbf{C}}$ in equations (15) and (16), and we get:

$$\hat{\mathbf{v}} = \mathbf{F}_v \mathbf{x}[k] + \mathbf{G}_v \left(\hat{\mathbf{f}}_m + \hat{\mathbf{f}}_e \right) \tag{26}$$

By algebraic manipulation we get

$$\hat{\mathbf{f}}_m = \mathbf{G}_v^{-1} \left(\hat{\mathbf{v}} - \mathbf{F}_v \mathbf{x}[k] \right) - \hat{\mathbf{f}}_e \tag{27}$$

This is the force $\hat{\mathbf{f}}_m$ that the machinery has to provide in order to move the buoy with the velocity $\hat{\mathbf{v}}$. Figure 4 shows the machinery force calculated by Equation (27) for the case of an incident regular wave of 3 m wave height and 9 s period. In contrast to the (frequency-domain) solution found under the additional constraint of sinusoidal motion (also shown in the figure) we see that the optimal solution exhibit a latching-like behaviour, where the transition between extreme positions is travelled during shorter intervals. This requires larger and more rapidly varying machinery forces. For both solutions it may be observed that for most of the time when the buoy is moving, the machinery force and the velocity have opposite signs, which means that we have positive power take-off (i.e. the machinery is working in generator mode). In the short time intervals where force and velocity have equal signs the power flow is inverter (i.e. the machinery is working in motor mode).

Instead of using Equation (12), we also attempted to formulate the objective function to be minimised (the negative absorbed energy, -E_a) directly as a product of velocity and machinery force:

$$\begin{aligned} -E_a &= \hat{\mathbf{v}}^{\mathrm{T}} \hat{\mathbf{f}}_m = \left(\mathbf{F}_v \mathbf{x}[k] + \mathbf{G}_v \hat{\mathbf{f}}_m + \mathbf{G}_v \hat{\mathbf{f}}_e \right)^{\mathrm{T}} \hat{\mathbf{f}}_m \\ &= \hat{\mathbf{f}}_m^{\mathrm{T}} \mathbf{G}_v^{\mathrm{T}} \hat{\mathbf{f}}_m + \left(\mathbf{F}_v \mathbf{x}[k] + \mathbf{G}_v \hat{\mathbf{f}}_e \right)^{\mathrm{T}} \hat{\mathbf{f}}_m \end{aligned} \tag{28}$$

This gave problems with inaccurate solutions, which improved, however, with decreasing time step and a corresponding increase in computational effort (see Figure 5). It was found empirically by numerical experiments that formulating the objective function according to Equation (19) and then using Equation (27) to find the force, was the best passable road.

3.2.2 Bounded force

The next step is to include constraints on the machinery force, which will be present in a real system. Then the optimisation must be solved anew, with the force constraints formulated in terms of velocity constraints. Using again Equation (27) together with a symmetric bound $|F_m(t)| \leq F_{max}$ we find, in analogy with expression (22),

$$\begin{aligned} \pm \mathbf{G}_v^{-1} \left(\hat{\mathbf{v}} - \mathbf{F}_v \mathbf{x}[k] - \mathbf{G}_v \hat{\mathbf{f}}_e \right) &\leq \mathbf{f}_{\max} \\ \pm \mathbf{G}_v^{-1} \hat{\mathbf{v}} &\leq \pm \mathbf{G}_v^{-1} \mathbf{F}_v \mathbf{x}[k] \pm \hat{\mathbf{f}}_e + \mathbf{f}_{\max} \end{aligned} \tag{29}$$

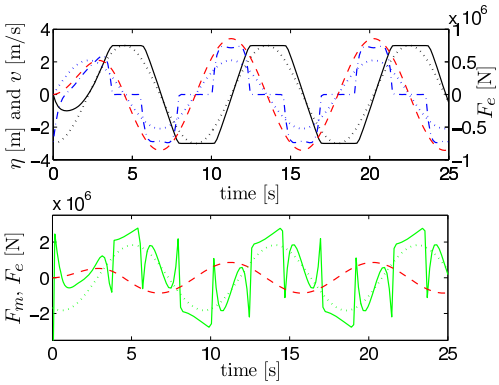

Figure 4: Optimal motion for an incident regular wave of period 9 s and height 3 m when the heave amplitude is restricted to 3 m while the machinery force is unconstrained. The upper diagram gives the position η (black, fully drawn) and velocity v (blue, dash-dotted), while the lower diagram gives the machinery force F_m (green, fully drawn). Both diagrams also contain the excitation force (red, dashed). The dotted curves, giving the optimal solution (position, velocity and machinery force) under the additional constraint of sinusoidal motion, are included for comparison.

where the N elements of $\mathbf{f}_{\max}$ all equal $F_{\max}$. In standard form these force constraints to be applied with the objective function (19) may be written

$$\begin{aligned} \mathbf{R}_F\hat{\mathbf{v}} &\leq \mathbf{c}_F, \quad \text{with} \\ \mathbf{R}_F &= \begin{bmatrix} \mathbf{G}_v^{-1} \\ -\mathbf{G}_v^{-1} \end{bmatrix} \\ \mathbf{c}_F &= \begin{bmatrix} \mathbf{G}_v^{-1}\mathbf{F}_v\mathbf{x}[k] + \hat{\mathbf{f}}_e + \mathbf{f}_{\max} \\ -\mathbf{G}_v^{-1}\mathbf{F}_v\mathbf{x}[k] - \hat{\mathbf{f}}_e + \mathbf{f}_{\max} \end{bmatrix} \end{aligned} \tag{30}$$

The example given in Figure 6 is an illustration of how the system response changes when these force constraints are taken into consideration.

A more conventional control engineering approach would be to formulate a reference tracking problem (see, e.g. [36], Chapter 4) by first finding the optimal velocity under amplitude constraints only (Equations (19) and (23)), and then to use this as a reference in a second problem, where the goal would be to minimise the deviation from the given reference under force constraints. Because the force constraint is then not included in the computation of the optimal velocity the solution will be suboptimal, but we still include it here for reference. Having found the suboptimal velocity $\mathbf{v}_{\text{ref}}$ we define the alternative objective function

$$J = (\hat{\mathbf{v}} - \hat{\mathbf{v}}_{\text{ref}})^{\text{T}}(\hat{\mathbf{v}} - \hat{\mathbf{v}}_{\text{ref}}) \tag{31}$$

The goal is now to keep the velocity $\mathbf{v}$ as close as possible to the reference $\mathbf{v}_{\text{ref}}$ under the force constraint $|F_m| < F_{\max}$. Inserting the prediction equation for $\hat{\mathbf{v}}$ it follows, after some

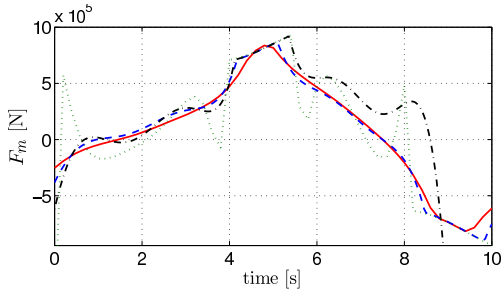

Figure 5: Convergence of the direct force optimisation as the time step is reduced; $T_s = 0.25\,\mathrm{s}$ (fully drawn), $0.05\,\mathrm{s}$ (dashed) and $0.02\,\mathrm{s}$ (dash-dotted). The solution found by velocity optimisation is included by the dotted curve. The excitation force is the same as given in the middle diagram of Figure 3 and the heave amplitude has in this case been constrained to $|\eta| \leq 1\,\mathrm{m}$. Due to the rapidly increasing computational burden as the time step is reduced, only one wave period has been solved for, although the solution is still in its transient phase.

algebraic manipulation and by omitting constant terms, that the problem can be written as

$$J' = \frac{1}{2}\hat{\mathbf{f}}_m^{\mathrm{T}}\mathbf{G}_v^{\mathrm{T}}\mathbf{G}_v\hat{\mathbf{f}}_m + \left\{(\mathbf{F}_v\mathbf{x}[k] + \mathbf{G}_v\hat{\mathbf{f}}_e - \hat{\mathbf{v}}_{\mathrm{ref}})^{\mathrm{T}}\mathbf{G}_v\right\}\hat{\mathbf{f}}_m \tag{32}$$

with constraints for the machinery force written as

$$\begin{aligned} \mathbf{R}_F\hat{\mathbf{f}}_m &\leq \mathbf{c}_F, \\ \mathbf{R}_F &= \begin{bmatrix} \mathbf{I} \\ -\mathbf{I} \end{bmatrix} \\ \mathbf{c}_F &= \begin{bmatrix} \mathbf{f}_{\max} \\ \mathbf{f}_{\max} \end{bmatrix} \end{aligned} \tag{33}$$

Again this is a QP problem solvable with standard numerical tools.

We have thus outlined two different ways of approaching the constrained optimisation of the machinery force. The first one is described by Equations (19) and (30), and gives a true optimisation with direct inclusion of force constraints in solving for the optimal velocity. The second description first uses Equations (19) and (23) to find the optimal velocity without force constraints, and then approximates the optimal machinery force by Equations (32) and (33). As must be expected, these two approaches give different results. Figure 7 compares the solutions found by the two methods for an incident regular wave. The absorbed power then varies from 509 kW in the case of unconstrained case down to 400 kW in the case of using the optimal velocity as reference. If the constraints on the machinery force was included already in the calculation of the optimal velocity, the power was 466 kW. It is thus evident that the force constraint should preferably be included in the optimisation problem from the start, if possible.

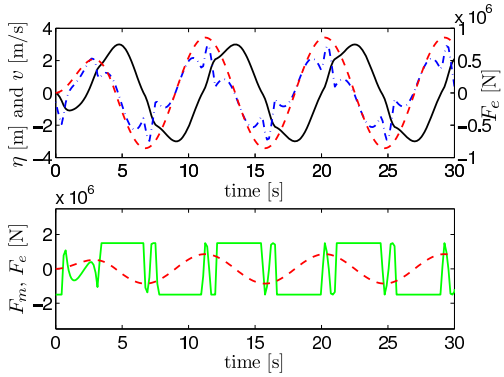

Figure 6: Optimal motion for an incident regular wave of period 9 s and height 3 m when the heave amplitude is restricted to ±3 m and the machinery force is restricted to ±1.5 MN. The upper diagram gives the position η (black, fully drawn) and velocity v (blue, dash-dotted), while the lower diagram gives the machinery force F_m (green, fully drawn). Both diagrams also contains the excitation force F_e (red, dashed). The results may be compared with the curves of Figure 4 obtained without force constraints.

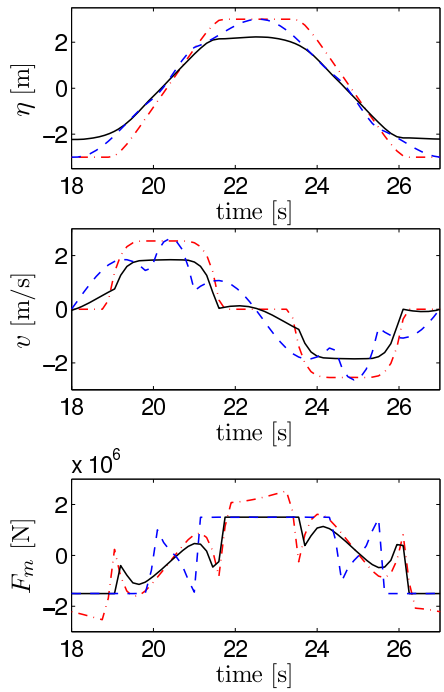

Figure 7: Optimal functions with an incident regular wave of period 9 s and height 2 m; for position (top), for velocity (middle) and for machinery force (bottom). The heave motion has been restricted to ±3 m, and the excitation has the same phase as in Figure 3. The dash-dotted curves result from unbounded machinery-force input, whereas the dashed curves have been calculated by including a force constraint of 1.5 MN in the velocity optimisation. Finally, the fully drawn curves stem from first optimising the velocity without input constraints, and then finding the constrained input that minimises the deviation from the found optimal velocity. One oscillation cycle at steady state is shown.

4 The Budal diagram – upper bounds for regular waves

We now take a step back to looking only at the optimal velocity under motion constraints, without limiting the machinery forces.

The point-absorber effect in wave-energy extraction was first described by Budal and Falnes [37], and shortly after theoretical limits for the ocean-wave absorption by oscillating bodies were derived by several authors, independently [38, 39, 40]. For a heaving, axisymmetric body oscillating without constraints in resonance with an incoming regular wave of period T and wave height H, their results showed that the average absorbed power $\overline{P}_a$ was limited by the expression

$$d_a \leq \frac{1}{k} = \frac{\lambda}{2\pi} \tag{34}$$

or equivalently,

$$\overline{P}_a \leq \frac{1}{k} J_{\mathrm{E}} = \frac{\rho}{128} \left(\frac{g}{\pi}\right)^3 T^3 H^2, \tag{35}$$

where $d_a = \overline{P}_a / J_E$ [m] is the absorption width, J_{E} [W/m] is the wave power level and k [1/m] is the wave number. The last equality is only valid for deep water conditions. If we define the excitation power $\overline{P}_e$ as the averaged product of the excitation force and the body velocity $\overline{P}_e = \overline{F_e(t)u(t)}$, and the average radiation power as $\overline{P}_r = \overline{F_r(t)u(t)}$, the absorbed power is $\overline{P}_a = P_e - P_r$. The theoretical limit may be reached provided the average absorbed power equals half the average excitation power, which happens when the radiated power equals the absorbed power, $\overline{P}_a = \overline{P}_r$ [34, Section 6.2].

As shown in the examples given by Pizer [17], the theoretical limit (34) can only be reached up to a certain wave height and period, depending on the constraint set for the motion amplitudes. Beyond, only a lower relative power absorption can be realised. This second limit is due to the finite volume swept by the body during its oscillation cycle. It was theoretically described by Budal and Falnes [41], and later elaborated in [42]. Their starting point was that the absorbed power must be less than the excitation power, and that equality can be approached only if the radiated power becomes negligible in comparison. By arguing further that the total volume V of the body sets limits for both the maximum excursion, velocity and excitation force in heave they arrived at an upper theoretical bound for the power $\overline{P}_a$ that can be absorbed by a heaving body,

$$\overline{P}_a < \frac{\pi \rho g H V}{4T} \tag{36}$$

The limits (35) and (36) tell us that no matter how well we control the motion of our device we will not be able to reach the region above any of them. But how close can we get?

It will depend on the constraints we put on the motion and on the machinery forces. The obvious requirement would be that the body is not allowed to leave the water. A more conservative restriction would normally be chosen in order to keep the motion within the desired operation range or to avoid the activation of end stops. Other aims could be to avoid excessive accelerations or machinery loads. A numerical optimisation in the time domain like the one we have carried out in Section 3 may then give an answer to our question. It allows for a non-linear controlled response to the force exerted on the body from the incident wave. The velocity functions found by numerical optimisation in the preceding section are

examples of this. And in waves large enough for the amplitude restrictions to be active, it enables a power absorption exceeding the limits found under the additional restriction of sinusoidal motion, as reported by Pizer [17] and Hals [27].

For the heaving-sphere example studied here, Figure 8 shows how close we can get to the theoretical bounds if we restrict the amplitude to $|\eta| \leq 3\,\mathrm{m}$ as the only constraint. The plotted values result from optimisation over horizons of between 4 and 8 wave periods, restricted by the computational time of the QP solver used. Initially the sphere is taken to be at rest, and the end position is required to lie within $\pm 1\,\mathrm{cm}$ in order to reduce end-point effects. The power values are found by averaging over a whole number of wave periods where the startup and fade-out regions are excluded. Because the horizon is not long enough to establish complete steady state, and because of the inherent inaccuracy of the sample-hold discretisation of the input assumed in the discretisation of the mathematical model, the solution must be expected to have a small inaccuracy. The first numerical results showed a significant exceedance of the left-hand, ascending limit of the Budal diagram for about 7 to 9 s wave periods. Alarmed by the violation of the theoretical limit, we tried to reduce the time step. This improved the accuracy and gave results in accordance with the theory as shown in the figure.

We observe that, with increasing wave period, the optimal power absorption follows the ascending limit up to a certain point, and from there it approaches Budal's upper bound asymptotically. A simple argument gives us some more insight into this behaviour: The Budal bound is based on the assumption that the radiated power is negligible, which happens when the body is small compared to the wavelength (i.e. for large wave periods). If we rather set the radiated power equal to half the excitation power, $P_r = 0.5\,P_e$ (which is the requirement for reaching the ascending limit), we get a curve at half the Budal bound, which has also been included in Figure 8. Any radiation less than half the excitation power will remove us from the ascending limit, and we may conclude that the crossing point A represents a limit to how far we can stay on the ascending line. With the chosen amplitude restriction of $|\eta| \leq 3\,\mathrm{m}$, we see that we depart from the ascending left-hand limit before we reach point A because we are not exploiting the whole volume of the absorber. The more we restrict the amplitude, the earlier the departure will take place.

As stated above, we also see from Figure 8 that in the region where the amplitude constraints apply, the optimal solution (which is non-sinusoidal) gives an absorbed power larger than what is achieved with a sinusoidal, constrained motion (which is the solution readily found by frequency domain analysis).

The Budal diagram in Figure 8 may be extended to a corresponding surface if we include the wave amplitude as a variable for the incident regular wave. We may label this a *Budal surface* and Figure 9 shows this surface for the heaving sphere we have been studying. This surface represents the upper bound to the absorption that can be achieved for a heaving device with a chosen body volume. The part on the right-hand side of the edge is independent of the body shape, while the part on the left-hand side of the surface may be altered by distributing the body volume non-symmetrically. For terminating devices (or, ideally, in the two-dimensional case, see e.g. [2]) the left-hand limit will be a straight line in the two-dimensional diagram and and a an inclined, single-curved surface in the three-dimensional diagram.

Equivalently, if constraints are imposed on motion, machinery force or other, the square-

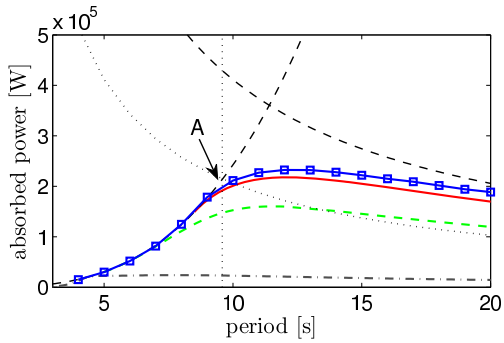

Figure 8: Absorbed useful power for the heaving sphere with excursions restricted to $\pm 3\,\mathrm{m}$ and an incident wave height of 1 m. The thin dashed curves show the theoretical upper bounds: the limit for heaving, axisymmetric bodies (Equation (35), ascending right) and Budal's upper bound (Equation (36), descending right). A thin dotted curve is drawn at half the Budal bound, and its intersection with the ascending limit is indicated by a vertical dotted line and the point A. The four remaining curves originate from different control strategies: passive (dash-dot), latching (dashed), reactive control restricted to sinusoidal oscillation (fully drawn) and constrained optimal control (with squares), of which the first three curves are taken from an earlier work [27].

marked curve in Figure 8 may be extended to a limiting surface for the power absorption in regular waves. It is shown in Figure 10, and would be completely concealed by the Budal surface if drawn in the same diagram and seen from above. This second surface is a more practical limit as it gives the maximum power absorption within the given constraints (in this case only the amplitude constraints of $|\eta| \leq 3\,\mathrm{m}$).

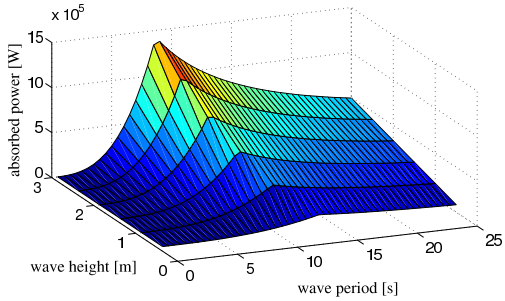

Figure 9: The Budal diagram extended to three dimensions by including the wave amplitude as a variable for the incident regular wave. This surface gives theoretical limits to the possible power absorption for an axisymmetric, heaving body of a chosen volume, in this case equal to 524 m^3. The crossing point of the limiting curves shift towards lower periods as the wave amplitude increases, giving the skew shape of the surface.

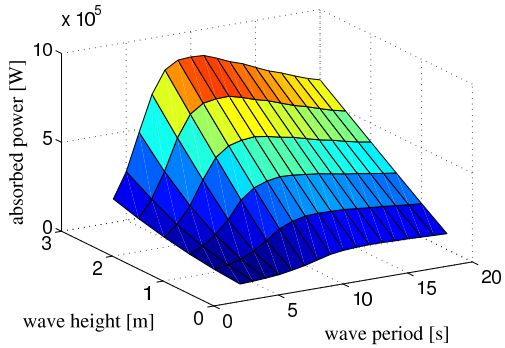

Figure 10: Surface giving the upper bound for the power that can be absorbed by a heaving sphere of diameter 10 m when the vertical excursion is restricted to ± 3 m. The surface would be covered by the surface in Figure 9, coinciding for low wave periods in the same way as the curves in Figure 8, where the amplitude restriction has not yet come into play.

5 Model-predictive control with online prediction

Using the optimisation tool outlined in Section 3 we can make an algorithm for model-predictive control (MPC) of the heaving sphere to work in irregular waves. The idea behind this control is to run the controller at a constant update rate, and to optimise the machinery force on the system over a chosen receding horizon T_h at each time step, based on the chosen optimisation criteria (objective function and constraints). From the calculated solution, which is in form of a vector such as Equation (13), only the first element is used, and the whole optimisation is done again at the next controller update. Therefore the controller adapts well to disturbances and errors in measurements, estimates and predictions. The other main advantage with an MPC controller is that it handles constraints in an efficient way, as we have seen for the optimisation algorithm.

If reasonably accurate short-time predictions of the wave force may be found, the MPC algorithm will work equally well with regular and irregular waves. The last part of this section therefore treats the problem of continuous adaptive control in irregular waves, but first we will establish the controller and make some comparisons with the results from the preceding sections.

In order to investigate the performance and behaviour of the MPC controller, numerical simulation of the semi-submerged heaving sphere has been used. Following Sørensen [43], the model of our wave-energy converter is broken down into two complexity levels: the *process plant model* and the *control plant model*, cf. Figure 11. After having defined these, we go on to investigate the properties of the controller.

5.1 Process plant model

The process plant model is supposed to reproduce the real dynamics of the system as closely as needed. For an actual prototype or device it would typically include all excited hydrodynamic modes of motion, mooring forces, important machinery dynamics as well as signal disturbances or errors. Because the intention in the present work is to investigate the idealised potential of MPC controllers in wave-energy conversion, and not to tailor a controller ready for implementation, only the heave mode will be included in the process plant model. It will consist of the continuous time equation (6), which, however, enables a more accurate numerical integration than the discretised model.

The integration is done by *ode15s*, a variable-step solver in Matlab [44] that is based on the numerical differentiation formulas (NDFs). The relative tolerance was set to 10^{-5}, whereas the absolute tolerances for the momentum p, position η and radiation model states $\mathbf{z}$ were set to $1\,\mathrm{kg\,m/s}$, $10^{-4}\,\mathrm{m}$ and 10^{-3}, respectively. As a part of the process plant model the controller is run at a constant update rate f_c, such that the controller input is kept piecewise constant in-between updates.

5.2 Control plant model

The control plant is usually a simplified version of the process plant model, and should capture the main physical properties such that it can be used by the controller to compute the control signal in a rapid and efficient way. It may also be used in analytic stability

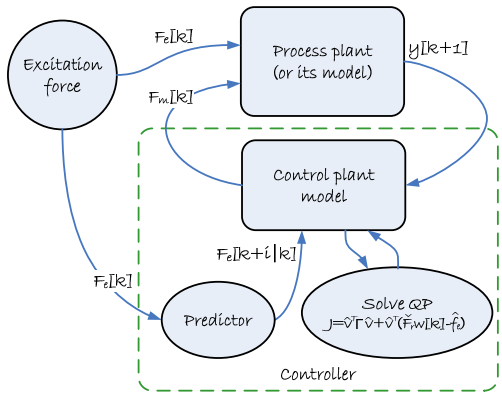

Figure 11: The system model is broken into two complexity levels: the *process plant model*, representing the real dynamics of the system, and the *control plant model*, used for calculation of the controller signal to the machinery. Measurements and predictions of the wave excitation force are fed into the controller, which computes the machinery force set-point using a quadratic programming (QP) optimisation algorithm.

analysis. Here, the control plant model is simply the discretised system model (based on equations (6) and (7)):

$$\begin{aligned} \mathbf{x}[k+1] &= \mathbf{A}\mathbf{x}[k] + \mathbf{B}\,F_m[k] + \mathbf{B}\,F_e[k] \\ \mathbf{y}[k] &= \mathbf{C}\,\mathbf{x}[k] \end{aligned} \tag{37}$$

At each controller update instant the control signal is found by solving the QP problem defined by the objective function (19) and constraints (23). There are thus several controller parameters that will affect the system response:

1. The controller update rate
2. QP time step
3. The optimisation horizon T_h
4. The prediction accuracy

Because the input to the system, the excitation force, varies continuously, the update rate should not necessarily correspond to the time step used in the QP problem. A study of the variation of these time steps showed that the dependence on them is weak as long as they are small enough, i.e. less than about 0.2 s. Because the QP solution becomes very time consuming for long horizons (many steps), it was decided to run the simulations with QP time step of 0.15 s and a controller update interval of 0.05 s.

We start by assuming ideal prediction of the future input to the system. This gives us a reference for evaluating the effect of prediction algorithms. Subsequently, the influence on performance from the optimisation horizon and the accuracy of the wave force prediction is addressed.

5.3 Performance with ideal prediction

In order to assess the potential of the MPC method applied to wave energy conversion, we first assume that we have a perfect prediction of the future wave force on the heaving sphere. In order to keep the computational time down, we set the optimisation horizon not longer than 8.8 s, twice the eigenperiod T_0. For waves with periods up to about the same value we then expect the controller to give close to optimal power absorption within the chosen amplitude constraint of ± 3 m. An example of position, velocity and machinery force time series is shown in Figure 12. In Figure 13 the power absorption curve for MPC controller with ideal prediction is drawn in the Budal diagram.

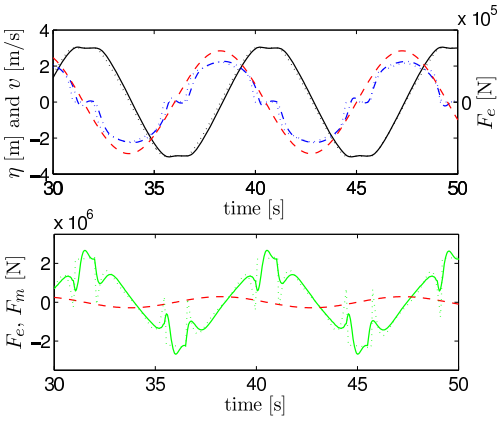

Figure 12: Example of time series for MPC control of the heaving sphere, with amplitude restricted to $\eta \leq 3$ m. The upper diagram gives the position η (black, fully drawn) and velocity v (blue, dash-dotted), while the lower diagram gives the machinery force F_m (green, fully drawn). The excitation force is represented by the red dashed curves, and corresponds to a regular wave of period 9.0 s and height 1.0 m. The dotted curves give the corresponding position, velocity and machinery force solutions found by the numerical optimisation described in Section 3.2.

We may observe that the machinery force is very large in comparison to the excitation force. The correspondingly large reactive power flowing through the machinery is known to be a challenge with reactive control strategies for wave energy devices that have rather narrow resonance bandwidth [27]. The diagram of Figure 14 shows extreme values of reactive power relative to the average power. A similar distribution is found for the extrema of the machinery force (although symmetrical about zero). The ratio between machinery and excitation force maxima for optimal control is typically between 5 and 10. It may be interesting to compare with the results for a typical latching control strategy also presented in Figure 14. This strategy has no reactive power flow, and the ratio of peak to average power is significantly lower. In the design of machinery and control concepts, the costs associated with having a machinery with higher capacity and the ability to supply reactive power must be weighted against the benefit of higher average output power. It is also worth noting that for reactive

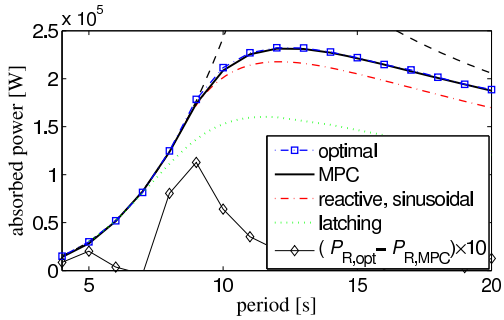

Figure 13: Performance of the MPC controller (fully drawn, black curve) compared to the optimal absorbed power (blue squared curve) under amplitude constraints $|\eta| \leq 3\,\mathrm{m}$ for incident regular waves with height 1.0 m and varying period. The difference between the optimal and MPC results is given by the black, diamond-marked curve, which has been scaled up by a factor of 10. The optimisation horizon is set to $T_h = 8.8\,\mathrm{s} \approx 2\,T_0$ and the predictor time step is 0.15 s. For comparison, the dashed, red curve gives the frequency domain solution for reactive control under the constraint of sinusoidal motion, and the green, dotted curve gives the result for latching control (both also shown in Figure 8). The dashed, black curves give the upper theoretical bounds.

control strategies the peak-to-average power ratios is even larger for operation in irregular waves due to the varying power level of the incident waves.

From the Budal diagram (Figure 13) we see that the absorption using the MPC controller is only slightly inferior to the (numerically estimated) optimal energy absorption found in Section 4 for the same wave input, and that this is true also for wave periods much longer than the chosen optimisation horizon. It tells us that the MPC algorithm has indeed the potential to give an energy absorption close to optimal within given constraints. In Figure 12 it may be seen how the motion response for the MPC controlled buoy differ from the optimal solution at the point where the difference in absorbed power is largest, namely at $T = 9\,\mathrm{s}$, as seen from the difference curve in Figure 13. It is also worth noticing that, within the validity of our process plant model, the accuracy of the MPC results are better than the estimate of optimal absorption, as the former are found by numerical integration of the continuous-time model of the system, rather than by the discretised one (see also the discussion on accuracy in Section 4).

Next, using the same controller, we turn to irregular waves and look at the influence of varying the optimisation horizon.

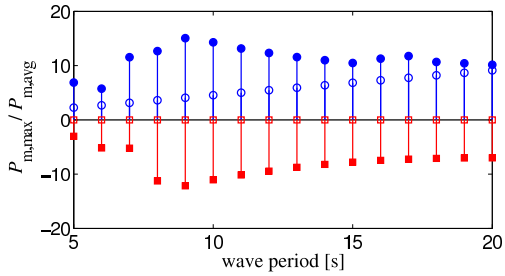

Figure 14: The ratio between extreme values of instantaneous power $P_{\mathrm{m,max}}$ flowing through the machinery and average absorbed power $P_{\mathrm{m,avg}}$ found from simulations with incident regular waves and the MPC controller using ideal predictions of the excitation force. The filled red squares gives the minima (machinery working as a motor) and the filled blue circles give the maxima (machinery working as a generator) for incoming regular waves of height $H = 1.0\,\mathrm{m}$ and varying wave period (given on the horizontal axis). The corresponding open squares and circles show the same ratio for latching control, which has no reactive power flow.

5.4 Sensitivity to optimisation horizon

The effect of varying the optimisation horizon was was assessed by simulation in irregular waves synthesised from the two-parameter Modified Pierson-Moskowitz spectrum (see e.g. [45]), and with restrictions only on the heave amplitude. Figures 15 and 16 summarise the results. In the latter figure the power absorption is given in terms of the absorption width d_a, (defined as the width of the incident wave that carries an amount of power equal to the absorbed power), relative to the buoy diameter $d = 10\,\mathrm{m}$.

In Figure 15 the power absorbed in irregular waves is given relative to the maximum power that can be absorbed in a corresponding regular wave, i.e. when the energy period T_e and the wave power level are the same. The first observation is that, for the $T_e = 6\,\mathrm{s}$ sea states, the absorption in irregular waves is better than in the corresponding regular waves, and as we shall see there is a beautiful reason for that. Comparing with Figure 10 or 13 we find that for these sea states, we are operating in waves corresponding to the region limited by the left-hand, convex part of the curve or surface, respectively. By illustrative arguments of Figure 17 we understand that when the limiting surface is convex, variation of the wave period and wave height will always lead to a possible increase in the absorbed power as compared to the regular wave case. Or, thinking of the irregular wave as a series of wave oscillations with different wave amplitudes and heights, the net effect of their variation is that the average absorbed power becomes larger as long as the limiting surface for corresponding regular waves is convex. Taking the numbers for $T_h = 2\,T_0$ in Figure 15, we see that the relative absorbed power for $T_e = 6\,s$ is reduced from about 1.45 to 1.04 as the wave height increases and we move from a convex towards a concave region of the limiting surface. All the other sea-states shown correspond to concave regions of Figure 10, and thus the relative absorbed power is necessarily less than one.

We may note, however, that as the significant wave height increases, the $T_e = 12\,\mathrm{s}$ results approach unity. This is in good agreement with the given explanation, and we expect the relative absorbed power to exceed 1 when we reach the convex right-hand region of the limiting surface. In other words, the convex shape of Budal's upper bound will enable the absorbed power for irregular waves to exceed the absorbed power in a corresponding regular wave for very high wave periods or very high wave amplitudes, or equivalently for small bodies (i.e. when we are at the right side of the Budal diagram). For the chosen body volume this will happen outside the range of sea states studied. The $T_e = 9\,\mathrm{s}$ curves have a quite steady relative power reduction because they are in the middle of the concave region for all wave heights considered.

A final comment to Figure 15 regards the dependence on the optimisation horizon. A rough generalisation is that all the curves are close to convergence at the longest optimisation horizon: $T_h = 2\,T_0$, in this case equal to about 8.8 s. A valuable observation is that the horizon can be reduced to $T_h = T_0$ with only small (less than 3 %) reductions in absorbed power, and even to $T_h = T_0/2$ with reduction less than 9 %. The strongest dependence on optimisation horizon is found for the shortest wave period and smallest wave height. This observation is not unreasonable, because in this situation, it is not necessary to limit heave amplitude by applying a large load force, which would imply widening of the resonance bandwidth, and thus reduce need for prediction.

For the geometry under investigation, the retardation function $k(t)$ (see Figure 2) is small

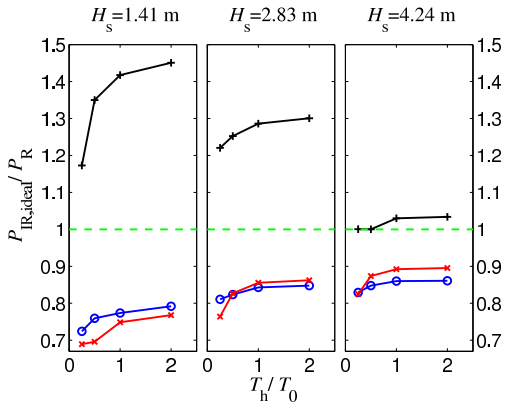

Figure 15: Performance of the MPC controller for varying optimisation horizons in irregular waves synthesised from a Modified Pierson-Moskowitz spectrum, and with restrictions on only the heave amplitude. On the horizontal scale the fraction of optimisation horizon T_h to eigenperiod $T_0 \approx 4.4\,\mathrm{s}$ is given. The vertical scale is absorbed power $P_{\mathrm{IR,ideal}}$ using an ideal predictor in irregular waves relative to the optimum absorbed power P_{R} for a regular wave of the same energy period and same wave power level. The three different diagrams correspond to different significant wave heights (given on top), and the plus, circle and cross marks refer to energy periods of 6, 9 and 12 s, respectively.

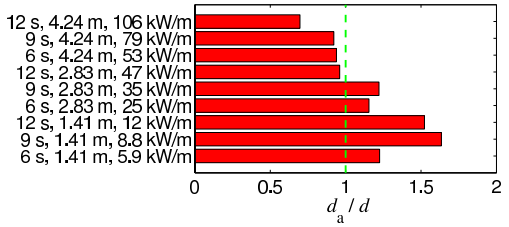

Figure 16: Performance achieved with a optimisation horizon of $T_h = 8.8\,\mathrm{s}$, corresponding to twice the resonance period T_0. This is the longest horizon studied here and from the convergence observed in Figure 15, the achieved performance is expected to be very close to optimal. The absorbed power on the horizontal scale is given as relative absorption width d_a/d, with the buoy diameter $d = 10\,\mathrm{m}$. The labels on the vertical scale indicates the energy period, significant wave height and wave-power level of the incident irregular wave, which was synthesised from a Modified Pierson-Moskowitz spectrum. The sea states on the vertical axis have been ordered according to increasing wave power level.

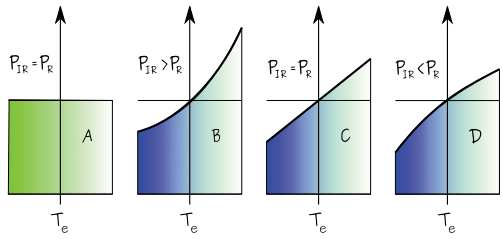

Figure 17: Illustration of how we may think that the shape of the limiting curve affects the ratio between power absorbed in irregular waves P_{IR} and regular waves P_{R} with the same energy period and wave energy transport. We may, as an approximation, think of an irregular wave as a series of half wave cycles having different wave periods and wave heights. If the ability to absorb power did not depend on the period of the incoming wave we would have case A. When there is a convex limit to the possible absorbed power, the absorbed power may increase when the incoming wave period is allowed to vary about T_e (case B). A straight-line limit (as in case C) compares to case A, whereas a concave limit (case D) causes a reduction in the absorbed power for irregular waves relative to the corresponding regular wave.

for $t > 4.5\,\mathrm{s}$ and negligible for $t > 9.0\,\mathrm{s}$. Firstly, this knowledge may serve to explain the convergence seen for the longest optimisation horizon. Referring again to the premonition time introduced by Price *et al.* [25], we see that the convergence is reached where it becomes zero; i.e. where the available knowledge (the horizon of the ideal prediction) becomes equal to or greater than the required knowledge (given by the retardation function). This also explains the small decrease observed when the horizon is reduced to 4.4 s; since the memory effect is only weak for $t < 4.5\,\mathrm{s}$ the available knowledge is enough to still give a good performance.

The right-end points in Figure 15 represent an approximation to the best absorption we can hope for by use of the MPC controller, and the previous result suggest that is is also close to the constrained optimum. In Figure 16 these values have been plotted as relative absorption width, and show that it ranges from about 0.7 to 1.8 in irregular waves. Although these numbers show the point-absorber effect ($d_a/d > 1$), the Budal diagram is a more interesting tool for assessing performance in that it tells how well the body volume is exploited for wave absorption.

The relative absorption width is highest for the sea states where the power of the incident waves matches the converter capacity, such that the full stroke is exploited for most of the time but the operation is not too far into the amplitude constrained region. This is the case for the $T_e = 9\,\mathrm{s}$ and 12 s sea states with $H_s = 1.41\,\mathrm{m}$. For higher wave power levels a larger part of the available power transported by the wave remains in the sea, and correspondingly the absorption width is reduced. For lower power levels the stroke of the converter is not fully exploited.

5.5 Performance with a simple predictor

5.5.1 The augmented Kalman filter

As input to the controller we wish to take only measurements of the wave excitation force on the buoy. It is assumed that this is done by deriving the force from a measurement of the wave elevation or pressure at the location of the buoy, as proposed earlier [34, Section 6.3], or calculated from force, acceleration and/or position measurements for the body.

Having access to instantaneous and historical values for the excitation we may use a model of the process behind the force signal to make a predictor for future values of the signal. In the example studied here we will use a Kalman filter with a simple damped harmonic oscillator as model for the wave force process. This is only one of several possible methods, but is well known and established, and may therefore serve as a benchmark. The role of the Kalman filter is to estimate the current state of the model variables, which are chosen to be the position x and velocity $u = \dot{x}$ of the harmonic oscillator;

$$\begin{aligned} \dot{\mathbf{x}}(t) = \begin{bmatrix} \dot{u}(t) \\ \dot{x}(t) \end{bmatrix} &= \mathbf{\Phi}(\omega, \lambda)\, \mathbf{x}(t) + \mathbf{w}_n(t) \\ \text{with} \quad \mathbf{\Phi}(\omega, \lambda) &= \begin{bmatrix} -2\omega\lambda & -\omega^2 \\ 1 & 0 \end{bmatrix}, \end{aligned} \tag{38}$$

(The state vector $\mathbf{x}$ used here and its elements has nothing to do with the state vector for the buoy dynamics defined earlier.) The oscillator is excited by gaussian white noise given by the vector $\mathbf{w}_n(t)$, where the subscript n has been used to distinguish it from the state vector of the kinematic model defined in Section 2. Furthermore, λ is the damping ratio, and ω is the natural frequency. The Kalman filter algorithm ensures that the estimate of the model states (in our case the excitation force) has minimum covariance [46].

A damped harmonic oscillator with constant frequency and constant damping coefficient is not a good model for the process of an irregular ocean wave, but it can be improved by letting the frequency and the damping coefficient vary. We may do this by including them as elements of the state vector $\mathbf{x}(t)$ estimated by the Kalman filter. Thus we get a non-linear, time-varying model as basis for the filter instead of the conventional linear, time-invariant model. In our case the discretised state equations for the model become:

$$\mathbf{x}[k+1] = \begin{bmatrix} u[k+1] & x[k+1] & \omega[k+1] & \lambda[k+1] \end{bmatrix}^{\mathrm{T}} \tag{39}$$

$$= \begin{bmatrix} \mathbf{\Phi}(\omega[k], \lambda[k]) & \frac{\partial \mathbf{\Phi}(\omega[k], \lambda[k])}{\partial [\omega[k] \quad \lambda[k]]} \begin{bmatrix} u[k] \\ x[k] \end{bmatrix} \\ \mathbf{0}_{2\times 2} & \mathbf{I}_{2\times 2} \end{bmatrix} \mathbf{x}[k] + \mathbf{w}_n[k] \tag{40}$$

$$F_e[k] = \begin{bmatrix} 0 & c_F & 0 & 0 \end{bmatrix} \mathbf{x}[k] + v_n[k] \tag{41}$$

In addition to the position and velocity the model state vector $\mathbf{x}[k]$ has now been expanded to also include the oscillator's angular frequency ω and damping ratio λ. It means these are updated on-the-go, and this adaptive configuration is known as the augmented Kalman filter. The input to the model is the vector of gaussian white noise sequences $\mathbf{w}_n[k]$ with dimension equal to the number of states. Measurement error is represented by $v_n[k]$. The constant c_F sets the strength of the excitation force. Using Euler integration with a time step equal to

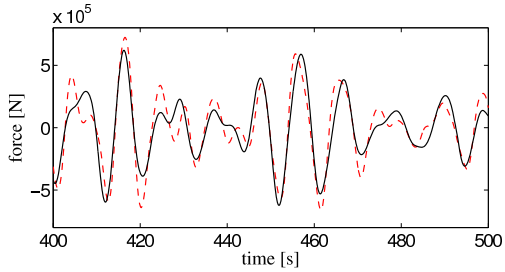

Figure 18: The augmented Kalman filter run on an excitation force time series resulting from a sea state of significant wave height $H_s = 1.41\,\mathrm{m}$ and energy period $T_e = 9\,\mathrm{s}$ (with a Modified Pierson-Moskowitz wave spectrum). The force signal is predicted 2.2 s ahead (dashed, red curve), and this is compared to the true values (fully drawn, black curve).

Table 1: Parameters used for the Kalman filter. During simulation states 3 and 4 of the filter (the angular frequency ω and the damping coefficient λ) were excited by white noise sequences of variance $2.25 \cdot 10^{-6}$. The values were chosen based on trial and error.

Parameter	Exp.	Value
Input noise covariance matrix	$E[\mathbf{w}_n[k]\mathbf{w}_n[k]^{\mathrm{T}}]$	$\mathrm{diag}(62.5,\ 2.50,\ 2.25,\ 2.25) \cdot 10^{-4}$
Measurement noise covariance	$E[v_n[k]v_n[k]]$	$1.0 \cdot 10^6$
Force scale factor	c_F	$1.5 \cdot 10^6\,\mathrm{N}$

T_s for discretising the oscillator model, the state transition matrix $\mathbf{\Phi}[k] = \mathbf{\Phi}(\omega[k], \lambda[k])$ is given by

$$\mathbf{\Phi}(\omega[k], \lambda[k]) = \begin{bmatrix} 1 - 2\omega[k]\lambda[k]T_s & -\omega[k]^2 T_s \\ T_s & 1 \end{bmatrix}. \tag{42}$$

Using this model, the augmented Kalman filter may be run recursively using the conventional filter equations [46] and with update of the transition matrix at each time step. Predictions of future values for the signal are then readily made by iterated operation with the current state transition matrix on the current estimate of the state vector.

An example of the predictor's performance is shown in Figure 18, and chosen filter parameters and some measures are given in Table 1. In order to assure filter stability it has been required that $\lambda \geq 0.05$. In general it is found that the prediction's deviation from the true signal is reasonably small within a horizon of about 2 s - values further ahead are usually very inaccurate and of little value.

5.5.2 MPC with predicted excitation

The model-predictive controller was run for the same set of irregular waves as before using the wave force predictor described above. The optimisation horizon was also varied in the same manner as for Figure 15. The results are presented in Figure 19.

The first observation is that for short horizons there is practically no reduction in the performance, whereas toward longer horizons there is a gradual decrease in the performance

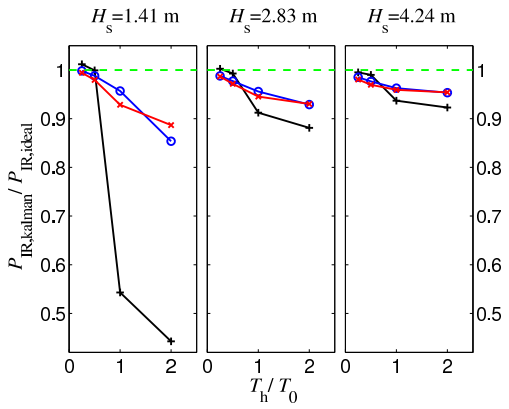

Figure 19: Performance of MPC controller when the force prediction is made by an augmented Kalman filter based on a damped harmonic oscillator model for the wave force. The vertical axis gives absorbed power $P_{\mathrm{IR,kalman}}$ relative to the corresponding case with ideal prediction, $P_{\mathrm{IR,ideal}}$, as shown in Figure 15. On the horizontal scale the fraction of optimisation horizon T_h to resonance period $T_0 \approx 4.4\,\mathrm{s}$ is given. The three different diagrams correspond to different significant wave heights (given on top), and the plus, circle and cross marks refer to energy periods of 6, 9 and 12 s, respectively. The waves were synthesised from a Modified Pierson-Moskowitz spectrum.

compared to what is achieved with ideal prediction. This agrees with what should be expected: The uncertainty of the prediction gets larger the longer into the future we try to predict. For longer horizons the control signal from the MPC algorithm is thus based on wrong data, and the performance decreases compared to what is achieved with an ideal predictor, while the short horizons give quite correct predictions and small or no reductions in the power absorption.

The reduced power absorption is especially pronounced for the short wave periods (cross-marked data: 6 s energy period) at low wave heights. Analysing the time series for these sea states when the controller uses ideal prediction, we find that the amplitude restriction is not reached for a large share of the time as opposed to the 9 and 12 s sea states where the buoy oscillation reaches the upper and lower constraint almost every cycle. For the case of the Kalman filter predictor, however, the controller drives the amplitude close to the constraint also for the 6 s cases when the optimisation horizon is long $(T_h/T_0) \geq 1$, leading to an excessive radiation of energy by outgoing waves. This is because the predictor we have defined has a tendency to overestimate the excitation force, as may be anticipated from Figure 18. Uncertainties in the prediction thus have a stronger negative effect on the power absorption when the wave energy converter is operating in the unconstrained region. This may be understood as an effect of a wider bandwidth for the absorber and its machinery as the operation moves into the region of constrained amplitudes, as was also commented for the dependence on optimisation horizon.

Finally, Figure 20 shows how the the power absorption varies with the optimisation horizon when using the Kalman filter predictor. It may be observed that the best value

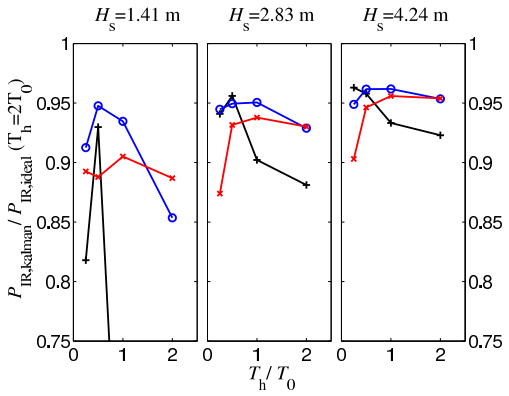

Figure 20: The same data and coding as for Figure 19, but here absorbed power $P_{\mathrm{IR,kalman}}$ is given relative to the absorbed power $P_{\mathrm{IR,ideal}}$ achieved with an ideal predictor and horizon $T_h = 2T_0$ (cf. Figure 16), which is expected to be very close to optimal. The two points on the left-most 6 s curve has been left out of the scale to keep a higher resolution. Their values are 0.53 for $T_h/T_0 = 1$, and 0.44 for $T_h/T_0 = 2$.

for the horizon is found around 0.5 to 1 times the eigenperiod of the heaving buoy for all the tested sea states. The reduction in absorbed power is then about 5 to 10 % in comparison to what is estimated using a long horizon and ideal prediction, which is non-realisable. For laboratory experiments using latching control in irregular waves generated by a JONSWAP spectrum, Budal *et al.* [47] commented that a reduction of about 14 % was observed when running the latching mechanism with a Kalman filter predictor, as compared to the ideal prediction case. We see that the current results suggest that about the same reduction is expected with the MPC type of control, which is more generic and expected to be closer to optimum. Remember also that the currently simulated results are based on the broader Modified Pierson-Moskowitz spectrum, such that a lower reduction (due to better predictions) may be expected for the current control method with sea states of the JONSWAP type.

During simulation work it has been observed that if there are fluctuations in the predicted force, they lead directly to strong fluctuations in the machinery force computed by the controller. Here we have circumvented this by choosing predictor parameters (Table 1) that give a smooth prediction, possibly at the cost of a larger average error. Another way of ensuring a smooth control of the machinery force, which will probably be part of a real implementation, would be to include a low-pass filter between the calculated control signal and the machinery.

6 Conclusion

A method for numerical computation of the constrained optimal motion of a wave energy converter has been demonstrated, using a semi-submerged heaving sphere as an example. It shows how amplitude and machinery force constraints affect the amount of power that

can be absorbed. In these calculations, the excitation force was assumed to be known in advance. The constrained optimisation method enabled calculation of upper limits for the power absorbed by the heaving sphere, and these were compared to the upper bounds given by the Budal diagram. It combines theoretical limits to the absorbed power achievable for a body having a circular radiation pattern with upper bounds due to the finite volume of the body. This diagram yields a good tool for assessing the performance of an implemented control strategy.

Furthermore, a model predictive controller (MPC) was established on the basis of the numerical optimisation procedure. The influence of predictor horizon, step length and accuracy was assessed. When run with a augmented Kalman-filter for the prediction of the wave excitation force, the controller yielded wave power absorption levels within about 90 % of the constrained optimum for a range of irregular wave sea states synthesised from a PM spectrum. If more knowledge about the future excitation force can be made available by measurement and estimation, the MPC algorithm will provide even better results.

Through simulation results it was discovered that under certain circumstances the optimal wave energy absorption in irregular waves may be better than the corresponding optimal absorption in regular waves, i.e. for the same energy period and wave-power level. It was shown how this phenomenon is connected to the shape of the limiting curves for the possible absorbed power.

Although the presented results give prospects for the implementation of constrained reactive control for real wave-energy devices, there are still challenges to be met: The reactive power power flow and the machinery-force amplitudes required to enforce an optimal motion of the wave-energy absorber largely exceed the average absorbed power and the wave excitation force, respectively.

The refinement of prediction methods has not been the aim of this work. With more sophisticated algorithms for the wave prediction, possibly combined with wave measurements at remote locations, it is expected that better prediction algorithms may be developed for the problem studied herein, and that this will the reduce the gap between the absorption achieved using an online prediction algorithm and what is achieved assuming full knowledge of the future force.

References

[1] Evans, D. V., 1981, "Power from water waves," Ann. Rev. Fluid Mech., **13**, pp. 157–187.

[2] Falnes, J., 2007, "A review of wave-energy extraction," Marine Structures, **20**(4), pp. 185–201.

[3] Salter, S. H., 1979, "Power conversion systems for ducks," *Proceedings of International Conference on Future Energy Concepts*, Institution of Electrical Engineers, London, pp. 100–108, publication 171.

[4] Nebel, P., 1992, "Maximizing the efficiency of wave-energy plants using complex-conjugate control," Journal of systems and control engineering, **206**(4), pp. 225–236, proceedings of the Institution of Mechanical Engineers. Part I.

[5] Salter, S. H., Jeffery, D. C., and Taylor, J. R. M., 1976, "The architecture of nodding duck wave power generators," The Naval Architect, pp. 21–24.

[6] Falnes, J., 1995, "On non-causal impulse response functions related to propagating water waves," Applied Ocean Research, **17**(6), pp. 379–389.

[7] Perdigão, J. N. B. A. and Sarmento, A. J. N. A., 1989, "A phase control strategy for OWC devices in irregular seas," *The fourth International Workshop on Water Waves and Floating Bodies*, J. Grue, ed., Dept. Mathematics, University of Oslo, pp. 205–209.

[8] Beirão, P. J. B. F. N., 2007, *Modelling and Control of a Wave Energy Converter: Archimedes Wave Swing*, Ph.D. thesis, Universidade Técnica de Lisboa, Instituto Superior Técnico.

[9] Valério, D., Beirão, P., and Sá da Costa, J., 2007, "Reactive control and phase and amplitude control applied to the archimedes wave swing," *Proceedings of the Sixteenth (2007) International Offshore and Polar Engineering Conference*, Lisbon, Portugal.

[10] Schoen, M. P., Hals, J., and Moan, T., 2008, "Wave prediction and fuzzy logic control of wave energy converters in irregular waves," *Proceedings of the 16th Mediterranean Conference on Control and Automation*, Ajaccio, France.

[11] Schoen, M. P., Hals, J., and Moan, T., 2008, "Robust control of heaving wave energy devices in irregular waves," *Proceedings of the 16th Mediterranean Conference on Control and Automation*, Ajaccio, France.

[12] Falnes, J. and Budal, K., 1978, "Wave-power conversion by point absorbers," Norwegian Maritime Research, **6**(4), pp. 2–11.

[13] Babarit, A., 2005, *Optimisation hydrodynamique et contrôle optimal d'un récupérateur de l'énergie des vagues*, Ph.D. thesis, Ecole Centrale de Nantes.

[14] Falcão, A. F. d. O., 2007, "Phase control through load control of oscillating-body wave energy converters with hydraulic pto system," *Proceedings of the 7th European Wave and Tidal Energy Conference*, Porto, Portugal.

[15] Lopes, M., Hals, J., Gomes, R., Moan, T., Gato, L., and de O. Falcão, A., 2009, "Experimental and numerical investigation of non-predictive phase control strategies for a point-absorbing wave energy converter," Ocean Engineering, **6**(5), pp. 386–402.

[16] Evans, D. V., 1981, "Maximum wave-power absorption under motion constraints," Applied Ocean Research, **3**(4), pp. 200–203.

[17] Pizer, D., 1993, "Maximum wave-power absorption of point-absorbers under motion constraints," Applied Ocean Research, **15**(4), pp. 227 – 234.

[18] Falnes, J., 2000, "Maximum wave-energy absorption by oscillating systems consisting of bodiew and water culumns with restricted or unrestricted amplitudes," Proceedings of the International Offshore and Polar Engineering Conference, **1**, pp. 420–426.

[19] Backer, G. D., Vantorre, M., Banasiak, R., Rouck, J. D., Beels, C., and Verhaeghe, H., 2007, "Performance of a point absorber heaving with respect to a floating platform," *Proceedings of the 7th European Wave and Tidal Energy Conference*, Porto, Portugal.

[20] Eidsmoen, H., 1995, "Optimum control of a floating wave energy converter with restricted amplitude," Proceedings of the International Conference on Offshore Mechanics and Arctic Engineering - OMAE, **1**(Part A), pp. 139 – 146.

[21] Nocedal, J. and Wright, S. J., 1999, *Numerical Optimization*, ISBN 0-387-98793-2, Springer-Verlag New York, Inc.

[22] Rossiter, J. A., 2004, *Model-based predictive control*, ISBN 0-8493-1291-4, CRC Press.

[23] Qin, S. J. and Badgewell, T. A., 2000, "An overview of nonlinear model predictive control applications," *Nonlinear Model Predictive Control*, F. Allgower and A. Zheng, eds., ISBN 3-7643-6297-9, Birkhauser Verlag, Basel, Switzerland, pp. 369–392.

[24] Gieske, P., 2007, *Model Predictive Control of a Wave Energy Converter: Archimedes Wave Swing*, Master's thesis, Delft University of Technology.

[25] Price, A. A. E., Forehand, D. I. M., and Wallace, A. R., 2009, "Time-span of future information necessary for theoretical acausal optimal control of wave energy converters," Proceedings of the European Control Conference 2009, pp. 3761–3766.

[26] Budal, K., Falnes, J., Iversen, L. C., Lillebekken, P. M., Oltedal, G., Hals, T., Onshus, T., and Høy, A. S., 1982, "The Norwegian wave-power buoy project," *Proc. Second International Symposium on Wave Energy Utilization*, H. Berge, ed., ISBN 82-519-0478-1, Tapir, Trondheim, Norway, pp. 323–344.

[27] Hals, J., Bjarte-Larsson, T., and Falnes, J., 2002, "Optimum reactive control and control by latching of a wave-absorbing semisubmerged heaving sphere," Proceedings of the International Conference on Offshore Mechanics and Arctic Engineering - OMAE, **4**, pp. 415 – 423.

[28] WAMIT, 2006, *WAMIT User Manual*, http://www.wamit.com, version 6.3.

[29] Newman, J. N., 1977, *Marine Hydrodynamics*, ISBN 0-262-14026-8, MIT Press, Cambridge, Massachusetts.

[30] Havelock, T., 1955, "Waves due to a floating sphere making periodic heaving oscillations," Proc. Royal Society, **231A**, pp. 1–7.

[31] Hulme, A., 1982, "The wave forces acting on a floating hemisphere undergoing forced periodic oscillations," Journal of Fluid Mechanics, **121**, pp. 443–463.

[32] Jefferys, E. R., 1984, "Simulation of wave power devices," Applied Ocean Research, 1984, Vol. 6, No. 1, **6**, pp. 31–39.

[33] Taghipour, R., Perez, T., and Moan, T., 2008, "Hybrid frequency–time domain models for dynamic response analysis of marine structrues," Ocean Engineering, **35**(7), pp. 685–705.

[34] Falnes, J., 2002, *Ocean waves and oscillating systems: linear interactions including wave-energy extraction*, ISBN 0-521-78211-2, Cambridge University Press, Cambridge.

[35] Chen, C.-T., 1999, *Linear System Theory and Design*, ISBN 0-19-511777-8, Oxford University Press, Inc., 198 Madison Avenu, New York.

[36] Naidu, D. S., 2003, *Optimal Control Systems*, ISBN 0-0493 0892-5, CRC Press LLC.

[37] Budal, K. and Falnes, J., 1975, "A resonant point absorber of ocean waves," Nature, **256**, pp. 478–479, with Corrigendum in Vol. 257, p. 626.

[38] Evans, D. V., 1976, "A theory for wave-power absorption by oscillating bodies," Journal of Fluid Mechanics, **77**, pp. 1–25.

[39] Newman, J. N., 1976, "The interaction of stationary vessels with regular waves," *Proc. 11th Symposium on Naval Hydrodynamics*, London, pp. 491–501.

[40] Budal, K. and Falnes, J., 1977, "Optimum operation of improved wave-power converter." Marine Science Communications, **3**(2), pp. 133 – 150.

[41] Budal, K. and Falnes, J., 1980, "Interacting point absorbers with controlled motion," *Power from Sea Waves*, B. Count, ed., Academic Press, London, pp. 381–399, (ISBN 0-12-193550-7).

[42] Falnes, J., 1994, "Small is beautiful: How to make wave energy economic," *1993 European Wave Energy Symposium*, Edinburgh, Scotland, pp. 367–372, (ISBN 0-903640-84-8).

[43] Sørensen, A. J., 2005, "Structural issues in the design and operation of marine control systems," Annual Reviews in Control, **29**(1), pp. 125 – 149.

[44] Matlab, 2006, URL http://www.mathworks.com/, version 7.2, The Mathworks Inc.

[45] Michel, W. H., 1999, "Sea spectra revisited," Marine Technology, **36**(4), pp. 211 – 227.

[46] Brown, R. G. and Hwang, P. Y. C., 1997, *Introduction to random signals and applied Kalman filtering*, ISBN 0-471-12839-2, John Wiley & Sons, New York, 3 ed.

[47] Budal, K., Falnes, J., Hals, T., Iversen, L. C., and Onshus, T., 1981, "Model experiment with a phase controlled point absorber," *Proceedings of Second International Symposium on Wave and Tidal Energy*, H. S. Stephens and C. A. Stapleton, eds., BHRA Fluid Engineering (Cranford, Bedford), Cambridge, UK, pp. 191–206, (ISBN 0-906085-43-9).

Article E: Hals et al., accepted for pulication in Journal of OMAE

A comparison of selected strategies for adaptive control of wave energy converters

Jørgen Hals*, Johannes Falnes, and Torgeir Moan
Centre for Ships and Ocean Structures (CeSOS)
Norwegian University of Science and Technology (NTNU)
Otto Nielsens v. 10
7491 Trondheim, Norway

November 20, 2009

Abstract

Wave-energy converters of the point-absorbing type (i.e. having small extension compare to the wave length) are promising for achieving cost reductions and design improvements because of a high power-to-volume ratio and better possibilities for mass production of components and devices as compared to larger converter units. However, their frequency response tends to be narrow-banded, which means that the performance in real seas (irregular waves) will be poor unless their motion is actively controlled. Only then the invested equipment can be fully exploited, bringing down the overall energy cost.

In this work various control methods for point-absorbing devices are reviewed, and a representative selection of methods are investigated by numerical simulation in irregular waves, based on an idealised example of a heaving semi-submerged sphere. Methods include velocity proportional control, approximate complex conjugated control, approximate optimal velocity tracking, phase control by latching and clutching, and model-predictive control; all assuming a wave pressure measurement as the only external input to the controller. The methods are applied for a single-degree-of-freedom heaving buoy.

Suggestions are given on how to implement the controllers, including how to tune control parameters and handle amplitude constraints.

On the basis of simulation results, comparisons are made on absorbed power, reactive power flow, peak-to-average power ratios and implementation complexity. Identified strengths and weaknesses of each method are highlighted and explored. It is found that overall improvements in average absorbed power of about 100 to 330 % are achieved for the investigated controllers as compared to a control strategy with velocity-proportional machinery force. One interesting finding is the low peak-to-average ratios resulting from clutching control for wave periods about 1.5 times the resonance period and above.

Key words: Ocean waves, renewable energy, reactive control

*Corresponding author, e-mail:jorgen.hals@ntnu.no, phone: +47 97 66 00 28

Nomenclature and abbreviations

β	filter frequency ratio [1]
η	heave position [m]
ω	angular frequency [rad/s]
ρ	ocean water density [1025 kg/m^3]
A	area [m^2]
$\mathbf{A}$	state-space system matrix
$\mathbf{B}$	state-space input matrix
$\mathbf{C}$	state-space output matrix
ACC	approximate complex conjugate (control)
AVT	approximate optimal velocity tracking
F	force [N]
FB	feedback
H	transfer function
H	wave height [m]
H_s	significant wave height [m]
MPC	model-predictive control
K	controller gain
P	power [W]
PMC	peak-matching clutching
PML	peak-matching latching
PTO	power take-off
R	resistance [kg/s]
RL	resistive loading
S	hydrostatic stiffness in heave [N/m]
T	period [s]
T_e	energy period [s]
TUC	threshold unclutching
TUL	threshold unlatching
X	reactance [kg/s]
Z	impedance [kg/s]
g	acceleration of gravity [9.81 m/s^2]
k	retardation function the radiation force [kg/s]
m	mass [kg]
m_r	added mass [kg]
s	Laplace variable [s^{-1}]
sign$(\cdot)$	signum function
t	time [s]
$u(\cdot)$	Heaviside step function
v	velocity [m/s]
x	element of $\mathbf{x}$
$\mathbf{x}$	state-space vector
$\mathbf{z}$	radiation model state vector

Subscripts

HP	high-pass
I	integral
LP	low-pass
P	proportional
R	radiation (total)
a	absorbed
c	constant
e	excitation
es	end stop
f	final
i	intrinsic
i	inertia
k	index
l	latching
lim	limit
m	machinery
max	maximum
h	horizon
r	radiation
ref	reference
s	stiffness
u	system/plant
u	useful
v	velocity
w	water plane
0	relating to resonance
∞	regarding $\omega \to \infty$
$a \times b$	dimensions, vertical $\times$ horizontal

Superscripts

opt	optimal
$*$	complex conjugate
$\bar{}$	mean value

1 Introduction

An early result of wave energy research (see review articles by Evans [1] and Falnes [2]) was that the maximum useful absorbed energy for a body oscillating in one mode is achieved provided that the intrinsic reactance $X_i(\omega)$ is cancelled and that the load resistance $R_m(\omega)$ equals the intrinsic resistance $R_i(\omega)$. (The word *intrinsic* is here used to signify the systems

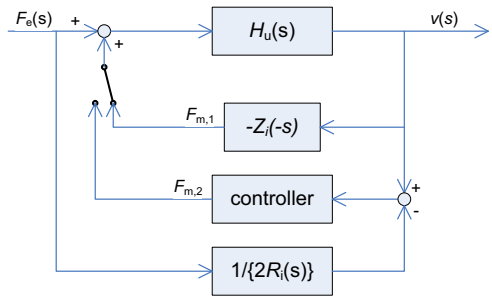

Figure 1: Block diagram showing alternatives paths for optimal control of the wave energy converter represented by $H_u(s)$. The choice between $F_{m,1}$ and $F_{m,2}$ corresponds to the choice between complex conjugate control, and phase and amplitude control, respectively [3, Fig. 6.7]. We have assumed that the hydrodynamic parameters can be approximated by rational Laplace transform functions, $R(\omega) \approx R(s)|_{s=i\omega}$ and $m_r(\omega) \approx m_r(s)|_{s=i\omega}$.

own impedance terms, including friction and viscous losses, but excluding machinery forces.) This corresponds to what in electric circuit theory is known as *impedance matching*.

Falnes [3, Chapter 6] describes two alternative strategies for achieving this:

1. Complex conjugate control
2. Phase and amplitude control

As illustrated by Figure 1, where Z_i is the complex intrinsic impedance, the first alternative corresponds to providing a direct feedback from the velocity of the buoy. Now this represents a challenge in that the velocity-to-force transfer function $-Z_i^*(\omega) = -R_i(\omega)+iX_i(\omega)$ becomes inherently *anti-causal* (i.e. transforms to a left-sided impulse response function) because of the complex conjugation. In other words, the optimal machinery force depends solely on future values of the buoy velocity, which is obviously impossible to implement in practice, as the velocity depends on our choice for the machinery force. We are thus compelled to search for realisable (sub-optimal) approximations for the practical implementation, and this will be treated here.

The other alternative, phase and amplitude control (shown as $F_m, 2$ in Figure 1), is to feed forward the excitation force through a transfer function $H_v(s) = 1/\{2R_i(s)\}$ yielding the optimal velocity $v^{\text{opt}}(s) = F_e(s)/\{2R_i(s)\}$ as a reference signal (where it is assumed that the radiation resistance $R_i(\omega)$ can be approximated by a rational Laplace transform function; $R(\omega) \approx R(s)|_{s=i\omega}$). A controller can then be programmed to track the desired velocity, a common application of control engineering. But this alternative is also encumbered by causality trouble; the transfer function is *non-causal* (i.e. transforms to a two-sided impulse response function [3, Section 6.3]), but this can be overcome in an approximative manner if we are able to predict the future excitation force, or by approximating the transfer function $H_v(s)$ by a causal function. In principle, the span of information about the future wave needed for optimal control depends on the geometry of the device, while the available information depends on the coherence of the incident wave as explained by Price *et al.* [4].

Both of these alternatives for optimal control imply that the machinery has to handle a reactive power flow, and may therefore be categorised under the broader classification of *reactive control*.

Perdigão et al. [5] reported a solution for approximating the complex conjugate control applied to an oscillating water column device. Looking at control alternatives for the Archimedes Wave Swing (AWS), Beirão [6] tried to apply internal model control as a means to approximate optimal velocity tracking, and achieved a reasonable performance. He also demonstrated the use of linearisation feedback control applied to a non-linear model of the AWS.

In a more recent approach Gieske [7] tried to apply model-predictive control (MPC) to wave energy conversion, also with AWS as the example. This method resembles what Eidsmoen [8] tried to do when he optimised the converter's response over a short future horizon by the use of force predictions. The application of MPC to wave energy converters was further studied by Hals et al. [9], and has shown to yield power absorption close to optimum in irregular waves.

All of approximations to optimal control described above requires that the machinery handles reactive power. A set of controllers for wave energy absorbers that do not involve reactive power flow may be classified as *resistive bang-bang controllers*. *Latching* and *clutching control* belong here. These ideas derived as an intuitive way of achieving optimum oscillation phase by keeping the absorber fixed during parts of the cycle (latching) or by coupling and decoupling the machinery at intervals (clutching) [10, 11]. Hoskin and Nichols [12] used a variational calculus approach, and showed that latching control belongs to a class of solutions that in optimal control theory is known as bang-bang control [13], i.e. the optimal solution is for the control variable to switch between its minimum and maximum allowed values. The same goes for clutching control.

The challenge in implementing latching and clutching control strategies is twofold: (i) Designing a durable mechanism or method to carry out the latching/unlatching (or coupling/decoupling in the case of clutching control). (ii) To determine the unlatching instants. In principle one needs to know the excitation ahead in the same manner as for the non-causal transfer function resulting from the optimality conditions referred to above. This task was already solved with promising results about 30 years ago [14, 15]. For more complex systems, with more than one degree of freedom, the application of latching control has shown to be more challenging [16, 17], although mathematical description inspired by Thévenin's for electrical circuits may ease the problem [18]. A simplified approach was taken by Falcão [19], who, inspired by rectifying hydraulic valves, omitted the need for prediction by introducing a threshold-triggered unlatching. This principle was verified and developed further by Lopes et al. [20].

Although very similar to latching, the clutching control idea appeared later and has received less attention in the wave energy literature. The key point is that instead of being locked, the oscillator is moving freely during parts of the oscillation cycle. The notions *freewheeling* [11] and *unlatching* [21] control has also been used for this strategy. Kamensky et al. [10] showed that for unconstrained oscillation of a harmonic oscillator, clutching can be preferable to latching in some conditions. In a recent study Babarit *et al.* [22] showed that clutching is theoretically superior to strategies of pseudo-continuous control that try to mimic the behaviour of e.g. a linear damper.

Evans [23], Pizer [24] and Falnes [25] consecutively discussed the influence of global motion constraints on wave energy absorption. Their results were based on a frequency-domain approach. Evans and Pizer both presented examples on how such constraints influences the performance of a heaving sphere absorber. Recently Hals et al. [9] studied optimal constrained motion for the same kind of absorber using a time-domain method. Many devices are designed with physical end-stop mechanisms like spring and dashpot components [26] or water brakes [27].

There have been numerous suggestions on how to predict the incoming wave, both in case of remote and local wave monitoring [4]. A standard solution for estimating and predicting signals is Kalman filtering (see e.g. [28]). By running the filter equations iteratively based on the current filter states, a priori estimates for future values may be extrapolated. In [9] an augmented Kalman filter was used to provide useful predictions 2-4 seconds ahead based solely on local monitoring, and the same method will be used here.

Another question is how to tune the control parameters. The classical solution for adaptive control is *gain scheduling* (see e.g. [29]). The parameters are then updated based on a predefined plan, which may be based on experience or on a model giving the optimal parameter settings for different operating conditions; in our case for different sea states. An old method for self-tuning regulators that has regained interest in recent years is *extremum-seeking control* [30]. It is a powerful method for real-time optimisation of the control parameter that only requires that a purposeful convex objective function may be defined, and which in general works at rates of adaptation almost as fast as the plant dynamics. Here we apply this method to maximise the power output from wave energy converters.

The purpose of this article is to study how a representative selection of the mentioned control strategies can be implemented for online control, and to compare their performance and properties. We begin, in Section 2, by presenting our model of a heaving semi-submerged sphere, which will serve as a generic example for the wave-absorbing body, and then proceed, in Section 3 by defining and explaining the control algorithms and the assumptions made. Finally, the simulation scheme, results and analysis are reported in Sections 4 and 5.

2 Converter model

In order to keep the investigation at a generic level, a heaving semi-submerged sphere will be used as an example for the wave energy converter. Dynamics of other types of converters will have similar properties, although they can be more complex. The model used is sketched in Figure 2 and includes the following effects:

Net restoring stiffness force $F_s = \rho\, g\, A_w\, \eta$, which is the difference of the gravitational and buoyancy forces, where ρ is the water density, g the acceleration of gravity, $A_w = \pi r^2$ the water plane area, and η the heave excursion.

Inertia force $F_i = m\, \ddot{\eta}$, due to the mass m of the moving body with acceleration $\ddot{\eta}$.

Wave excitation force F_e, which is the sum of pressure forces on the body surface due to incident and diffracted waves.

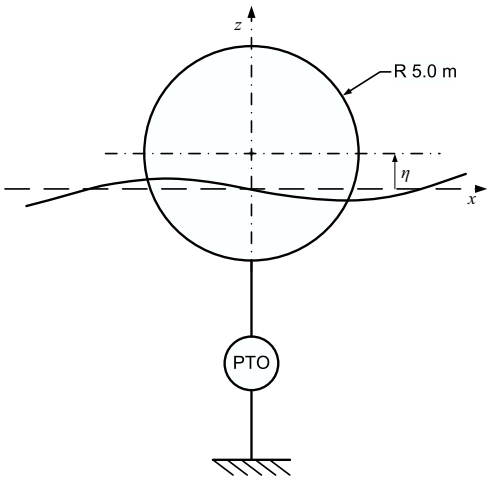

Figure 2: An illustration of the heaving sphere used as a wave energy absorber in this work. Its radius r is 5 m and it is semi-submerged at its equilibrium position, i.e. the mass $m = \rho 2\,\pi\, r^3/3$. A power take-off system (PTO) is connected between the buoy and a fixed reference, giving a force F_m on the buoy.

Wave radiation force F_R due to the radiated wave when the body moves. It may be written as $F_R = m_\infty\,\ddot{\eta} + \int_0^t k(\tau)\,\dot{\eta}(t-\tau)\,d\tau$, where the retardation function $k(t)$ is related to the radiation resistance (or wave damping coefficient) R_r by $k(t) = (2/\pi)\,\int_0^\infty R_r(\omega)\,\cos(\omega t)\,d\omega$ [31]. The factor $m_\infty = \lim_{\omega\to\infty} m_r(\omega)$, where $m_r(\omega)$ is the added mass. The convolution term, which we will denote F_r, may be approximated by a state-space model [32, 33]; $\mathbf{z} = \mathbf{A}_r\mathbf{z} + \mathbf{B}_r\dot{\eta}$, with output equation $F_r = \mathbf{C}_r\mathbf{z}$, where $\mathbf{z}$ is an additional state vector, and $\mathbf{A}_r$, $\mathbf{B}_r$ and $\mathbf{C}_r$ are state, input and output matrices, respectively.

Machinery force F_m, which is the subject of this work, and which is assumed to follow the command given by the controller, i.e. it is assumed strong and fast enough to immediately follow a set-point.

The hydrodynamic forces (excitation and radiation) are approximated by linear theory, i.e. both motions and wave amplitudes are assumed to be small. The reference point against which the machinery works is assumed to be rigid, and possible dynamics of connecting wires or struts are not accounted for.

An equation of motion for the heave mode may then be given as [31]

$$F_i + F_R + F_s = F_e + F_m \tag{1}$$

or, explicitly,

$$\begin{aligned}(m + m_\infty)\ddot{\eta} + \int_0^t k(\tau)\,\dot{\eta}(t-\tau)\,d\tau \\ + \rho\,g\,A_w\,\eta = F_e + F_m\end{aligned} \tag{2}$$

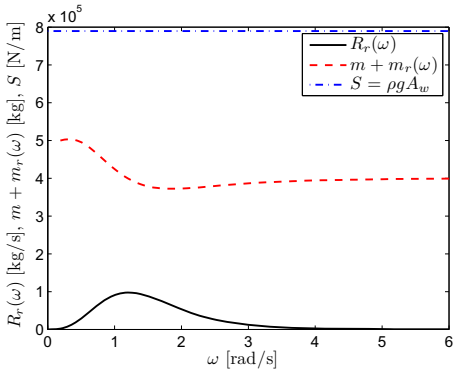

Figure 3: Hydrodynamic parameters for a semi-submerged heaving sphere of radius 5 m. The radiation resistance $R_r(\omega)$ is given by the black curve, the red dashed curve gives the sum of physical mass and added mass $m + m_r(\omega)$, and the hydrostatic stiffness S, which is approximated by a constant, is shown by the blue dash-dotted curve.

With a state-space approximation for the convolution term as mentioned above, the whole model may be rewritten in state-space form as

$$\begin{aligned}
\dot{\mathbf{x}}(t) &= \begin{bmatrix} 0 & \frac{-\rho g A_w}{1+m_\infty/m} & \frac{-\mathbf{C}_r}{1+m_\infty/m} \\ 1/m & 0 & \mathbf{0}_{1\times 4} \\ \mathbf{B}_r/m & \mathbf{0}_{4\times 1} & \mathbf{A}_r \end{bmatrix} \mathbf{x}(t) \\
&\quad + \begin{bmatrix} \frac{1}{1+m_\infty/m} \\ 0 \\ \mathbf{0}_{4\times 1} \end{bmatrix} (F_m(t) + F_e(t)) \\
&\equiv \mathbf{A}\,\mathbf{x}(t) + \mathbf{B}\,(F_m(t) + F_e(t))
\end{aligned} \tag{3}$$

where $x_1 = m\dot{\eta}$, $x_2 = \eta$ and $[x_3, \ldots x_N]^{\mathrm{T}} = \mathbf{z}$, where N-2 is the order of the state-space approximation for the convolution term F_r. For the heaving sphere a model of order four has shown to be sufficient for F_r. The total model thus consists of six first-order ordinary differential equations and may be solved by conventional tools for numerical integration. In block diagrams to be shown later, the model is represented by the system transfer function $H_u(s) = (s\mathbf{I} - \mathbf{A})^{-1}\mathbf{B}$, giving the system states as output.

In the following we will need the notion of intrinsic resistance R_i and reactance X_i [3, p. 184]. These are frequency dependent (in a manner governed by the body mass and geometry), and their functions for the heaving sphere are shown in Figure 3. In our case we have assumed that there is no viscous or frictional loss, so the intrinsic resistance $R_i(\omega)$ is equal to the radiation resistance $R_r(\omega)$, which is due to outgoing waves. The reactance depends on the added mass $m_r(\omega)$ and the buoyancy stiffness $S = \rho g A_w$ for heave motion, and is defined by $X_i(\omega) = \omega(m + m_r(\omega)) - S/\omega$.

The hydrodynamic parameters are shown in Figures 3 and 4.

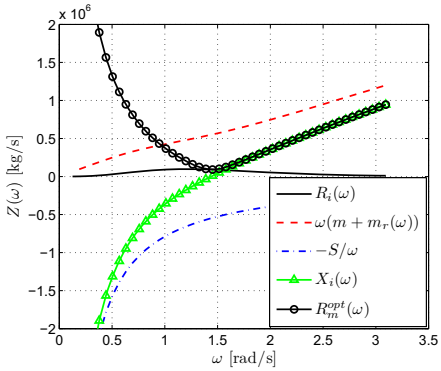

Figure 4: Intrinsic impedance terms for the heaving sphere. Also shown is the optimal load resistance $R_m^{\text{opt}} = \sqrt{R_i(\omega)^2 + X_i(\omega)^2}$ for non-reactive control.

3 Control methods

In this section the various control algorithms considered in this study and their implementation are described and discussed. The question is how to control the machinery force F_m.

3.1 Resistive loading (RL)

A very common assumption within wave energy modelling has been to assume the following form for the machinery force,

$$F_m(t) = -R_m\,\dot{\eta}(t), \tag{4}$$

such that the machinery force depends linearly on the velocity $\dot{\eta}$, with a resistance R_m as coefficient of proportionality. The strategy defined by Equation (4) may be given as the block diagram shown in Figure 5. We include it here for reference and because it is often used as a useful starting point in modelling and simulation studies as well as laboratory experiments and prototyping. Time series of force, position and velocity signals for this strategy are shown in Figure 6.

With such a machinery force, the optimal setting for the load resistance is known to be $R_m^{\text{opt}}(\omega) = \sqrt{R_i^2(\omega) + X_i^2(\omega)}$, where R_i and X_i are the intrinsic resistance and reactance, respectively [34].

It may be seen from Figure 4 that the further we are from resonance, the larger the optimal R_m^{opt} term will be. This lowers the response amplitude, but reduces the phase difference between force and velocity (cf. phase and amplitude control). As the resulting machinery force is proportional to the velocity there is no reactive power flow, and with the requirement $R_m > 0$, the machinery never has to work in motor mode. For irregular waves we explore a simplified approach by choosing a constant R_m, different for each sea state.

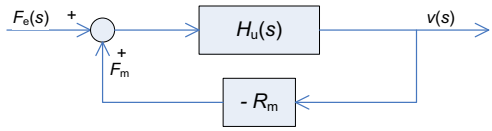

Figure 5: Block diagram for the resistive loading (RL) strategy. It gives a machinery force directly proportional to the buoy velocity $v(s)$. The dynamics of the heaving buoy is represented by the transfer function $H_u(s)$.

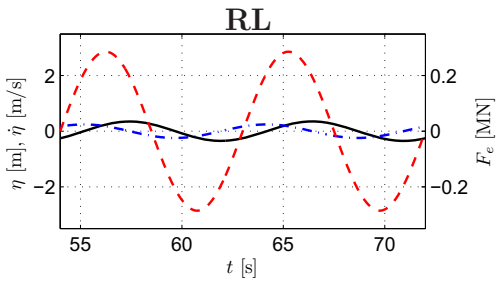

Figure 6: Regular wave ($T = 9\,\mathrm{s}$ and $H = 1\,\mathrm{m}$) time series example for the RL strategy. The red dashed curve gives the excitation force F_e, the blue dash-dotted curve gives the velocity $v = \dot{\eta}$, and the fully drawn black curve gives the heave position η.

3.2 Approximate complex-conjugate control (ACC)

With impedance matching, the optimal control force may be written $F_m^{\mathrm{opt}}(\omega) = -Z_m^{\mathrm{opt}}(\omega)\,u(\omega) = -Z_i^*(\omega)\,u(\omega)$, i.e. the optimal machinery impedance Z_m^{opt} equals the complex-conjugate of the intrinsic impedance $Z_i(\omega) = R_i(\omega) + iX_i(\omega)$ [35, 3]. (The minus sign occurs because of the way we have defined the machinery force, see Equation (1).) As discussed in Section 1 we then need to find a causal approximation $Z_m(s)|_{s=i\omega}$ to the optimal feedback function $Z_m^{\mathrm{opt}}(\omega)$ giving a system as illustrated in Figure 7.

For a monochromatic wave input of angular frequency ω_k this optimal force may be written as the time-domain function

$$F_m^{\mathrm{opt}}(t) = (m + m_r(\omega_k))\ddot{\eta}(t) - R_i(\omega_k)\,\dot{\eta}(t) + S\,\eta(t) \tag{5}$$

Keeping the same function with constant coefficients (from a properly chosen ω_k) for operation in irregular waves could serve as a simple approximation. We must, however, be careful in order to ensure that the controlled system becomes stable.

Let us now simplify the WEC model (3) by replacing the frequency-dependent parameters m_r and R_i by constants so that we get

$$\begin{aligned}\dot{\mathbf{x}}(t) &= \begin{bmatrix} -R_c/m_c & -S \\ 1/m_c & 0 \end{bmatrix}\mathbf{x}(t) \\ &\quad + \begin{bmatrix} 1 \\ 0 \end{bmatrix}(F_m(t) + F_e(t))\end{aligned} \tag{6}$$

with $x_1 = m_c\dot{\eta}$. Using the velocity variable $v(s) = \mathcal{L}\{\dot{\eta}(t)\}$ Equation (6) has the Laplace-plane equivalent

$$m_c\, s\, v(s) + R_c\, v(s) + S\frac{v(s)}{s} = F_e(s) + F_m(s) \tag{7}$$

In this case the intrinsic impedance is

$$Z_i(s) = m_c\, s + R_c + \frac{1}{s}\, S = \frac{m_c\, s^2 + R_c\, s + S}{s} \tag{8}$$

and the machinery impedance may be written

$$Z_m(s) = \frac{m_m\, s^2 + R_m\, s + S_m}{s} \tag{9}$$

with optimal values $m_m = -m_c$, $R_m = R_c$ and $S_m = -S$ according to the complex-conjugate relation behind Equation (5). The machinery force is now

$$F_m(s) \equiv -Z_m(s)\, v(s) = -\,\frac{m_m\, s^2 + R_m\, s + S_m}{s}\, v(s) \tag{10}$$

By cancellation of m_c and S terms this gives the optimal response velocity

$$v(s) = \frac{F_e(s)}{2R_c} \tag{11}$$

as it should. The force-to-velocity transfer function of the total controlled system becomes

$$\begin{aligned} H_{v,F_e} &= \frac{1}{Z_i(s) + Z_m(s)} \\ &= \frac{1}{(m_c - m_m)\, s^2 + (R_c + R_m)\, s + (S - S_m)} \end{aligned} \tag{12}$$

Now to the point: We see that if the values $|m_m|$ and $|S_m|$ have a larger magnitude than the intrinsic values, the coefficients become negative (giving positive poles) and the controlled system will be unstable. Using this as a simplification for the wave energy converter, we may place the poles of the controller such that we are sure not to get positive poles. It can be done by looking at the minimum values for $m + m_r(\omega)$ and S and choosing the controller parameters m_m and S_m with some safety margin, see Figure 3. We see that stability may be ensured by choosing constant values $m_m \leq 3.72 \cdot 10^5\,\mathrm{kg}$ and $S_m \leq 7.90 \cdot 10^5\,\mathrm{N/m}$. (We have used the values $3.5 \cdot 10^5\,\mathrm{kg}$ and $7.5 \cdot 10^5\,\mathrm{N/m}$, respectively.) The parameter R_m may be taken as a parameter to be optimised for each sea state. Figure 8 shows a time series example for the ACC strategy.

3.3 Tracking of approximate optimal velocity (AVT)

As mentioned in Section 1, the phase and amplitude control yields an expression for the optimal velocity, and may therefore be seen as a velocity tracking problem. The question is how to approximate the optimal velocity function $v^{\mathrm{opt}}(\omega) = F_e/\{2R_i(\omega)\}$. Here we will

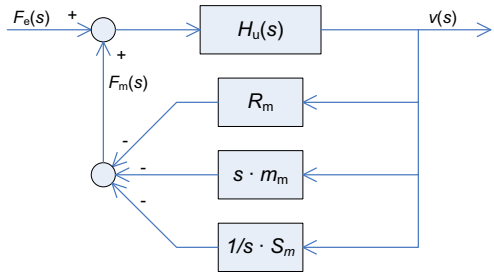

Figure 7: Block diagram for the approximate complex conjugate (ACC) control. The machinery force is the sum of terms proportional to position, velocity and acceleration.

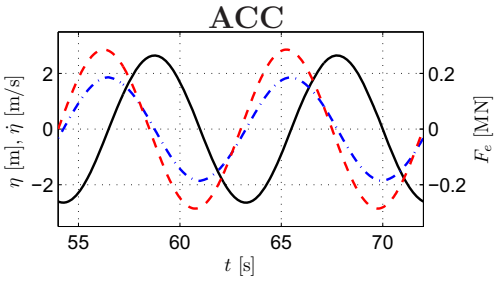

Figure 8: Regular wave ($T = 9\,\mathrm{s}$ and $H = 1\,\mathrm{m}$) time series example for the ACC strategy. Line patterns as in Figure 6.

simply replace $R_i(\omega)$ by a constant R_c so that $v_{\mathrm{ref}} = F_e/\{2R_c\}$, and we will see how the choice of its value influences the result. We have not tried to find a frequency dependent approximation to $1/\{2R_i(\omega)\}$ although it could be worthwhile investigating, for instance as described in [5] and also in [3, Sec. 6.3].

Once having defined the reference signal, the tracking can be done with a simple P or PI controller. Thus the whole scheme can be pictured as in Figure 9, with

$$Z_{\mathrm{PI}}(s) = \beta K_{\mathrm{P}} \frac{1 + T_i s}{1 + \beta T_i s} \tag{13}$$

We have used $K_{\mathrm{P}} = 5 \cdot 10^7\,\mathrm{Ns/m}$, $\beta = 1.2$ and $T_i = 4.2\,\mathrm{s}$. A time series example for operation in regular waves is shown in Figure 10.

3.4 Model-predictive control (MPC)

The application of model-predictive control to this problem was studied in a recent work [9], and we only outline the principles here. The idea is to optimise the expected response of the system over a short future horizon T_h using a discrete-time model of the conversion unit together with a prediction of the input force. The maximisation of power output under the chosen constraints may be cast into a quadratic programming (QP) optimisation problem, which guarantees that a solution is found. By moving the time window of predictions along

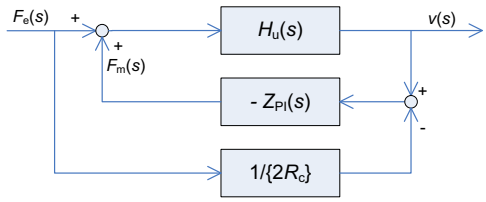

Figure 9: Block diagram for the approximate optimal velocity tracking (AVT) strategy. The velocity reference signal is tracked by the use of a PI controller $Z_{PI}(s)$.

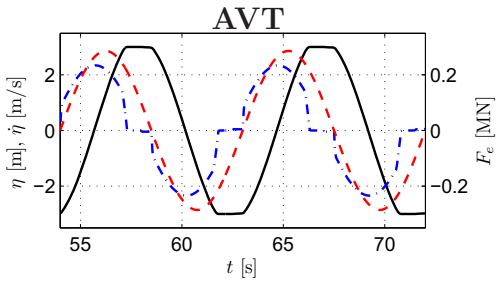

Figure 10: Regular wave ($T = 9\,\mathrm{s}$ and $H = 1\,\mathrm{m}$) time series example for the AVT strategy. Line patterns as in Figure 6.

as the time is running, the optimisation may be solved anew at predefined intervals, finding the best control force at each instant given the instantaneous states and conditions. The scheme is illustrated by Figures 11 and 12. A time series example of MPC is shown in Figure 13.

The MPC controller fully exploits our knowledge about the system (including constraints) and is therefore able to provide a control that is close to constrained optimal.

3.5 Phase control by latching (PML and TUL)

Latching control is achieved by halting the motion each time the velocity becomes zero, and release it according to a certain rule such that the phase between velocity and excitation force is improved compared to the passive (RL) case. For regular waves the unlatching rule may be defined as fixed intervals of latching, but in irregular waves this doesn't work well because the time interval between force maxima varies. A fruitful strategy is to aim at aligning the peaks of the force and velocity signals [36, 37], and this may be approximately achieved by releasing the buoy approximately $T_0/4$ before the next (predicted) peak for the wave force ($T_0 \approx 4.4\,\mathrm{s}$ being resonance period). Here we denote this strategy by *peak-matching latching control*, abbreviated PML, and a block diagram for the controller is shown in Figure 14. The time series example follows in Figure 15.

Instead of aligning peaks, Falcão [19] and Lopes et al. [20] suggested a method that do not rely on predicted values for the excitation, but rather only on an estimation of the instantaneous excitation force. The principle tells that the buoy should be released once

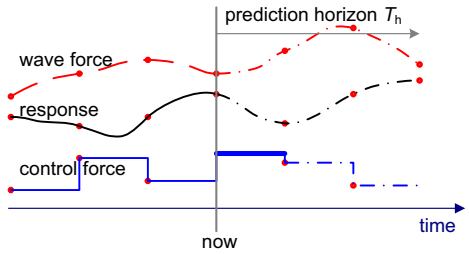

Figure 11: The moving prediction horizon principle of model-predictive control (MPC). The control force is changed in discrete time steps that are short compared to the system dynamics (i.e. in practice shorter than shown here). At each discrete time step a new optimisation of the predicted response is calculated using the predicted excitation force as input, and the first element of the machinery force vector is applied to the system (indicated by the thick line).

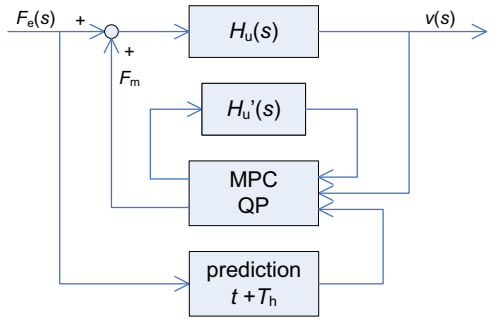

Figure 12: Block diagram for the model predictive control (MPC) strategy. A quadratic programming (QP) optimisation problem is solved at each discrete time step of the controller. The prediction horizon is set to span an interval over which the force prediction is reasonably accurate. Here $T_h = 2.2\,\mathrm{s}$ have been used.

the force passes a chosen threshold, thus we will refer to it as threshold unlatching control (TUL). In regular waves the result is identical to PML, but in irregular waves there will be differences in the unlatching instants. Obviously, either strategy is best suited for incident waves of typical period $T > T_0$. Luckily, at least for heaving point absorbers, the physics of the problem tells that this will most often be the case. (It should be mentioned that Babarit *et al.* [37] showed that latching may also be useful for the case where $T < T_0$.)

During the unlatched intervals the machinery load resistance, R_m, is kept constant at a value that may be optimised for each sea state. In real-world designs the latching may be achieved by clamping brakes, hydraulic control valves or other. For modelling and simulation purposes, two alternative methods have been common. The first method is to have two models for the system; one for the latched state ($v = 0$) and one for the moving state ($v = f(F_e(t), R_m, t)$), and to switch between these at the right instants. The other is to introduce an additional large resistance R_l in the mathematical model, which is active during

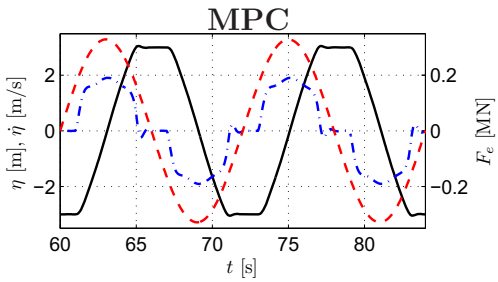

Figure 13: Regular wave ($T = 9\,\mathrm{s}$ and $H = 1\,\mathrm{m}$) time series example for the MPC strategy. Line patterns as in Figure 6.

latching intervals and zero otherwise. Thus here no assumption is made about how the latching mechanism is realised, although the latter method may be seen as a simple model of a clamping brake. The two methods give practically no difference in the result as long as the resistance is chosen large enough. We use the second approach with $R_l \geq 1 \cdot 10^9\,\mathrm{kg/s}$. Because the power take-off is only resistive, the latching control machinery has no reactive power flow.

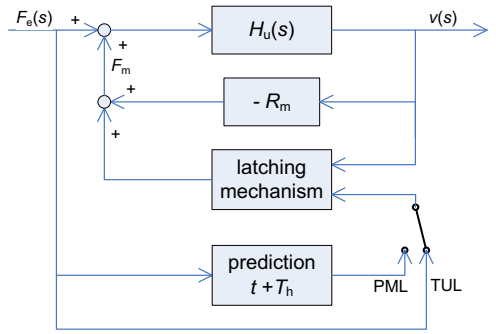

Figure 14: Block diagram for the peak matching latching (PML) and threshold unlatching (TUL) control strategies. The latching mechanism is used to hold the buoy in a fixed position. During motion the machinery force is proportional to the buoy velocity.

3.6 Phase control by clutching (PMC and TUC)

The only difference between clutching and latching is that the resistance is switched between zero and a constant instead of between a (different) constant and a very large value (in principle infinite). This results in time series as shown in Figure 17, and a block diagram is given in Figure 16. Although very similar, there are, as we shall see, some important differences in the performance of latching and clutching controllers. With clutching control the power is harvested during a slow sliding motion from the outer positions (see Figure 17), whereas with latching it is harvested during the transitions between outer steady positions

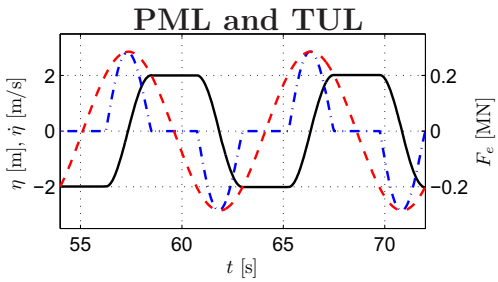

Figure 15: Regular wave ($T = 9\,\mathrm{s}$ and $H = 1\,\mathrm{m}$) time series example for the PML and TUL strategies. Line patterns as in Figure 6.

(see Figure 15).

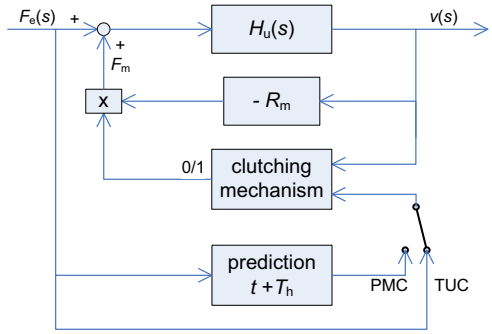

Figure 16: Block diagram for the peak-matching clutching (PMC) and threshold unclutching (TUC) control strategies. The clutching mechanism is used to engage and disengage the machinery force. When engaged, the machinery force is proportional to the buoy velocity.

3.7 Parameter tuning

The MPC controller optimises the control input to the system on a wave-to-wave time scale. Because of this it can lead to a performance close to what is the theoretical optimum. All the controllers defined above have a structure where parameters need to be tuned on a longer time scale, say from a duration corresponding to wave-group or sea-state variation. Here we will consider the adaptive schemes referenced in the introduction, namely gain scheduling and extremum-seeking control.

3.7.1 Gain scheduling

If we disregard end-stop interference, most of the controller parameters depend on the wave frequency only (once the device geometry has been set). A good approximation to the optimal parameter settings is then achieved by using knowledge about the average wave

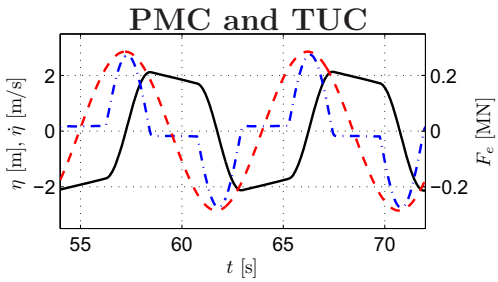

Figure 17: Regular wave ($T = 9\,\mathrm{s}$ and $H = 1\,\mathrm{m}$) time series example for the PMC and TUC strategies. Line patterns as in Figure 6.

period. All that is needed is then an online estimate of the instantaneous average period, and the parameters may be set according to a predefined schedule. If the relation between wave frequency and parameter settings is not known, the schedule may be established based on experience or trial and error. For the threshold unlatching and unclutching strategies information about the wave heights are also needed [20].

In our implementation we have processed the last 100 zero up-crossing periods in computing the needed statistical measures.

3.7.2 Extremum seeking

Extremum seeking control is a powerful method for real-time optimisation where a modulation of the control input is used to drive the control parameters to their optimum value. The method does not depend on having a model of the process; all that is needed is that the control goal can be formulated as an objective function that is convex in the control parameters. It may be freely defined by the control designer. The scheme is illustrated by Figure 18.

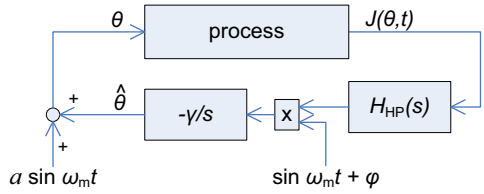

Figure 18: Block diagram for the extremum-seeking control algorithm. A modulation signal $a\sin(\omega_m t)$ is added to the parameter setting $\hat{\theta}$. The objective function J is chosen as the output from the process, and it is high-pass filtered (H_{HP}) to retain only value changes. The multiplication serves as a demodulation, and the result is low-pass filtered by the $-\gamma/s$ block [38, 30].

The crucial point in order to succeed with extremum-seeking design is thus the definition of the objective function. For the application to wave energy we wish to maximise the

average converted power, and therefore need to filter out the power variation due to the zero-crossings of velocity (which gives instants of zero power conversion). And we wish for a measure that represents the absorbed useful power, but which is quite constant even though the incident wave power level is changing. On this background we have defined the objective function J as an approximation to the absorption width by low-pass filtering the useful power $P_u(t) = F_m(t)\, v(t)$ and dividing by the low-pass filtered squared excitation force:

$$J(t) = \frac{h_{\mathrm{LP}}(t) \star P_u(t)}{h_{\mathrm{LP}}(t) \star F_e(t)^2} \tag{14}$$

where $h_{\mathrm{LP}}(t)$ is the low-pass filter, and $\star$ signifies convolution. A second-order low-pass filter $H(s) = 1/(1+Ts)^2$ with $T = 57.3\,\mathrm{s}$ has been used here.

3.8 Constraint handling/state saturation

In the same way as physical end stops may be introduced in order to restrict the stroke of moving bodies, virtual end stops may be incorporated in the controller in order to avoid that the bodies reach the physical end stops, or to reduce the impact when limits are reached. Control methods for handling this kind of state saturation is common in motion planning for robots, where obstacles may be represented by repulsive potentials (see e.g. [39, Chapter 5]). For the problem at hand a corresponding effect may be achieved by adding spring and/or damper terms to the calculation of the machinery force set-point, for instance

$$\begin{aligned} F_m = R_m\dot{\eta} &- \mathrm{sign}(\eta)\, S_{\mathrm{es}}\, (|\eta| - \eta_{\mathrm{lim}})\, u(|\eta| - \eta_{\mathrm{lim}}) \\ &- R_{\mathrm{es}}\, \dot{\eta}\, u(|\eta| - \eta_{\mathrm{lim}}) \end{aligned} \tag{15}$$

where $u(\cdot)$ is the Heaviside step function, and S_{es} and R_{es} are the spring and damping constants for the end stop mechanism. The constant η_{lim} gives the excursion for which the mechanism starts acting. Once included in the simulation model, the added force terms may be seen as either representing a physical end stop, or as a part of the control force. In the calculation of power output we have in this paper done the former, i.e. the power dissipated due to the additional terms are not included in the numbers for useful absorbed energy.

For the velocity tracking control (AVT) it is, however, better to modify the reference signal in order to avoid conflict with the PI controller. It can be done by requiring that the velocity never exceeds a value corresponding to oscillation at a chosen frequency ω_{max} and with amplitude equal to the stroke limit η_{max}. This is illustrated by Figure 19. In mathematical terms this may be written as

$$v_{\mathrm{max}} = \begin{cases} 0 \quad \text{for} \quad (|\eta| > \eta_{\mathrm{max}}) \wedge (v_{ref}\eta > 0), \\ \omega_{\mathrm{max}} \sqrt{\eta_{\mathrm{max}}^2 - \eta^2} \quad \text{otherwise.} \end{cases} \tag{16}$$

We thus modify the velocity reference v_{ref} according to

$$v'_{\mathrm{ref}} = \mathrm{sign}(v_{\mathrm{ref}})\, \max(|v_{\mathrm{ref}}|, v_{\mathrm{max}}) \tag{17}$$

This principle has similarities with *sliding-mode control* [40], although the goal is not to drive the state to a chosen reference, but rather to ensure that it stays within the given state limits.

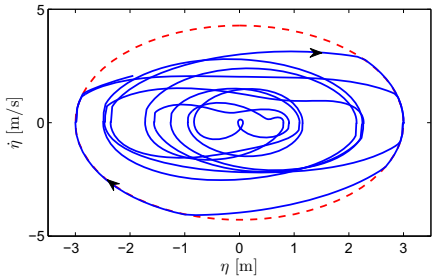

Figure 19: Phase plot showing the amplitude constraints principle for velocity tracking control. The red dashed line gives a saturation limit for the combined state of position η and velocity $\dot{\eta}$.

Table 1: Wave power level J [kW/m] for the irregular wave sea states studied.

	T_e [s]		
H_s [m]	6.0	9.0	12.0
4.24	53.0	79.5	106
2.83	23.5	35.3	47.1
1.41	5.89	8.83	11.8

This method is also a fruitful alternative to the virtual end stop (Equation (15)) for the other controllers (except MPC). By modifying the machinery force with a term that is proportional to the deviation from the limiting velocity/position characteristics, one can get a smoother behaviour of the virtual end stop; for instance by adding a term

$$F_v = -R_v \left(|\dot{\eta}| - v_{\max}\right) u(|\dot{\eta}| - v_{\max}) \operatorname{sign}(\dot{\eta}) \tag{18}$$

to the machinery force of Equation (15) to get $F'_m = F_m + F_v$. This has been tested and gives a smoother impact with the end stop, which can be adjusted by the parameter $\omega_{\max}$, but it has not been used for the results to be presented in Section 5.

4 Simulation set-up

The example model (Section 2) has been simulated with the controllers defined in Section 3 for a range of regular and irregular waves. The mathematical model (3) and the controllers were implemented in Matlab/Simulink [41], and the hydrodynamic parameters and excitation force coefficients were calculated by WAMIT [42]. A range of regular and irregular waves were then defined based on wave period T and wave height H. For irregular waves, the energy period T_e and significant wave height H_s were used as parameters and 9 different sea states were synthesised from a Bretschneider spectrum, see table 1. The irregular wave time series have length equal to about 160 times the energy period of the sea state. Exactly the same time series were used for all runs with the same sea state parameters. In the

calculation of average and peak values, short intervals of about five average wave periods at the beginning and on average wave period at end of the time series were excluded in order to avoid transient and end-point effects.

Due to the non-linearities introduced by end stops and control strategies, the mathematical model occasionally becomes very stiff. A variable step solver, Matlab's *ode23tb* algorithm, has therefore been used for the numerical integration of the model (3). The relative tolerance was set to 10^{-4}, and the absolute tolerance to 10^{-3} for most of the simulations.

In order to study adaptive parameter tuning we also define a set of cases where the sea state changes gradually. This is done by adding time series for two different sea states, where each series is weighted such that the resulting time series is changing linearly with time from one to the other:

$$F_e(t) = F_{e,1}(t)\,(1 - \frac{t}{T_f}) + F_{e,2}(t)\,\frac{t}{T_f} \tag{19}$$

where $T_f = 43.2\,\text{ks}$ (12 hours) is the length of the time series. For the results to be presented here, $F_{e,1}$ was synthesised from a Bretschneider spectrum with parameters $T_e = 6\,\text{s}$ and $H_s = 1.41\,\text{m}$, and $F_{e,2}$ correspondingly with parameters $T_e = 12\,\text{s}$ and $H_s = 2.83\,\text{m}$.

5 Results and discussion

In this section the results are presented in three parts. First we look at regular wave results, which indicate some basic properties of the different controllers. We then turn to the irregular wave results where the real potential of different strategies may be revealed. Finally some examples of adaptive control are given with the use of gain scheduling and extremum-seeking control in a changing sea state.

5.1 Regular waves

A Budal diagram [43] giving the absorbed power as a function of wave height is shown in Figure 20. Because the waves are regular, the simulations have been run using ideal

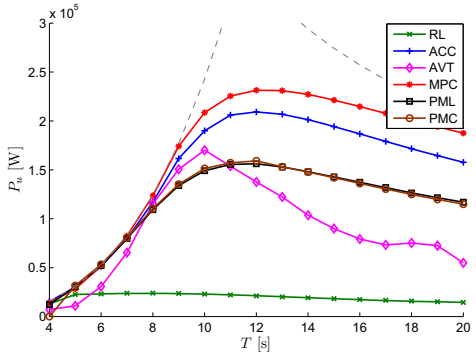

Figure 20: Budal diagram showing the average absorbed power for the different control strategies with varying wave period of regular waves with height $H = 1\,\text{m}$.

prediction (i.e. the future is assumed known). Most of the control strategies are able to give close to optimal absorption in the low-period range. The exceptions are the RL and ATV control strategies. For resistive loading, the reason for the discrepancy is the phase deviation between excitation force and velocity. On the other hand, the reason why the AVT control, which gives perfect phase, fails to reach optimum for low periods is that the amplitude is non-optimal. For this strategy all the wave periods have been run with the same value $1/\{2R_c\}$ for the force-to-velocity feed-forward function, where R_c was set equal to $R_i(\omega_k)$ with $\omega_k = 2\pi/(9\,\mathrm{s}) = 0.70\,\mathrm{rad/s}$. It means that unconstrained oscillations will have the right phase but the amplitude will only be correct for $T = 2\pi/\omega_k = 9\,\mathrm{s}$. This may be seen from the curve, which shows good absorption for wave periods in the range 8-10 s. The force-to-velocity feed-forward function was defined as a constant in order to see the effect of varying wave period. If we had instead optimised its value at each wave period, the result would be similar to approximate complex conjugate (ACC) control.

The amplitude restriction causes the absorption curves to eventually depart from the theoretical ascending limit included in Figure 20. We observe that, for long wave periods, the MPC controller performs better than the other strategies, and this is because it is able to account for the amplitude restriction in an optimal way. The difference between ACC and latching/clutching algorithms is somewhat more complex. For low wave height the ACC controller performs better because it supplies reactive power so that the optimum amplitude may be achieved where the natural "unaided" amplitude response would be too low. For larger wave heights this is not needed, and the time-variant latching and clutching strategies are able to yield a larger absorbed power, as seen in Figure 21. Their oscillation pattern is beneficial in comparison to the linear time-invariant (sinusoidal) response we get with ACC control. As shown by Budal *et al.* [36], an explanation for this is that with latching control, the amplitude of the first harmonic component of the position response has a larger amplitude than the physical amplitude (which has here been restricted to 3 m). This also applies to the MPC time series in Figure 13, which is the constrained optimal solution [9]. It resembles a latching control response. As we can see, the result is that the PML algorithm gives higher absorbed power than ACC for high wave amplitudes (due to the amplitude restriction), which has also been reported before [34].

As mentioned before, in regular waves, the threshold unlatching (TUL) and unclutching (TUC) strategies become identical to the corresponding peak-matching counterparts (PML and PMC, respectively). This is the reason why they are not included in Figures 20 and 21.

An important issue, which should be given thorough consideration for wave energy appliances, is the peak-to-average power ratio [34]. For the reactive control algorithms (ACC, AVT and MPC) it is shown in Figure 22. For the RL strategy this ratio is always equal to two in regular waves because the instantaneous absorbed power is oscillating harmonically about the average absorbed power $\overline{P}_a$ with frequency twice the wave frequency and with amplitude $\overline{P}_a$. We see that the MPC strategy requires higher instantaneous power than the ACC controller. With these controllers the maximum inverted power (i.e. machinery working as a motor) is almost as large as the maximum converted power.

The large peak-to-average power ratios for the AVT strategy is due to the low average values — for the range of periods where the absorbed power is close to optimum (8-9 s), the peak to-average ratio is close to the MPC result.

The corresponding data for the latching and clutching control strategies are given in Fig-

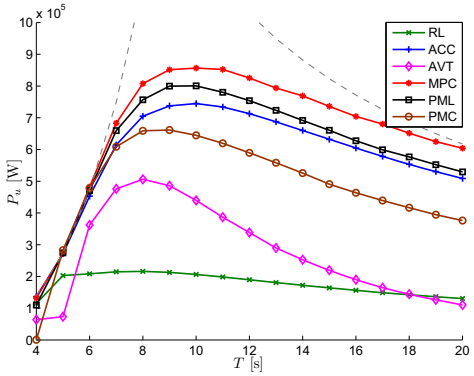

Figure 21: Budal diagram showing the average absorbed power for the different control strategies with varying wave period. The incident waves were regular with height $H = 3\,\mathrm{m}$.

ure 23. These two strategies give no reactive power flow (and thus no power inversion), and have similar levels of average absorbed power. The curves reveal a very interesting trend: whereas the ratio for latching control is increasing almost linearly with T, the clutching control control gives a decreasing peak-to-average ratio as the wave period increases. This is easy to understand: As the period increases, the transition intervals (where the latching algorithm extracts power) becomes shorter and shorter relative to the intervals of high resistance (where the clutching algorithm extracts power). The clutching strategy eventually even gives a lower ratio than the RL strategy. In general, the latching and clutching controllers have smaller peak-to-average power ratios than the reactive controllers ACC, AVT and MPC.

5.2 Irregular waves

For the simulations with irregular wave time series, the controllers are run as if they were operating in real time with access to accurate estimates of the system states and the instantaneous excitation force F_e. The MPC and peak matching controllers need knowledge of F_e ahead, and for these and augmented Kalman filter has been used for prediction, identical to the one used in [9]. In practice, forecasts may be obtained from a pressure transducer measuring the hydrodynamic pressure close to the buoy by using an estimator to derive an estimate for the excitation force from this measurement. For the peak-matching strategies a prediction equal to $T_0/4 \approx 1.1\,\mathrm{s}$ has been used, and for the MPC strategy the prediction horizon was equal to 2.2 s.

In each case the control parameters, including the ATV feed-forward constant, have been optimised to yield the maximum average absorbed power over the irregular wave time series. The optimisation was done with a simplex algorithm (Matlab's *fminsearch* function [41]).

Figure 24 shows the resulting numbers for the average absorbed power. There is a significant gain in power for all controllers compared to the RL case (which has also been optimised for each sea state). As expected, the MPC controller gives the superior perfor-

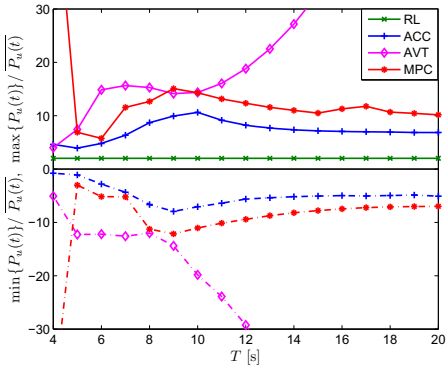

Figure 22: Peak-to-average ratiofor the absorbed power in regular waves with height 1 m for the controllers giving reactive power flow.

mance in terms of converted power. Overall, the ACC strategy is the second best in terms of absorbed power, with a reduction in the range of 10-25 % compared to the MPC algorithm. The ACC control always gives higher absorbed useful power than the AVT control the way we have implemented them, but in some cases only slightly. Because the AVT feed-forward constant has been optimised for each sea state, the drastic performance reduction for large wave periods (see Figure 20) has been avoided.

In the sea states of smaller waves, the latching and clutching strategies, which give similar results, are significantly weaker than the reactive control algorithms, although this gap is reduced or even vanishing when the wave heights become high enough. A corresponding effect would thus be expected if the size of the buoy was reduced and run in the same sea state.

It may be surprising to see that the threshold unlatching and unclutching strategies in some cases give more power than the peak-matching strategies. This, however, is due to inaccurate predictions. Runs with ideal prediction (future assumed known) in irregular waves showed that then the peak matching always gives an absorbed power higher than or equal to the threshold strategies. It is also a general trend that the threshold unlatching strategy (TUL) gives a somewhat higher converted power than the corresponding clutching strategy (TUC). It should be mentioned that the clutching gives higher power dissipation in the end stops than the other control methods. If this energy can be converted to useful energy, our data show that the difference between clutching and latching algorithms would be reduced, but not cancelled.

In general it is seen that the absorption width is decreasing with increasing wave amplitudes/heights. This is due to increasing influence from the amplitude restriction as the wave height increases.

Turning now to the peak-to-average ratios in Figure 25, an important observation is the large instantaneous power flow required by the MPC, especially for low wave periods, where the ratios exceed 25 for the reactive power controllers. High peak-to-average ratios will probably be a strong cost driver for most types of machinery, and it is therefore crucial to

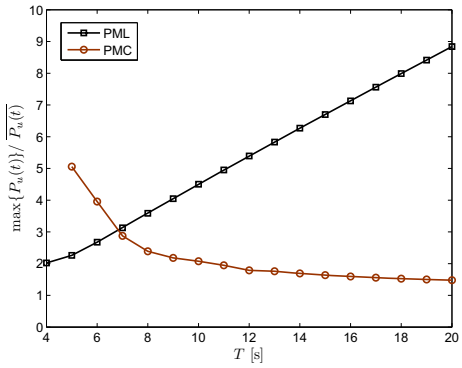

Figure 23: Peak-to-average power ratio in regular waves with height 1 m for the controllers without reactive power flow.

find machinery and controller designs that can meet this challenge.

The ACC strategy has negative ratios (motor mode) comparable to the MPC controller, whereas the positive ratios (generator mode) are considerably lower. This is interesting, because the reduction in converted power is in most cases modest. The ACC strategy may therefore occur as an attractive alternative to MPC when trade-offs between power output and peak-to-average ratios have to be made in the design of machinery and controller.

On the other hand, a large advantage with MPC control is the flexibility for including constraints. For a real machinery, force constraints could be set such that these excessive peak-to-average ratios would have been reduced, of course with a due reduction in absorbed power. The large negative power peaks observed for the AVT strategy are due to large accelerations demanded by the controller when the velocity reference is returning to the valid area of the phase plane after having been outside (Figure 19). These can probably be mitigated by including additional constraints on the velocity reference signal.

However, the most encouraging observation is perhaps the low ratios found for the clutching strategies, as was also observed for regular waves. This fact, together with the absence of reactive power flow, leads to a conclusion that clutching would be a very interesting alternative if it can be implemented with a viable machinery design. For the sea states used here, the latching control algorithms give positive peak-to-average ratios comparable to the ACC and AVT controllers, except for the case of small waves and small wave periods, where the ratios are smaller.

Between latching and clutching strategies, the threshold strategies give lower peak-to average ratios than the peak matching algorithms. It is also worth noticing that in the direction of large amplitudes and large wave periods, the primitive RL strategy eventually gives higher peak-to-average ratios than the high-yield ACC and AVT strategies. For the ACC controller the need for reactive power mainly depends on wave period (and not wave height) once the amplitude constraint is reached [34], and because the average absorbed power increases for increasing wave heights, the peak-to-average therefore decreases monotonically with increasing wave height. For the RL strategy it is quite constant compared to

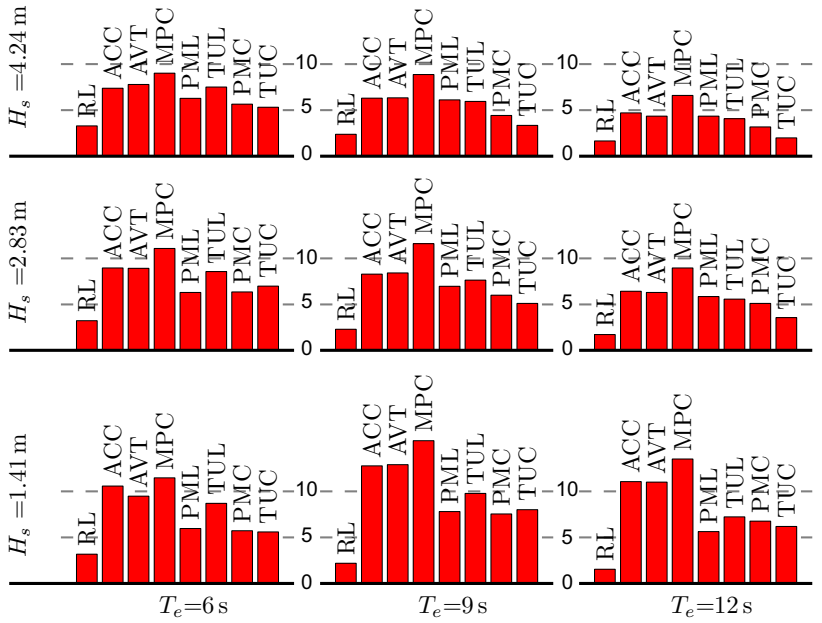

Figure 24: Absorption width $d_a = \overline{P}_u/J$ [m] (based on absorbed useful energy) for the simulation in irregular waves and different control strategies. Horizontal dashed lines are drawn at $d_a = 5\,\text{m}$ and $d_a = 10\,\text{m}$. The sea states were synthesised from a Bretschneider spectrum, and significant wave height and energy period are given to the left and on the bottom of the graph, respectively. The wave power level for each sea state may be read from Table 1.

the other strategies.

Table 2 gives a schematic summary of the properties and performance observed for the strategies that have been investigated.

5.3 Adaptive control

Examples of automatic parameter tuning are shown in Figures 26 and 27. From the curves of accumulated energy it is verified that the tuning gives an increased energy yield as compared to the constant parameter case for all the shown strategies (RL, ACC and TUL). It may also be observed that the gain scheduling strategy partly gives a parameter variation similar to the extremum seeking strategy, only slightly delayed. We interpret the delay to be due to the computation of average values, which are based on analysis of the last 100 wave up-crossing periods. The effect of the parameter tuning is largest for the RL and ACC strategies. The TUL controller is only weakly sensitive to changes in the threshold setting. Towards the end of the time series for ACC control (Figure 27b) runs with constant parameter give very poor results for the absorbed power, which even decays towards the end. This is due to heavy

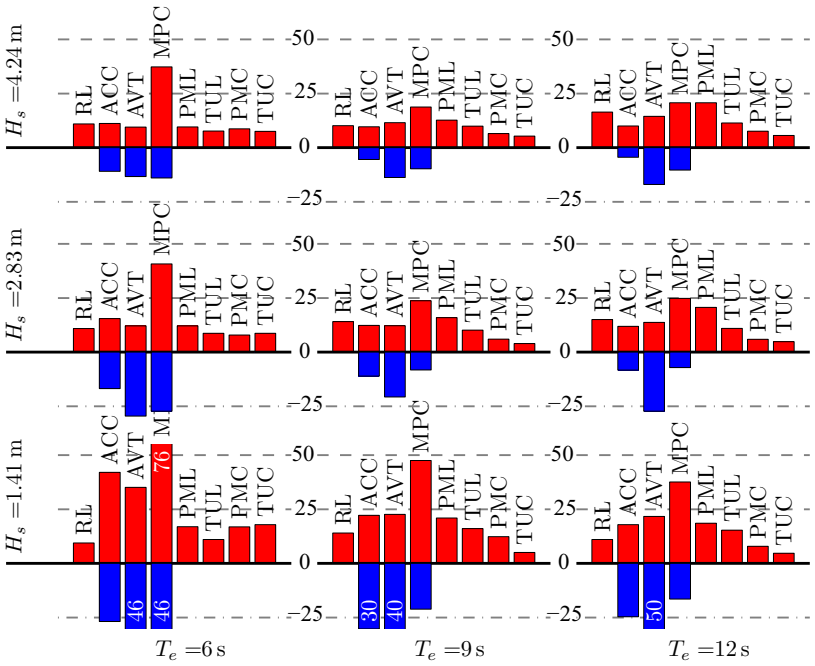

Figure 25: Peak-to-average ratio for the power flowing through the machinery for incident irregular waves. The wave excitation corresponds to the results presented in Figure 24. Horizontal dashed lines are drawn at the values -25, 25 and 50. Some of the bars go outside the scale. Their sizes are then given by the white numbers.

power dissipation in the end stops instead of conversion to useful power. The gain scheduling strategy is not able to capture the effect of constrained amplitudes as the parameter setting only depends on the wave period. This is the reason why the extremum-seeking strategy performs better for ACC and TUL control when the sea changes to a state with high power level ($T_e = 12\,\mathrm{s}$ and $H_s = 2.83\,\mathrm{m}$). This could be compensated for by finding a parameter mapping where the gain scheduling also depends on the wave amplitude. However, this has not been done herein.

The simulation work has shown that we could not manage to tune/optimise the control parameters on a shorter time scale than corresponding to sea state average (about 15–30 minute intervals). Thus only the MPC control, which works on a wave-to-wave time scale, is able to approach the theoretical optimum when the motion is constrained.

6 Conclusion

A selection of strategies for real-time control of wave energy converters has been defined and applied to the example of a heaving-buoy wave absorber. The strategies include velocity

Table 2: Comparison of properties and performance for the investigated control strategies. The second and third columns give the feedback (FB) route, while the fourth column indicates the need for feeding forward an estimate of the excitation force. The column with relative average power gives values in percentage compared to the power converted using the MPC algorithm. The last column gives the mean peak-to-average ratio. All numbers are found as an average over the 9 sea states that were simulated, see Table 1 and Figures 24 and 25.

Method	direct velocity FB	velocity tracking	F_e feed forward	F_e prediction needed	constrained optimal	reactive power flow	nonlinear F_m	relative average power	mean peak-to-average
RL	x							23	12
ACC	x						x	78	17
AVT		x	x				x	77	17
MPC		x	x	x	x	x	x	100	36
PML	x		x	x			x	59	18
TUL	x		x				x	68	11
PMC	x		x	x			x	53	9
TUC	x		x				x	47	6

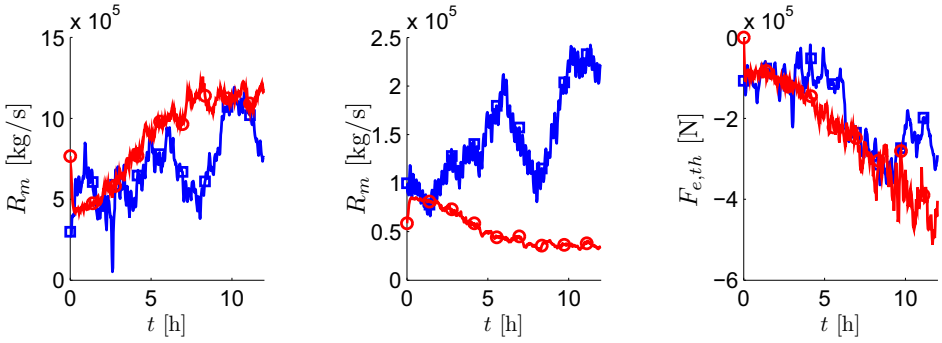

(a) RL (b) ACC (c) TUL

Figure 26: Control parameter values for the three of the control strategies with automatic tuning. The red circle-marked curves result from parameter tuning by gain scheduling, and the blue square-marked curves are due to extremum seeking control. The sea state is a weighted sum (cf. Equation (19)) of two sea states, one with $T_e = 6\,\mathrm{s}$ and $H_s = 1.41\,\mathrm{m}$ and the other with $T_e = 12\,\mathrm{s}$ and $H_s = 2.83\,\mathrm{m}$.

proportional and approximate complex-conjugate control, PI-controlled tracking of the approximate optimum velocity, latching and clutching algorithms as well as a model-predictive controller. The controller aim has been to maximise the power output from the converter

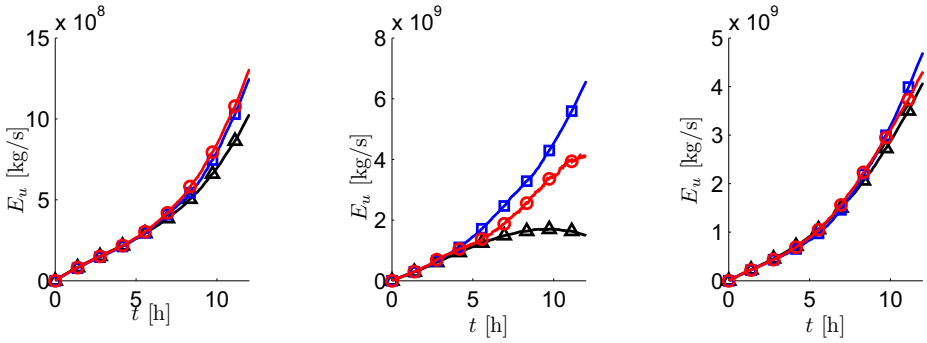

(a) RL (b) ACC (c) TUL

Figure 27: Accumulated useful energy corresponding to the cases presented in Figure 26. The black triangle-marked curve gives the energy absorbed without parameter tuning (i.e. keeping the initial setting throughout the simulation).

in a set of sea states representative for irregular deep-water waves. The controllers were provided with different means to handle amplitude constraints, and were run for irregular waves without assuming any a priori knowledge of the forces from the incident waves.

It was found that real-time extremum-seeking control and gain scheduling using short-time historical wave data both are promising methods for parameter tuning in these controllers for wave energy conversion. In irregular waves, improved power conversion was achieved with both methods as compared to running with constant control parameters in a simple test case.

Constraints on the motion amplitude were implemented as spring and damper elements for most of the control algorithms investigated. For the velocity tracking controller a phase-plane constraint was implemented, which worked well in avoiding impact with the end-stop mechanism.

It was found that a common challenge for several of the controllers is the large reactive power through the machinery needed in order to supply the computed machinery force. This means that the machinery must be designed for a much larger instantaneous power than the average power that the converter is able to deliver. This is an important challenge to the design of machinery systems for wave energy converters. If the intention is to apply reactive control, the system should be designed with an energy storage as early as possible in the conversion chain such that only the upstream part has to be designed to support the large reactive power.

Although simple, the latching and clutching strategies have several properties that make them attractive despite the fact that their performance in terms of absorbed power is inferior to the best performing controllers in this study. They may be very easy to implement and ideally do not require any reactive power flow through the machinery. Compared to the MPC controller, the absorbed useful power is in the range of about 40 to 80 %, but the peak-to-average power ratio is typically about 20-50 % for the latching control and 20-30 % for the clutching control. In the constrained case (relatively high waves) the peak-to-average

ratio is comparable to approximate complex-conjugate and optimal velocity control for the latching control strategy. Interestingly, for clutching control, the ratios are in fact lower than for pure resistive loading.

Acknowledgements

The authors would like to thank the Norwegian Research Council for financial support through the Centre for Ships and Ocean Structures (CeSOS). Special thanks go to Professor Thor Inge Fossen for fruitful discussions in connection with this work.

References

[1] Evans, D. V., 1981, "Power from water waves," Ann. Rev. Fluid Mech., **13**, pp. 157–187.

[2] Falnes, J., 2002, "Optimum control of oscillation of wave-energy converters," International Journal of Offshore and Polar Engineering, **12**(2), pp. 147–155.

[3] Falnes, J., 2002, *Ocean waves and oscillating systems: linear interactions including wave-energy extraction*, Cambridge University Press, Cambridge.

[4] Price, A. A. E., Forehand, D. I. M., and Wallace, A. R., 2009, "Time-span of future information necessary for theoretical acausal optimal control of wave energy converters," *Proceedings of the European Control Conference 2009*, ISBN 978-963-311-369-1, Budapest, Hungary, pp. 3761–3766.

[5] Perdigão, J. N. B. A. and Sarmento, A. J. N. A., 1989, "A phase control strategy for OWC devices in irregular seas," *The fourth International Workshop on Water Waves and Floating Bodies*, J. Grue, ed., Dept. Mathematics, University of Oslo, pp. 205–209.

[6] Beirão, P. J. B. F. N., 2007, *Modelling and Control of a Wave Energy Converter: Archimedes Wave Swing*, Ph.D. thesis, Universidade Tecnica de Lisboa, Instituto Superior Tecnico, Delft.

[7] Gieske, P., 2007, *Model Predictive Control of a Wave Energy Converter: Archimedes Wave Swing*, Master's thesis, Delft University of Technology, Delft.

[8] Eidsmoen, H., 1995, *On the theory and simulation of heaving-buoy wave-energy converters with control*, Ph.D. thesis, NTH (now NTNU), Trondheim.

[9] Hals, J., Falnes, J., and Moan, T., 2009, "Constrained optimal control of a heaving buoy wave energy converter," Accepted for publication in the Journal of Offshore Mechanics and Arctic Engineeringl.

[10] Kamenský, M. and Guglielmi, M., 2007, "Optimal control of power take-off from mass-spring-damper system," *16th International on Process Control 2007*.

[11] Nolan, G., Ringwood, J., Leithead, W., and Butler, S., 2005, "Optimal damping profiles for a heaving buoy wave energy converter," *Proceedings of the fifteenth intenatinal offshore and polar engineering conference*, ISBN 1-880653-64-8, ISOPE, Seoul, Korea.

[12] Hoskin, R. E. and Nichols, N. K., 1987, "Optimal strategies for phase control of wave energy devices." *Utilization of Ocean Waves - Wave to energy conversion*, M. E. McCormick and Y. C. Kim, eds., American Society of Civil Engineering, New York, pp. 184 – 199.

[13] Naidu, D. S., 2003, *Optimal Control Systems*, ISBN 0-0493 0892-5, CRC Press LLC.

[14] Budal, K. and Falnes, J., 1980, "Interacting point absorbers with controlled motion," *Power from Sea Waves*, B. Count, ed., Academic Press, London, pp. 381–399, (ISBN 0-12-193550-7).

[15] Budal, K., Falnes, J., Iversen, L. C., Lillebekken, P. M., Oltedal, G., Hals, T., Onshus, T., and Høy, A. S., 1982, "The Norwegian wave-power buoy project," *Proc. Second International Symposium on Wave Energy Utilization*, H. Berge, ed., ISBN 82-519-0478-1, Tapir, Trondheim, Norway, pp. 323–344.

[16] Babarit, A., 2005, *Optimisation hydrodynamique et contrôle optimal d'un récupérateur de l'énergie des vagues*, Ph.D. thesis, Ecole Centrale de Nantes, Nantes.

[17] Hals, J., Taghipour, R., and Moan, T., 2007, "Dynamics of a force-compensated two-body wave energy converter in heave with hydraulic power take-off subject to phase control," *Proceedings of the 7th European Wave and Tidal Energy Conference*, Porto, Portugal.

[18] Falnes, J., 1999, "Wave-energy conversion through relative motion between two single-mode oscillating bodies," Journal of Offshore Mechanics and Arctic Engineering (ASME Transactions), **121**, pp. 32–38.

[19] Falcão, A. F. d. O., 2007, "Phase control through load control of oscillating-body wave energy converters with hydraulic PTO system," *Proceedings of the 7th European Wave and Tidal Energy Conference*, Porto, Portugal.

[20] Lopes, M., Hals, J., Gomes, R., Moan, T., Gato, L., and Falcao, A. O., 2009, "Experimental and numerical investigation of non-predictive phase-control strategies for a point-absorbing wave energy converter," Ocean Engineering, **36**(5), pp. 386 – 402.

[21] Salter, S. H., Taylor, J. R. M., and Caldwell, N. J., 2002, "Power conversion mechanisms for wave energy," *Poceedings of Institute of mechanical engineers, Part M: Engineering for the Maritime Environment*, vol. 216, pp. 1–27.

[22] Babarit, A., Guglielmi, M., and Clement, A. H., 2009, "Declutching control of a wave energy converter," Ocean Engineering, **36**(12-13), pp. 1015 – 1024.

[23] Evans, D. V., 1981, "Maximum wave-power absorption under motion constraints," Applied Ocean Research, **3**(4), pp. 200–203.

[24] Pizer, D., 1993, "Maximum wave-power absorption of point-absorbers under motion constraints," Applied Ocean Research, **15**(4), pp. 227 – 234.

[25] Falnes, J., 2000, "Maximum wave-energy absorption by oscillating systems consisting of bodiew and water culumns with restricted or unrestricted amplitudes," Proceedings of the International Offshore and Polar Engineering Conference, **1**, pp. 420–426.

[26] Leijon, M., Danielsson, O., Eriksson, M., Thorburn, K., Bernhoff, H., Isberg, J., Sundberg, J., Ivanova, I., Sjöstedt, E., Agren, O., Karlsson, K., and Wolfbrandt, A., 2006, "An electrical approach to wave energy conversion," Renewable Energy, **31**(9), pp. 1309 – 1319.

[27] Prado, M. S., Gardner, F., Damen, M., and Polinder, H., 2006, "Modelling and test results of the Archimedes wave swing," Proceedings of the Institution of Mechanical Engineers, Part A: Journal of Power and Energy, **220**(8), pp. 855 – 868.

[28] Brown, R. G. and Hwang, P. Y. C., 1997, *Introduction to random signals and applied Kalman filtering*, ISBN 0-471-12839-2, John Wiley & Sons, New York, 3 ed.

[29] Astrom, K. J. and Wittenmark, B., 2008, *Adaptive Control*, ISBN 978-0486462783, Dover Publications.

[30] Ariyur, K. B. and Krstic, M., 2003, *Real-time optimization by extremum-seeking control*, ISBN 0-471-46859-2, John Wiley & Sons, Inc.

[31] Cummins, W. E., 1962, "The impulse response function and ship motions," Schiffstechnik, **9**, pp. 101–109.

[32] Jefferys, E. R., 1984, "Simulation of wave power devices," Applied Ocean Research, 1984, Vol. 6, No. 1, **6**, pp. 31–39.

[33] Taghipour, R., Perez, T., and Moan, T., 2008, "Hybrid frequency–time domain models for dynamic response analysis of marine structrues," Ocean Engineering, **35**(7), pp. 685–705.

[34] Hals, J., Bjarte-Larsson, T., and Falnes, J., 2002, "Optimum reactive control and control by latching of a wave-absorbing semisubmerged heaving sphere," Proceedings of the International Conference on Offshore Mechanics and Arctic Engineering - OMAE, **4**, pp. 415 – 423.

[35] Nebel, P., 1992, "Maximizing the efficiency of wave-energy plants using complex-conjugate control," Journal of systems and control engineering, **206**(4), pp. 225–236, proceedings of the Institution of Mechanical Engineers. Part I.

[36] Budal, K., Falnes, J., Hals, T., Iversen, L. C., and Onshus, T., 1981, "Model experiment with a phase controlled point absorber," *Proceedings of Second International Symposium on Wave and Tidal Energy*, H. S. Stephens and C. A. Stapleton, eds., ISBN 0-906085-43-9, BHRA Fluid Engineering (Cranford, Bedford), Cambridge, UK, pp. 191–206.

[37] Babarit, A., Duclos, G., and Clement, A. H., 2004, "Comparison of latching control strategies for a heaving wave energy device in random sea," Applied Ocean Research, **26**(5), pp. 227 – 238.

[38] Killingsworth, N. and Krstic, M., 2005, "Auto-tuning of PID controllers via extremum seeking," pp. 2251–2256 vol. 4.

[39] Spong, M. W., 2006, *Robot modeling and control*, Wiley, Hoboken, N.J.

[40] Edwards, C. and Spurgeon, S. K., 1998, *Sliding Mode Control*, CRC Press.

[41] Matlab, 2006, URL http://www.mathworks.com/, version 7.2, The Mathworks Inc.

[42] WAMIT, 2006, *WAMIT User Manual*, http://www.wamit.com, version 6.3.

[43] Falnes, J., 2007, "A review of wave-energy extraction," Marine Structures, **20**(4), pp. 185–201.

Appendix B

Modelling of integrated WEC systems

As an addition to Chapter 2, this appendix gives a brief overview of bond graph models for the remaining parts of a typical system for wave energy conversion that has not yet been treated, namely machinery, power conversion equipment and mooring arrangements. With the aim of making so-called *wave-to-wire* models for two example systems to be presented in Section B.4, we start by looking closely at typical subsystems of wave energy converters.

B.1 Machinery systems

In idealised work the machinery can be modelled as a modulated source of effort, for instance for generic studies of control strategies as carried out in this thesis. For design and analysis of full conversion systems, a more detailed representation of the machinery is needed. So far there is no consensus reached within wave energy research whereas to which type of machinery is the most cost-effective choice (and it will also depend on the chosen conversion principle). The three main types of machinery currently under development for wave energy conversion is

1. hydraulic piston pumps together with pressure accumulators and a rotary hydraulic motor

2. direct-coupled generators

3. rectifying air turbines

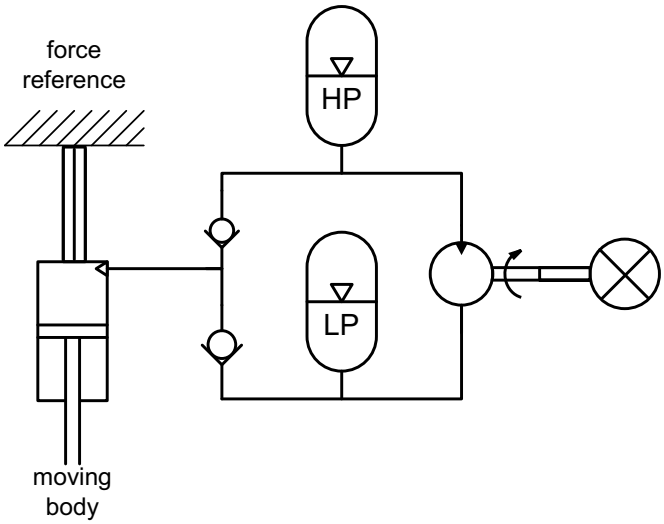

Figure B.1: Sketch of a simple hydraulic system for power take-off.

For electricity generation, alternatives one and three will have a conventional rotating electric machine as a second conversion step. Emphasis will here be put on the two first alternatives, suggesting their bond graph representations and including these in models for the whole conversion systems.

B.1.1 Hydraulic equipment

A conventional hydraulic system consists of a hydraulic liquid, tubes, valves, pumps, motors and accumulators. Standard bond graph representations of these elements are given in [69] and [97]. A simple hydraulic circuit for the conversion of wave energy is sketched in Figure B.1 and a bond graph for this system is shown in Figure B.2.

Notice the structural similarity between the sketch and the graph. The piston pump and the motor are represented by transformers, liquid flowing through the tubes gives fluid inertia (not included in the model presented here), the gas accumulators and the compliance of the piston chamber are represented by capacitor elements. Furthermore, both valves and losses in the motor are modelled by resistor elements. The power is converted to useful work at the shaft, which is represented by the crossed circle at the right of Figure B.1. This is modelled by a resistor. The system is very similar to the model presented in Article A, so we will not look further into the modelling details here.

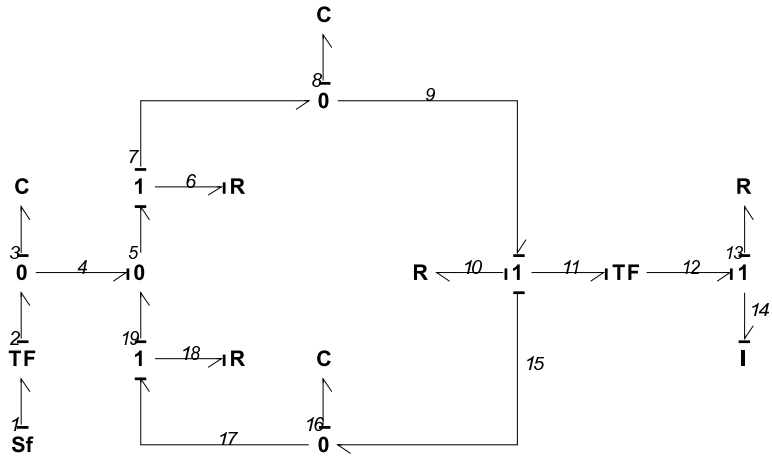

Figure B.2: A bond graph for the system sketched in Figure B.1.

B.1.2 Electric generators

Working principle of electric generators

An electric generator is based on the principle of an electric alternator (which gives AC voltage) or a dynamo (which gives pulsing DC voltage). The working principle is that a conductor is swept over a magnetic field, resulting in an electro-motive force, a voltage, being set up in the conductor. The voltage level is proportional to the speed of the conductor. In an alternator/dynamo, permanent-magnets or electro-magnets are placed one after the other in such a manner that a nonuniform magnetic field is set up. Coiled conductors then repeatedly sweeps over that field, which at constant speed will create a harmonic voltage signal in the conductor. Depending on the geometric arrangement of coils and magnets, overharmonics in the voltage signal may be produced.

In order to accurately model a generator, the whole electromagnetic field must be solved for, by establishing Maxwell's equations for the configuration. This generally requires a finite element approach [32]. A more simplified model could be established by a lumped description of the electromagnetic interactions. Such a formulation is given by Karnopp *et al.* [67; 69] using bond graph representations. They give a general model for an electromagnetic assembly converting between electric and mechanical energy, see Figures B.3 and B.4. It incorporates the following effects:

- The direct induced electric voltage e_4 and reaction force F_1 due to rate change in the rotor/slide position (which changes the magnetic field through the coil due to the rotor/slide magnets). It can usually

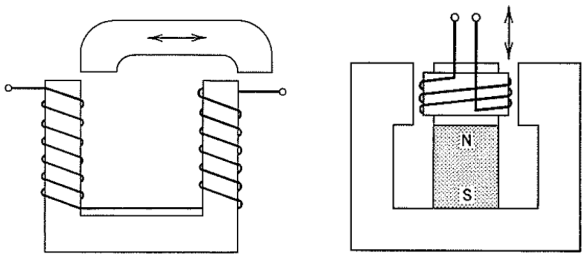

(a) Variable reluctance (b) Voice coil

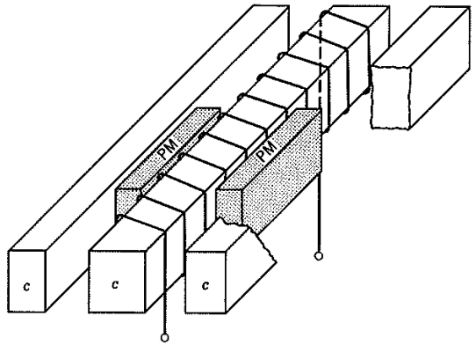

(c) Linear motor

Figure B.3: Examples of electromagnetic devices [69].

be computed directly from the Lorentz force, or from a flux linkage consideration between the coil and permanent magnets.

- A force F_2 due to the magnetic energy for the assembly depending on the position of the rotor/slide. The slide has a preferred position (minimum energy) where the magnetic reluctance is minimum.

- An energy-storing IC field due to self-inductance in the electric coil. If the inductance depends on the position of the rotor/slide, an induced force F_3 will be experienced on the mechanical side. If not, the mechanical force vanishes and the inductance may be modelled as a simple I-element on the electrical side, giving rise only to the induced voltage e_5.

- The resistive loss in the generator modelled by an electrical resistance R giving a voltage drop e_6.

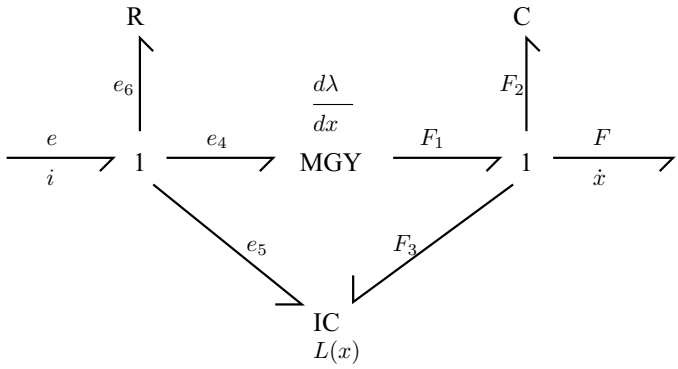

Figure B.4: Bond graph representation of the electromagnetic device sketched in Figure B.3 [69].

Synchronous versus asynchronous machines

A **synchronous generator** works mainly through the flux linkage between rotor/slide and stator electro-magnets (possibly one side of permanent magnets). This means that velocity in the mechanical domain translates to voltage in the electric domain. The magnetic susceptibility of the rotor/slide is usually made to be quite constant over the geometry, such that there is little change in coil inductance with rotor/slide position. This means that the force F_3 referred above may be disregarded, and the the inductance I_5 can be approximated by a constant.

On the contrary, an **asynchronous generator** has a small flux linkage, as there is no magnetic field in the machine at zero current. The main effect for force generation is the self-induced magnet field which varies with rotor/slide motion. The stator current induces a magnetic field in the rotor/slide metal, and this field works back at the stator coils in a manner depending on the rotor/slide movement. The time-varying inductance of the stator coils results in an induced current and a force τ_3 on the rotor or slide, opposing its motion.

The d-q axis model

Bond graph models for different types of electrical machines have been described by, among others, Sahm [107] and Karnopp [68]. These articles show how d-q models for generators can be made and how d-q transforms to phase voltages and currents in the physical three-phase (a,b,c) frame. Using the d-q axis model for generators and electrical motors is common

because this makes it much easier to implement control algorithms for them. The assumption made in order to simplify in this manner are:

- The machine has a two-pole character;
- Saturation, hysteresis and mechanical losses are neglected;
- The armature windings of phases a, b, c are sinusoidally distributed around the circumference of the rotor (or length of the slide). This results in uniformly distributed fictitious commutator windings.

The d-q model is the transformation of the physical parameters into a fictitious set of voltage and current axis. The mathematical model for the synchronous generator may be summarised as [107; 99]

$$\begin{aligned}
\dot{\psi}_d &= u_d - R_d i_d + \psi_q n_p \omega_r \\
\dot{\psi}_q &= u_q - R_q i_q - \psi_d n_p \omega_r \\
\dot{\psi}_f &= u_f - R_f i_f \\
\dot{\psi}_D &= -R_D i_D \\
\dot{\psi}_Q &= -R_Q i_Q
\end{aligned} \tag{B.1}$$

where n_p is the number of pole pairs for the machine. Furthermore, $\mathbf{i} = [i_d \quad i_q \quad i_f \quad i_D \quad i_Q]^{\mathrm{T}}$ are the d-q, field and D-Q (stator) axis currents, and $\boldsymbol{\psi} = [\psi_d \quad \psi_q \quad \psi_f \quad \psi_D \quad \psi_Q]^{\mathrm{T}}$ the corresponding flux linkages (describing the electromagnetic coupling). These are connected by

$$[i_d \quad i_q \quad i_f \quad i_D \quad i_Q]^{\mathrm{T}} = \mathbf{L}^{-1} [\psi_d \quad \psi_q \quad \psi_f \quad \psi_D \quad \psi_Q]^{\mathrm{T}} \tag{B.2}$$

The inductance matrix $\mathbf{L}$ depends on the self inductances and mutual inductances of the d-q axis, field and stator circuits.

A bond graph for the d-q model of the synchronous machine is shown in Figure B.5. It is related to the physical quantities of the real three-phase configuration by a power-invariant transformation as discussed by Sahm[107]. Figure B.6 gives a bond graph for the transform itself. In mathematical form it is given by

$$\begin{bmatrix} u_d \\ u_q \\ u_0 \end{bmatrix} = \mathbf{C} \begin{bmatrix} u_a \\ u_b \\ u_c \end{bmatrix}, \qquad \text{and} \qquad \begin{bmatrix} u_a \\ u_b \\ u_c \end{bmatrix} = \mathbf{D} \begin{bmatrix} u_d \\ u_q \\ u_0 \end{bmatrix}, \tag{B.3}$$

with

$$\mathbf{C} = \mathbf{D}^{-1} = \mathbf{D}^{\mathrm{T}} = \sqrt{\frac{2}{3}} \begin{bmatrix} \cos(\nu) & \cos(\nu - \frac{2\pi}{3}) & \cos(\nu - \frac{4\pi}{3}) \\ \sin(\nu) & -\sin(\nu - \frac{2\pi}{3}) & -\sin(\nu - \frac{4\pi}{3}) \\ \frac{1}{\sqrt{2}} & \frac{1}{\sqrt{2}} & \frac{1}{\sqrt{2}} \end{bmatrix} \tag{B.4}$$

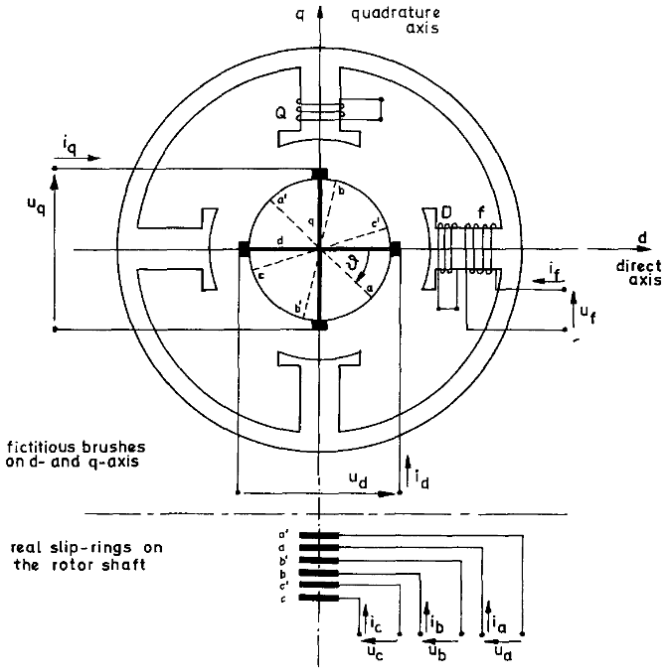

(a) dq-model machine

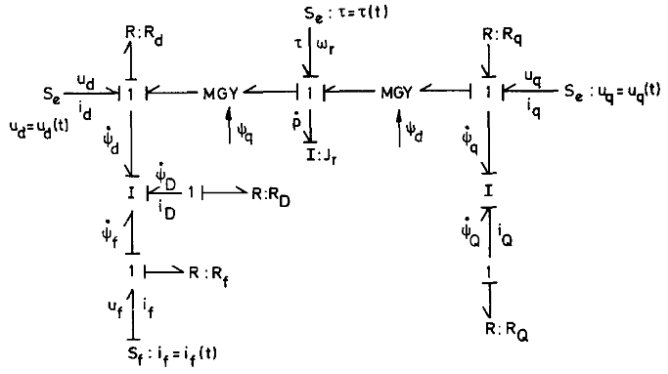

(b) Bond graph

Figure B.5: Sketch (a) and bond graph (b) for the d-q model of a synchronous generator [107].

where ν is the time-varying angle between the axis of phase a and the d axis, starting at ν_0 for time $t = 0$: $\nu(t) = \nu_0 + \int_0^t \nu \, dt$.

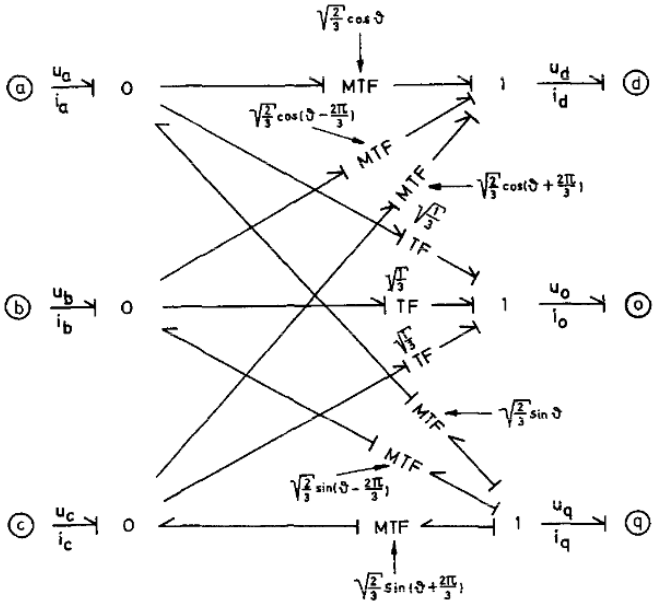

Figure B.6: A bond graph relating the d-q frame variables to the real phase variables [107].

Direct-coupled linear generator

Although it is possible to make linear asynchronous machines, linear generators are usually of the synchronous type using permanent magnets on the slide (which corresponds to the rotor on a rotating machine). Following the model of Figure B.4 of an electromagnetic device, we may suggest a bond graph for such a linear generator by assuming that the inductance on the electric side is independent of the slide position. The IC field then reduces to a normal I element, and we arrive at the model given in Figure B.7, where all three phases have been included, resulting in a triple-bond representation.

The corresponding equations become:

$$\begin{aligned}
\dot{\psi}_a &= u_a - R_a i_a + \frac{d\psi_{pm}(x+x_a)}{dx}\,\dot{x} \\
\dot{\psi}_b &= u_b - R_b i_b + \frac{d\psi_{pm}(x+x_b)}{dx}\,\dot{x} \\
\dot{\psi}_c &= u_c - R_c i_c + \frac{d\psi_{pm}(x+x_c)}{dx}\,\dot{x}
\end{aligned} \tag{B.5}$$

where x is the position of the slide and x_a, x_b and x_c are the reference position of the evenly distributed pole pairs for each phase.

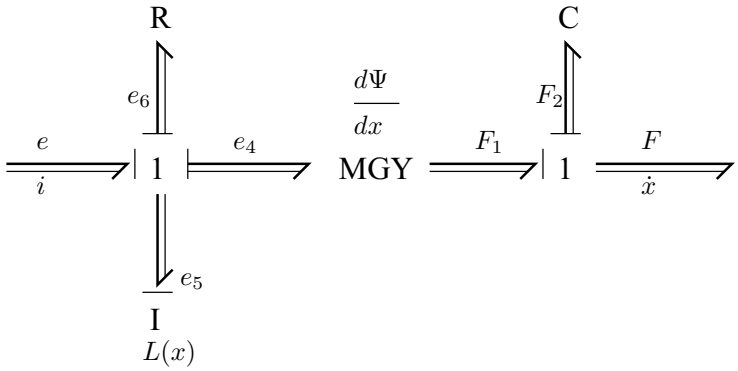

Figure B.7: A bond graph for a linear permanent-magnet generator with causality assigned.

Motor-driven rotating generator

For operation with a hydraulic motor or an air turbine it could be desirable to use an asynchronous generator, which has almost been the standard solution within the wind-turbine industry. However, for simplicity, we will here assume a synchronous generator and use the same generator model as discussed in the above section about about the d-q axis model. (Unlike for the linear generator model, which had permanent magnets, this time the field circuit will be included in the model).

B.1.3 Latching control using a direct-coupled generator

The latching strategy for phase control have been discussed extensively in this thesis. It relies on the ability to halt the motion of the wave-absorbing body during parts of the cycle. From the bond graph of Figure B.7 we may see that when using a synchronous machine, a high resistance to motion on the mechanical side is achieved by lowering the resistance on the electrical side. This indicates that latching (or something close to latching) of the motion can be done by short-circuiting the generator, making the resistance a minimum and thus the current a maximum. But, of course, having a generator directly coupled to the oscillating body with the possibility of working in reverse mode (supplying power to the buoy) may call for a more advanced control strategy involving reactive power.

It should be noted that this consideration about latching by short-circuits is only valid when the ferromagnetic material is un-saturated. Saturation will eventually lead to a decrease in the induced force.

B.2 Power conditioning and grid connection

If the configuration allows for a generator operating at constant speed it may in principle be connected directly to the electricity grid. The frequency of the grid voltage then sets the speed of the generator, which may however be designed by the use of mechanical gears. On the contrary, if the design relies on a variable generator speed, power electronics must be included as an intermediate stage before connection to the mains. It involves two steps: Converting from AC to DC via a rectifier, and converting back to AC via a power inverter.

B.2.1 Power converters

Rectifiers

A standard passive rectifier consists of semiconductor diodes that (roughly speaking) conduct when the voltage across them exceed zero, and works as insulators otherwise. A three-phase rectifier setup is shown in Figure B.8. For sinusoidally varying phase voltages, the output voltage will look as shown in Figure B.9. In order to smoothen the DC voltage a (large) capacitor is coupled between the upper and lower levels. A bond graph for the diode rectifier is presented in Figure B.10, where the diodes are represented by R elements. If a varying DC level is needed, controllable semiconduc-

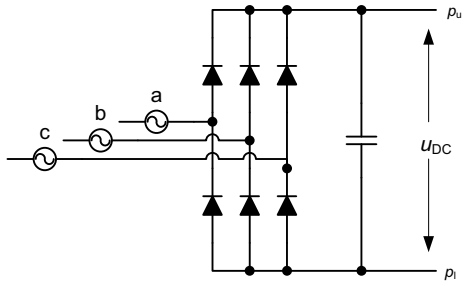

Figure B.8: Circuit diagram of a diode rectifier.

tor elements (like thyristors or bipolar junction transistors) may be used instead of passive diodes, such that the switching can be made at instants decided by a control algorithm.

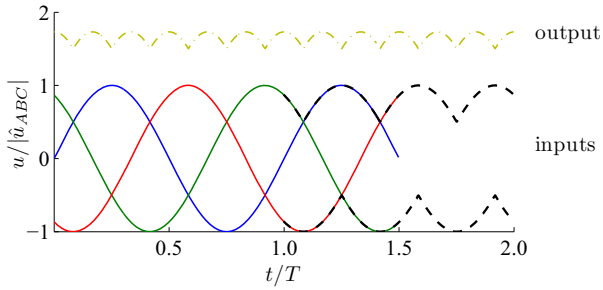

Figure B.9: Time series for the rectifier input (3-phase) and output signals. The vertical scale gives the relative amplitude to the phase voltage, and the horizontal scale gives fractions of an oscillation period.

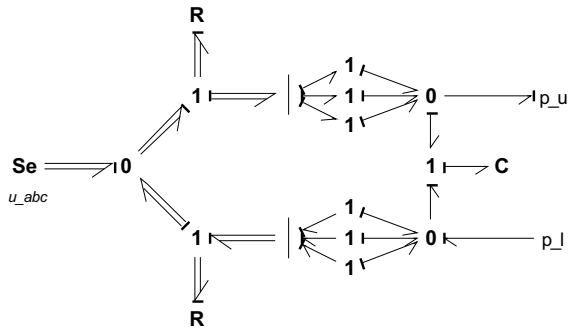

Figure B.10: A bond graph for the diode rectifier.

Power inverters

The power inverter is used for converting from DC to AC. It is usually a controllable semiconductor device of the same type as mentioned for the controlled rectifier.

Adding a power rectifier and an inverter we get a device called a power converter that is capable of transforming a set of AC signals into an other set of AC signals with independent voltage level and frequency. Schematically it may be represented by Figure B.11.

Control algorithms and dynamics for controlled power converters may be quite complex, so here these devices will only be represented by an *average model*.

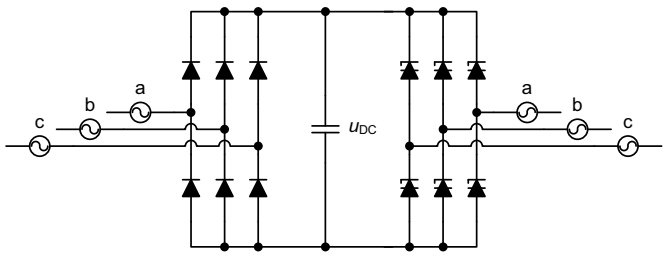

Figure B.11: A schematic view of the full power converter.

Average models

In an average model the rectifier may be represented by an R field as shown in Figure B.12. A control signal must be passed to the field for determining the outputs. This sets the d-q currents. The only undecided output is then the DC-current i_{DC}. If we assume that the rectifier operates at an efficiency η, such that the power $P_{\mathrm{DC}} = \eta P_{\mathrm{abc}}$ and that the currents are related to the voltages by $i_{abc} = G u_{abs}$, with G $[\Omega^{-1}]$ being a control parameter, we get the relation [99]

$$i_{\mathrm{DC}} = \eta \, \frac{u_a \, i_a + u_b \, i_b + u_c \, i_c}{u_{\mathrm{DC}}}. \tag{B.6}$$

Furthermore, the power on the AC side is then

$$P_{abc} = G(u_a^2 + u_b^2 + u_c^2). \tag{B.7}$$

The requirement for the average description to be valid is that the effects of the semiconductor switching operations (high frequency) may be neglected, and that the voltage and current levels of the rectifier and inverter components do not violate their working principles. This will not be discussed any further here.

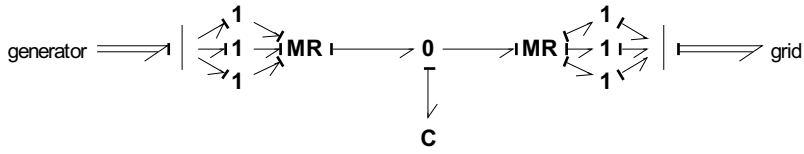

Figure B.12: A bond graph for the average model of a power converter. The left-side and right-side R fields are average-model representations of the rectifier and the inverter, respectively.

Controlling power converters

Now there are different possibilities for controlling the converter. If a passive rectifier is used, the force from the generator must be controlled by varying the DC level of the DC link, and this must be done by controlling the inverter. The other possibility is to set the inverter to hold the DC link at a constant voltage level and to use a controllable rectifier to set the generator force. Here only the second alternative will be shown. The inverter is then programmed to provide a constant voltage over the DC bridge, sufficiently high for the rectifier to work properly.

By equating the three-phase power of the inverter to the desired power conversion through the generator we get $P_{abs} = F_m v$. The set-point for the machinery force F_m can thus be used together with the measured velocity v to find an expression for the control parameter G,

$$G = \frac{F_m v}{u_a^2 + u_b^2 + u_c^2}. \tag{B.8}$$

In the case of pure resistive loading, $F_m = R_m v$, we see that the G parameter must be set according to

$$G = \frac{R_m v^2}{u_a^2 + u_b^2 + u_c^2}. \tag{B.9}$$

It is interesting to note that the control parameter, which may be regarded as a conductance, on the electrical side has to be proportional to the mechanical resistance R_m that we try to emulate.

B.2.2 Hydraulic and electric analogies

Having defined the converter model it might be worth having a look a t the similarity between the hydraulic and electric power take-off systems. As seen by comparing Figures B.2 and B.10, the structure of the hydraulic circuit and the electric power converter is very similar. This might be an aid in assessing different design alternatives. How and where can energy storage be incorporated in the conversion system in order to improve the quality (reduce fluctuations) of the delivered power? Which alternative is likely to give the lower cost? How can motion control be implemented – what is the controllable variable? The bond graph is a good aid in answering such questions as already exemplified with the considerations on electrical latching (see Section B.1.3)

B.2.3 The electric distribution grid

If there are long cables between the conversion device and the grid connection point these will impose resistance, capacitance and inductance effects that may be modelled as a normal electric circuit.

The grid itself is in this context usually sufficiently modelled as an ideal voltage source with an inductance in series, although that will depend on the local grid configuration. A bond graph including these elements might for a three-phase AC grid may look like in Figure B.13.

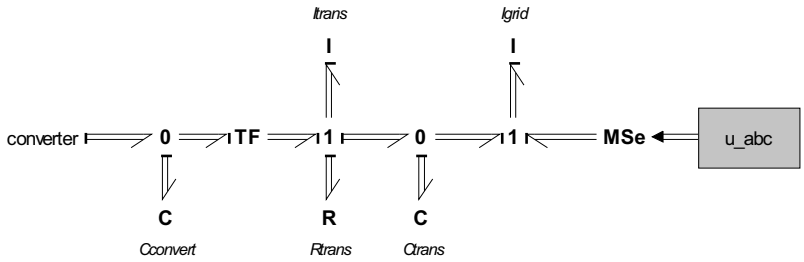

Figure B.13: A multi-bond graph for a 3-phase grid connection including resistance, inductance and capacitance for transmission and grid.

B.3 Mooring systems

Two of the salient questions in design and analysis of mooring systems for a wave energy converters are

- Will the moorings be able to fulfil their function throughout the life time or service time?
- How do the mooring forces influence the body motions and thereby the absorbed power?

Mooring models help us to answer these questions. Based on published works on the modelling of mooring lines we first look at a linearised model for the dynamic forces, with possible extensions to include nonlinear viscous damping if desired. Subsequently the mooring attachment to the floating body is discussed and two alternative coordinate transformations are proposed.

B.3.1 Approximation based on equivalence to FEM results

Detailed and accurate models for mooring line forces and dynamics may be found by the use of finite element representations of the fluid and the mooring line itself. However, these representations very easily become too computationally demanding (i.e. with today's normal processing capacity) for combination with total system models of wave energy converters, where efficient calculations for a wide range of sea states are needed.

A linearised model for the tangential forces from catenary mooring lines was developed by Larsen and Sandvik [74]. It shows that the dynamics of the mooring line under tangential motions can be well represented by the use of generalised mass $m^*(\omega)$, damping R^* and stiffness S^* factors, where the mass is frequency dependent, giving a tangential displacement-to-tension transfer function of the form:

$$H_{Fx}(\omega) = \frac{F_{l||}}{\dot{x}_{||}} = \frac{S_E S^* + i\omega S_E R^* - S_E^2 - \omega^2 S_E m^*(\omega)}{S^* + i\omega R^*}. \tag{B.10}$$

The factor S_E is the elastic line stiffness.

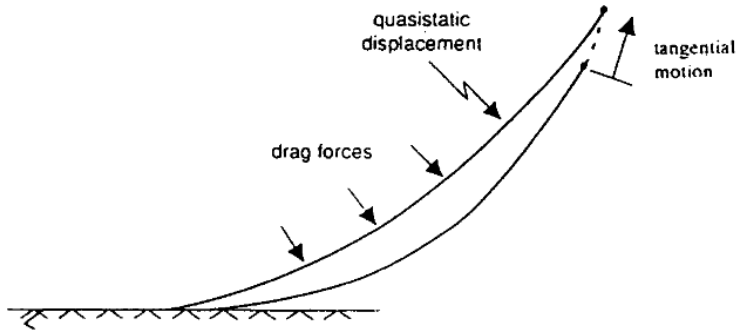

Figure B.14: Sketch of a mooring line and its displacement under tangential motion of the attachment point [77].

Lie and Sødal [77] studied a further simplification of this where the mass terms were neglected. An equivalent spring-damper system for this approximation is shown in Figure B.15, with a corresponding bond graph also shown. The state-space representation for this model becomes:

$$\dot{q}_u = f_{\text{in}} - \frac{S_E q_E - S_u q_u}{R} \tag{B.11}$$

$$\dot{q}_e = \frac{S_E q_E - S_u q_u}{R}. \tag{B.12}$$

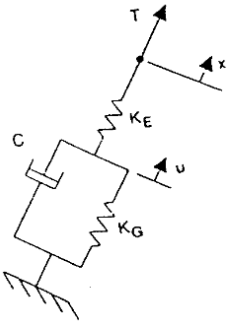

(a) Mechanical equivalent

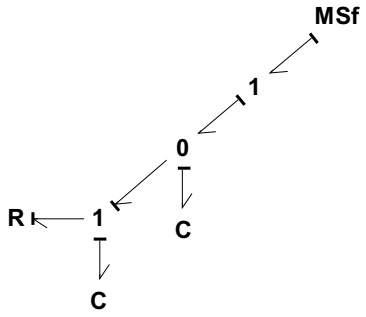

(b) Bond graph model

Figure B.15: A bond graph representation for the simplified mooring line model proposed by Lie and Sødahl [77].

A similar approach were taken by Fitzgerald *et al.* [48]. They made frequency domain models where they linearised all three lateral modes for two types of catenary mooring; one with direct attachment to the floating body and one with a surface-floating mooring buoy as a connecting link. Computed responses calculated by a non-linear method (the MODEX software) were fitted to a second-order model, described by the mass, damping and stiffness terms, i.e. it would be a 1 junction with I, C, and R elements bonded to it. They applied the results in the study of a small buoy-type wave energy converter having four mooring lines.

B.3.2 Lumped mooring line model

A more physically direct alternative for modelling the mooring system is to lump each mooring line in discrete sections and use the mass, damping and

stiffness properties of each cable element and its interaction with the water to derive a mathematical model. The idea is illustrated by Figure B.16. In this way the motion of the whole cable is represented by the model, and this will yield a more correct model when the attachment point moves away from the initial position. The elastic properties of the cable can be used directly as parameters for the C-elements, and Morison's equation gives the drag forces with a suitable choice for the drag coefficient. The method can be seen as a coarse parallel to the finite element approach.

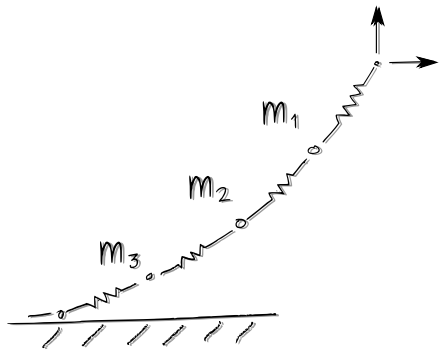

Figure B.16: Illustration of a lumped model for the mooring line. In addition to the shown springs and masses, damping may be added to both the longitudinal and transversal motion of the line, representing viscous and frictional losses.

A similar approach was taken by Pedersen in his modelling of towed marine seismic cables [98]. Assuming that the cables will always be in tension and remain relatively straight, his model did not include bending stiffness. Thus only longitudinal compliance was accounted for, as well as inertia forces (in all three lateral directions) and drag upon transversal motions. In addition, skin friction was included for the longitudinal motion.

The resulting bond graph was similar to the one given in Figure B.17, which have been adopted here to be modified and applied in the modelling of mooring lines.

If there is risk that the line tension will drop to zero or below, the cable's bending stiffness will be important for the dynamic behaviour. One way to include it would be to include a calculation of the difference angles between each segment in the same manner as the difference of longitudinal positions is already calculated, and to add corresponding C and R elements. Here we will only use the same model as Pedersen, assuming the line will always be in tension.

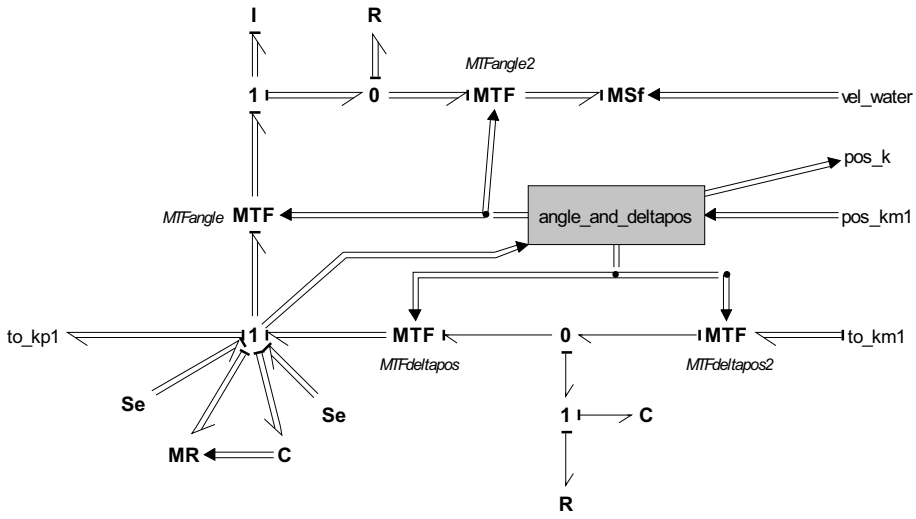

Figure B.17: Bond graph for a segment of the mooring line.

B.3.3 Coordinate transform: Forces linearised about the mean body position

For all of the above mentioned descriptions a coordinate transform is needed in order to relate the mooring force from the cable to the dynamics of the floating structure described in the body-centred, inertial coordinate system. This transform can be approximated by a linear transform, or more accurately done by a non-linear transform.

The easiest formulation is to transform the coordinates directly between the mooring force system and the mean body-position system. Both these systems are fixed relative to the earth system. If we consider the transformation between rotational coordinates as fixed, the rotational moments do not update correctly when the body is rotated. However, for small excursions the error will be small. The translational coordinates transform correctly in this formulation.

In Figure B.18 a bond graph for this system is shown. It uses the Cardan angle transformation with constant angles to transform between the mooring coordinate system and the body average coordinate system.

This transformation is defined by the following matrices [69, Chapter 9]:

$$\mathbf{\Psi} = \begin{bmatrix} \cos(\psi) & -sin(\psi) & 0 \\ \sin(\psi) & cos(\psi) & 0 \\ 0 & 0 & 1 \end{bmatrix} \tag{B.13}$$

$$\mathbf{\Theta} = \begin{bmatrix} \cos(\theta) & 0 & \sin(\theta) \\ 0 & 1 & 0 \\ -\sin(\theta) & 0 & \cos(\theta) \end{bmatrix} \tag{B.14}$$

$$\mathbf{\Phi} = \begin{bmatrix} 1 & 0 & 0 \\ 0 & \cos(\phi) & -\sin(\phi) \\ 0 & \sin(\phi) & \cos(\phi) \end{bmatrix} \tag{B.15}$$

The velocity transform (going from right to left in the figure) sums contri-

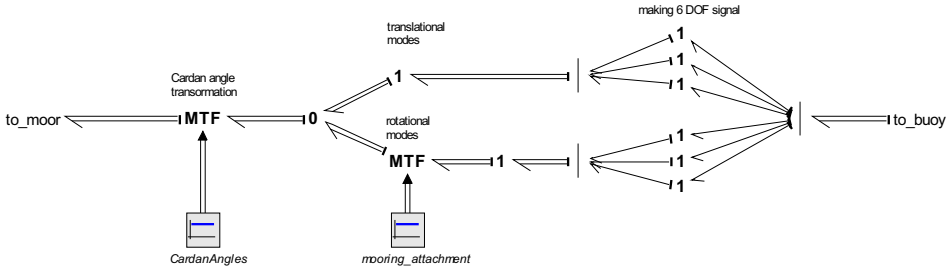

Figure B.18: Bond graph for the linear coordinate transform, assuming the angles to be constant or only slightly varying.

butions from the translational and rotational modes.

B.3.4 Coordinate transform: Nonlinear coupling through body-fixed coordinates

A more accurate model results if we first transform the mooring forces into the body-fixed coordinate system. In this system the attachment point has fixed coordinates, but now the rotation of the body relative to the mooring system is included, and thus the rotational moments transform correctly. The body-fixed coordinates must further be transformed into the mean-position system where the hydrodynamic forces are defined. A bond graph for the extension of the previous transformation (Figure B.18) to this non-linear transformation is shown in Figure B.19. Observe that the Cardan angle transformation of the attachment point now is updated with time-dependent rotation angles.

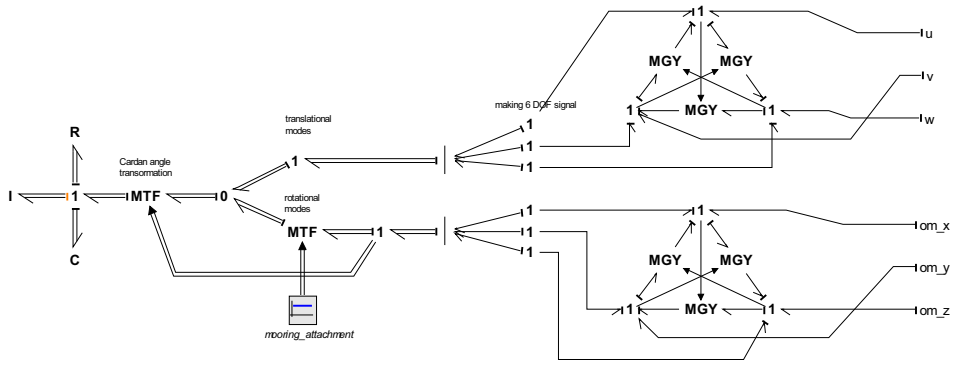

Figure B.19: Bond graph for the nonlinear transformation to body-fixed coordinates. See e.g. Karnopp *et al.* [69] for details about body-fixed coordinates and the triangular bond graph structures to the right in the model graph.

B.4 Wave-to-wire models

This section shows how subsystem models may be assembled to yield full wave-to-wire models for wave energy conversion systems. The models presented here are meant as illustrative examples only, thus no validation has been sought for them, nor have the systems been analysed in detail.

B.4.1 Wave energy converter with hydraulic power take-off

A two-body wave energy converter may be defined as sketched in Figure B.20. The power is extracted from the relative motion using a double-acting hydraulic piston pump connected to a system like the one proposed in Section B.1.1. The reaction force is provided by the inertia of the submerged structure, which is made hollow in order to hold a large amount of water. It is open at the lower end, and should not have any air inside. Due to the shaft the structure has a small vertical buoyancy stiffness which will help in keeping it close to its initial un-forced position.

The system has catenary moorings with mooring buoys to reduce the vertical load on the absorber system. The bond graph representation used is explained by Figure B.21. The mooring lines are modelled with segments as given by Figure B.17. The two floating bodies are represented by a simplified version of the bond graph shown in Figure 2.14, where only the translatory modes have been used in calculation of the dynamics and the relative motion. Furthermore, the power take-off system is equal to the

hydraulic system defined by Figures B.1 and B.2, with the electric side in this case modelled by a simplified generator and grid model.

Setting reasonable parameters for all component, of which some important ones are given in Table B.1, the system may be simulated as described earlier in this thesis. Regular waves coming from a freely selectable direction have been chosen for the excitation. Excerpts of the results from a simulation run are shown in Figures B.22 to B.24.

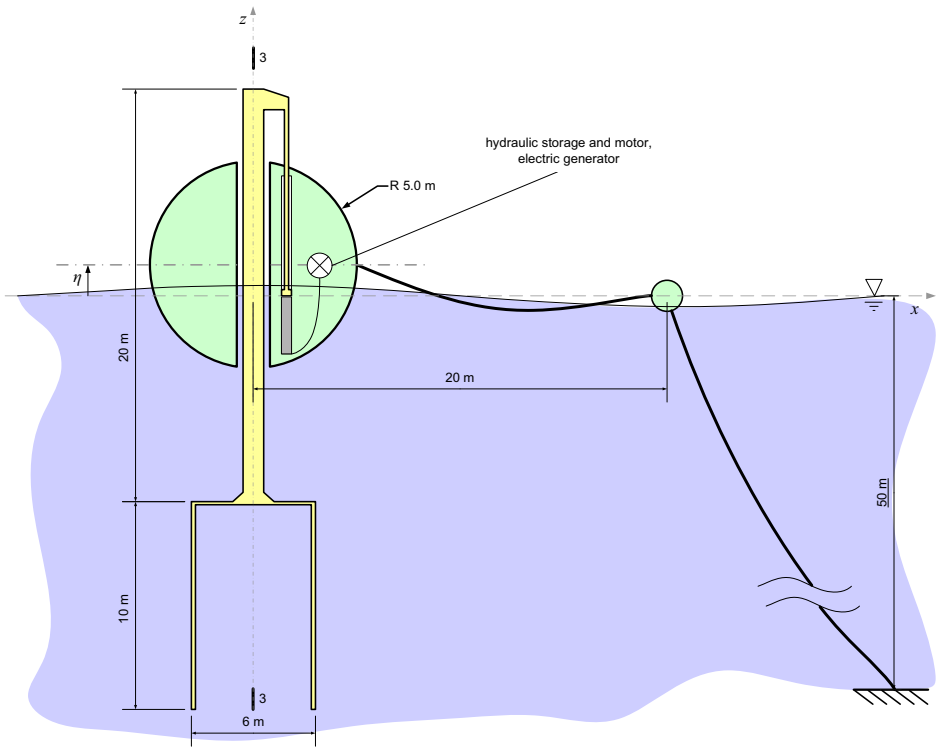

Figure B.20: Sectional drawing (note the 3-number symmetry) of a floating two-body system for wave energy conversion, having catenary moorings and a hydraulic power take-off system.

Table B.1: Some of the parameters for the two-body example. See also Figure B.20.

Quantity	Symbol	Value	Unit
Hydraulic piston diameter	D_p	0.36	m
Hydraulic cylinder length	l_h	6.5	m
Pressure level, HP accumulator	p_{HP}	~ 3	MPa
Pressure level, LP accumulator	p_{LP}	~ 70	kPa
Buoy diameter	D_b	10	m
Mooring line length	l_m	67	m
Mooring line axial stiffness	S_m	60	kN/m
Mooring buoy diameter	D_{mb}	1.0	m
Water depth	h	50	m

B.4.2 Wave energy converter with direct-coupled electric generator

A second system design is shown in Figure B.25. It consists of a heaving buoy reacting against the sea bottom through a direct-coupled permanent-magnet linear generator placed at the sea bed. A pretension mechanism is pulling the buoy down to a semi-submerged position on calm water. The buoy is thus under-ballasted, and it is free to move in all directions.

The component-level bond graph of Figure B.26 shows how the system has been modelled. Again, the line connecting the buoy and the generator is modelled with segments equal to that of Figure B.17. The buoy itself is represented by a six-degree-of-freedom one-junction, like each body of Figure 2.14, while the generator and conversion equipment follow the modelling shown in Figures B.7, B.12 and B.13.

Table B.2 gives a summary of the model parameters. The excitation is also here regular waves, and Figures B.27 to B.30 present a selection of simulation results.

Table B.2: Some of the parameters for the one-body example with a bottom-fixed direct-coupled generator. See also Figure B.25.

Quantity	Symbol	Value	Unit
Buoy mass	m_b	$134{\cdot}10^3$	kg
Slide weight	m_s	$134{\cdot}10^3$	kg
Connection line stiffness	k_s	1.0	MN/m
Generator flux linkage	λ_{gen}	$\cdot 10^3$	Vs
Pole-pole distance		0.2	m
DC-link capacitance		0.01	F

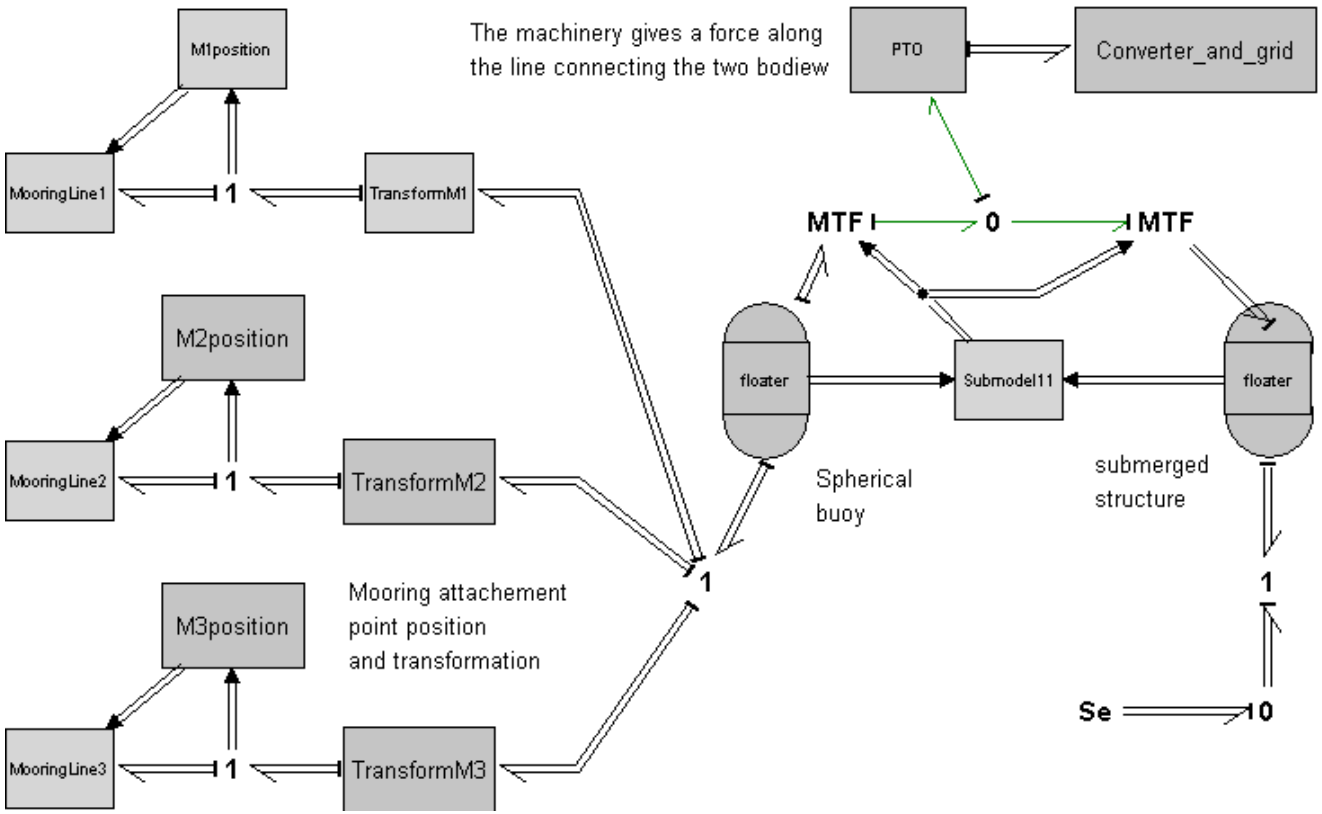

Figure B.21: A bond graph for the system sketched in Figure B.20. The subsystems are composed of the models described in the preceding sections.

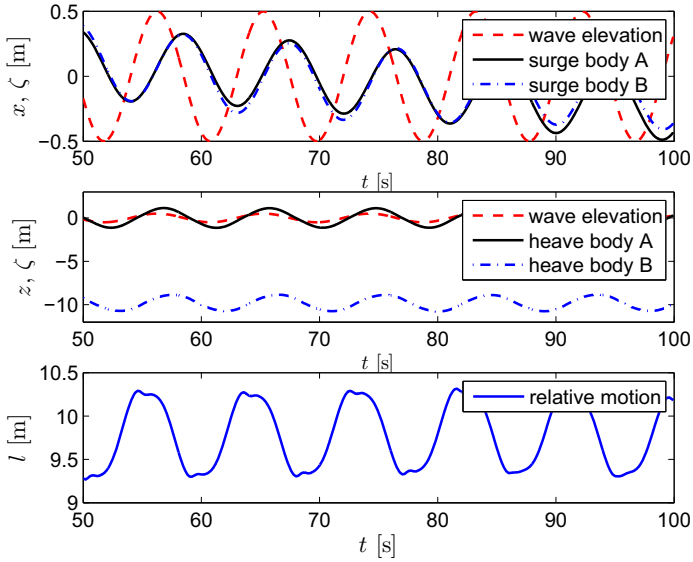

Figure B.22: Motions of the two bodies: the sphere (A) and the submerged structure (B). The upper figure shows the horizontal postitions, the middle figure the vertical positions, and the lower figure shows the relative motion. The wave elevation is given by the dashed red line.

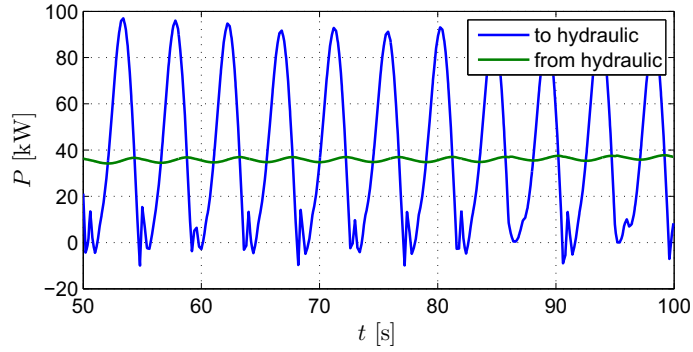

Figure B.23: Power input to the hydraulic system from the relative motion of the bodies, and power output from the hydraulic motor driving the electric generator.

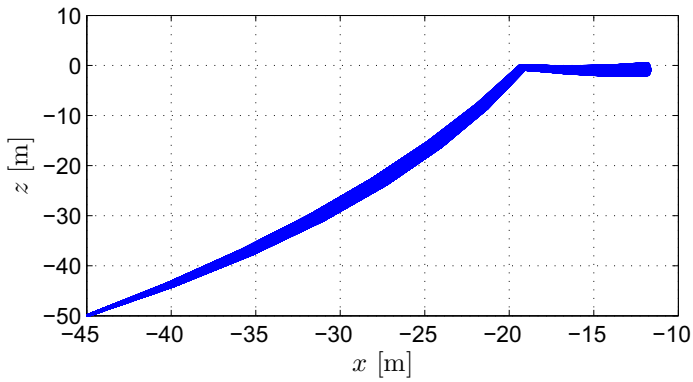

Figure B.24: Snapshots of the mooring-line position, giving the envelope of its oscillation.

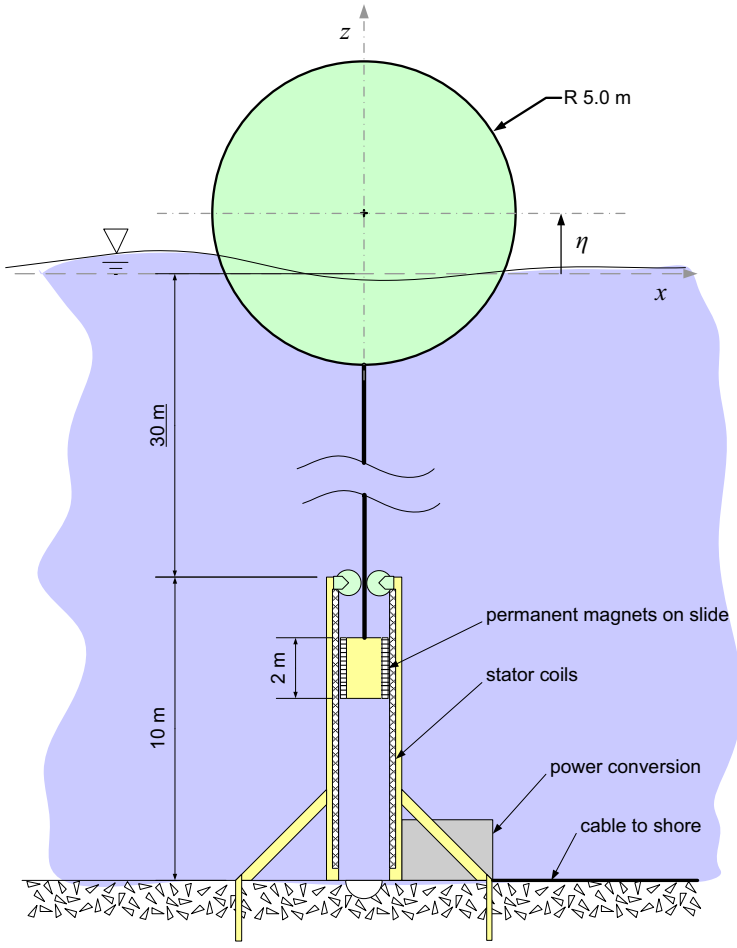

Figure B.25: Sketch of a wave energy converter consisting of a heaving buoy connected to a direct-coupled linear generator placed at the sea bottom.

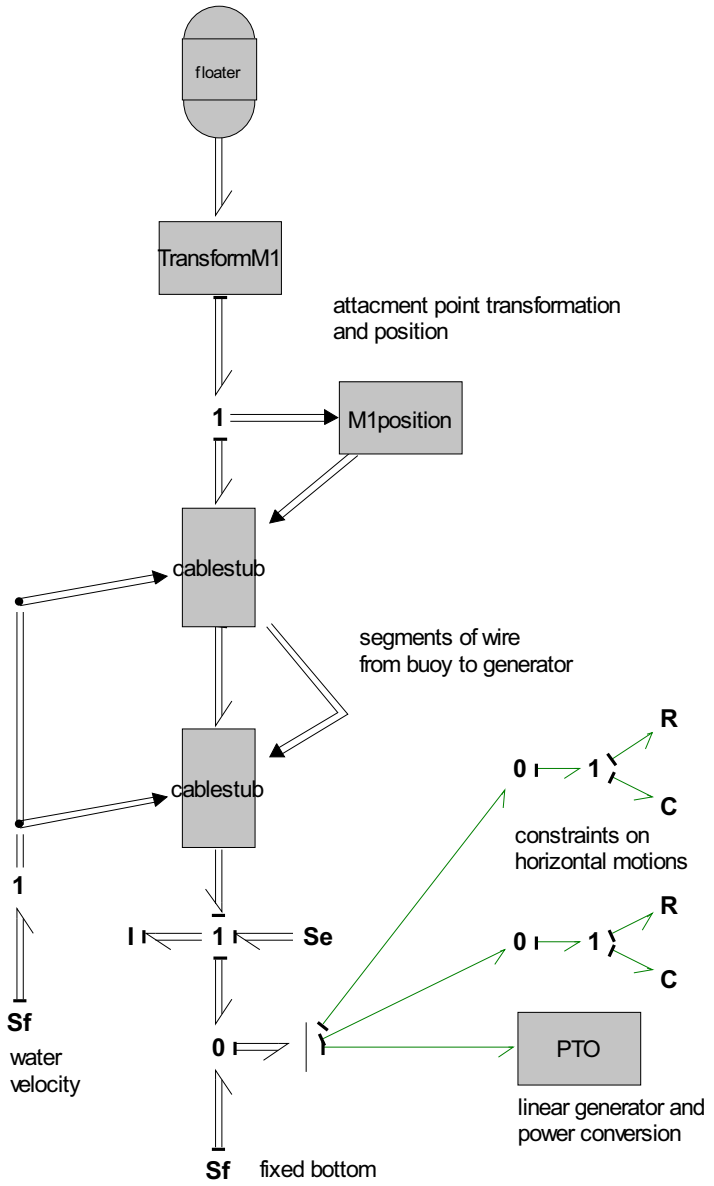

Figure B.26: A bond graph for the system sketched in Figure B.25.

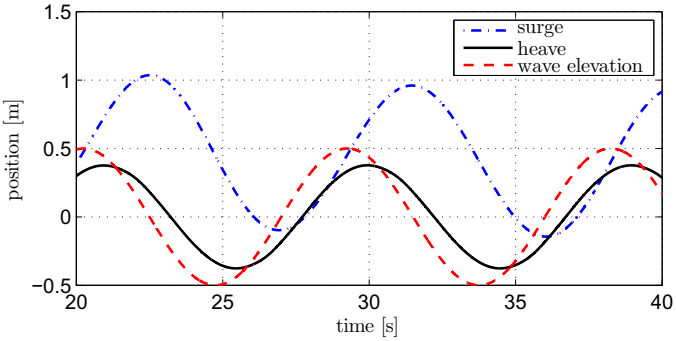

Figure B.27: Wave elevation and buoy motion.

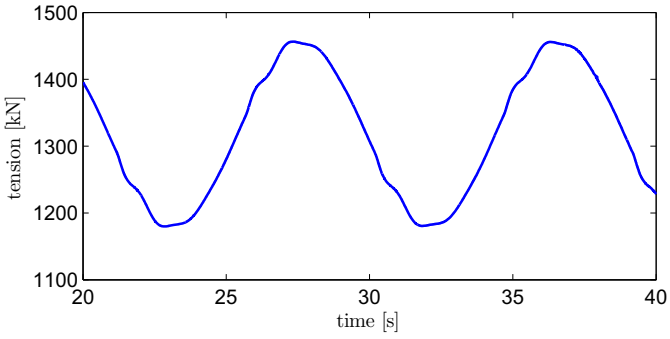

Figure B.28: Tension of the wire connecting the buoy and the generator.

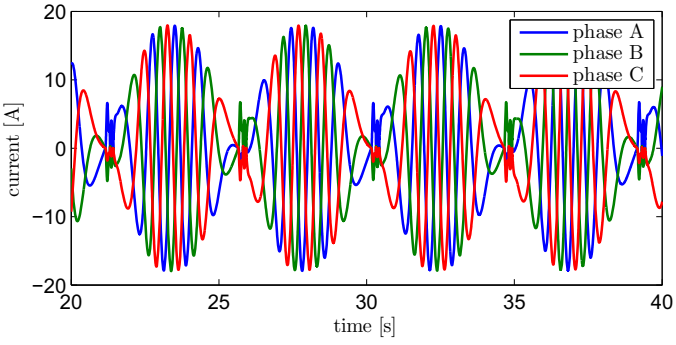

Figure B.29: Phase currents through the stator coils of the electric generator.

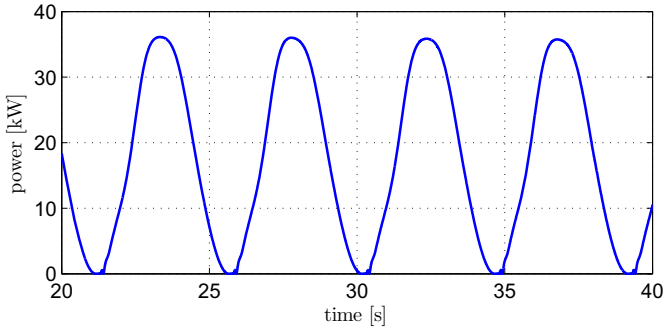

Figure B.30: Power delivered to the grid.

Appendix C

Structure of simulation algorithms

An overview is here given of the structure of Matlab [79] scripts and functions that have been developed during the work with this thesis. It is intended to be an aid for other who want to extend or verify all or parts of the simulation results presented herein.

C.1 Functional level

For the numerical simulation of defined mathematical models, the following tasks must be handled:

Define the geometry The device geometry is here either drawn in the hull design software *Multisurf* or defined by geometric parameters directly in the geometry definition file (.gdf) of *Wamit* [120], which is a velocity potential solver for hydrodynamic parameters.

Compute the hydrodynamic parameters These are computed by *Wamit* and stored in the standard output files. With the definition file *WECsim_def* for the other system parameters, the hydrodynamic parameters are loaded and scaled correctly. At the same time a state-space approximation to the radiation parameters is computed.

Define parameters for the system model This is done in a setup file, *WECsim_def.m*.

Load or generate wave input The following alternatives have been defined for the wave input:

wavefile Load a pre-defined wave elevation time series from file. The corresponding excitation force is calculated by use of the excitation force coefficients in the frequency plane (after Fourier transform).

expfile Use the same time series as for a stored experimental measurement. The corresponding excitation force is calculated by use of the excitation force coefficients in the frequency plane (after Fourier transform)

spectrumfile Load spectrum file (discretised spectrum with phase info). With this option, several simulations can be run for the same synthesised wave input. Wave elevation and excitation force are calculated as described by Equations (4.2) and (2.18), respectively.

spectrumpar The wave spectrum is synthesised for every run based on input parameters. Otherwise as for *spectrumfile*.

regular A discrete wave spectrum with only one frequency component is made based on the user input, and wave elevation time series are synthesised in the same way as for *spectrumfile*

During simulation the wave elevation and excitation force is calculated by interpolation between stored values as described in Section 4.3.

Numerical integration For Matlab/Simulink this is done by the *ODE solvers*, see Section 4.1. The state-space model is stored in the file *WECsim_ss.m*.

Machinery force control The control algorithms are programmed to be separated from the system model such that they easily can be changed. The same goes for the wave prediction algorithm.

Store data The input and output data for simulation *refnum* are stored as data structures in binary files (Matlab format *.mat*) according to the following naming

refnum.sim.mat: Data file containing raw simulation output.

refnum.res.mat: Data file containing treated output.

refnum.lab.mat: Data file containing experimental measurements.

device.par.mat: Contains the geometric parameters of the device in the structure *par*. This includes the geometric dimensions, weight, volume, hydrodynamic parameters and excitation force coefficients (both in transfer function, impulse response and state-space form).

All data that has to do with geometry and system parameters are saved in a structure named *par*, and everything that has to do with wave or force input, and with output response, is stored in the structure *var*.

Analyse results A post-processing algorithm which structures the output data and computes standard statistical measures is provided in a separate file, *WECsim_res.m*. Measures include position and velocity, average and instantaneous absorbed and useful power, radiated power, accumulated absorbed and useful energy.

Graphical presentation Two scripts have been made for standard graphical presentation of simulation results and comparisons between simulation runs, namely *WECsim_plots.m* and *WECsim_comp.m*. Alternative plots include position and velocity in combinations with input waves and excitation forces, instantaneous power and accumulated absorbed energy.

Run multiple simulations Multiple runs is enabled by variable input to the function *WECsim_settings.m* which starts the simulation.

C.2 Routines

Figure C.1 presents the structure of routines needed for the simulations. The tasks of each routine are:

WECsim_def.m Defines the parameters of the conversion system and reads the hydrodynamic data from stored files. Furthermore it calls routines for finding the radiation state-space approximation. The results are stored in the file *device.par.mat*.

R2ss.m Calculates the retardation function from the radiation force parameters, and calls *k2ss.m*

k2ss.m Calculates a state-space approximation to the radiation force convolution term.

WECsim_synt.m Algorithm for synthesising a wave elevation time series from spectral parameter input.

WECsim_w2f.m Reads wave data from experimental results or from wave elevation data saved on file, and store these in structure *var*. Calls subfunction *zeta2Fe.m* in order to convert from wave elevation to excitation force.

zeta2Fe.m Calculates excitation force time series from wave elevation time series based on the excitation force coefficients for the chosen device.

WECsim_settings.m Defines initial values and settings for the simulation, and calls *WECsim_main.m* to start the solver algorithm. The settings include wave input (regular, irregular or time series), device parameters to load, time step, tolerances, and control strategy.

WECsim_main.m This is the main file for the numerical integration. It calls the state-space model solver and collects the simulation results. The *par* and *var* structures are passed to the state-space function *WECsim_ss.m*.

WECsim_ss.m Calculates the derivatives in the state-space model for each time step.

WECsim_run.m Script file for running various simulations belonging to one simulation campaign.

WECsim_cont.m Computes the controller effort at each time step.

WECsim_augKF.m Implementation of the augmented Kalman filter used for wave elevation and excitation force prediction.

augKF_define.m Defining parameter for the augmented Kalman filter.

WECsim_res.m Reads stored simulation data, calculates chosen quantities, and saves result to file.

WECsim_output.m Defines actions to be taken at each instant defined by the time vector. It is need by the controller algorithms contained in *WECsim_cont.m*.

WECsim_plots.m Makes selected plots from saved data.

WECsim_comp.m Reads treated data from file and compares between different runs.

C.3 Stored variables

As mentioned above, the *par* and *var* structures contain the device parameters and the simulation inputs and outputs, respectively. It is assumed that all vectors based on discretised time or frequency are defined as column vectors.

Fields of the *par* structure

g	Acceleration of gravity [m/s^2]
rho	Water density [kg/m^3]
h	Water depth [m]
omega	Angular frequency vector for the hydrodynamic parameters and transfer functions [rad/s]
k	Wave number [m^{-1}]
m	Body mass [kg]
m_r	Added mass [kg]
m_inf	Added mass at infinity [kg]
R_r	Radiation resistance [kg/s]
S	Hydrostatic stiffness [N/m]
H_F	Excitation force coefficients [N/m]
Ar	State-space system matrix for approximation of the radiation force

Br	State-space input matrix for approximation of the radiation force
Cr	State-space output matrix for approximation of the radiation force
Dr	State-space feed-through matrix for approximation of the radiation force
predictor	Name of prediction function
controller	Name of controller function
ssfile	Name of state-space function
inputfile	Name of input file
inputtype	Chosen input method
refnum	Name of simulation run
parfile	Name of the file containing the hydrodynamic parameters
neqs	Number of equations in system model
nradstates	Number of equations in radiation model
nstates	Total number of equations in model to be integrated, nstates=neqs+nradstates
unit	Contains units of all fields as substructure
desc	Contains description of all fields as substructure

Fields of the *var* structure

t	Time vector [s]
dt	Time step [s]
spectrum	Substructure containing wave-spectrum parameters
y	State vector
y0	Initial values
velocity	The body velocity time series [m/s]
mom	The linear momentum time series [kg m/s]
position	The body position time series [m]
zeta	Wave elevation time series at reference point [m]
Fe	Excitation force time series [N]
Fm	The machinery force time series [N]
Fr	The radiation force time series [N]
Pe	The excitation power time series [W]
Pu	The useful power time series (converted by the machinery) [W]
Pr	The radiated power time series [W]
Pa	The absorbed power time series [W]

Pu_avg	The average useful power [W]
Pa_avg	The average absorbed power [W]
Eu	Accumulated useful energy [J]
Ea	Accumulated absorbed energy [J]
J	The wave power level (average for irregular waves) [W/m]
cont	Chosen control strategy for simulation
unit	Contains units of all fields as substructure
desc	Contains description of all fields as substructure

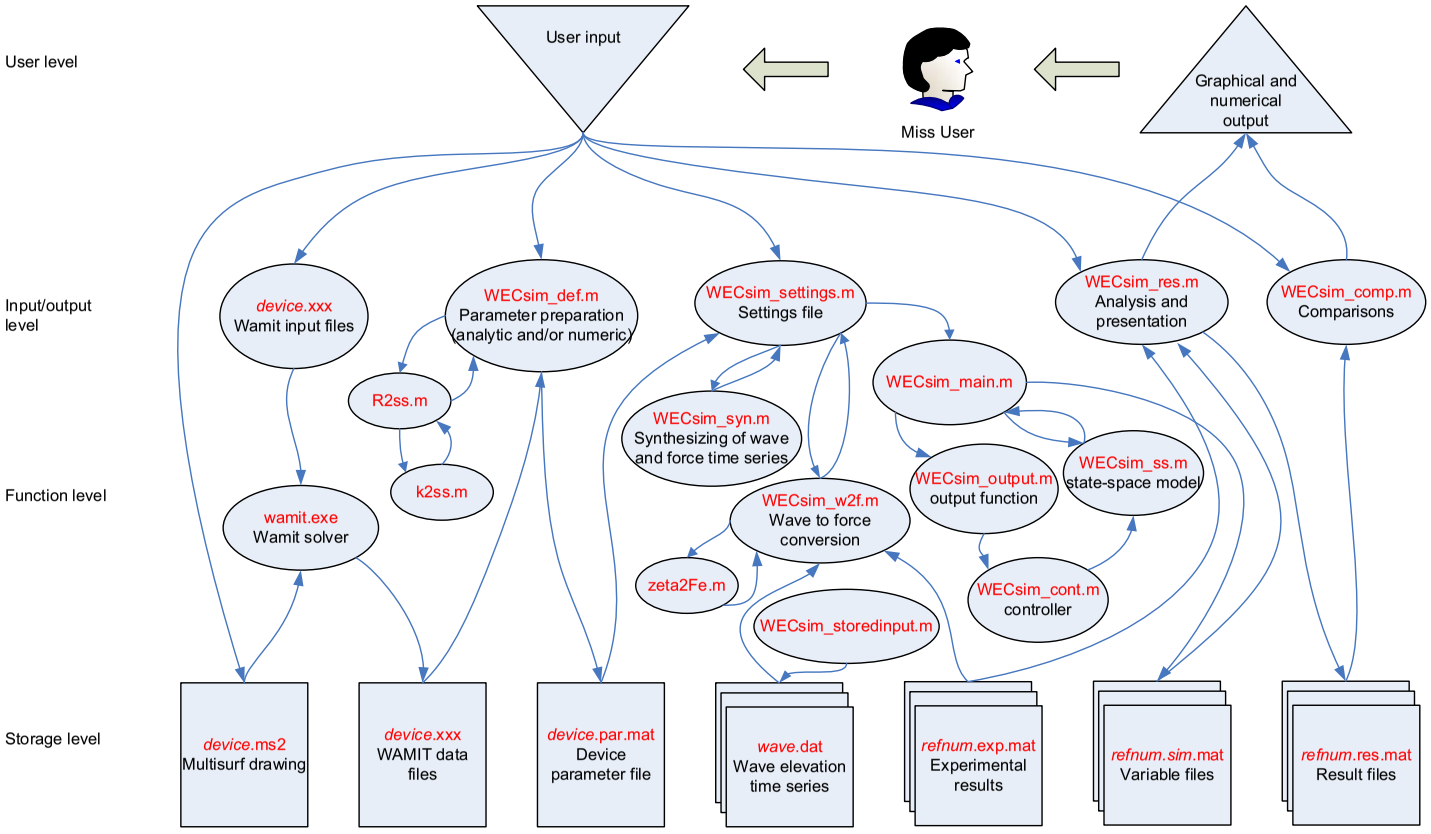

Figure C.1: The structure of simulation and analysis routines

R A P P O R T E R
UTGITT VED
INSTITUTT FOR MARIN TEKNIKK
(tidligere: FAKULTET FOR MARIN TEKNIKK)
NORGES TEKNISK-NATURVITENSKAPELIGE UNIVERSITET

Report No.	Author	Title
	Kavlie, Dag	Optimization of Plane Elastic Grillages, 1967
	Hansen, Hans R.	Man-Machine Communication and Data-Storage Methods in Ship Structural Design, 1971
	Gisvold, Kaare M.	A Method for non-linear mixed -integer programming and its Application to Design Problems, 1971
	Lund, Sverre	Tanker Frame Optimalization by means of SUMT-Transformation and Behaviour Models, 1971
	Vinje, Tor	On Vibration of Spherical Shells Interacting with Fluid, 1972
	Lorentz, Jan D.	Tank Arrangement for Crude Oil Carriers in Accordance with the new Anti-Pollution Regulations, 1975
	Carlsen, Carl A.	Computer-Aided Design of Tanker Structures, 1975
	Larsen, Carl M.	Static and Dynamic Analysis of Offshore Pipelines during Installation, 1976
UR-79-01	Brigt Hatlestad, MK	The finite element method used in a fatigue evaluation of fixed offshore platforms. (Dr.Ing. Thesis)
UR-79-02	Erik Pettersen, MK	Analysis and design of cellular structures. (Dr.Ing. Thesis)
UR-79-03	Sverre Valsgård, MK	Finite difference and finite element methods applied to nonlinear analysis of plated structures. (Dr.Ing. Thesis)
UR-79-04	Nils T. Nordsve, MK	Finite element collapse analysis of structural members considering imperfections and stresses due to fabrication. (Dr.Ing. Thesis)
UR-79-05	Ivar J. Fylling, MK	Analysis of towline forces in ocean towing systems. (Dr.Ing. Thesis)
UR-80-06	Nils Sandsmark, MM	Analysis of Stationary and Transient Heat Conduction by the Use of the Finite Element Method. (Dr.Ing. Thesis)
UR-80-09	Sverre Haver, MK	Analysis of uncertainties related to the stochastic modeling of ocean waves. (Dr.Ing. Thesis)
UR-81-15	Odland, Jonas	On the Strength of welded Ring stiffened cylindrical Shells primarily subjected to axial Compression

UR-82-17	Engesvik, Knut	Analysis of Uncertainties in the fatigue Capacity of Welded Joints
UR-82-18	Rye, Henrik	Ocean wave groups
UR-83-30	Eide, Oddvar Inge	On Cumulative Fatigue Damage in Steel Welded Joints
UR-83-33	Mo, Olav	Stochastic Time Domain Analysis of Slender Offshore Structures
UR-83-34	Amdahl, Jørgen	Energy absorption in Ship-platform impacts
UR-84-37	Mørch, Morten	Motions and mooring forces of semi submersibles as determined by full-scale measurements and theoretical analysis
UR-84-38	Soares, C. Guedes	Probabilistic models for load effects in ship structures
UR-84-39	Aarsnes, Jan V.	Current forces on ships
UR-84-40	Czujko, Jerzy	Collapse Analysis of Plates subjected to Biaxial Compression and Lateral Load
UR-85-46	Alf G. Engseth, MK	Finite element collapse analysis of tubular steel offshore structures. (Dr.Ing. Thesis)
UR-86-47	Dengody Sheshappa, MP	A Computer Design Model for Optimizing Fishing Vessel Designs Based on Techno-Economic Analysis. (Dr.Ing. Thesis)
UR-86-48	Vidar Aanesland, MH	A Theoretical and Numerical Study of Ship Wave Resistance. (Dr.Ing. Thesis)
UR-86-49	Heinz-Joachim Wessel, MK	Fracture Mechanics Analysis of Crack Growth in Plate Girders. (Dr.Ing. Thesis)
UR-86-50	Jon Taby, MK	Ultimate and Post-ultimate Strength of Dented Tubular Members. (Dr.Ing. Thesis)
UR-86-51	Walter Lian, MH	A Numerical Study of Two-Dimensional Separated Flow Past Bluff Bodies at Moderate KC-Numbers. (Dr.Ing. Thesis)
UR-86-52	Bjørn Sortland, MH	Force Measurements in Oscillating Flow on Ship Sections and Circular Cylinders in a U-Tube Water Tank. (Dr.Ing. Thesis)
UR-86-53	Kurt Strand, MM	A System Dynamic Approach to One-dimensional Fluid Flow. (Dr.Ing. Thesis)
UR-86-54	Arne Edvin Løken, MH	Three Dimensional Second Order Hydrodynamic Effects on Ocean Structures in Waves. (Dr.Ing. Thesis)
UR-86-55	Sigurd Falch, MH	A Numerical Study of Slamming of Two-Dimensional Bodies. (Dr.Ing. Thesis)
UR-87-56	Arne Braathen, MH	Application of a Vortex Tracking Method to the Prediction of Roll Damping of a Two-Dimension

		Floating Body. (Dr.Ing. Thesis)
UR-87-57	Bernt Leira, MK	Gaussian Vector Processes for Reliability Analysis involving Wave-Induced Load Effects. (Dr.Ing. Thesis)
UR-87-58	Magnus Småvik, MM	Thermal Load and Process Characteristics in a Two-Stroke Diesel Engine with Thermal Barriers (in Norwegian). (Dr.Ing. Thesis)
MTA-88-59	Bernt Arild Bremdal, MP	An Investigation of Marine Installation Processes – A Knowledge - Based Planning Approach. (Dr.Ing. Thesis)
MTA-88-60	Xu Jun, MK	Non-linear Dynamic Analysis of Space-framed Offshore Structures. (Dr.Ing. Thesis)
MTA-89-61	Gang Miao, MH	Hydrodynamic Forces and Dynamic Responses of Circular Cylinders in Wave Zones. (Dr.Ing. Thesis)
MTA-89-62	Martin Greenhow, MH	Linear and Non-Linear Studies of Waves and Floating Bodies. Part I and Part II. (Dr.Techn. Thesis)
MTA-89-63	Chang Li, MH	Force Coefficients of Spheres and Cubes in Oscillatory Flow with and without Current. (Dr.Ing. Thesis
MTA-89-64	Hu Ying, MP	A Study of Marketing and Design in Development of Marine Transport Systems. (Dr.Ing. Thesis)
MTA-89-65	Arild Jæger, MH	Seakeeping, Dynamic Stability and Performance of a Wedge Shaped Planing Hull. (Dr.Ing. Thesis)
MTA-89-66	Chan Siu Hung, MM	The dynamic characteristics of tilting-pad bearings
MTA-89-67	Kim Wikstrøm, MP	Analysis av projekteringen for ett offshore projekt. (Licenciat-avhandling)
MTA-89-68	Jiao Guoyang, MK	Reliability Analysis of Crack Growth under Random Loading, considering Model Updating. (Dr.Ing. Thesis)
MTA-89-69	Arnt Olufsen, MK	Uncertainty and Reliability Analysis of Fixed Offshore Structures. (Dr.Ing. Thesis)
MTA-89-70	Wu Yu-Lin, MR	System Reliability Analyses of Offshore Structures using improved Truss and Beam Models. (Dr.Ing. Thesis)
MTA-90-71	Jan Roger Hoff, MH	Three-dimensional Green function of a vessel with forward speed in waves. (Dr.Ing. Thesis)
MTA-90-72	Rong Zhao, MH	Slow-Drift Motions of a Moored Two-Dimensional Body in Irregular Waves. (Dr.Ing. Thesis)
MTA-90-73	Atle Minsaas, MP	Economical Risk Analysis. (Dr.Ing. Thesis)
MTA-90-74	Knut-Aril Farnes, MK	Long-term Statistics of Response in Non-linear Marine Structures. (Dr.Ing. Thesis)
MTA-90-	Torbjørn Sotberg, MK	Application of Reliability Methods for Safety

75		Assessment of Submarine Pipelines. (Dr.Ing. Thesis)
MTA-90-76	Zeuthen, Steffen, MP	SEAMAID. A computational model of the design process in a constraint-based logic programming environment. An example from the offshore domain. (Dr.Ing. Thesis)
MTA-91-77	Haagensen, Sven, MM	Fuel Dependant Cyclic Variability in a Spark Ignition Engine - An Optical Approach. (Dr.Ing. Thesis)
MTA-91-78	Løland, Geir, MH	Current forces on and flow through fish farms. (Dr.Ing. Thesis)
MTA-91-79	Hoen, Christopher, MK	System Identification of Structures Excited by Stochastic Load Processes. (Dr.Ing. Thesis)
MTA-91-80	Haugen, Stein, MK	Probabilistic Evaluation of Frequency of Collision between Ships and Offshore Platforms. (Dr.Ing. Thesis)
MTA-91-81	Sødahl, Nils, MK	Methods for Design and Analysis of Flexible Risers. (Dr.Ing. Thesis)
MTA-91-82	Ormberg, Harald, MK	Non-linear Response Analysis of Floating Fish Farm Systems. (Dr.Ing. Thesis)
MTA-91-83	Marley, Mark J., MK	Time Variant Reliability under Fatigue Degradation. (Dr.Ing. Thesis)
MTA-91-84	Krokstad, Jørgen R., MH	Second-order Loads in Multidirectional Seas. (Dr.Ing. Thesis)
MTA-91-85	Molteberg, Gunnar A., MM	The Application of System Identification Techniques to Performance Monitoring of Four Stroke Turbocharged Diesel Engines. (Dr.Ing. Thesis)
MTA-92-86	Mørch, Hans Jørgen Bjelke, MH	Aspects of Hydrofoil Design: with Emphasis on Hydrofoil Interaction in Calm Water. (Dr.Ing. Thesis)
MTA-92-87	Chan Siu Hung, MM	Nonlinear Analysis of Rotordynamic Instabilities in Highspeed Turbomachinery. (Dr.Ing. Thesis)
MTA-92-88	Bessason, Bjarni, MK	Assessment of Earthquake Loading and Response of Seismically Isolated Bridges. (Dr.Ing. Thesis)
MTA-92-89	Langli, Geir, MP	Improving Operational Safety through exploitation of Design Knowledge - an investigation of offshore platform safety. (Dr.Ing. Thesis)
MTA-92-90	Sævik, Svein, MK	On Stresses and Fatigue in Flexible Pipes. (Dr.Ing. Thesis)
MTA-92-91	Ask, Tor Ø., MM	Ignition and Flame Growth in Lean Gas-Air Mixtures. An Experimental Study with a Schlieren System. (Dr.Ing. Thesis)
MTA-86-92	Hessen, Gunnar, MK	Fracture Mechanics Analysis of Stiffened Tubular

		Members. (Dr.Ing. Thesis)
MTA-93-93	Steinebach, Christian, MM	Knowledge Based Systems for Diagnosis of Rotating Machinery. (Dr.Ing. Thesis)
MTA-93-94	Dalane, Jan Inge, MK	System Reliability in Design and Maintenance of Fixed Offshore Structures. (Dr.Ing. Thesis)
MTA-93-95	Steen, Sverre, MH	Cobblestone Effect on SES. (Dr.Ing. Thesis)
MTA-93-96	Karunakaran, Daniel, MK	Nonlinear Dynamic Response and Reliability Analysis of Drag-dominated Offshore Platforms. (Dr.Ing. Thesis)
MTA-93-97	Hagen, Arnulf, MP	The Framework of a Design Process Language. (Dr.Ing. Thesis)
MTA-93-98	Nordrik, Rune, MM	Investigation of Spark Ignition and Autoignition in Methane and Air Using Computational Fluid Dynamics and Chemical Reaction Kinetics. A Numerical Study of Ignition Processes in Internal Combustion Engines. (Dr.Ing. Thesis)
MTA-94-99	Passano, Elizabeth, MK	Efficient Analysis of Nonlinear Slender Marine Structures. (Dr.Ing. Thesis)
MTA-94-100	Kvålsvold, Jan, MH	Hydroelastic Modelling of Wetdeck Slamming on Multihull Vessels. (Dr.Ing. Thesis)
MTA-94-102	Bech, Sidsel M., MK	Experimental and Numerical Determination of Stiffness and Strength of GRP/PVC Sandwich Structures. (Dr.Ing. Thesis)
MTA-95-103	Paulsen, Hallvard, MM	A Study of Transient Jet and Spray using a Schlieren Method and Digital Image Processing. (Dr.Ing. Thesis)
MTA-95-104	Hovde, Geir Olav, MK	Fatigue and Overload Reliability of Offshore Structural Systems, Considering the Effect of Inspection and Repair. (Dr.Ing. Thesis)
MTA-95-105	Wang, Xiaozhi, MK	Reliability Analysis of Production Ships with Emphasis on Load Combination and Ultimate Strength. (Dr.Ing. Thesis)
MTA-95-106	Ulstein, Tore, MH	Nonlinear Effects of a Flexible Stern Seal Bag on Cobblestone Oscillations of an SES. (Dr.Ing. Thesis)
MTA-95-107	Solaas, Frøydis, MH	Analytical and Numerical Studies of Sloshing in Tanks. (Dr.Ing. Thesis)
MTA-95-108	Hellan, Øyvind, MK	Nonlinear Pushover and Cyclic Analyses in Ultimate Limit State Design and Reassessment of Tubular Steel Offshore Structures. (Dr.Ing. Thesis)
MTA-95-109	Hermundstad, Ole A., MK	Theoretical and Experimental Hydroelastic Analysis of High Speed Vessels. (Dr.Ing. Thesis)
MTA-96-110	Bratland, Anne K., MH	Wave-Current Interaction Effects on Large-Volume Bodies in Water of Finite Depth. (Dr.Ing. Thesis)

MTA-96-111	Herfjord, Kjell, MH	A Study of Two-dimensional Separated Flow by a Combination of the Finite Element Method and Navier-Stokes Equations. (Dr.Ing. Thesis)
MTA-96-112	Æsøy, Vilmar, MM	Hot Surface Assisted Compression Ignition in a Direct Injection Natural Gas Engine. (Dr.Ing. Thesis)
MTA-96-113	Eknes, Monika L., MK	Escalation Scenarios Initiated by Gas Explosions on Offshore Installations. (Dr.Ing. Thesis)
MTA-96-114	Erikstad, Stein O., MP	A Decision Support Model for Preliminary Ship Design. (Dr.Ing. Thesis)
MTA-96-115	Pedersen, Egil, MH	A Nautical Study of Towed Marine Seismic Streamer Cable Configurations. (Dr.Ing. Thesis)
MTA-97-116	Moksnes, Paul O., MM	Modelling Two-Phase Thermo-Fluid Systems Using Bond Graphs. (Dr.Ing. Thesis)
MTA-97-117	Halse, Karl H., MK	On Vortex Shedding and Prediction of Vortex-Induced Vibrations of Circular Cylinders. (Dr.Ing. Thesis)
MTA-97-118	Igland, Ragnar T., MK	Reliability Analysis of Pipelines during Laying, considering Ultimate Strength under Combined Loads. (Dr.Ing. Thesis)
MTA-97-119	Pedersen, Hans-P., MP	Levendefiskteknologi for fiskefartøy. (Dr.Ing. Thesis)
MTA-98-120	Vikestad, Kyrre, MK	Multi-Frequency Response of a Cylinder Subjected to Vortex Shedding and Support Motions. (Dr.Ing. Thesis)
MTA-98-121	Azadi, Mohammad R. E., MK	Analysis of Static and Dynamic Pile-Soil-Jacket Behaviour. (Dr.Ing. Thesis)
MTA-98-122	Ulltang, Terje, MP	A Communication Model for Product Information. (Dr.Ing. Thesis)
MTA-98-123	Torbergsen, Erik, MM	Impeller/Diffuser Interaction Forces in Centrifugal Pumps. (Dr.Ing. Thesis)
MTA-98-124	Hansen, Edmond, MH	A Discrete Element Model to Study Marginal Ice Zone Dynamics and the Behaviour of Vessels Moored in Broken Ice. (Dr.Ing. Thesis)
MTA-98-125	Videiro, Paulo M., MK	Reliability Based Design of Marine Structures. (Dr.Ing. Thesis)
MTA-99-126	Mainçon, Philippe, MK	Fatigue Reliability of Long Welds Application to Titanium Risers. (Dr.Ing. Thesis)
MTA-99-127	Haugen, Elin M., MH	Hydroelastic Analysis of Slamming on Stiffened Plates with Application to Catamaran Wetdecks. (Dr.Ing. Thesis)
MTA-99-128	Langhelle, Nina K., MK	Experimental Validation and Calibration of Nonlinear Finite Element Models for Use in Design of Aluminium Structures Exposed to Fire. (Dr.Ing.

		Thesis)
MTA-99-129	Berstad, Are J., MK	Calculation of Fatigue Damage in Ship Structures. (Dr.Ing. Thesis)
MTA-99-130	Andersen, Trond M., MM	Short Term Maintenance Planning. (Dr.Ing. Thesis)
MTA-99-131	Tveiten, Bård Wathne, MK	Fatigue Assessment of Welded Aluminium Ship Details. (Dr.Ing. Thesis)
MTA-99-132	Søreide, Fredrik, MP	Applications of underwater technology in deep water archaeology. Principles and practice. (Dr.Ing. Thesis)
MTA-99-133	Tønnessen, Rune, MH	A Finite Element Method Applied to Unsteady Viscous Flow Around 2D Blunt Bodies With Sharp Corners. (Dr.Ing. Thesis)
MTA-99-134	Elvekrok, Dag R., MP	Engineering Integration in Field Development Projects in the Norwegian Oil and Gas Industry. The Supplier Management of Norne. (Dr.Ing. Thesis)
MTA-99-135	Fagerholt, Kjetil, MP	Optimeringsbaserte Metoder for Ruteplanlegging innen skipsfart. (Dr.Ing. Thesis)
MTA-99-136	Bysveen, Marie, MM	Visualization in Two Directions on a Dynamic Combustion Rig for Studies of Fuel Quality. (Dr.Ing. Thesis)
MTA-2000-137	Storteig, Eskild, MM	Dynamic characteristics and leakage performance of liquid annular seals in centrifugal pumps. (Dr.Ing. Thesis)
MTA-2000-138	Sagli, Gro, MK	Model uncertainty and simplified estimates of long term extremes of hull girder loads in ships. (Dr.Ing. Thesis)
MTA-2000-139	Tronstad, Harald, MK	Nonlinear analysis and design of cable net structures like fishing gear based on the finite element method. (Dr.Ing. Thesis)
MTA-2000-140	Kroneberg, André, MP	Innovation in shipping by using scenarios. (Dr.Ing. Thesis)
MTA-2000-141	Haslum, Herbjørn Alf, MH	Simplified methods applied to nonlinear motion of spar platforms. (Dr.Ing. Thesis)
MTA-2001-142	Samdal, Ole Johan, MM	Modelling of Degradation Mechanisms and Stressor Interaction on Static Mechanical Equipment Residual Lifetime. (Dr.Ing. Thesis)
MTA-2001-143	Baarholm, Rolf Jarle, MH	Theoretical and experimental studies of wave impact underneath decks of offshore platforms. (Dr.Ing. Thesis)
MTA-2001-144	Wang, Lihua, MK	Probabilistic Analysis of Nonlinear Wave-induced Loads on Ships. (Dr.Ing. Thesis)
MTA-2001-145	Kristensen, Odd H. Holt, MK	Ultimate Capacity of Aluminium Plates under Multiple Loads, Considering HAZ Properties. (Dr.Ing. Thesis)

MTA-2001-146	Greco, Marilena, MH	A Two-Dimensional Study of Green-Water Loading. (Dr.Ing. Thesis)
MTA-2001-147	Heggelund, Svein E., MK	Calculation of Global Design Loads and Load Effects in Large High Speed Catamarans. (Dr.Ing. Thesis)
MTA-2001-148	Babalola, Olusegun T., MK	Fatigue Strength of Titanium Risers – Defect Sensitivity. (Dr.Ing. Thesis)
MTA-2001-149	Mohammed, Abuu K., MK	Nonlinear Shell Finite Elements for Ultimate Strength and Collapse Analysis of Ship Structures. (Dr.Ing. Thesis)
MTA-2002-150	Holmedal, Lars E., MH	Wave-current interactions in the vicinity of the sea bed. (Dr.Ing. Thesis)
MTA-2002-151	Rognebakke, Olav F., MH	Sloshing in rectangular tanks and interaction with ship motions. (Dr.Ing. Thesis)
MTA-2002-152	Lader, Pål Furset, MH	Geometry and Kinematics of Breaking Waves. (Dr.Ing. Thesis)
MTA-2002-153	Yang, Qinzheng, MH	Wash and wave resistance of ships in finite water depth. (Dr.Ing. Thesis)
MTA-2002-154	Melhus, Øyvin, MM	Utilization of VOC in Diesel Engines. Ignition and combustion of VOC released by crude oil tankers. (Dr.Ing. Thesis)
MTA-2002-155	Ronæss, Marit, MH	Wave Induced Motions of Two Ships Advancing on Parallel Course. (Dr.Ing. Thesis)
MTA-2002-156	Økland, Ole D., MK	Numerical and experimental investigation of whipping in twin hull vessels exposed to severe wet deck slamming. (Dr.Ing. Thesis)
MTA-2002-157	Ge, Chunhua, MK	Global Hydroelastic Response of Catamarans due to Wet Deck Slamming. (Dr.Ing. Thesis)
MTA-2002-158	Byklum, Eirik, MK	Nonlinear Shell Finite Elements for Ultimate Strength and Collapse Analysis of Ship Structures. (Dr.Ing. Thesis)
IMT-2003-1	Chen, Haibo, MK	Probabilistic Evaluation of FPSO-Tanker Collision in Tandem Offloading Operation. (Dr.Ing. Thesis)
IMT-2003-2	Skaugset, Kjetil Bjørn, MK	On the Suppression of Vortex Induced Vibrations of Circular Cylinders by Radial Water Jets. (Dr.Ing. Thesis)
IMT-2003-3	Chezhian, Muthu	Three-Dimensional Analysis of Slamming. (Dr.Ing. Thesis)
IMT-2003-4	Buhaug, Øyvind	Deposit Formation on Cylinder Liner Surfaces in Medium Speed Engines. (Dr.Ing. Thesis)
IMT-2003-5	Tregde, Vidar	Aspects of Ship Design: Optimization of Aft Hull with Inverse Geometry Design. (Dr.Ing. Thesis)
IMT-2003-6	Wist, Hanne Therese	Statistical Properties of Successive Ocean Wave

		Parameters. (Dr.Ing. Thesis)
IMT-2004-7	Ransau, Samuel	Numerical Methods for Flows with Evolving Interfaces. (Dr.Ing. Thesis)
IMT-2004-8	Soma, Torkel	Blue-Chip or Sub-Standard. A data interrogation approach of identity safety characteristics of shipping organization. (Dr.Ing. Thesis)
IMT-2004-9	Ersdal, Svein	An experimental study of hydrodynamic forces on cylinders and cables in near axial flow. (Dr.Ing. Thesis)
IMT-2005-10	Brodtkorb, Per Andreas	The Probability of Occurrence of Dangerous Wave Situations at Sea. (Dr.Ing. Thesis)
IMT-2005-11	Yttervik, Rune	Ocean current variability in relation to offshore engineering. (Dr.Ing. Thesis)
IMT-2005-12	Fredheim, Arne	Current Forces on Net-Structures. (Dr.Ing. Thesis)
IMT-2005-13	Heggernes, Kjetil	Flow around marine structures. (Dr.Ing. Thesis
IMT-2005-14	Fouques, Sebastien	Lagrangian Modelling of Ocean Surface Waves and Synthetic Aperture Radar Wave Measurements. (Dr.Ing. Thesis)
IMT-2006-15	Holm, Håvard	Numerical calculation of viscous free surface flow around marine structures. (Dr.Ing. Thesis)
IMT-2006-16	Bjørheim, Lars G.	Failure Assessment of Long Through Thickness Fatigue Cracks in Ship Hulls. (Dr.Ing. Thesis)
IMT-2006-17	Hansson, Lisbeth	Safety Management for Prevention of Occupational Accidents. (Dr.Ing. Thesis)
IMT-2006-18	Zhu, Xinying	Application of the CIP Method to Strongly Nonlinear Wave-Body Interaction Problems. (Dr.Ing. Thesis)
IMT-2006-19	Reite, Karl Johan	Modelling and Control of Trawl Systems. (Dr.Ing. Thesis)
IMT-2006-20	Smogeli, Øyvind Notland	Control of Marine Propellers. From Normal to Extreme Conditions. (Dr.Ing. Thesis)
IMT-2007-21	Storhaug, Gaute	Experimental Investigation of Wave Induced Vibrations and Their Effect on the Fatigue Loading of Ships. (Dr.Ing. Thesis)
IMT-2007-22	Sun, Hui	A Boundary Element Method Applied to Strongly Nonlinear Wave-Body Interaction Problems. (PhD Thesis, CeSOS)
IMT-2007-23	Rustad, Anne Marthine	Modelling and Control of Top Tensioned Risers. (PhD Thesis, CeSOS)
IMT-2007-24	Johansen, Vegar	Modelling flexible slender system for real-time simulations and control applications
IMT-2007-25	Wroldsen, Anders Sunde	Modelling and control of tensegrity structures. (PhD

		Thesis, CeSOS)
IMT-2007-26	Aronsen, Kristoffer Høye	An experimental investigation of in-line and combined inline and cross flow vortex induced vibrations. (Dr. avhandling, IMT)
IMT-2007-27	Gao, Zhen	Stochastic Response Analysis of Mooring Systems with Emphasis on Frequency-domain Analysis of Fatigue due to Wide-band Response Processes (PhD Thesis, CeSOS)
IMT-2007-28	Thorstensen, Tom Anders	Lifetime Profit Modelling of Ageing Systems Utilizing Information about Technical Condition. (Dr.ing. thesis, IMT)
IMT-2008-29	Berntsen, Per Ivar B.	Structural Reliability Based Position Mooring. (PhD-Thesis, IMT)
IMT-2008-30	Ye, Naiquan	Fatigue Assessment of Aluminium Welded Box-stiffener Joints in Ships (Dr.ing. thesis, IMT)
IMT-2008-31	Radan, Damir	Integrated Control of Marine Electrical Power Systems. (PhD-Thesis, IMT)
IMT-2008-32	Thomassen, Paul	Methods for Dynamic Response Analysis and Fatigue Life Estimation of Floating Fish Cages. (Dr.ing. thesis, IMT)
IMT-2008-33	Pákozdi, Csaba	A Smoothed Particle Hydrodynamics Study of Two-dimensional Nonlinear Sloshing in Rectangular Tanks. (Dr.ing.thesis, IMT)
IMT-2007-34	Grytøyr, Guttorm	A Higher-Order Boundary Element Method and Applications to Marine Hydrodynamics. (Dr.ing.thesis, IMT)
IMT-2008-35	Drummen, Ingo	Experimental and Numerical Investigation of Nonlinear Wave-Induced Load Effects in Containerships considering Hydroelasticity. (PhD thesis, CeSOS)
IMT-2008-36	Skejic, Renato	Maneuvering and Seakeeping of a Singel Ship and of Two Ships in Interaction. (PhD-Thesis, CeSOS)
IMT-2008-37	Harlem, Alf	An Age-Based Replacement Model for Repairable Systems with Attention to High-Speed Marine Diesel Engines. (PhD-Thesis, IMT)
IMT-2008-38	Alsos, Hagbart S.	Ship Grounding. Analysis of Ductile Fracture, Bottom Damage and Hull Girder Response. (PhD-thesis, IMT)
IMT-2008-39	Graczyk, Mateusz	Experimental Investigation of Sloshing Loading and Load Effects in Membrane LNG Tanks Subjected to Random Excitation. (PhD-thesis, CeSOS)
IMT-2008-40	Taghipour, Reza	Efficient Prediction of Dynamic Response for Flexible amd Multi-body Marine Structures. (PhD-thesis, CeSOS)
IMT-2008-41	Ruth, Eivind	Propulsion control and thrust allocation on marine vessels. (PhD thesis, CeSOS)

IMT-2008-42	Nystad, Bent Helge	Technical Condition Indexes and Remaining Useful Life of Aggregated Systems. PhD thesis, IMT
IMT-2008-43	Soni, Prashant Kumar	Hydrodynamic Coefficients for Vortex Induced Vibrations of Flexible Beams, PhD thesis, CeSOS
IMT-2009-43	Amlashi, Hadi K.K.	Ultimate Strength and Reliability-based Design of Ship Hulls with Emphasis on Combined Global and Local Loads. PhD Thesis, IMT
IMT-2009-44	Pedersen, Tom Arne	Bond Graph Modelling of Marine Power Systems. PhD Thesis, IMT
IMT-2009-45	Kristiansen, Trygve	Two-Dimensional Numerical and Experimental Studies of Piston-Mode Resonance. PhD-Thesis, CeSOS
IMT-2009-46	Ong, Muk Chen	Applications of a Standard High Reynolds Number Model and a Stochastic Scour Prediction Model for Marine Structures. PhD-thesis, IMT
IMT-2009-47	Hong, Lin	Simplified Analysis and Design of Ships subjected to Collision and Grounding. PhD-thesis, IMT
IMT-2009-48	Koushan, Kamran	Vortex Induced Vibrations of Free Span Pipelines, PhD thesis, IMT
IMT-2009-49	Korsvik, Jarl Eirik	Heuristic Methods for Ship Routing and Scheduling. PhD-thesis, IMT
IMT-2009-50	Lee, Jihoon	Experimental Investigation and Numerical in Analyzing the Ocean Current Displacement of Longlines. Ph.d.-Thesis, IMT.
IMT-2009-51	Vestbøstad, Tone Gran	A Numerical Study of Wave-in-Deck Impact usin a Two-Dimensional Constrained Interpolation Profile Method, Ph.d.thesis, CeSOS.
IMT-2009-52	Bruun, Kristine	Bond Graph Modelling of Fuel Cells for Marine Power Plants. Ph.d.-thesis, IMT
IMT 2009-53	Holstad, Anders	Numerical Investigation of Turbulence in a Sekwed Three-Dimensional Channel Flow, Ph.d.-thesis, IMT.
IMT 2009-54	Ayala-Uraga, Efren	Reliability-Based Assessment of Deteriorating Ship-shaped Offshore Structures, Ph.d.-thesis, IMT
IMT 2009-55	Kong, Xiangjun	A Numerical Study of a Damaged Ship in Beam Sea Waves. Ph.d.-thesis, IMT/CeSOS.
IMT 2010-56	Kristiansen, David	Wave Induced Effects on Floaters of Aquaculture Plants, Ph.d.-thesis, IMT/CeSOS.
IMT 2010-57	Ludvigsen, Martin	An ROV-Toolbox for Optical and Acoustic Scientific Seabed Investigation. Ph.d.-thesis IMT.